KIT SCIENTIFIC REPORTS 7567

Melt Dispersion and Direct Containment Heating (DCH) Experiments for KONVOI Reactors

L. Meyer, G. Albrecht, M. Kirstahler, M. Schwall, E. Wachter, X. Gaus-Liu

Institut für Kern- und Energietechnik
Programm Nukleare Sicherheitsforschung

KIT Scientific Publishing

L. Meyer, G. Albrecht, M. Kirstahler, M. Schwall, E. Wachter,

X. Gaus-Liu

Melt Dispersion and Direct Containment Heating (DCH) Experiments for KONVOI Reactors

Karlsruhe Institute of Technology
KIT SCIENTIFIC REPORTS 7567

Melt Dispersion and Direct Containment Heating (DCH) Experiments for KONVOI Reactors

by
L. Meyer,
G. Albrecht,
M. Kirstahler,
M. Schwall,
E. Wachter,
X. Gaus-Liu

Institut für Kern- und Energietechnik
Programm Nukleare Sicherheitsforschung

KIT Scientific Publishing

Report-Nr. KIT-SR 7567

Impressum

Karlsruher Institut für Technologie (KIT)
KIT Scientific Publishing
Straße am Forum 2
D-76131 Karlsruhe
www.ksp.kit.edu

KIT – Universität des Landes Baden-Württemberg und nationales
Forschungszentrum in der Helmholtz-Gemeinschaft

KIT Scientific Publishing 2011
Print on Demand

ISSN 1869-9669
ISBN 978-3-86644-579-6

Abstract

The DISCO-H test facility was set up to perform scaled experiments that simulate melt ejection scenarios under low system pressure in Severe Accidents in Pressurized Water Reactors (PWR). These experiments are designed to investigate the fluid-dynamic, thermal and chemical processes during melt ejection out of a breach in the lower head of a PWR pressure vessel at pressures around and below 2 MPa with an iron-alumina melt and steam.

The main components of the facility are scaled about 1:18 linearly to large European pressurized water reactors. Standard test results are: pressure and temperature history in the RPV, the cavity, the reactor compartment and the containment, post test melt fractions in all locations with size distribution of the debris, video film in reactor compartment and containment (timing of melt flow and hydrogen burning), and pre- and post test gas analysis in the cavity and the containment.

Eight tests were performed in Konvoi geometry with holes in the center of the reactor pressure vessel (RPV) lower head (1 m diameter scaled), using an iron-alumina melt driven out of the RPV by steam, and an atmosphere of air, steam and 5% hydrogen with 0.2 MPa in the containment vessel. The geometries of the reactor pit of the Konvoi plant and the European Pressurized Reactor (EPR) are similar with two distinct differences regarding the flow paths out of the lower pit: In the EPR the flow path into the refueling room above the reactor pit can be considered to be closed for all possible DCH cases, while in the Konvoi reactor it is open if the overpressure in the pit is more than 0.2 MPa. The Konvoi cavity has a biological shield and pressure venting flaps behind the shield, which can be assumed to be open and serve as a large path into the neighboring compartments. This flow path could be blocked by water during an accident if its level is high enough.

For the base case of the tests series both of these flow paths were closed. The standard flow path out of the pit was that along the 8 main cooling lines leading into a subcompartment which is connected to the containment dome by large openings. To investigate the effect of the breach size one test was conducted with a smaller hole in the lower head (0.5 m diameter scaled). Two tests were performed with lower RPV pressures and one with a higher hydrogen concentration in the containment atmosphere. In one test the flow path into the refueling room was open, and another test was conducted with open pressure venting flaps and water behind the bio-shield and in the subcompartment.

With identical initial conditions in the EPR and the Konvoi plants similar results for the containment pressure can be expected, provided the flow paths into the refueling room and behind the bio-shield stay closed and the space behind the bio-shield remains dry. Lower initial RPV pressures and smaller breach sizes lead to less melt dispersion out of the reactor pit and thus to lower containment pressure increase.

If the flow path through the vessel support into the refueling room is open, a mitigating effect occurs. A considerable amount of debris and hydrogen is trapped in this small compartment and does not contribute to pressure increase in the containment, provided that the concrete slaps, which cover this room, stay in place. However, if the overpressure in the pit is high enough to open the path at the vessel support it might also be high enough to lift the con-

crete plates in the refueling room, and a direct path into the containment would be available, which means an enhancing effect for DCH.

The open flow path behind the bio-shield together with the presence of water leads to low values of the containment pressure increase. About half of the melt dispersed out of the pit is entrained through the venting flaps behind the bio-shield and enters the water where it is quenched. Very little hydrogen is produced and little burned, and consequently the pressure increase is low.

A higher initial hydrogen concentration in the containment leads to substantial higher containment pressures. The more hydrogen exists before the blowdown the higher is the fraction of burnt hydrogen. The total amount of hydrogen burnt correlates with the containment pressure increase. The maximum pressure increase in the containment measured was 0.4 MPa.

Experimente zur Dispersion der Kernschmelze und der direkten Aufheizung des Sicherheitsbehälters (DCH) für KONVOI Reaktoren

Zusammenfassung

Die Versuchsanlage DISCO-H wurde gebaut um Experimente durchzuführen, zur Untersuchung der Dispersion der Kernschmelze und der direkten Aufheizung des Containments (DCH) bei Versagen des Druckbehälters bei niedrigem Systemdruck während eines schweren Störfalles eines Leichtwasser Druckreaktors. Es werden die fluid-dynamischen, thermischen und chemischen Prozesse modelliert, die bei einem Versagen der Bodenkalotte des Reaktordruckbehälters (RDB) und dem anschließenden Ausströmen der Schmelze auftreten. Eine Eisen-Aluminiumoxid Schmelze wird durch Dampf bei Drücken von etwa 2 MPa oder weniger ausgetrieben.

Die wichtigen Komponenten der Anlage sind im Maßstab 1:18 in Bezug auf einen großen europäischen Reaktor modelliert. Folgende Größen werden im Versuch bestimmt: die Druck- und Temperaturverläufe im RDB, in der Reaktorgrube, den Reaktorräumen und dem Sicherheitsbehälter; die Schmelzeanteile an allen Orten, zusammen mit der Größenverteilung der Partikel; Videofilme im Reaktorraum und im Sicherheitsbehälter zur Bestimmung der Dauer des Partikelfluges und der Wasserstoffflamme; und Gasanalysen an drei Orten vor, während und nach dem Versuch.

Acht Versuche wurden in der Konvoi-Geometrie durchgeführt, mit einem zentralen Loch in der unteren Kalotte (1 m Durchmesser skaliert) des Reaktordruckbehälters (RDB), mit einer dampfgetriebenen Eisen-Aluminiumoxid-Schmelze und einer Atmosphäre im Containmentbehälter von 0.2 MPa bestehend aus Luft, Dampf und 5% Wasserstoff. Die Geometrien der Reaktorgrube des Konvoi Reaktors und des Europäischen Druckwasserreaktors EPR sind ähnlich mit zwei wichtigen Unterschieden in Bezug auf die Strömungspfade aus der Grube: Beim EPR kann angenommen werden, dass der Strömungspfad in den Reaktorraum oberhalb des RDB für DCH relevante Fälle geschlossen ist, während dieser Pfad beim Konvoi Reaktor ab einer Druckdifferenz von 0.2 MPa als offen angenommen werden muss. Die Konvoi-Grube besitzt ein biologischen Schild und Druckausgleichsklappen im Tragschild, die einen großen Strömungspfad in dahinterliegende Räume freigeben. Allerdings kann dieser Strömungspfad während eines Unfalles durch Wasser blockiert sein, wenn der Wasserstand hoch genug ist.

Im Basisversuch waren diese beiden Strömungspfade verschlossen. Der normale Strömungspfad aus der Grube führt entlang der Kühlmittelleitungen in einen Ringraum, der durch große Öffnungen mit dem Kuppelbereich des Sicherheitsbehälters verbunden ist. Ein Versuch wurde mit einem kleineren Versagensquerschnitt durchgeführt (0.5 m Durchmesser skaliert). Zwei Versuche wurden bei niedrigeren RDB-Versagensdrücken und ein Versuch mit höherer Wasserstoffkonzentration im Sicherheitsbehälter durchgeführt. Bei einem Versuch war der Strömungspfad in den Reaktorraum oberhalb des RDB offen und in einem anderen waren die Druckausgleichsklappen hinter dem biologischen Schild geöffnet. In diesem Fall befand sich Wasser hinter dem Schild und in dem angrenzenden Raum.

Mit gleichen Anfangsbedingungen können ähnliche Ergebnisse für den EPR und den Konvoi Reaktor in Bezug auf die Druckerhöhung im Sicherheitsbehälter erwartet werden, vorausgesetzt die Strömungspfade in den oberen Reaktorraum und hinter dem biologischen Schild bleiben geschlossen und der Raum hinter dem Schild bleibt trocken. Niedrigere Drücke beim Versagen des RDB und kleinere Versagensquerschnitte führen zu weniger Schmelzedispersion und niedrigeren Druckanstiegen im Sicherheitsbehälter.

Ein offener Strömungspfad in den oberen Reaktorraum verursacht einen geringeren Druckaufbau. Ein beträchtlicher Anteil von Schmelze und Wasserstoff gelangt in diesen kleinen Raum und trägt nichts zum Druckanstieg im Containment bei, vorausgesetzt die Abdeckplatten aus Beton bleiben intakt. Wenn jedoch der Überdruck in der Grube hoch genug ist um die Dichtbleche an der RDB Tragkonstruktion zu öffnen, könnte der Druck auch in dem darüberliegenden Reaktorraum hoch genug werden die Betonplatten anzuheben, so dass ein direkter Pfad von der Grube in den Containmentdom vorhanden wäre, was zu einer Verstärkung des DCH Effektes führt.

Ein offener Strömungspfad hinter dem biologischen Schild zusammen mit der Anwesenheit von Wasser führt zu geringem Druckanstieg im Containment. Etwa die Hälfte der aus der Grube ausgetragenen Schmelze gelangt durch die Lüftungsklappen ins Wasser, wo sie abgeschreckt wird. Sehr wenig Wasserstoff wird erzeugt und wenig wird verbrannt, und daraus folgt ein niedriger Druckanstieg.

Eine hohe Anfangskonzentration von Wasserstoff im Containment führt zu hohen Containmentdrücken. Je mehr Wasserstoff anfangs im Containment vorhanden ist, umso höher ist der Anteil des Wasserstoffs der verbrennt. Die verbrannte Menge des Wasserstoffs korreliert direkt mit dem Druckanstieg im Containment. Der maximal gemessene Druckanstieg betrug 0.4 MPa.

TABLE OF CONTENTS

LIST OF TABLES

LIST OF FIGURES

1 Introduction

In case of a core meltdown accident in a nuclear power plant, liquid corium containing metals and oxides may relocate into the lower head of the reactor vessel. If the lower head fails in this condition, with an in-vessel pressure higher then the containment pressure, the molten corium will be forcefully ejected into the reactor pit, finely fragmented and eventually transported outside the reactor pit. The efficient heat transfer from the melt particles to the gas, together with combustion of hydrogen previously released into the reactor building and produced during melt dispersion, will heat-up and pressurize the containment atmosphere. These processes, referred to as Direct Containment Heating (DCH), may endanger the integrity of the containment.

The safety philosophy applied to all plants worldwide is to prevent high pressure core melt situations by depressurization of the primary system below 2 MPa. The consequences of DCH depend on the pressure at RPV failure, the breach characteristics, the amount and characteristics of the molten mass and on the layout of the reactor pit and reactor building. Therefore, the evaluation of DCH consequences must be plant dependent.

DCH phenomena have been extensively investigated between 1986 and 1998 for reactors of US-design (PWR: Zion and Surry, Westinghouse), which are characterized by a large instrumentation tunnel connecting the reactor pit with relatively small compartments [Bla96, Pil96a]. A few experiments were performed for a cavity without such connection and an annular cavity design (PWR: Calvert Cliffs, Combustion Engineering), where the main large pathway out of the cavity is along the annular gap between the RPV and the cavity wall with direct access to the containment dome [Bla97, Bla99]. The state of the art as of 1996 was given by Pilch et al. [Pil97] and in a topical issue on DCH in Nuclear Engineering Design [Nuc96].

In 1998 a program was started to investigate the DCH issue for European reactor designs. Two test facilities were built at Forschungszentrum Karlsruhe (FZK). The facility DISCO-C was suited for the investigation of fluid dynamic phenomena, such as the two-phase jet, liquid fragmentation, liquid film formation at walls, entrainment and trapping of liquid, and liquid dispersion and deposition [Mey03] and [Mey06]. In the other facility, DISCO-H, integral tests can be performed including all relevant DCH phenomena [Mey04]. Both facilities can model specific reactor geometries in sufficient detail, to take account of the geometry dependence of the processes.

Most European PWRs have an annular cavity design, with a flow path around the main cooling lines into pump and steam generator rooms, and in some cases with a direct flow path from the reactor pit into the upper dome of the containment. These reactor geometries were investigated experimentally and analytically at Forschungszentrum Karlsruhe (FZK), comprising the EPR [Mey04], the French 1300 MWe plant P'4 [Mei05], the VVER 1000/320 [Mia08] and finally the German Konvoi plant. A compilation and comparison of these results is presented in [Mey09]. The results of eight experiments with Konvoi geometry are presented in the present report.

2 Geometry of the KONVOI reactor cavity and its modeling for DCH experiments

2.1 Flow cross sections and reactor room volumes

Since the effect of the DCH processes in respect to containment pressure increase depends on the size and location of the flow paths out of the reactor pit into the containment dome and the volumes of the intermediate reactor rooms, the Konvoi geometry has been analysed accordingly by GRS[1] [Löf02], [Lin01], [Sch07], [Spe07]. Fig. 2-1 shows a scheme of the cross section of the reactor pit and four potential flow paths (A through D).

The total flow cross section along the 8 main cooling lines (A) was evaluated to 2.0 m² if the insulation stays intact, and to 3.3 m² if the insulation is discharged (removed or burned by the hot debris). In the DISCO facility this flow path is modeled by 8 annular channels with a total cross section of 2.74 m² scaled 1:18.5, that is an average value between the minimum and the maximum to be expected.

The flow cross section B from the pit into the reactor room above the pressure vessel is difficult to assess, because it is above (downstream) of the vessel support structure, which blocks any direct flow path. Also, during normal operation, the cross section is closed by sealing plates, which may break down when the overpressure in the pit is above 2 bar. Again, there is a large difference in the cross section, whether insulation stays in place or is removed. However, the actual size of the flow cross section is less critical for the DCH effect, because the reactor room above is relatively small and has only small connections to adjoining rooms. Assuming the breakdown of the sealing plates the flow cross section was estimated to be 1.8 m² with intact insulation and 5.7 m² without. Due to the blocking by the vessel support structures these values should be reduced by 55 %, which results in an assumed flow cross section of 0.8 m² minimum and 2.5 m² maximum. In the DISCO facility the flow path B was formed by eight holes with a total cross section of 2.48 m² scaled, with a plate in front of the holes blocking the straight flow path.

The 8 pressure venting flaps (C) can be assumed to be open (0.94 m² each) during the accident and water would be behind the biological shield. According to experts judgment this flow path can be assumed to be closed for the DCH scenario. It should, however, be checked if the water column can be driven out during the DCH time scale.

The inspection door (D) can be assumed to be closed and not available as a flow path.

Thus, there are only two open flow paths out of the pit, (A) along the main cooling lines into steam generator rooms and (B) through the vessel support structure into the refueling room 27, which may be closed, if the pressure difference is not high enough. A possible third flow path through the pressure venting flaps (C) may exist, if the water level is low enough.

---

[1] Gesellschaft für Anlagen- und Reaktorsicherheit (GRS) mbH, Köln

Fig. 2-2 and Fig. 2-3 show a sketch of the reactor rooms adjacent to the cavity. Rooms 27 (640 m³) and 28 (405 m³) are connected by a large opening of 10 m² (F). Therefore, these two rooms are combined to one room in the DISCO model, named subcompartment 2 (SC2). Room 27 is connected to the steam generator rooms by two pressure venting flaps with a cross section of 1 m² each, which open at 80 mbar differential pressure (path E). These openings are modeled in DISCO accordingly, but without flaps. The reactor room 27 (refueling room) is covered with concrete slabs, which stay in place up to an overpressure of 0.8 bar. The experiment can be conducted with or without the cover plate (closed or open).

The steam generator and connected rooms (combined volume of 16630 m³) are modeled as one compartment (SC1). They are closed against the upper containment dome with approximately 240 rectangular burst diaphragms with a total cross section of 200 m² scaled. Since they would fail at a differential pressure of 48 mbar, this cross section is modeled as an open path with four large holes in the cover of subcompartment 1 (SC1) (see Fig.3-3).

2.2 Geometric scaling

In the DISCO facility the outer diameter of the reactor pressure vessel model is a parameter which cannot be varied much. Therefore it was kept unchanged relative to the preceding experiments with EPR and P'4 geometry. The scaling of the experiment is defined by the ratio between the diameter of the KONVOI reactor pressure vessel and the DISCO model. The linear scale is determined to 1:18.47, accordingly the area scale is 1:341 and volumes should scale by 1:6300.

Because the volume of the containment vessel cannot be changed easily the model volume is too large by 2.4 m³ (almost 20%). All other model volumes come very close to the correct scale. Table 2-1 shows a summary of the scaling characteristics, exact data can be found in Table 3-1.

Table 2-1 Geometric scaling of the KONVOI reactor by the DISCO setup

		KONVOI	DISCO	scale
RPV outer diameter	mm	5512	298.5	18.47
Containment volume	m³	72300	13.88	17.34
Room 27+28 = subcompartment 2	m³	1045	0.146	19.10
Equipment rooms = subcompartment 1	m³	16630	2.78	18.15
Pressure venting flaps (E)	m²	2	0.003	18.25
Burst diaphragms (G) (4 x Ø 0,433 m)	m²	200	0.59	18.41
Vessel support (B) (8 x Ø 0,034 m)	m²	*2.28*	0.0073	18.47
Main cooling lines (A) (8 x 0,0584 m)	m²	*2.73*	0.008	18.47
Pressure venting flaps (C) (8 x 0,94 m²)	m²	*7.52*	0.0226	18.24

2.3 Test matrix

GRS suggested conducting tests with modifications of the geometry and the initial conditions for model validation purposes in the codes COCOSYS and ASTEC. The following test matrix was proposed:

Table 2-2 Intended test matrix

	Reference case	Variation Pressure		Variation Leak diameter	Variation cavity	Variation H2-concentration	Variation pressure venting flaps
Pressure [bar]	20	**12**	**8**	20	20	20	20
Leak diameter [mm]	56	56	56	**28**	56	56	56
H2-concentration [mol-%]	5	5	5	5	5	**10**	5
Cavity	closed	closed	closed	closed	**open**	closed	closed
Pressure venting flaps	closed	closed	closed	closed	closed	closed	**open**

Test No.	KH02	KH05	KH06	KH03	KH01 KH04	KH07	KH08

Because of difficulties to obtain exactly the planned RPV pressure at plug failure and the initial hydrogen concentration in the containment, the initial conditions in the performed tests deviated from the planned in this respect.

Table 2-3 Performed tests

Test	**Breach diameter [mm]**	**RCS/RPV Pressure [MPa]**	**Hydrogen %**	**Path to refueling room**	**Pressure venting flaps**
KH01	56	2.6	5.4	**open**	closed
KH02	56	2.0	5.4	closed	closed
KH03	28	2.0	6.7	closed	closed
KH04	56	2.0	5.7	**open**	closed
KH05	56	1.2	5.2	closed	closed
KH06	56	1.0	6.5	closed	closed
KH07	56	1.8	8.7	closed	closed
KH08	56	2.1	5.4	closed	Open with water

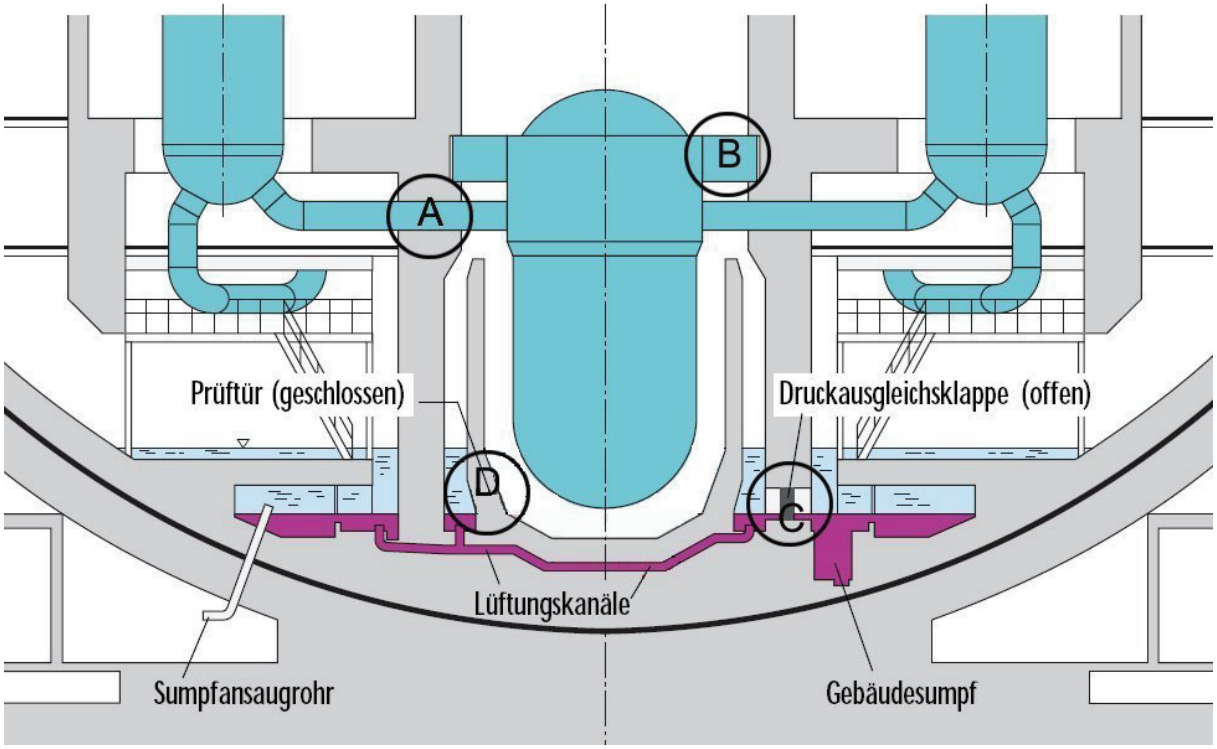

Fig. 2-1. Cross section of reactor pit and potential flow paths to adjacent reactor rooms

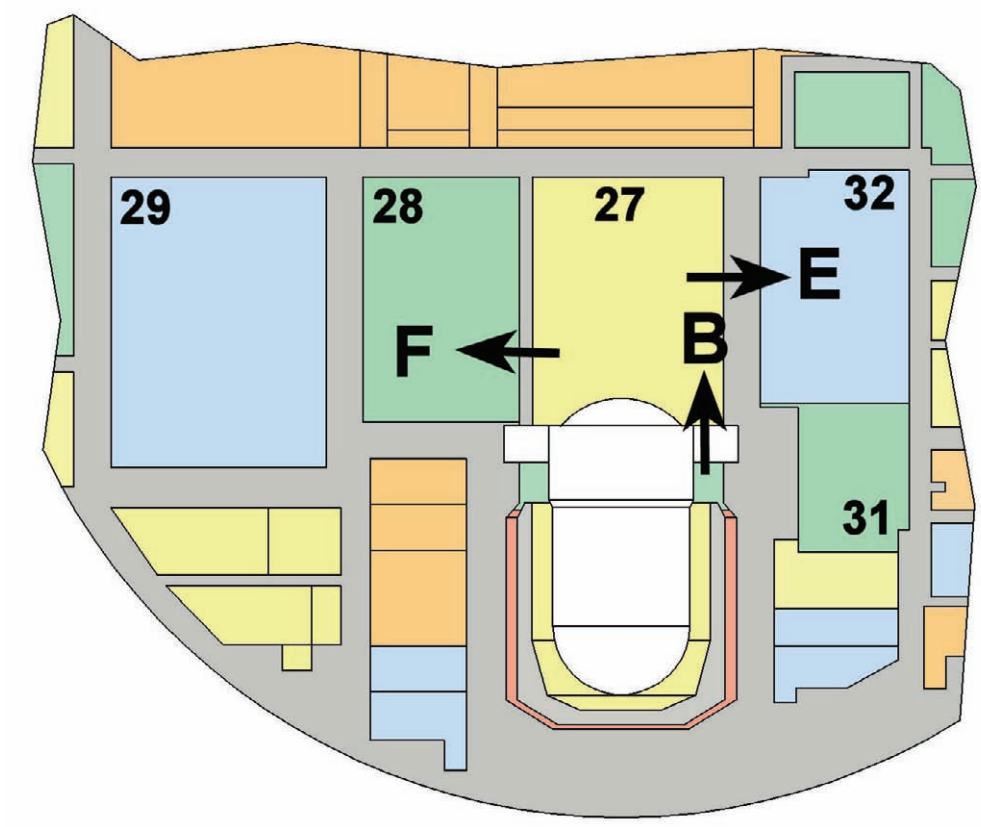

Fig. 2-2. Vertical cross section of reactor pit and adjacent reactor rooms

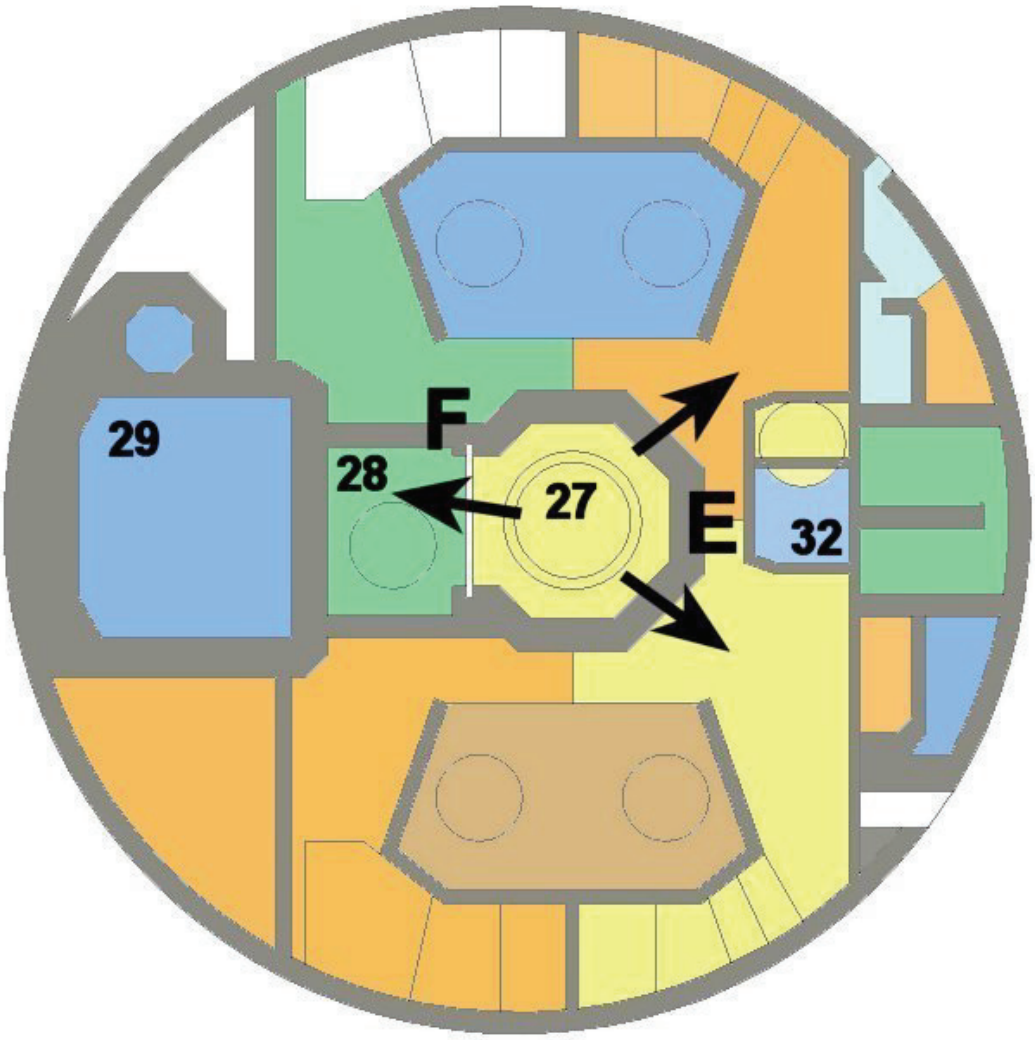

Fig. 2-3. Horizontal cross section of reactor pit and adjacent reactor rooms

3 Facility and Experiment Description

3.1 Components of the facility

3.1.1 The containment pressure vessel (CPV)

The containment pressure vessel is a cylindrical pressure vessel made of 15 mm steel and is rated at 1.0 MPa and 200°C. It has an outer diameter of 2.20 m and a height of 4.60 m; with the pedestal and the top port its total height is 5.80 m (see Fig. 3-1 and Fig. 3-2, for data see Table 3-1). The pressure vessel consists of two segments and a lower and an upper head. Each segment has six instrument penetration ports at two levels each labeled A through D. One of the level C ports is closed with a safety rupture disk (diameter 200 mm), with a burst pressure of 1 MPa. The lower head is filled with concrete that forms a level floor. All internal structures are bolted to that floor. At the center of the floor is a large vertical pipe that contains the condensate draining piping and has a connection to the bottom port. The connection of this pipe with the containment volume is via one 10 mm draining pipe in the concrete cavity floor and several draining pipes in the containment floor. The entire vessel is insulated against heat loss on the outside by 100 mm thick fiberglass insulation. The empty volume of the containment vessel is 14.18 m³.

3.1.2 Subcompartment 1(SC1)

The subcompartment 1 is an annular space around the cavity and the subcompartment 2 (SC2). The flow path (A) from the cavity into SC1 is along the eight stubs modeling the main cooling lines. The top cover of the subcompartment has four openings with a diameter of 433 mm (Fig. 3-2 through Fig. 3-6). In case there is water in SC1, a separation plate with large covered openings is installed in order to prevent melt which enters SC1 through flow path (A) or the opening in the top cover, dropping into water (Fig. 3-14).

3.1.3 Subcompartment 2 (SC2)

The subcompartment 2 is also an annular space which is located above the RPV and cavity. The outer wall includes two small opposing apertures acting as a connection to the subcompartment 1 (flow path E). Eight openings located in the top plate of the cavity lead into the subcompartment 2 (flow path B). (Fig. 3-2, Fig. 3-7 and Fig. 3-8). These openings can be closed by steel plates for modeling the case where the overpressure in the cavity is not high enough to open this flow path. The top cover of subcompartment 2 can be taken off for the simulation of removal of the concrete slabs by overpressure in this room.

3.1.4 The pressure vessel modeling the RCS and RPV volume

The RCS-RPV pressure vessel models the volumes of both the reactor cooling system (RCS) and the reactor pressure vessel (RPV) (Fig. 3-2, Fig. 3-6 and Fig. 3-8) and has a total volume of 0.0883 m³. A disk holding 8 pipes (46 mm I.D., 255 mm length) separates the two partial volumes. This arrangement models the main cooling lines with respect to the flow

constriction between RCS and RPV. The cylinders (I.D. 200 mm) modeling the RCS and RPV are heated electrically and are insulated over the whole length and on the top.

3.1.5 The reactor pressure vessel (RPV) model

The RPV model that serves as crucible for the generation of the melt, is bolted to a plate carrying the RCS-RPV pressure vessel (Fig. 3-8**,** Fig. 3-9 and Fig. 3-11). An insulation material of magnesium oxide (MagneRam®) is filled between the outer shell of the RPV model and an inner steel cylinder that contains the thermite powder. The hole at the bottom of the melt generator is formed by a graphite annulus (Fig. 3-22). It is closed with a brass plate (weight 425 g, Fig. 3-16 and Fig. 3-17).

3.1.6 The reactor pit

The cavity and RPV-hold-down were designed to withstand a pressure of 10 MPa with a safety factor of 2 to yield. The reactor pit is made of concrete (Fig. 3-10 and Fig. 3-11) and is installed inside a strong steel cylinder (30 mm thick wall). This cylinder is clamped by 8 bolts (56 mm diameter) between a base plate and a top plate, both 90 mm thick (see Fig. 3-2). There are three potential exits out of the pit, (A) along the main cooling lines leading into SC1 with 0.008 m², (B) through the vessel support leading into SC2 with 0.0073 m² cross section and (C) the eight pressure venting flaps behind the bio-shield also leading into SC1, but near the bottom, with a total cross section of 0.0226 m² (Fig. 3-13, Table 3-1).

3.1.7 Steam accumulator

The steam accumulator is a cylindrical pressure vessel placed outside of the containment pressure vessel with approximately the same volume as the RCS-RPV pressure vessel and is rated at 3.0 MPa and 250°C (Fig. 3-2 and Fig. 3-23). Both vessels are connected by a 25 mm diameter pipe with an electro-pneumatically actuated valve. The vessel is electrically heated from the outside and is insulated by fiberglass. The required amount of steam is generated inside the steam accumulator.

3.1.8 Steam generator

The steam generator serves for heating up the containment vessel and providing the steam for the initial containment atmosphere. It has a capacity of 42 kg/h steam (32 kW) at 1 MPa.

3.2 Instrumentation and measurements

3.2.1 Temperature

Temperatures are measure by steel sheathed K-type thermocouples (NiCr-Ni) with an outer diameter of 0.36 mm. The time constant for gas temperature measurement is between 0.5 s and several seconds, depending on the heat transfer coefficient, with an estimate for our conditions of 0.6 s < τ < 1.2 s. Therefore all temperature signals for gas will be attenuated. The steam temperature in the accumulator tank is measured by two thermocouples, one near the top and one near the bottom. There are two thermocouples within the RCS-RPV

pressure vessel, one in each compartment (RCS and RPV, Fig. 3-8). Six thermocouples are located at different levels in the containment pressure vessel (CPV, level A through D) to measure the bulk gas temperature. Four thermocouples are within the subcompartment 1 and 2 at different positions listed in Table 3-2 and shown in Fig. 3-15. The data acquisition system records the signals of the 25 thermocouples that are listed in Table 3-2, at a rate of 2000 samples per second per channel. A large number of thermocouples are installed at the outside of the steam accumulator tank and the RCS-RPV pressure vessel to control the electric heaters. These temperatures are monitored at the heater control board.

The brass plate serving as melting plug at the bottom of the lower head is instrumented with three thermocouples to monitor the progress of the melting and thereby opening process (Fig. 3-16 and Fig. 3-17).

3.2.2 Pressure

A total of 15 strain gauge-type pressure transducers (13 Kulite® and 2 Kistler®) with ranges of 0–1.7 MPa, 0–3.5 MPa and 0–5.0 MPa are used to measure steam and gas pressures (Table 3-3). The compensated operating temperature range is 27°C – 232°C, with a thermal drift of +/- 5% of full scale output for the Kulite transducers. The Kistler transducers were mounted outside the facility in cold environment connected with a pipe to the measurement position. They were used as reference for the Kulite transducers during stationary periods of the experiment. The Kulite transducers were adjusted at the operating temperature just before the start of the experiment. All gages are mounted in tapped holes that are connected gas tight with the outside atmosphere at their backsides. In case of the transducers in the RCS-RPV pressure vessel, the compartment, and the cavity, this connection is achieved by flexible steel hoses. The gages in the containment pressure vessel are mounted in blind flanges of the ports at different levels (see Fig. 3-18 and Table 3-3). The data acquisition system records data at a rate of 2000 data points per second per channel.

3.2.3 Gas composition

Ten pre-evacuated 500-cm³ gas grab sample bottles are used to collect dry-basis gas samples at three positions, in the subcompartment 1 and 2 respectively, and in the upper part of the containment (Fig. 3-19). The sample lines and the sample bottles are at room temperature, thus the bottles are being filled with non-condensable gases and steam that condenses. One pretest sample is taken just prior to the start of the melt ejection to determine the initial gas composition. One sample at all three stations each is taken 5 seconds and one 5 minutes after the blow down. The gas samples are analyzed at the Engler-Bunte-Institut at the University of Karlsruhe. The objective of the gas composition measurements and gas analysis is to obtain data on the chemical reactions taking place during the blow-down, that is, the production of hydrogen by the metal/steam reaction and the hydrogen combustion.

3.2.4 Debris recovery and sieve analysis

The total debris mass dispersed into the DISCO vessel and the debris mass in specific locations are determined by a post test debris recovery procedure. Loose particles are collected by a vacuum cleaner and weighed separately for each location. The total weight of crusts is

determined by pre- and post-test weighing of all parts of the test facility, or if not possible, by removing the crusts from the parts and weighing of them. Basically, the debris is determined in four locations, reactor pit, subcompartments 1 and 2, and the containment vessel. A finer subdivision is made during the collecting procedure, which can be seen in the detailed debris recovery results. The mass balance between initial thermite charge and recovered debris must take into account the additional masses from the molten part of the brass plug (between 180 g and 425 g), possible melting of the inner wall of the crucible in the RPV, ablation of concrete in the cavity, contaminants (break wire, thermocouples, etc.) and oxidation of metallic debris (mainly iron). For each g-mole of produced hydrogen approximately 16 g of additional debris (iron oxide) must be considered. With an average amount of 30 g-moles of produced hydrogen, additional 480 g of debris should be recovered.

A post test sieve analysis of the debris recovered from different locations is performed for each test (Fig. 3-25 and Fig. 3-26). A standard set of 17 sieves is used (10 mm to 40 µm). Except for small pieces, crusts are generally not included in the sieve analysis. The information on the original size of the melt droplets that have formed a crust by hitting a wall is not available. This has to be taken into account when the results of the sieve analysis are evaluated.

3.2.5 Debris particle analysis

The morphology and chemical compositions of the debris particles collected from the containment, the subcontainment 1 (SC1) and the subcontainment 2 (SC2) in the test KH01 were analyzed with scanning electron microscopy (SEM). To observe the cross section of the particles they were firstly embedded in a 30-mm-diameter mould with thin epoxy resin mixture (Epofix and hardener from Struers). Different embedding methods were applied to large particles (> 2 mm) and to small particles (< 2 mm). Large particles are easily to be fixed in the resin and thus the resin was filled into the mould directly to the normal height of about 2 cm. For the fixing of small particles, a little amount of the particle powder was firstly well mixed in several drops of epoxy in the mould, after hardening of this resin in 12 hours, the rest of the resin was filled into the mould to the height of 2 cm. After hardening of the resin, the samples were taken out of the mould and the surface to be observed was ground. The grinding and polishing were performed on a grinding machine with sandpapers, stepwise from the grit size 180, 400, 800, 1200 to 2400 (< 8 µm of surface finishing). Then the prepared sample surface was coated with a thin layer of carbon to gain the electrical conductivity which is a prerequisite for the SEM analysis.

Back Scattered Electron images (BSE) were taken for the samples under 15 kV of the electron beam. For the elemental analysis energy dispersive X-ray spectroscopy (EDX) was performed on small areas in certain positions in the cross section of the particles. The composition shown in the BSE-images is in atomic percentage.

3.2.6 Additional measurements

Three video cameras are used in the experiment. Two cameras look down from the dome into the containment. A third camera is installed at the level B port looking into the subcompartment 1, to observe the melt discharging from subcompartment 2 and from the openings

around the main cooling lines (Fig. 3-20). In some tests a high speed video camera was used.

Break wires are placed across the RPV exit hole (Fig. 3-22) to give timing information on entry of debris into the cavity.

3.3 Melt scaling considerations

The geometrical linear scale is 1:18.5, thus volumes of gas and liquid are scaled accordingly by the length scale to the power of 3. Geometric scaling of the melt mass for the experiment is not strictly applicable because of material property differences between corium and thermitic iron-alumina melt. Table 3-4 shows the composition of the used thermite and of the reaction product melt. Before ejection, the major part of the melt separates into the two main components, iron on the bottom and alumina on top. Note that the melt has excess aluminum. The properties of the thermite melt mixture and those of a typical corium mixture are listed in Table 3-5 together with specific energies determined by the two-cell equilibrium (TCE) model [Pil96b] applied to a Calvert Cliffs reactor case [Bla96, Bla97, Bla99]. These data cannot be generalized, because they depend on the melt composition, temperature ranges and assumptions on the DCH processes, but they give a general idea on the order of magnitude of the differences between corium and thermite melt. The data have to be adapted to specific reactor cases.

The mass of thermite used in the experiments should be selected so that the experiments would have the same potential for pressurization as in reactor case. Important for the similarity of the thermal and chemical processes is the energy content of the melt. The chemical energy is that by the exothermic steam/metal reaction and a part of the hydrogen combustion. The maximum potential hydrogen produced by the reaction with steam is 101 moles with iron and 6 moles with aluminum. With the data from Table 3-5, the combined thermal and chemical energy is 1.49 MJ/kg for corium and 2.86 MJ/kg for the model melt. Thus the scaling of melt mass is difficult, as is shown in **Table 3-6**. The scaled up mass of 10.6 kg melt gives 66780 kg that has a volume of 17 m³ and a combined energy of 189000 MJ. On the other hand, the volume of 17 m³ corium would have a mass of 138000 kg and a total energy of 205000 MJ. The volume and energy content is scaled relatively correct (less than 10% discrepancy), while the volume to mass scaling is off by a factor of 2.

The initial pressure can be scaled 1:1, and the duration of the blowdown is scaled as the length scale. Then, the gas velocity and the droplet size are mainly functions of the properties of the model fluids used.

3.4 Melt Composition

3.4.1 Thermite composition and melt temperature

For a comparison of the experiments performed in the DISCO-H facility and tests performed in the Surtsey facility in Sandia National Laboratory (SNL) similar compositions of the melt have been used (Table 3-4) (Bla99). This specific mixture has the same ratio of iron and alu-

mina and the same temperature and energy content as that used at SNL. The stoichiometric reaction is:

$$17\ \text{mol}\ Fe_3O_4 + 22\ \text{mol}\ Fe_2O_3 + 94\ \text{mol Al} + 3\ \text{mol}\ Al_2O_3 + 5\ \text{mol Fe} \rightarrow$$
$$\rightarrow 47\ \text{mol}\ Al_2O_3 + 101\ \text{mol Fe} + 4\ \text{mol Al}$$

The theoretical temperature considering realistic reaction rates, was 2830 K. Taking account of the heat losses a temperature of 2500 K was determined for the SNL experiments. The heat losses due to radiation and conduction lead to a temperature reduction roughly given by

$$\Delta T \sim A\, \Delta t\ /\ m$$

with A, the total surface of the melt, Δt, the length of time between start of the reaction and ejection of the melt, and m, the mass of the melt. These parameters are not the same for experiments in different scales. There is the heat loss due to radiation and conduction, which is proportional to the respective surfaces, the heat sink by melting part of the liner and by vaporizing part of aluminum and brass. It is impossible to determine those losses without a large uncertainty, but they are smaller in DISCO than in the larger scale of the SNL experiment. On the other hand, the melt mass in DISCO is only about 1/6 of that in the SNL experiment, which would lead to a higher temperature reduction. The time between ignition and plug failure is shorter in DISCO, between 3.5 and 6 seconds versus approximately 13 seconds in SNL tests. If we introduce the respective data into the above relation, we see that the temperature drop of the melt in DISCO should be similar to that in the SNL experiments. However, the total uncertainty in the melt temperature is in the order of $\pm$ 100 K. Measurements with pyrometers gave similar uncertainties.

3.4.2 Preparation of the thermite

The grain size of the used components (Al, Fe, Fe_3O_4, Fe_2O_3) was 44 µm. The iron oxide powder is dried for 18 hours at 200°C. The powders are sieved and then mixed for 15 minutes. The density of the thermite powder is 0.8 g/cm³. The mixture is filled into the RPV-crucible and pressed (Fig. 3-24). The main purpose of the compaction of the powder is to reduce the probability for a channeling of the chemical reaction, which could lead to a premature melt plug failure. The ignition wire (about 20 cm of Pyrofuze® wire) is placed onto the surface of the pressed thermite and is covered with a layer of thermite powder.

3.5 Conduct of the experiment

The containment vessel is closed at atmospheric pressure and room temperature. For a period of up to 8 hours steam is filled into the containment vessel in addition to the air atmosphere until the pressure reaches 0.2 MPa and the gas temperature is close to 100 °C, while the condensate is frequently drained. At the end of heat-up a metered amount of hydrogen gas is added through pipes leading into the subcompartment and the upper dome. Two fans are running until the blowdown is started, to ensure a well mixed atmosphere. A gas sample is taken just before the start of the experiment.

The pressure vessel modeling the RPV and RCS volume, which is inside the containment vessel, is electrically heated to the saturation temperature of steam at the planned blowdown

pressure, e.g. to 485 K (212°C at 2.0 MPa). Before the initiation of the experiment it contains nitrogen at that temperature at 0.1 MPa.

The steam accumulator is outside of the containment vessel. The accumulator is filled with a measured amount of water. Then it is heated electrically to the saturation temperature of close to twice the planned burst pressure, e.g. 521K (248°C at 3.8 MPa). The RCS pressure vessel and the accumulator are connected by a 25 mm diameter pipe with an electro-pneumatically actuated valve.

The model of the RPV that is directly flanged to the RCS pressure vessel contains aluminum-iron oxide thermite. The experiment is started by igniting the thermite electro-chemically (Pyrofuze®) at the upper surface of the pressed thermite powder. When a pressure increase in the RPV-RCS pressure vessel verifies that the thermite reaction has started, the valve in the line connected to the accumulator is opened and steam enters the pressure vessel. The valve is closed again after one second, by that time the pressure in the RPV-RCS vessel and the accumulator has equilibrated. The amount of steam that is initially in the RCS-RPV pressure vessel is determined by the amount of water originally in the accumulator minus the water left in the accumulator. During steam flow and thereafter the thermite reaction progresses until it reaches the bottom of the RPV vessel. Three to five seconds after ignition the brass plug at the bottom of the RPV vessel is melted by the hot iron-alumina mixture. That initiates the melt ejection. By that time the pressure in the RCS-RPV pressure vessel will be higher than the preset value due to radiation heat transfer from the hot melt to the steam. The melt is driven out of the breach by the steam and is dispersed into the cavity and the containment. Due to the melt-to-gas heat transfer, exothermic metal/oxygen reactions, and hydrogen combustion the pressure and temperature in the containment pressure vessel will rise. Ten seconds after blow-down, the fans, which had been shut down before the start of the test, are started again to reach a well mixed atmosphere. Five minutes after ignition the post test gas samples are taken.

Table 3-1 Geometric parameters of the test facility (reference case)

Containment Pressure Vessel		
Diameter (inner)	m	2.170
Total empty volume of containment	m³	14.180
Volume of internal structures (RPV, cavity, etc)	m³	0.300
Total freeboard volume (incl. subcompartments)	**m³**	**13.880**
Subcompartment 1 (top part)		
Outer diameter of the annular SC1	m	1.810
Inner diameter of the annular SC1	m	0.868
Height	m	0.530
Volume	m³	1.050
Subcompartment 1 (lower part)		
Outer diameter of the annular SC1	m	1.810
Inner diameter of the annular SC1	m	0.600
Height	m	0.780
Volume	m³	1.786
Total volume subcompartment 1 (minus bolts etc.)	**m³**	**2.78**
Subcompartment 2		
Outer diameter of the annular SC2	m	0.868
Inner diameter of the annular SC2	m	0.500
Height	m	0.37
Volume	**m³**	**0.146**
RCS and RPV pressure vessel		
Inner diameter of RCS	m	0.200
Height of RCS	m	1.593
Volume of RCS	m³	0.0500
Volume of the line connecting to accumulator valve	m³	0.0011
Total volume of RCS	m³	0.0511
Height of upper RPV (same diameter as RCS)	m	0.430
Volume of upper RPV *(between RCS and flange)*	m³	0.0135
Inner diameter of lower RPV	*m*	*0.232*
Height of lower RPV	*m*	*0.071*
Volume of lower RPV(between flange and crucible)	*m³*	*0.003*
Inner diameter of lower RPV (crucible)	*m*	*0.2685*
Height of lower RPV (crucible)	*m*	*0.420*
Volume of lower RPV (crucible)	*m³*	*0.0237*
Total empty volume of RPV	m³	0.0372
Total volume of RCS and RPV	**m³**	**0.0883**
Volume of the steam accumulator	**m³**	**0.0820**

Table 3-1, continued

Cavity		
Diameter of cavity (steel)	m	0.540
Height of cavity (steel)	m	0.700
Outer diameter of RPV	m	0.2985
Volume of RPV (outer)	m³	0.0378
Inner diameter of cavity (concrete)	m	0.3595
Inner height of cavity (concrete)	m	0.440
Length from RPV bottom (lower head) to cavity floor	m	0.038
Length of annular cross section	m	0.316
Gap width between RPV and cavity wall	m	0.0305
Flow area of annulus	m²	0.0315
Flow area into bio shield	m²	0.0397
Cut out diameter at nozzles (around main cooling lines)	m	0.0584
Diameter of nozzles (main cooling lines)	m	0.0462
Flow area at nozzles (pit to subcompartment 1)	m²	0.008
Empty volume of cavity (without RPV)	m³	0.0949
Free volume of cavity (with RPV)	m³	0.0571
RPV- exit hole (carbon liner diameter)	m	0.056/0.028
RPV- exit hole area (RPV to pit)	m²	0.00246 / 0.00062
Diameter of direct path (A), pit to subcompartment 2 (8x)	m	0.034
Flow area of direct path (A), pit to subcompartment 2 (8x)	m²	0.0009
Total flow area of direct path, (pit to subcompartment 2)	m²	0.0073
Diameter of pressure venting flaps (C) (8x)	m	0.060
Total flow area of pressure venting flaps (C)	m²	0.0226

Table 3-2 Thermocouple summary for KH01

No. T	Location	Position		
		height from containment floor cm	distance from containment wall cm	angular degree
1	accumulator low			
2	accumulator top			
3	RCS top (4.4 cm)			
4	RCS low (164 cm)			
5	accumulator (water)			
6	CPV A1 (SC1)	48	46	45
7	CPV-A2 (SC1)	52	40	-177
8	CPV-A3 (SC1)	88	40	-135
9	CPV-B1 (SC1)	117	40	-177
10	CPV-B2 (SC2)	93	71 (5)*[1]	-177
11	CPV-B3 (SC2)	106	71 (5)*[1]	-177
12	CPV-C1 (CPV)	316	33	135
13	CPV-C2 (CPV)	213	69	135
14	CPV-D2 (CPV)	213	40	135
15	CPV-D3 (CPV)	256	35	-135
16	CPV-D3 (CPV)	274	9.5	-135
17	CPV-B1 (SC1)	52	40	45
18	RPV	brass melt plug - lateral		0
19	RPV	brass melt plug - lateral		45
20	RPV	brass melt plug - middle position		-
21	n/a	n/a		
22	CPV-B2 (SC2)	103	71 (5)*[1]	62
23	RPV	lower trigger		
24	CPV-B3 (SC2)	99	75 (9)*[1]	-56
25	CPV-C1 (CPV)	189	36	225
26-30	n/a	n/a		
31	building	ambient temperature		

*CPV = Containment Pressure Vessel

()*[1] = distance from SC2 wall

Table 3-3 Pressure transducer summary

No. P	Position		Position	
		range MPa	Height* cm	Angular degree
1	RPV outside, flush valve	5 (Kistler)		
2	Accumulator top flange, gauge	5 (Kistler)		
3-1	RCS top flange	3,5		
3-2	RCS top flange	3,5		
4	RCS top flange	3,5		
5	CPV A1	1,7	45	45
6	CPV A2	1,7	45	135
7	CPV B1	1,7	115	45
8	CPV C2	1,7	215	135
9	CPV B3	1,7	115	-135
10	cavity – 1 top	1,7	42	90
11	cavity – 2 bottom (bio shield)	1,7	20	-90
12	cavity – 3 top	1,7	42	-90
13	cavity – 4 bottom (bio shield)	3,5	20	90
14	Subcompartment 1	1,7		
15	Subcompartment 2 (top)	1,7		

*from concrete pit floor

Table 3-4 Thermite and melt composition

	Thermite		Melt					
	Mass kg	**Moles**	**Mass kg**	**Moles**	**Volume cm³**	**Mass Fraction**	**Mole Fraction**	**Volume Fraction**
Fe	0.30	5.37	5.64	101.03	887.2	0.53	0.66	0.33
Al	2.54	94.14	0.11	4.24	58.9	0.01	0.03	0.02
Fe_3O_4	4.00	17.28	-	-	-	-	-	-
Fe_2O_3	3.50	21.92	-	-	-	-	-	-
Al_2O_3	0.30	2.94	4.88	47.89	1733.5	0.46	0.31	0.65
Total	10.64	141.65	10.64	153.16	2679.6	1.00	1.00	1.00

Table 3-5 Material properties of the melt

Property			**Corium**	**Simulant melt**
Effective molecular weight	MW_{eff}	kg/mole	0.2247	0.0691
Specific heat	C_p	J/mole/K	119.1	82.8
Specific heat	c_p	J/kg/K	525.7	1198.4
Thermal conductivity	k	W/m/K	5.0	19.7
Density	ρ	kg/m^3	8045	3878
Density	ρ	$mole/m^3$	3.58×10^4	5.61×10^4
Dynamic Viscosity	μ	Pa s	0.0151	0.0073
Kinematic Viscosity	$\nu = \mu/\rho$	m^2/s	1.88×10^{-6}	1.88×10^{-6}
Surface tension	σ	N/m	0.973	0.932
Melting point of oxide	$T_{mp,oxide}$	K	2450	2200
Temperature of melt	T_{melt}	K	2800	2500
Specific heat of reaction	$\Delta e_{reaction}$	MJ/mole	0.0371	0.0160
Specific thermal energy	$\Delta e_{thermal}$	MJ/mole	0.2980	0.1820
Specific combined energy	$\Delta e_{combined}$	MJ/mole	0.3350	0.1980
Specific combined energy	$\Delta e_{combined}$	MJ/kg	1.491	2.865

Table 3-6 Scaling of melt mass

	DISCO	KONVOI
Linear scale	1:18.47	1:1
Volume scale	1:6300	1:1
Mass, Iron-Alumina (kg) (Konvoi scaled by 1:6300)	10.6	66 780
Volume, Iron-Alumina (m^3) (Konvoi scaled by 1:6300)	2.74×10^{-3}	17.26
Volume × density of corium (8000 kg/m^3) (kg)		138 000
Thermal + chemical energy of 138000kg corium (MJ)		205 000
Thermal + chemical energy of simulant melt[1] (MJ)	30	
Thermal + chemical energy of simulant melt scaled by 1:6300		189 000
Mass of corium containing 189 000 MJ		127 000

[1] data for specific corium see NUREG/CR-5746,

Thermal + chemical energy of simulant melt 2.86 MJ/kg

Thermal + chemical energy of corium 1.49 MJ/kg

Fig. 3-1. The DISCO-H test facility

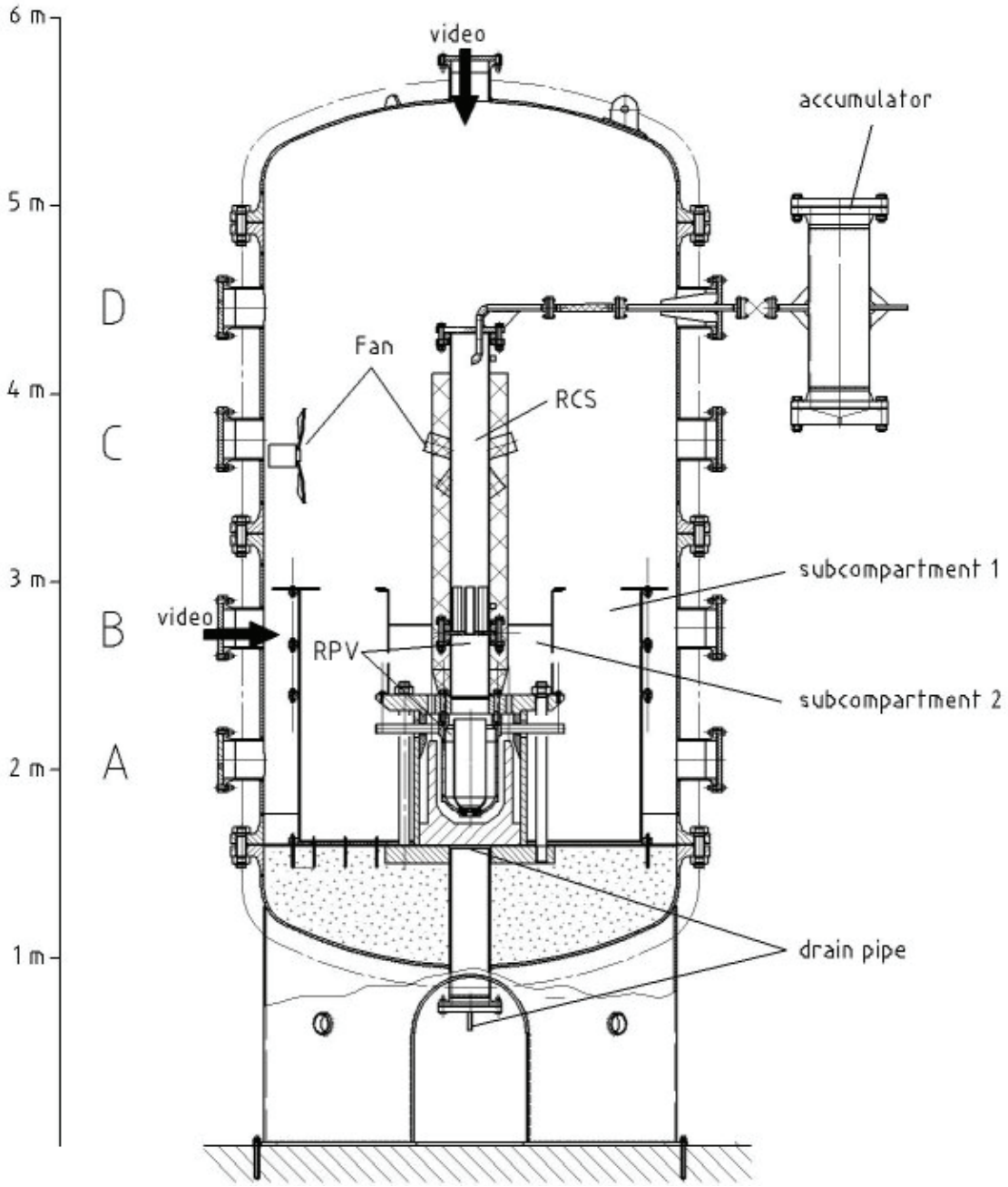

Fig. 3-2. The Containment pressure vessel with internal structures

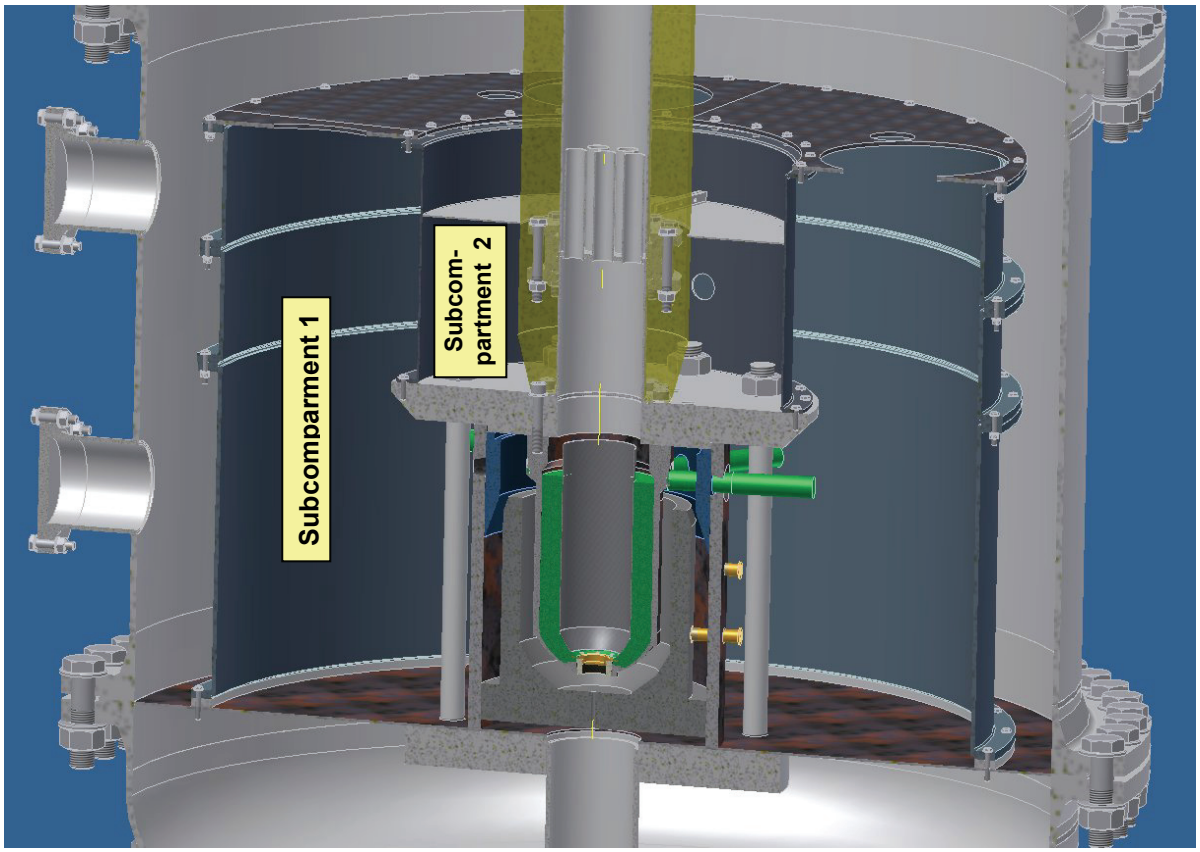

Fig. 3-3. Design of subcompartments 1 and 2

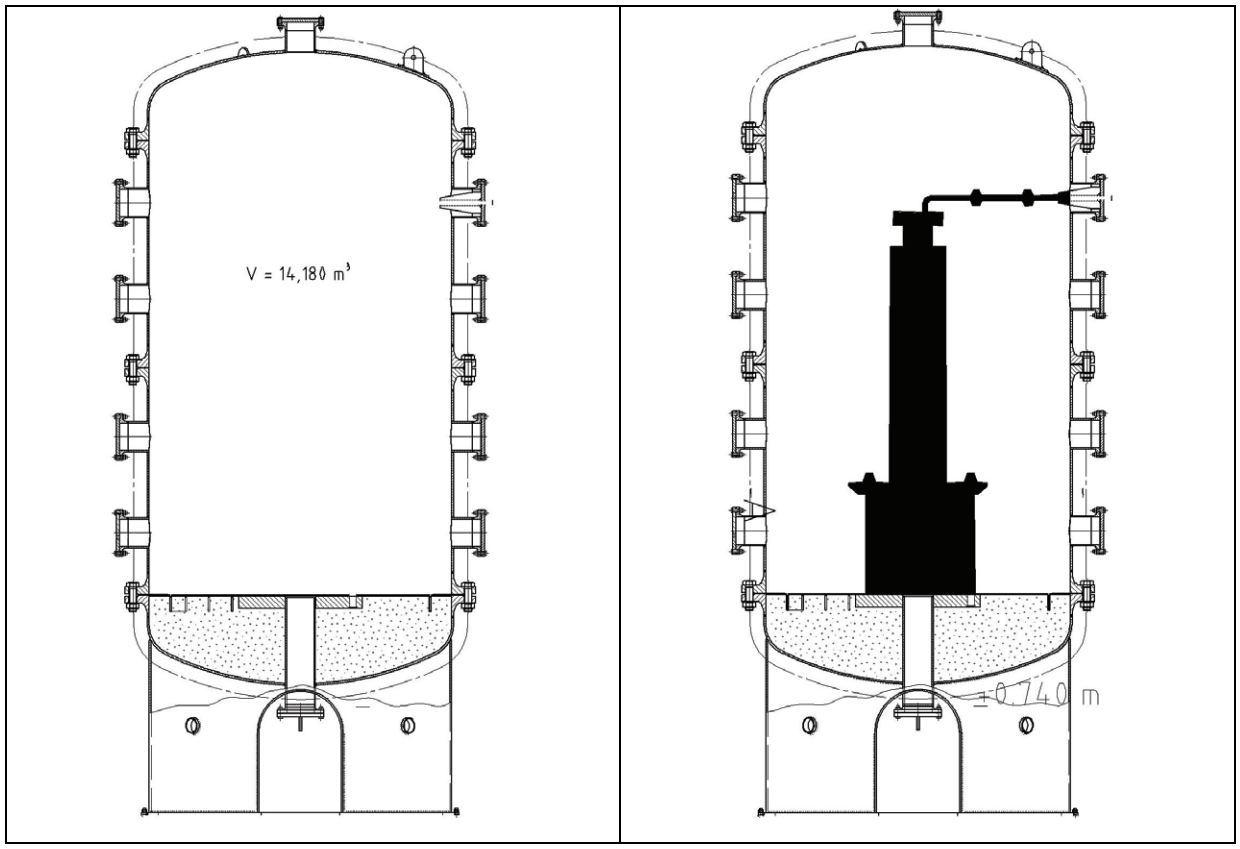

Fig. 3-4. Volumes of the facility (empty containment vessel, internal structures)

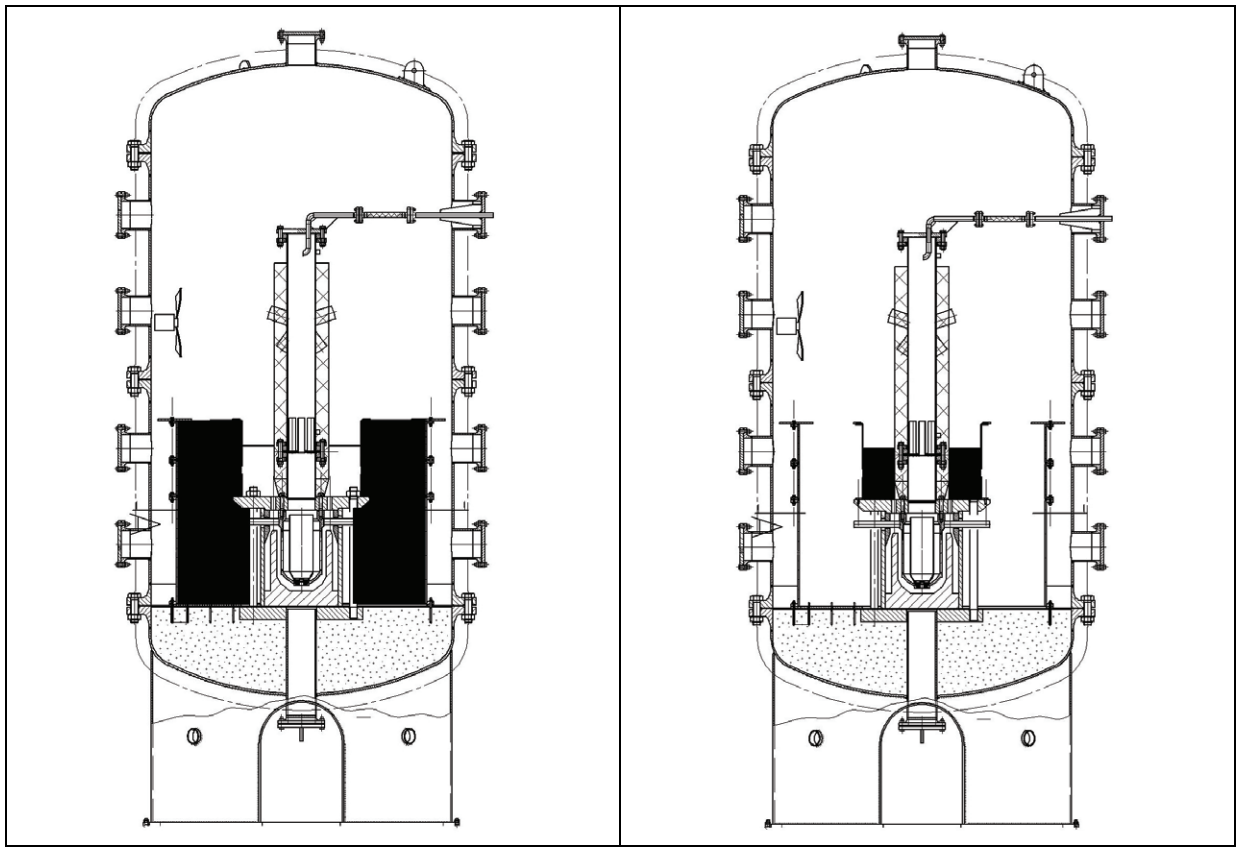

Fig. 3-5. Volumes of the facility (left: subcompartment 1, right: subcompartment 2)

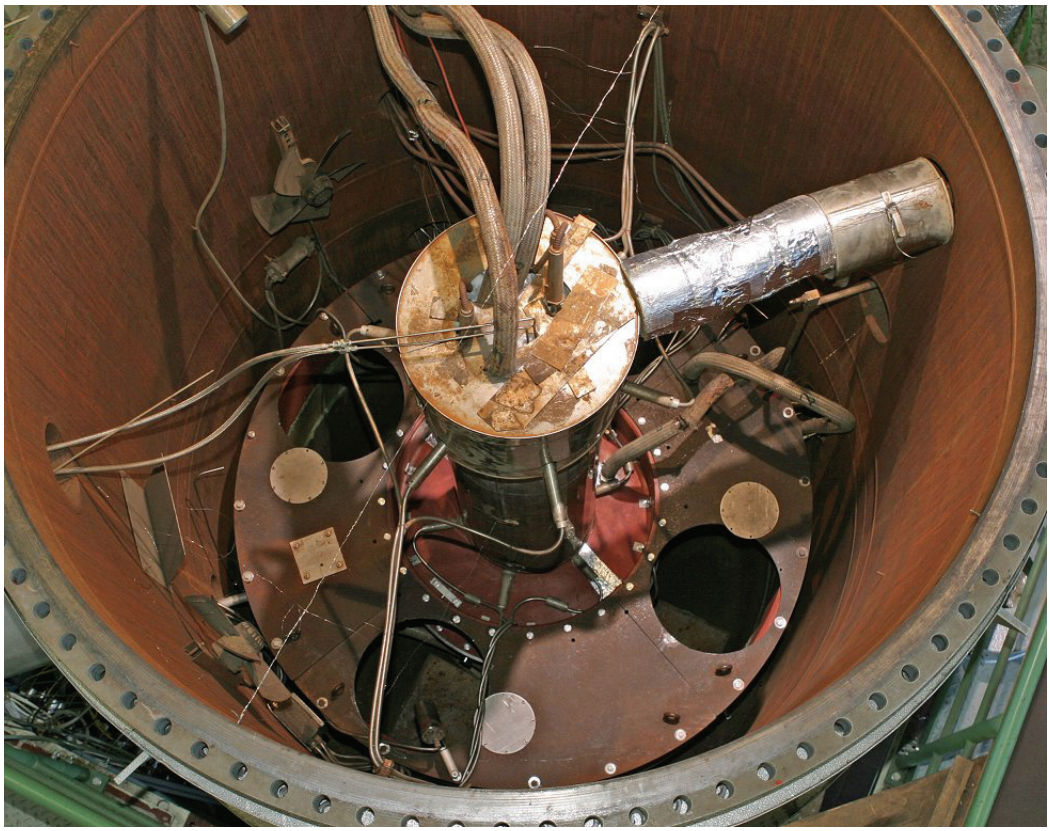

Fig. 3-6. View into containment pressure vessel, with RCS-RPV pressure vessel

Fig. 3-7. Top view of the cavity top plate with exit holes leading into subcompartment 2

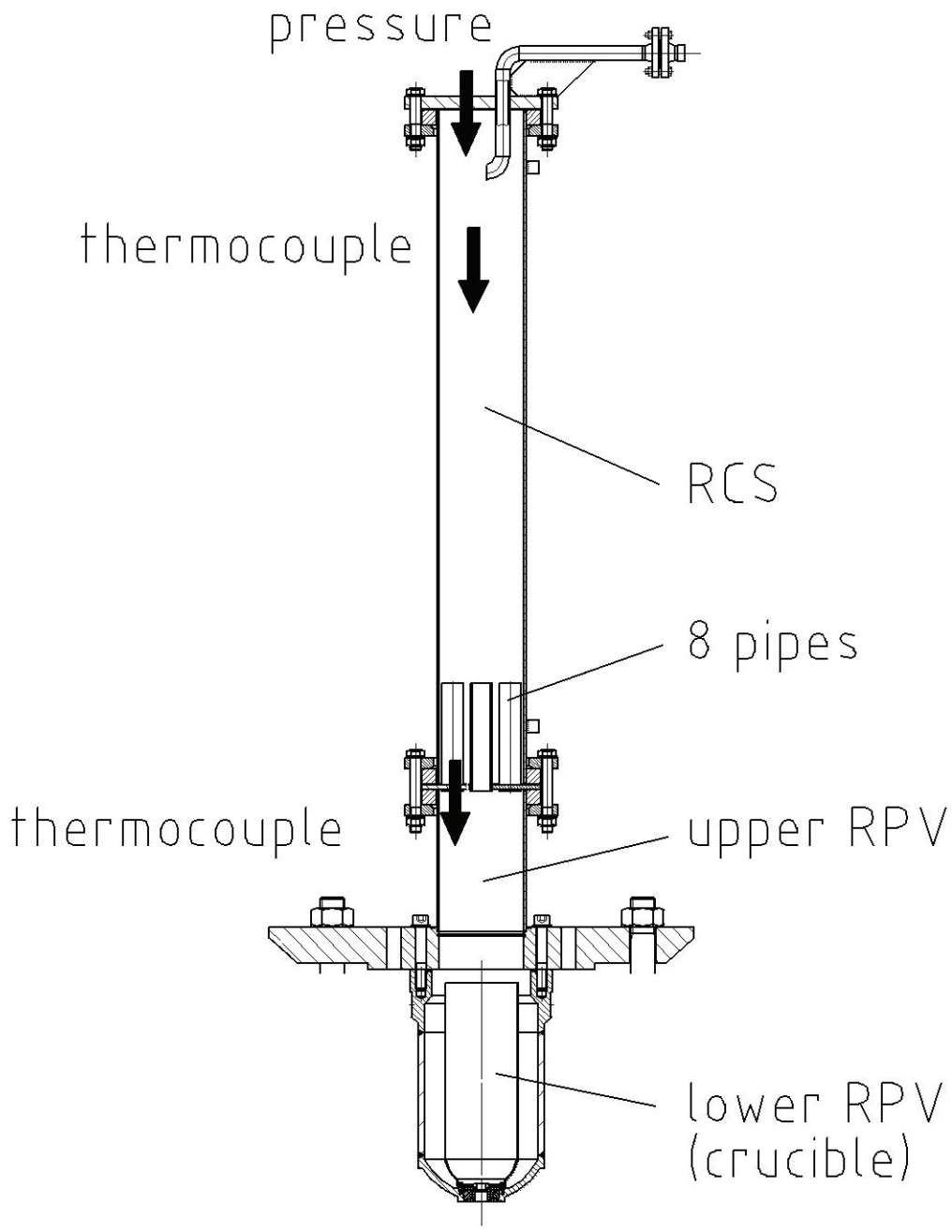

Fig. 3-8. The model of the RCS and RPV vessel

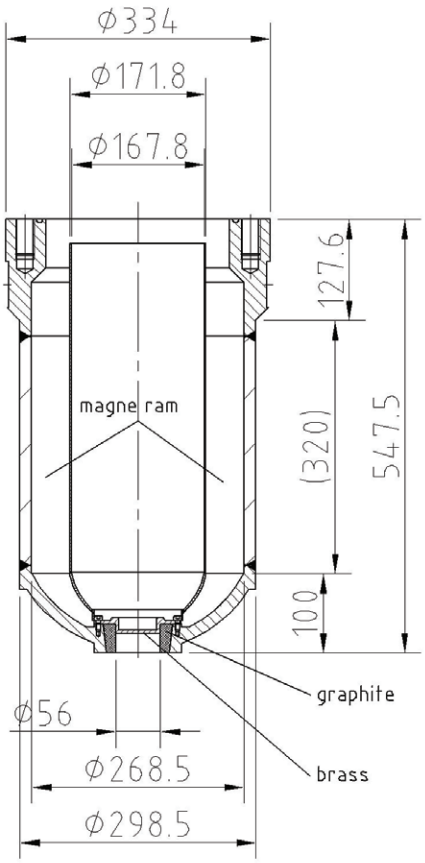

Fig. 3-9. The RPV model, crucible for the thermite melt

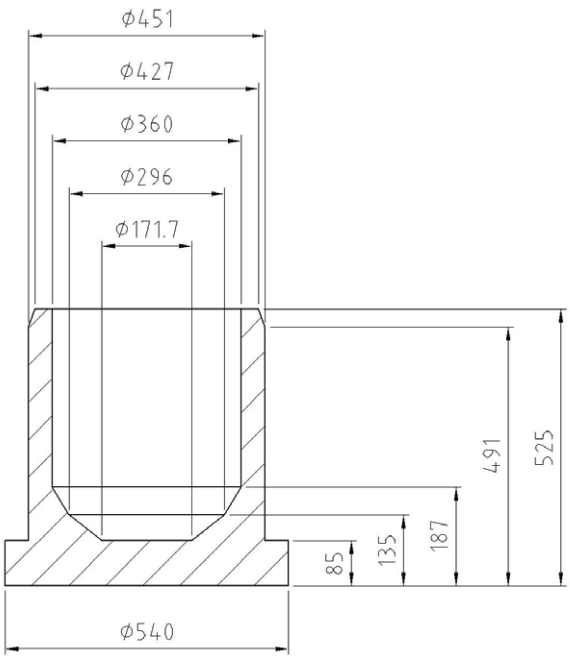

Fig. 3-10. The concrete reactor pit

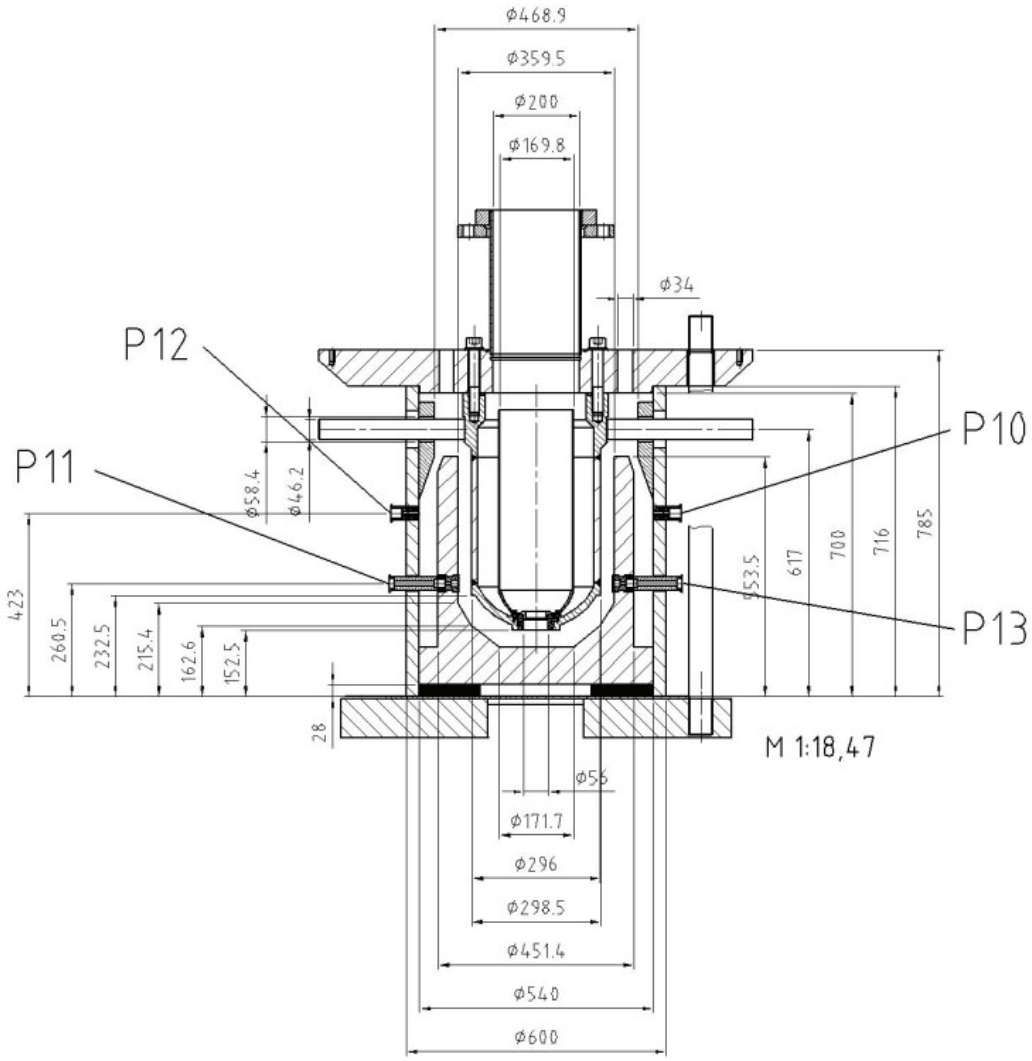

Fig. 3-11. The RPV-model (crucible) and cavity and positions of pressure transducers

Fig. 3-12. Photograph of the cavity model

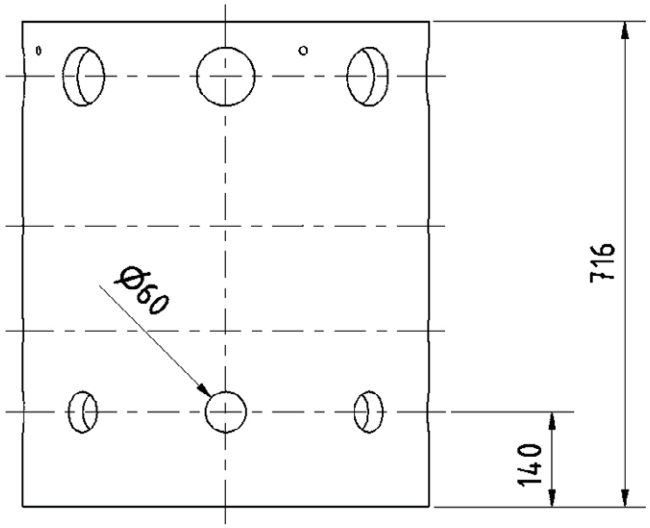

Fig. 3-13. Pressure venting openings in cavity cylinder in test KH08

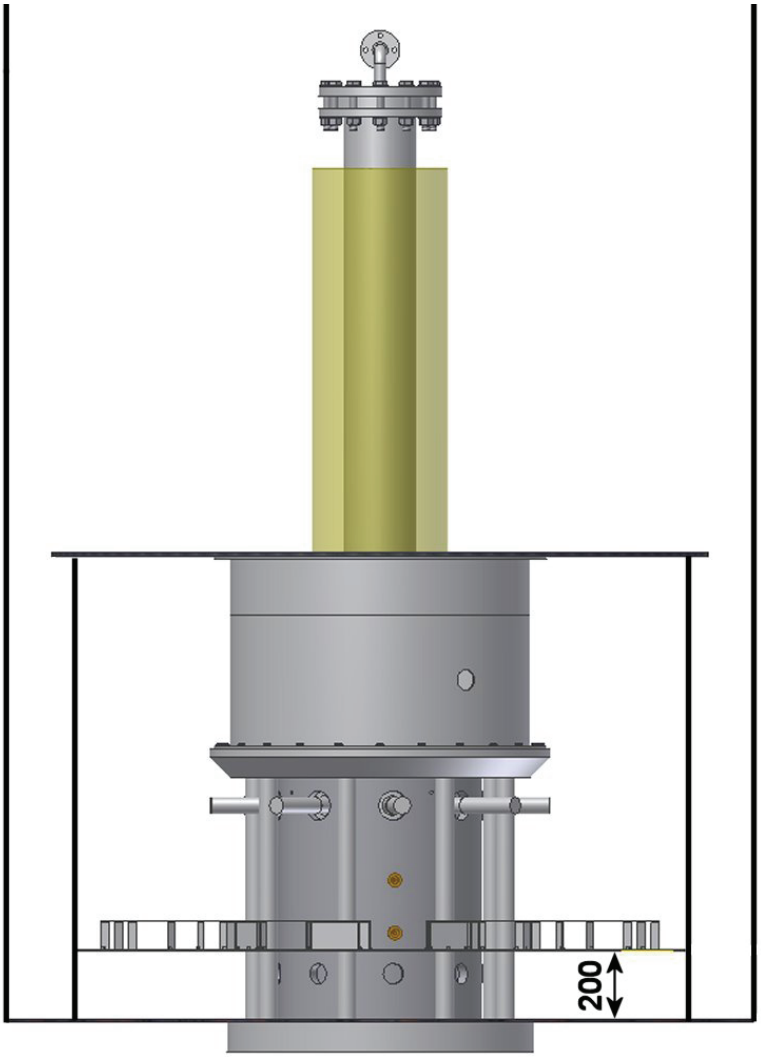

Fig. 3-14. Arrangement of separation plate in subcompartment 1 for test KH08

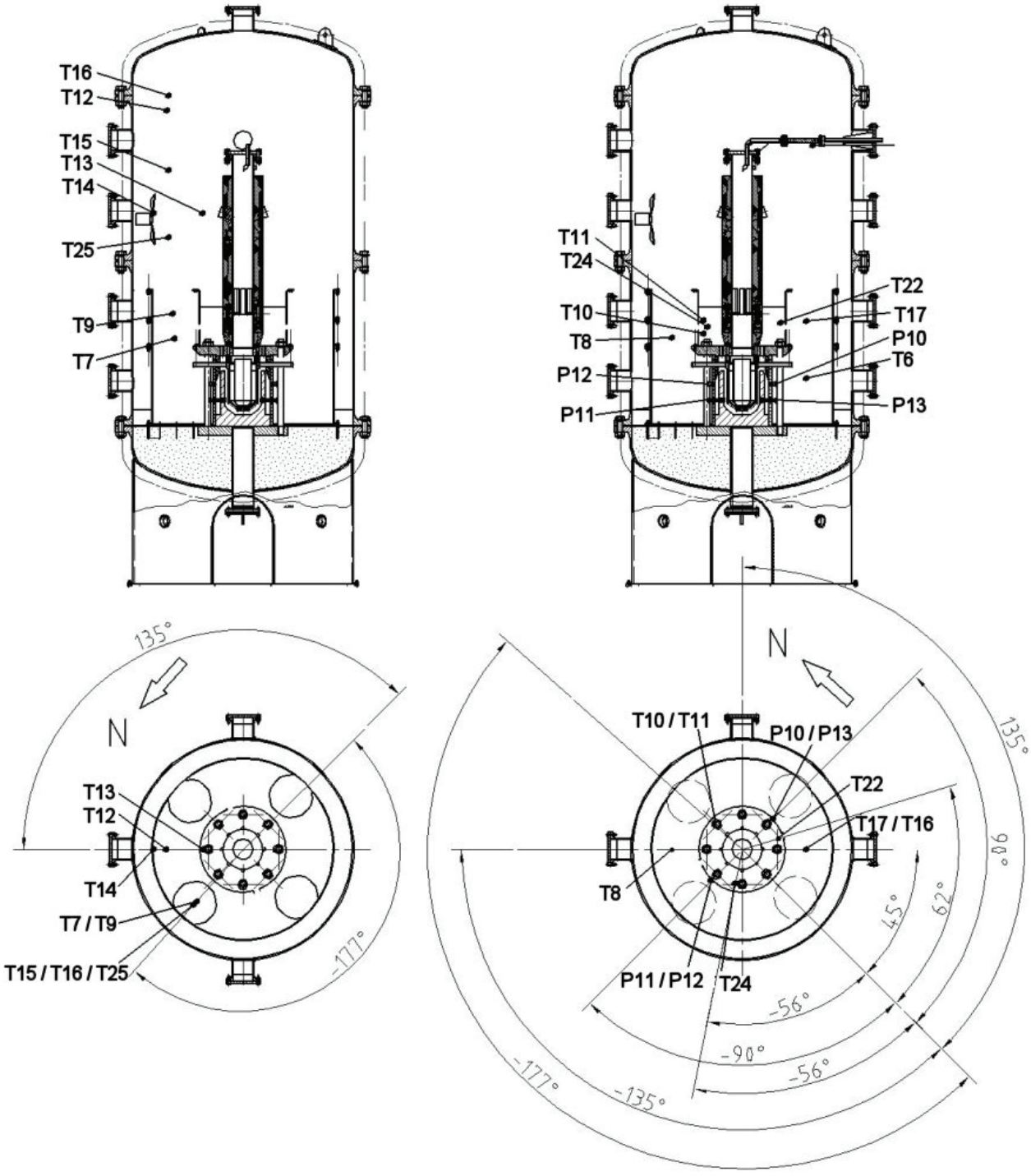

Fig. 3-15. Positions of thermocouples

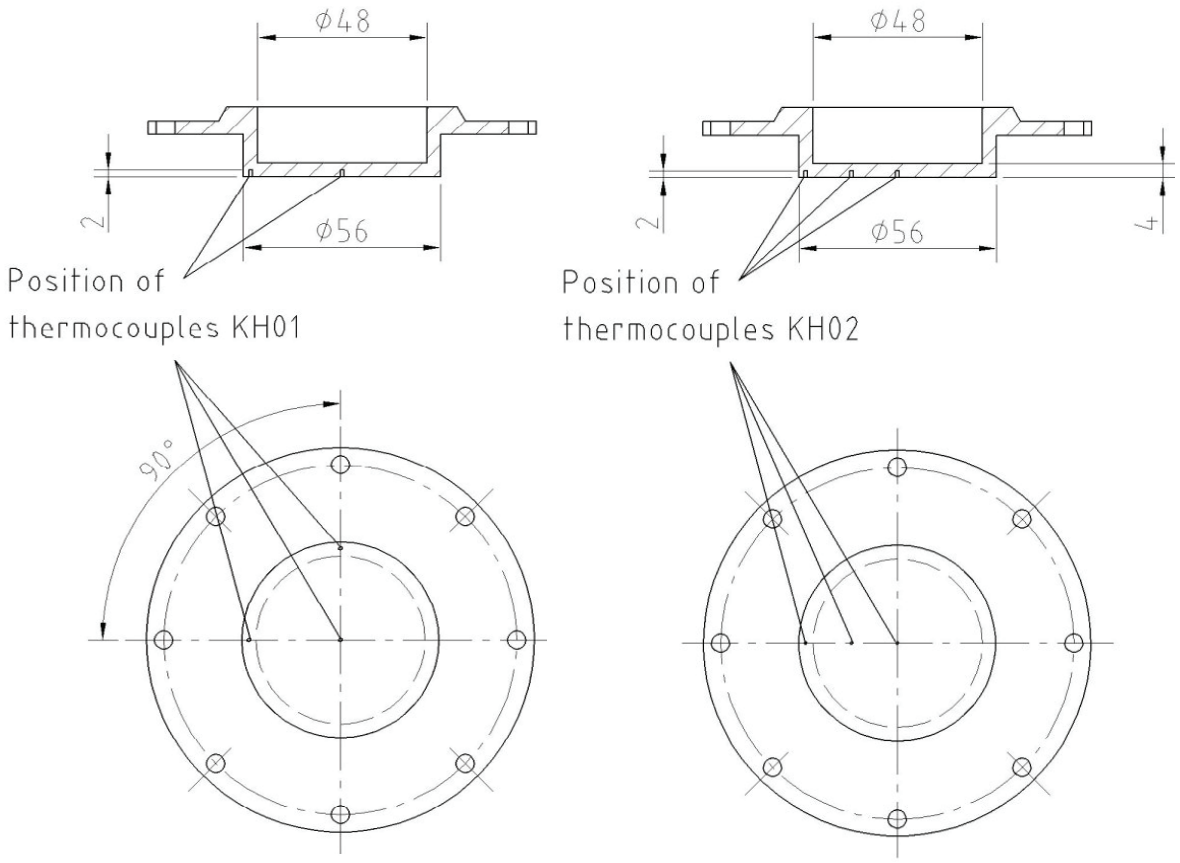

Fig. 3-16. Geometry of the brass melt plug and instrumentation with thermocouples

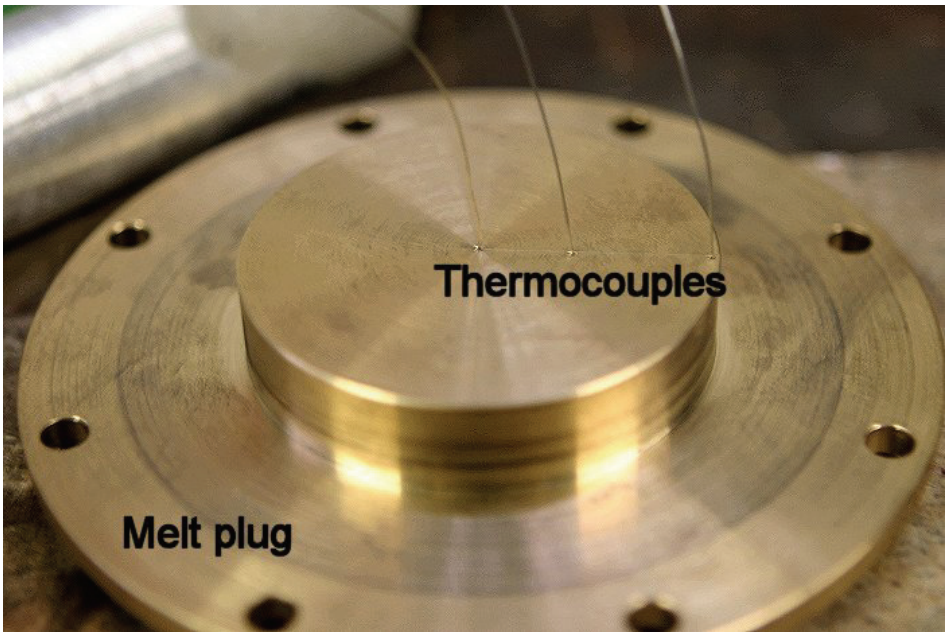

Fig. 3-17. Photo of melt plug

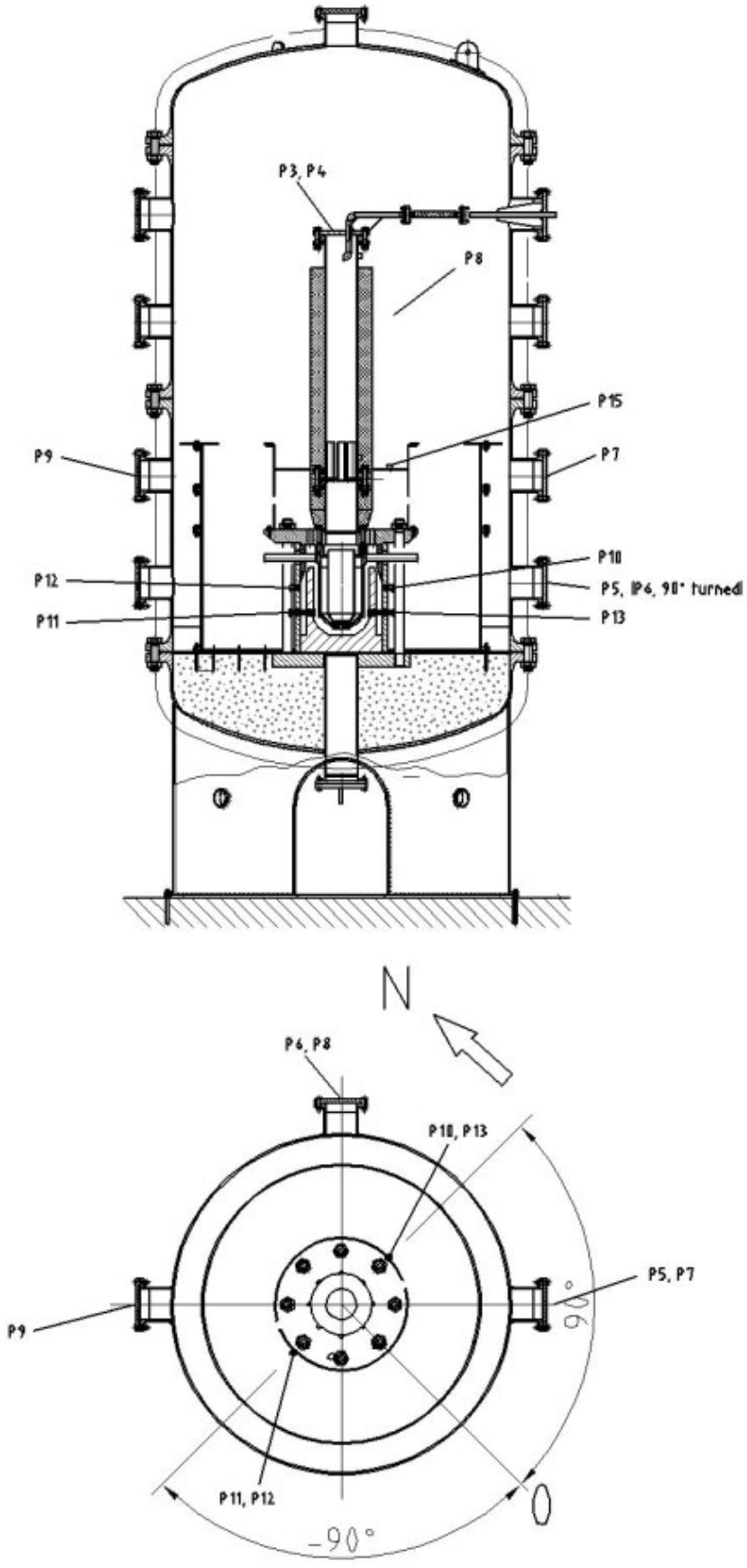

Fig. 3-18. Positions of pressure transducers

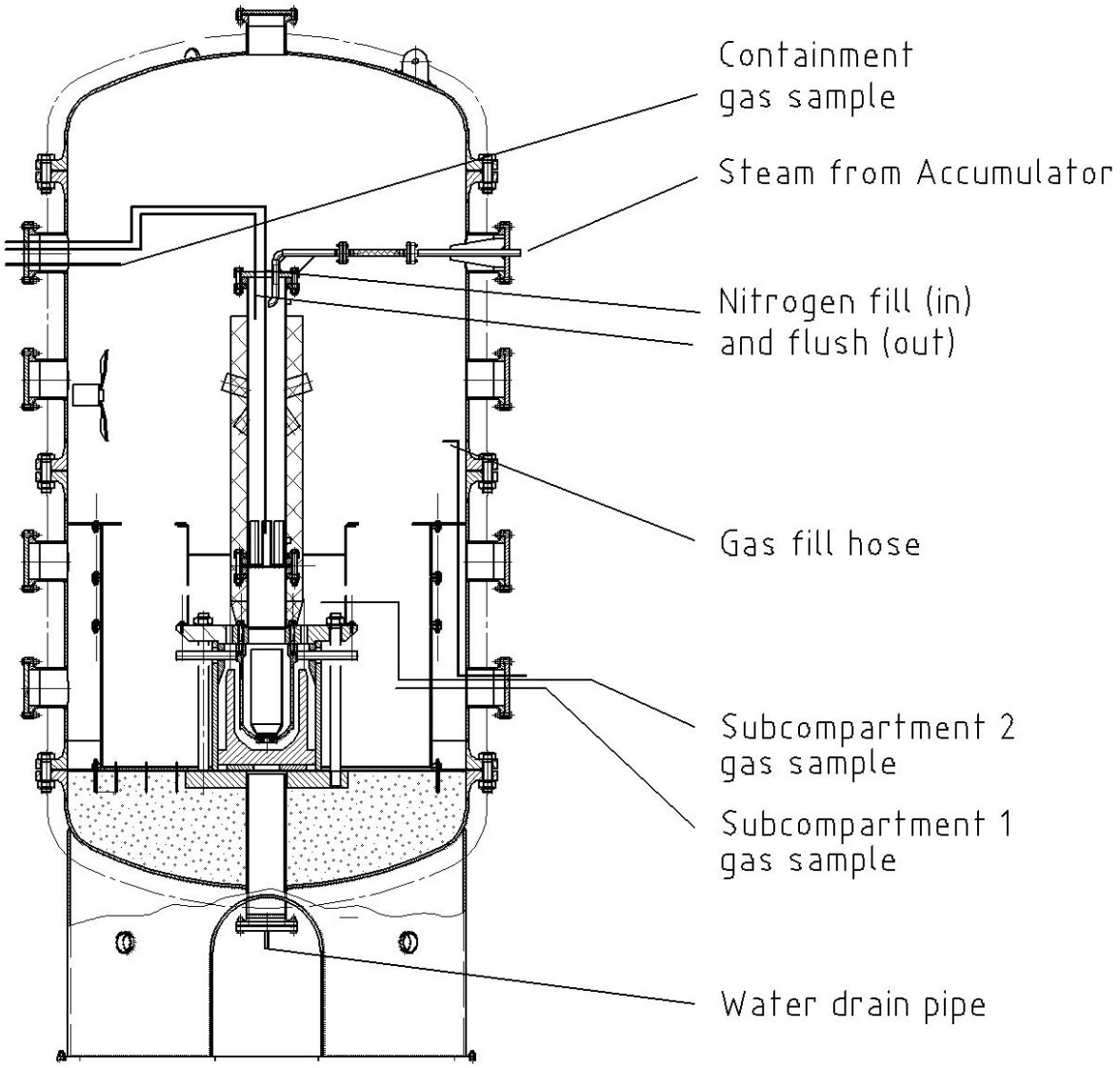

Fig. 3-19. Gas filling piping and gas sampling positions

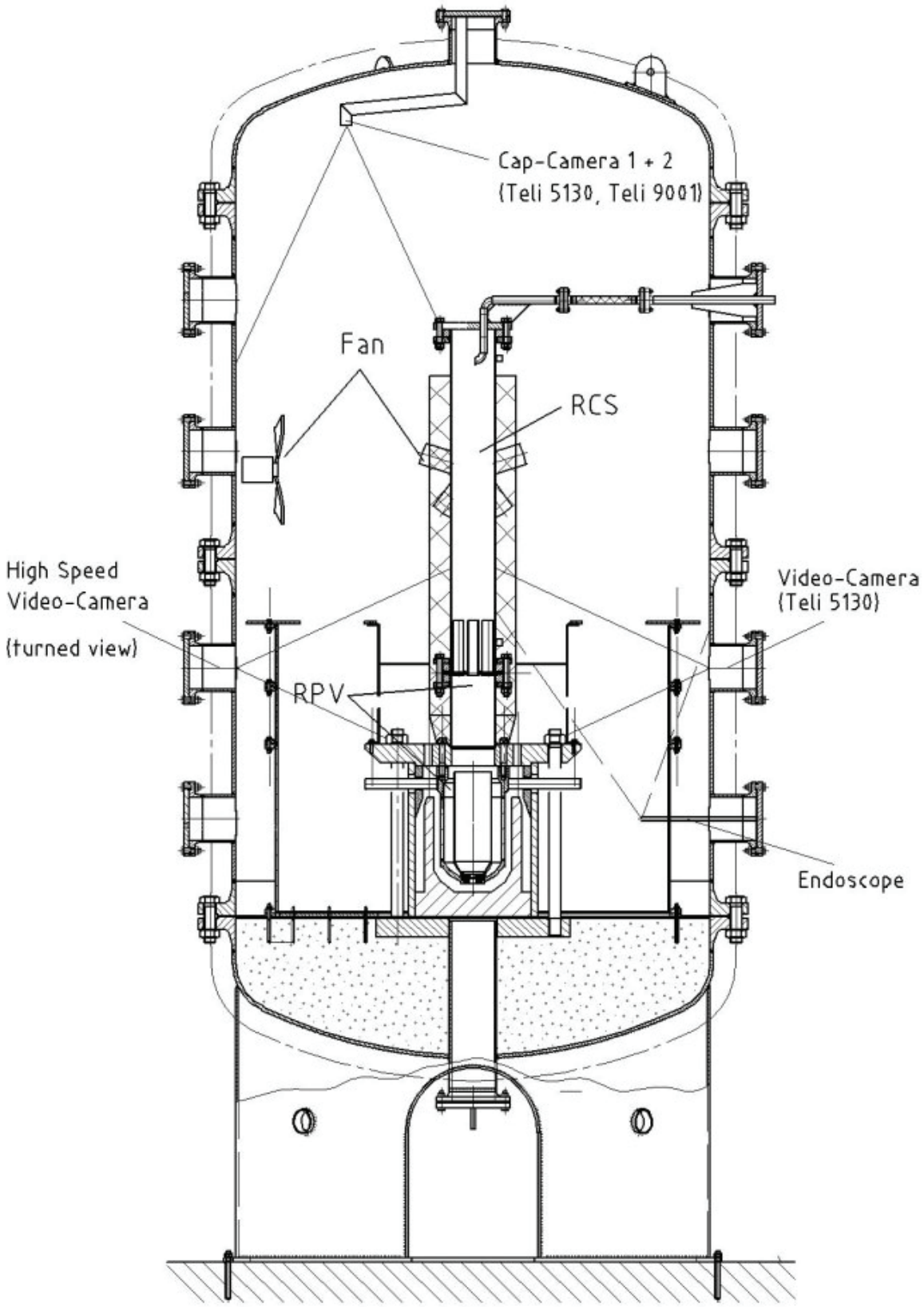

Fig. 3-20. Camera positions and viewing angles

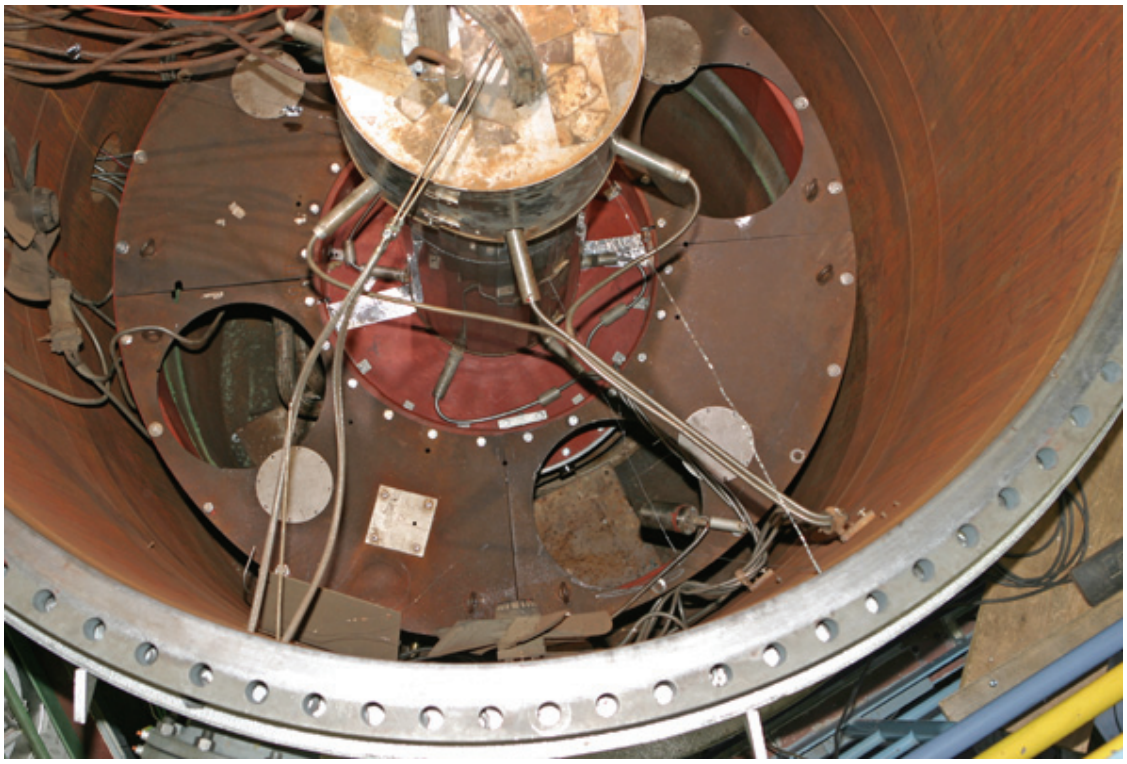

Fig. 3-21. View into containment vessel

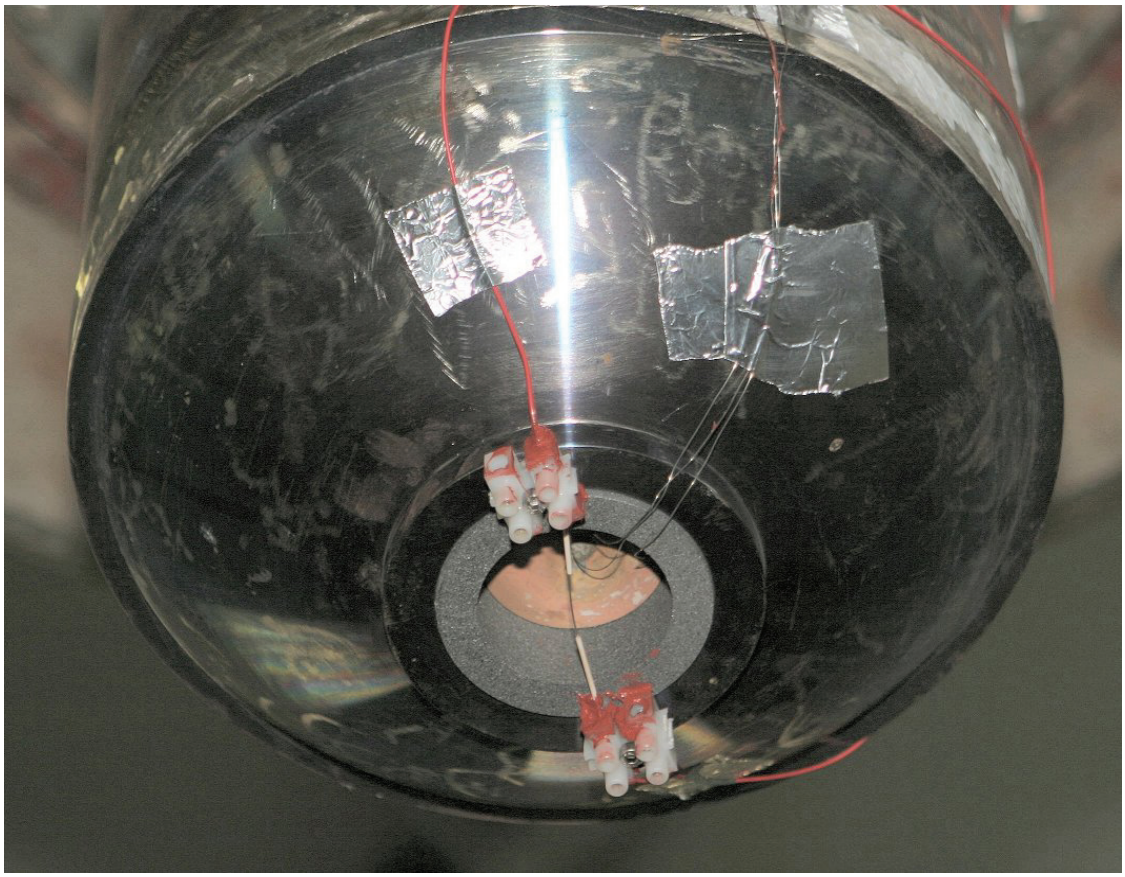

Fig. 3-22. Graphite annulus, brass plate and breakwires at the RPV exit hole

Fig. 3-23. The steam accumulator (left) and the steam generator (right)

Fig. 3-24. Crucible with thermite powder, filled (left) and pressed with ignition wire (right)

Fig. 3-25. Sieving vibrating unit with 8 of 17 sieves

Fig. 3-26. Weighing of a sieve with particles

4 Description of the Experiments and Results

4.1 Test KH01

The experiment KH01 was performed with an open path from the reactor pit to subcompartment 2 (SC2), with prototypical conditions concerning the steam driven ejection out of the RPV, and a containment atmosphere, that was part air and part steam at an elevated pressure, with 5.4 mole-% hydrogen. The exact initial conditions are listed in Table 4-1, Table 4-2 and Table 4-3.

4.1.1 Pressure and temperature data

Fig. 4-2 shows the pressure and temperature history in the steam accumulator, the RCS-RPV pressure vessel and the cavity from the time of thermite ignition till 4 seconds after plug failure. The sequence of events as described in chapter 3.5 can be perceived in the data curves. After ignition of the thermite the pressure and temperature in the RPV starts to rise. The temperature signal is well above 1000°C and is limited by the amplifier range at 1378°C. When the valve has opened and steam flows from the accumulator into the RCS-RPV vessel, the pressure increases rapidly until it balances with the pressure in the accumulator, which has decreased at the same time. The temperature in the lower part of the RCS-RPV vessel (T-RPV) drops due to the relatively cold steam flow (for a short time only in this test). The temperature in the lower part depends on the mixing of the hot and cold steam and the duration of the thermite reaction. In the upper part (T-RCS) the temperature also drops first and than increases again up to of 244°C (saturation temperature at 3.6 MPa) at the instant of plug failure, which means a superheat of 19 K at 2.6 MPa.

The behavior of the melt plug can be inferred from the signals of the three thermocouples, which were mounted inside the brass plate (Fig. 4-3 and Fig. 4-4). The temperature at the edge of the plate starts to rise 1 s before plug failure. It rises linearly up to about 400°C. This temperature increase is probably due to heat conduction through the steel liner. The temperature at the center of the brass plate remains constant low up to 0.47 s before plug failure, but then rises steeply up to 820°C just before failure. This increase is probably due to the thermite reaction near by. The melt temperature of the brass plate is around 900°C. The signal from the center thermocouple indicates that it comes into contact with the hot melt at t = -5 ms while the temperature is already at 1100°C. Consequently, between t = -17 ms (T=900°C) and t = - 5 ms the brass plate at the center failed. One thermocouple at the edge indicates melt arrival at t = +9 ms. Thus, the plug opening takes between 14 ms and 26 ms.

Fig. 4-5 shows the blow-down pressure and the pressures in the cavity and containment. The blow-down ends when the RPV-pressure curve meets the rising cavity pressure. It lasts approximately 0.43 seconds in the test KH01 with the 56-mm-hole (8 seconds in prototypic time scale). Three distinct stages can be recognized in the curves of the RPV pressure: first, a slow decrease, second, a steep drop up to a maximum slope, and third a slowing down of the pressure drop. These stages can be detected better if the pressure gradient dp/dt is plotted versus time, as shown in Fig. 4-6. A low gradient exists for a certain time at the beginning of the blow-down, which can be interpreted as a liquid single-phase or nearly single-phase

jet. The second stage is a two-phase flow, reaching a peak volume flow when the single-phase steam flow begins. At this point in time the pressure ratio of the vessel pressure and cavity pressure is still supercritical, and choked flow prevails. In Table 4-4 the times of these three flow stages are listed. Also given is the theoretical velocity of the liquid jet determined by the driving pressure difference Δp and the density of the melt, ρ_M,

$$u_L = (2\,\Delta p/\rho_M)^{1/2}, \tag{4.1}$$

and the duration of the melt ejection, assuming that all melt is ejected single-phase,

$$t_s = V_M/(\varepsilon\,\pi\,d^2/4\,u_L) \tag{4.2}$$

with V_M, the volume of the melt and ε, the contraction factor. However, the two components of the melt have separated, with the iron (ρ = 6.35 g/cm^3) at the bottom and the alumina (ρ = 2.8 g/cm^3) on top. Therefore, the iron will be ejected first with a lower velocity and the alumina second. The velocity ratio is 1.5. Since the volume ratio of iron to alumina is 0.5, the duration of the iron ejection is approximately 43% and that of the alumina 57% of the total ejection time, provided that all melt is ejected single-phase. The total ejection time does not change significantly whether the well mixed melt or the separated components are ejected. For a contraction factor ε = 0.6 the calculated ejection time is similar to the time inferred from the pressure gradient.

Fig. 4-7 and Fig. 4-8 allow a closer inspection of the pressure transients in the cavity, subcompartments and containment. During the ejection of the melt the pressure in the cavity is higher than in the other rooms. The highest pressure is observed in the lower pit (P11 and P13, Fig. 3-11), with a peak pressure 1.55 bar higher than in the containment. The pressure behind the biological shield (P10 and P12) is somewhat lower, and the pressure in the upper part of the pit lies probably between these and those in the lower pit. The maximum overpressure in SC2 compared to containment pressure is 0.3 bar, which is less than the necessary 0.8 bar to lift the concrete slabs which cover the reactor room 27 (refueling room). With the open path into the SC2 the maximum pressure between pit and SC2 is in the order of 0.75 bar, less than the failure pressure of the sealing plates (2 bar). Therefore, a test with initially closed flow path has to be conducted, in order to check if the sealing plates fail due to overpressure.

The maximum pressure in the containment is reached at t = 0.9 s with p = 0.418 MPa, with almost zero gradient between t = 0.6 s and t = 1.2 s (Fig. 4-7). Due to heat losses to the vessel walls the pressure decreases again. After approximately 10 s the pressure increase has dropped to half of its maximum value (Fig. 4-9).

Fig. 4-10 through Fig. 4-12 show the gas temperature development in the two subcompartments and the containment dome. In both subcompartments the gas temperature rises to 1100°C in less than 0.4 seconds. Unfortunately, more than half of the thermocouples reach their upper range at 1380°C, in most cases probably because of a direct hit by melt droplets. After having reached the maximum at around t = 0.7 s the temperature decreases steeply within 4 seconds. The maximum average gas temperature in the containment dome reaches only roughly 400°C not before t = 2 s, at a time when the pressure has dropped already by 0.2 bar. This means that the pressure maximum is mainly due to the early temperature increase in the subcompartments.

4.1.2 Gas analysis

The initial composition of non-condensable gas in the containment vessel is given by the pressure and temperature at closing of the vessel and the added hydrogen mass. Its total mass is defined by the total empty volume of the vessel. The steam content is determined by the pressure and temperature at the start of blowdown. These data are listed in Table 4-3. The gas concentrations determined from dry-basis gas samples are listed in Table 4-6. In order to compare both sets of data, dry basis data must be converted to wet basis data (including steam). The samples taken pretest should yield the same composition of non-condensable gases. The corresponding data for hydrogen and oxygen concentrations are listed in the last two lines of Table 4-3. Unfortunately, the differences are quite considerable (5.41% vs. 6.34% for hydrogen and 12.48% vs. 11.01% oxygen), and the origin of this error could not be identified. However, more careful experimental and analyzing procedures led to better agreement in the last four experiments performed.

The pretest data in Table 4-6 show that the mixing of the initial hydrogen is not complete in SC2; probably due to the small passage to the containment (6.6% vs. 9.9%). However, the high concentration of hydrogen (46%) in SC2 shortly after blow down (t = 2 s and t = 5 s) is remarkable. There is also a considerable amount of carbon monoxide and carbon dioxide in this compartment. This is due to the sealing material used, which was hit by the melt and burnt. This was avoided in later experiments.

The results from the gas analysis (see appendix A) are shown in Table 4-14. A total of 37 mol of hydrogen was produced. Since only 28 mol of blow down steam was available some metal must have been oxidized by the steam or the oxygen in the containment. It can be assumed that most of the blow down steam was consumed for oxidation inside the cavity, which means that mainly hydrogen was blown into the subcompartments. On the other hand, not all metal in the melt was oxidized, or in other terms, more hydrogen could have been produced with the existing metal. The potential maximum hydrogen production would be 101 moles by iron and 6 moles by aluminum (see Table 3-4). The ratio of hydrogen moles produced to iron moles oxidized depends on the kind of iron oxide formed. Based on the experience at the Sandia National Laboratories, Blanchat [Bla99] gives a ratio of 1:1, which implies that in a first step only FeO is formed. For aluminum it is 1.5:1; 3 moles of hydrogen are produced by the oxidation of 2 moles of aluminum with water.

Out of 97 mol total available hydrogen, 53 mol burned, which is more than was produced, but only 55% of the existing hydrogen. The post test hydrogen concentration was 4.5%, based on 975 mol of gas including steam in the containment (947 initial steam/gas plus 28 mol blow down steam).

4.1.3 Debris recovery data

The debris in the cavity was found in the concrete pit, behind the biological shield, at the outside of the RPV vessel and at all surfaces near the exits A and B (Fig. 4-15 through Fig. 4-18). The melt crust at the vertical cavity wall was thin (< 1 mm). Much of the debris in the SC1 was found as crust at the vertical wall opposite of the cooling line stubs (Fig. 4-19 through Fig. 4-21). Likewise, it was found at the inside of the top cover of SC2 (Fig. 4-23 and

Fig. 4-24). Most of the melt which hit this top cover dropped back onto the floor inside SC2 (Fig. 4-22). Some of the melt hitting the inside of the cover on SC2 burnt holes into the sealing and escaped from SC2 into the containment. The debris in the containment was generally collected as small particles on all horizontal areas, such as the subcompartment covers and hoses (Fig. 4-25 and Fig. 4-26), except those parts which had leaked from SC2 and were found as larger particles or crusts.

Table 4-15 gives the detailed recovery results, and in Table 4-16 the debris recovery summary is shown including the mass balance. A recovery factor greater than one indicates that the total mass recovered was greater than the initial thermite charge, which may have various reasons, such as ablation of concrete in the cavity, melting of the crucible steel wall, contaminants (break wires, melt plug, thermocouples, etc.), and oxidation of metallic debris. Also listed are the fractions of the debris with diameters smaller than 10 mm and smaller than 2.5 mm. The particle sieve mass median diameter (SMMD) of these fractions is given in the last three lines.

Most of the ejected melt was transported into the two subcompartments (77.5%). No deflector was installed in front of the exit holes, thus a straight line of flight into SC2 existed. Less than 10% were transported into the containment dome, mostly as fine particles.

The detailed results of the sieve analysis are listed in

Table **4-17** and are shown in graphical form as particle size distribution in Fig. 4-13, separate for particles collected in the two subcompartments and the containment. The particles larger than 5 mm are generally flat, because they hit a wall while still liquid (Fig. 4-27).

Fig. 4-14 shows the cumulative particle size distribution. The sieve mass median diameter (SMMD) of the debris particles found in SC2 is quite large with 5.2 mm. In SC1, the mean diameter is only 1.7 mm, because the debris has to take a 90 degree turn on its way into this room. Only very fine particles could enter the containment dome, except those parts which had leaked from SC2, The mean diameter is 0.08 mm. These particles probably were already solid when they entered the containment dome.

4.1.4 Debris particle analysis

For selected particles in containment, SC1 and SC2 morphological and chemical analyses were performed. Fig. 4-35 to Fig. 4-60 show the SEM-BSE images and composition of the particles. Generally following kinds of particle structure are observed existing either alone or in combination:

a) Compact metal alloys composed mainly of iron, with little addition of Cu and some times Cr. This structure is observed in Fig. 4-36, 1A, Fig. 4-38, 2A, Fig. 4-53, A, Fig. 4-56, A, Fig. 4-57, A, Fig. 4-58, B, Fig. 4-59 and Fig. 4-60, A.

b) Loose iron oxide in not completely oxidized form, probably in Fe_3O_4-FeO combination. This structure is observed in Fig. 4-38, 2C, Fig. 4-39, Fig. 4-41, Fig. 4-44, Fig. 4-45 A, Fig. 4-46, Fig. 4-47 C, Fig. 4-49 and Fig. 4-52. The oxidation of Fe can be in different

stages: the oxidation begins on the surface of the liquid iron, when iron is completely consumed, the whole particle can be either hollow (Fig. Fig. 4-39 and Fig. 4-44) or porous (Fig. 4-46).

c) Solidified non-eutectic mixture of Al_2O_3 and iron oxides or other minerals. Such structure is not homogenous, but relatively compact, such as in Fig. 4-37 1Ba and 1Bb, Fig. 4-38, B, Fig. 4-45, B, Fig. 4-52, Fig. 4-53, B, Fig. 4-55, A and B, Fig. 4-56 B and C, Fig. 4-57 B, Fig. 4-58 A and Fig. 4-60 B.

d) Oxides of Si, Al, Mg and Ca. A little amount of oxides can be found frequently in the above structures. However they appear also alone as single particles such as in Fig. 4-40, Fig. 4-50 and Fig. 4-54.

4.1.5 Video observation results

Not all three video cameras that were installed delivered useful pictures in each test. Therefore a selection is presented here.

The view of one of the ceiling cameras is shown in Fig. 4-61. Between 40 and 80 ms it can be seen that the melt jet hits the cover of SC2 from below (lower left side). The bright light inside SC1 subsides around t = 200 ms. Fig. 4-62 shows pictures taken through the endoscope from the inside of SC1. The sensitivity of this camera was higher, therefore the pictures are overexposed up to t = 300 ms. After that time hot glowing melt particles can be seen for a long time, which could not be seen from the ceiling camera due to a smoke cloud and a lower sensitivity of the camera.

4.2 Test KH02

This test is the reference case for all other tests (**Table 2-2**). The RPV burst pressure is 2 MPa, the breach has a diameter of 56 mm (1 m scaled) and the hydrogen concentration is around 5 % (Table 4-2). The flow path B at the vessel support is closed, thus no direct flow path exists from the pit into the reactor room above the pressure vessel (SC2). Also the pressure venting flaps behind the biological shield are closed.

4.2.1 Pressure and temperature data

The starting sequence from thermite ignition until brass plug melting was similar as in KH01 (Fig. 4-63). Only the temperature signal from the RPV was lower, due to a different position of the thermocouple tip caused by a faulty fixture.

The temperature at the melt plug starts to rise about 1 second before failure (Fig. 4-64). The opening process lasts from – 5 ms until +10 ms (Fig. 4-65).

Although the RPV pressure was lower than in KH01 by 0.57 MPa, the duration of blowdown is practically the same. The pressure increase in the containment is higher (0.290 MPa vs. 0.205 MPa in KH01), and consequently the blowdown ends at a higher cavity pressure (Fig. 4-66). The time of transition from two-phase melt-steam ejection to single-phase steam flow is less clear (Fig. 4-67). The end of melt ejection is reached definitely at t=230 ms, 50 ms later than in KH01 (Table 4-4).

Fig. 4-68 and Fig. 4-69 show the development of pressures in the reactor pit, subcompartments and containment. Because of the closed path leading straight up into SC2 (refueling room), a higher pressure in the pit was expected. However, the pressure difference between reactor pit and containment is practically the same as in KH01. At the same time pressures in SC2 and containment are identical. Hence, the pressure difference between cavity and SC2 is 0.153 MPa at most and thereby below the threshold of 0.2 MPa, which is assumed to be necessary to open the path through the vessel support structure into the refueling room.

The gas temperatures in subcompartment 1, shown in Fig. 4-71, rise very fast and reach 1100°C in the upper part of SC1 (s. Fig. 3-2, port B), similar as in KH01. Unfortunately, these thermocouples are destroyed by hits of melt early. In the lower part (port A) 1000°C are reached only after 1.2 seconds. The thermocouple wires leading into SC2 were hit by melt and therefore no temperature data for SC2 are available. The gas temperatures in the containment vessel (Fig. 4-72) are higher than in KH01, and most of them reach their peak around 600°C at early times between 1 and 1.5 seconds. This is later than the pressure peak at t = 0.6 s, but earlier than the temperature peak in KH01, which was not before t = 2 s.

4.2.2 Gas analysis

The gas sample data (Table 4-7) pointed to a higher initial hydrogen concentration than in KH01 and the gas analysis (Table 4-14) yields a greater amount of hydrogen burnt. These data have a high uncertainty (Annex A), and more reliable for comparing the hydrogen com-

bustion may be the fraction of burned hydrogen related to the total available hydrogen. This fraction is larger in KH02 (0.67) than in KH01 (0.55), which may be part of the reason for the higher pressure increase. Consequently, the post test hydrogen concentration is less than in KH01.

4.2.3 Debris recovery data

The comparison of the debris distribution in Fig. 4-1 shows that the fraction of melt which entered the refueling room (SC2) in KH01 remained in the reactor pit in KH02. Almost no debris reached SC2 except for very little fine dust via SC1 and containment. The fraction that reached SC1 was somewhat larger than in KH01, with a similar size distribution (Fig. 4-73 and Fig. 4-74). Without the larger particles, that entered the containment dome via the leak in SC2 in test KH01, the fraction and size distribution in the containment would be similar in KH01 and KH02.

4.2.4 Video observation results

The view of one of the ceiling cameras is shown in Fig. 4-76. Similar as in KH01 the bright light inside SC1 subsides around t = 240 ms while the endoscope camera inside the sub-compartment 1 (Fig. 4-77) sees hot glowing melt particles until t = 500 ms. Black smoke develops and obscures the view from the top.

4.2.5 Conclusions from comparison of tests KH01 and KH02

The maximum pressure increase in the containment in test KH02 is 0.29 MPa (0.50 MPa absolute), and only 0.205 MPa in KH01. The main reason for this high value in KH02 seems to be the higher hydrogen combustion rate (see Table 4-14). However, the data of the gas sampling imply also a higher initial hydrogen concentration contrary to the measured amount during the gas filling process. The reason for this discrepancy is not known.

In test KH01 a large fraction of melt was trapped in the small reactor room SC2 and the hydrogen content increased to 46 % (Table 4-6, dry basis). This hydrogen did not burn within the first 5 seconds and did not contribute to pressure increase. Also the thermal energy of the melt trapped there could not contribute much to pressure increase, because thermal equilibrium in the small room prevented major energy transfer to the atmosphere. In test KH02 the small reactor room was practically passive, only some small particles were blown in from the containment.

On the other hand, more melt entered the SC1, and because it was the only exit from the pit all gas had to take this way to reach the containment dome. This probably increased the gas velocity and hydrogen burning rate, and thereby the temperature in the containment. In both tests the average temperature maximum in the SC1 was approximately 1000°C, while in the containment it was higher in KH02 with 500 – 600°C (Fig. 4-72), versus 350 – 450°C in KH01 (Fig. 4-12).

4.3 Test KH03

Test KH03 was conducted with a closed flow path into SC2, as in KH02, but with a smaller breach size in the lower head (28 mm, 0.5 m scaled).

4.3.1 Pressure and temperature data

The period between thermite ignition and melt plug failure was much longer this time (Fig. 4-78). This cannot be attributed to the smaller hole size since it occurred in former test series as well, independently of the hole size. Again, no gas temperature signal from the RPV is available.

The temperature at the brass plug starts to rise about 2 seconds after thermite ignition, analogous to the preceding tests (Fig. 4-79). However, if the 600°C mark was reached within 1 second in KH01 and KH02, it takes 7.5 seconds in KH03. For unknown reasons the thermite reaction proceeded much slower than before.

If the melting of the brass plug is assumed to occur at 900°C, the opening process would have taken only 4 ms (Fig. 4-80). The thermocouples are not destroyed by the more than 2000°C hot melt and show temperatures between 900°C and maximum range of 1380°C for up to 55 ms. At this time the thermocouple positioned below the RPV, which had come loose from the brass plug, signals the arrival of melt.

Due to the smaller breach size the blowdown takes longer and lasts 1.4 seconds (Fig. 4-81). The single-phase melt ejection takes 250 ms, which is 4 times as long as in KH02 (Fig. 4-82).

The pressure increase in the containment (Fig. 4-83) is 0.192 MPa, about 0.1 MPa less than in KH02 with similar conditions except the larger breach size. The peak pressure is reached at t = 1.4 s, much later than in KH02 (see also Table 4-29). The short peak of overpressure of 0.052 MPa in the pit is negligible (Fig. 4-84).

The gas temperatures in the subcompartments are shown in Fig. 4-86. In SC1 the maximum temperatures are between 750°C and 1000°C, only slightly lower than the corresponding ones in test KH02. The peaks are reached at 1.2 seconds for the higher values and after 2 seconds for the lower ones. The peak temperatures in SC2 are between 300°C and 500°C. Here, the high temperature signal has a narrow peak at 1 second and at the same time one of the signals from the containment vessel indicates a peak temperature. Obviously hydrogen combustion inside SC2 occurred. In the containment vessel the maximum gas temperatures are between 350°C and 400°C with their flat peaks between 4 and 6 seconds.

4.3.2 Gas analysis

Due to technical failures of the gas sampling the results of gas analysis are equivocal and should be used with care as a basis for conclusions.

4.3.3 Debris recovery data

The distribution of debris is similar to that in KH02, with the difference that roughly 10% more remained in the reactor pit instead of entering SC1 (Fig. 4-1, Table 4-16). The size distribution of debris particles shown in Fig. 4-88 and Fig. 4-89 is also similar as in test KH02.

4.3.4 Video observation results

The cameras looking down from the containment vessel ceiling (Fig. 4-95) recorded a light between 60 and 200 ms. Smoke must have obscured the view later, because the camera looking directly into subcompartment 1 observed moving hot debris particles between 400 and 1300 ms (Fig. 4-96).

4.3.5 Summary of results

Compared to test KH02, a smaller breach size leads to a longer blowdown time, to less overpressure in the reactor pit and to 0.1 MPa less pressure increase in the containment.

4.4 Test KH04

Because in test KH01 the RPV pressure was too high and melt had passed through a leak in SC2 into the containment, this test was repeated as KH04 without these deficiencies. The flow path from the reactor pit to SC2 was open, but in order to retard the straight flow out of the flow cross section B, a deflection device was installed at each opening (Fig. 4-109, Fig. 4-113).

4.4.1 Pressure and temperature data

The thermite reaction time, the opening of the melt plug and the blow down were similar as in KH01, with the burst pressure very close to the planned 2 MPa (Fig. 4-97 through Fig. 4-101). Two thermocouples in the brass plate (melt plug) failed to show signals for unknown reasons.

The overpressure in the pit in regard to the containment is lower than in KH01, with 0.11 MPa vs. 0.155 MPa (Fig. 4-103). The maximum overpressure in SC2 compared to containment pressure is higher with 0.075 MPa (0.030 MPa in KH01), which is still less than the necessary 0.08 MPa to lift the concrete slabs which cover the reactor room 27 (refueling room). With the open path into the SC2 the maximum pressure between pit and SC2 is in the order of 0.04 MPa.

The pressure rise in the containment occurs within 0.4 s, while a second slower rise ends at 0.9 s (Fig. 4-102 and Fig. 4-104). The pressure rise seems to be governed by the temperature in subcompartment 1 (Fig. 4-105), which rises up to 1000°C within this time scale, while the temperatures in the containment reach their peaks later (Fig. 4-106). The increase of

0.179 MPa in containment pressure it lower than in KH01 with 0.205 MPa, which is corresponding to the lower RPV blowdown pressure.

4.4.2 Gas analysis

The gas sampling was defect; therefore no reliable data are available.

4.4.3 Debris recovery data

The distribution of the debris into the compartments is different from that in KH01 (Table 4-15, Table 4-16, Fig. 4-1). More mass remains in the reactor pit and in SC2, less reaches SC1 and the containment. Possible reasons may be the lower driving pressure and, regarding the containment part, the absence of the leak in SC2.

The size distribution of the debris particles smaller than 10 mm is similar in the compartments in both tests (Fig. 4-14 and Fig. 4-108), with the exception of the average SMMD. Due to the larger fraction of debris in SC1 in test KH01 with an SMMD of 2 mm, the average SMMD is only 2.9 mm in KH01 vs. 3.9 mm in KH04.

4.4.4 Video observation results

The cameras looking down from the containment vessel ceiling recorded a light between 40 and 300 ms. The endoscope camera looking directly into subcompartment 1 observed moving hot debris particles between up to 1100 ms. The camera looking from the side into the containment vessel also registered moving hot debris particles until 1000 ms.

4.5 Test KH05 and KH06

The purpose of tests KH05 and KH06 was to examine the effect of the blowdown pressure. They were scheduled to have 1.2 MPa and 0.8 MPa RPV pressure, respectively. In KH06, contrary to the intended value of 0.8 MPa, the burst pressure turned out to be 1.0 MPa.

4.5.1 Pressure and temperature data

The pressure and temperature history in the RPV-RCS vessel during thermite reaction did not show any extreme characteristics (Fig. 4-116, Fig. 4-131). However, in both tests the pressure in the RPV increased shortly after plug opening and showed a peak at t = 0.2 s (Fig. 4-119, Fig. 4-134). The reason for this is not clear. Another irregularity is the longer duration of the blowdown. In experiments with cold model fluids it was found, that the duration of the blowdown is shorter for lower pressures [Mey06]. Consequently, the longer duration in the present tests must have another cause. There may have been a leak in the RPV-RCS vessel or in the tubing connected to it, and steam may have entered the vessel during the heating period. The fact that about 20% of the melt was not ejected but was found in the upper parts of the RPV-RCS vessel also indicates the presence of humidity or even water in the thermite.

The overpressure in the cavity is less than in test KH02, with 0.033 MPa in KH05 and 0.060 MPa in KH06 (Fig. 4-103, Fig. 4-122). The higher overpressure in KH06 may be due to the higher hydrogen concentration or production, but could also stem from the irregularities mentioned above.

The lower RPV pressure in HK05 and HK06 compared to that in test HK02 has a strong effect on the pressure increase in the containment, which is much lower (Fig. 4-123, Fig. 4-138, Fig. 4-170). However, the difference between the maximum containment pressures between the tests with 1.2 and 1.0 MPa RPV pressure is small. A change in the pressure gradient at t = 2.5 s in KH05 hints to late hydrogen combustion. This must have occurred in the containment vessel, since no such trace is shown in the temperature data from SC1 (Fig. 4-124). The temperatures in SC1 show peaks in the range between 800°C and 1000°C in HK05 and between 900°C and 1100°C in HK06 (Fig. 4-139). In SC2 the temperature rises only up to 200°C, while in the containment the temperature is around 300°C in KH05 (Fig. 4-125) and 250°C in KH06 (Fig. 4-140).

4.5.2 Gas analysis

Although it was not planned to vary the hydrogen concentration in the containment vessel, it was higher in KH06 than in KH05 by 1.3% (6.45% vs. 5.15%) according to the weighing method, but only 0.29% (5.48% vs. 5.19%) according to the sampling method. The discrepancy between the two methods of determination of hydrogen concentration in test KH02 was even larger with 1.96% (5.37% weight and 7.33% sampling). These uncertainties should be kept in mind when interpreting the results.

The amount of burned hydrogen is roughly proportional to the amount of pre-existing hydrogen (Fig. 4-173), while the amount of produced hydrogen does not correlate (Fig. 4-174, Table 4-14 and Table 4-29). The pressure increase in the containment vessel is proportional to the amount of burnt hydrogen regarding KH02 and KH05 (Fig. 4-175). However, this does not apply to KH06 in respect to KH05.

4.5.3 Debris recovery data

The debris distribution in the compartments for both tests is almost identical, but more remained in the cavity and less reached SC1 and the containment, compared to test KH02 (Fig. 4-1). The size distribution does not show significant differences between the three tests.

Post test pictures of test KH05 showed frozen melt at the lower part of the RPV outside (Fig. 4-129) and quite a large amount inside (Fig. 4-130). In test KH06, more frozen melt at the outside of the RPV was found and a cluster of melt had formed between lower head and pit floor (Fig. 4-143, Fig. 4-144).

4.5.4 Video observation results

The cameras looking down from the containment vessel ceiling recorded a light between 20 and 320 ms; afterward smoke obscured the view. The endoscope camera looking directly into subcompartment 1 observed moving hot debris particles up to 900 ms. The camera look-

ing from the side into the containment vessel also registered moving hot debris particles between 160 and 500 ms.

4.6 Test KH07

In this test the hydrogen concentration in the containment should have been twice as high (10% wet basis) as in the reference case KH02. Due to an error during the filling procedure only 8.7% or 9.2% were reached, regarding to the weighing and the sampling method, respectively. With 1.8 MPa RPV burst pressure, the reference pressure of 2.0 MPa was not quite reached.

4.6.1 Pressure and temperature data

The thermite reaction and RPV steam filling procedure proceeded as usual (Fig. 4-145). The melting of the brass plate took approximately 28 ms (Fig. 4-147). The blowdown time was similar as in KH02 (Fig. 4-148, Fig. 4-149). The pressure in the reactor pit was about 0.05 MPa above the containment pressure during blowdown and did not show any peak (Fig. 4-151).

Due to the higher hydrogen concentration the pressure increase in the containment was higher than in KH02, with 0.4 MPa vs. 0.29 MPa (Fig. 4-152).

The gas temperatures in SC1 were between 1200°C and 1400°C, and in the containment between 700°C and 800°C, both about 200°C higher than in KH02 (Fig. 4-153, Fig. 4-154).

4.6.2 Gas analysis

In the test with the largest pretest hydrogen concentration in the containment the tendency is corroborated: the more hydrogen exists before the blowdown the higher is the fraction of burnt hydrogen. More hydrogen burnt (109 mol) than initially available (89 mol, Fig. 4-173) and only very little hydrogen remained unburnt (10 mol). Also the fact that the initial hydrogen concentration is the main factor for the pressure increase in the containment is demonstrated clearly in Fig. 4-175. No correlation between amount of pre-existing hydrogen and amount of produced hydrogen can be seen (Fig. 4-174).

4.6.3 Debris recovery data

Although the blowdown pressure was only little less than in KH02 (1.8 vs. 2.0 MPa), more melt remained in the pit (0.59 vs. 0.48) and less reached the SC1 (0.40. vs. 0.50, Fig. 4-1).

The results regarding the fraction of melt that is dispersed out of the pit can be correlated with the KUTATELADZE number (Fig. 4-176), for the tests having the same pit geometry, i.e. the same flow cross sections out of the pit (KH02, 03, 05, 06 and 07). This correlation had been established for the test series for the EPR geometry, with cold fluids modeling the melt [Mey06].

The KUTATELADZE number is defined by

$$Ku = \rho_G u_G^2 / (\rho_L g \sigma)^{1/2} \quad (4.3)$$

with u_G, steam velocity in the annular space around the RPV, ρ_G density of the steam in the pit, and ρ_L and σ density and surface tension of the melt. The velocity of the steam u_G was determined from the blow-down pressure gradient in the RPV obtaining the steam mass flow, together with the properties of the steam in the pit and the flow cross section of the annular space around the RPV (Fig. 4-171, Fig. 4-172). For the KUTATELADZE number the average velocity was used. This was determined by integrating the velocity data which are higher than about 10 m/s.

The KUTATELADZE number represents the conditions to levitate droplets against gravity, and the threshold for droplet levitation according to the KUTATELADZE criterion is usually Ku > 14. However as before, a sharp threshold was not found in the results. The dispersed melt fraction correlates with

$$f_d = 0.4 \log_{10}(Ku) \leq 0.76 . \quad (4.4)$$

4.6.4 Video observation results

The cameras looking down from the containment vessel ceiling recorded flames in SC1 between 20 and 200 ms; afterward smoke obscured the view. The endoscope camera looking directly into SC1 observed flames and later moving hot debris particles up to 500 ms. The camera looking from the side into the containment vessel also registered flames and moving hot debris particles between 60 and 800 ms.

4.7 Test KH08

Test KH08 was performed with open pressure venting flaps (C) behind the biological shield. Eight holes with a diameter of 60 mm connected the pit behind the bio-shield with subcompartment 1 (Fig. 3-13). The water level behind the bio-shield and SC1 was 125 mm above SC1 floor and 15 mm above the lower rim of the 60-mm holes. A separation plate with large covered openings is installed in SC1 above the water level in order to prevent melt dropping into water from above. This melt enters SC1 through flow path (A) or through the large openings in the SC1 cover plate, (Fig. 3-14). The flow path B was closed.

4.7.1 Pressure and temperature data

In this test the thermite burning time was extremely short with only 1.78 seconds between ignition and plug failure (Table 4-5). The reason is unknown. Because it takes generally about 1.2 seconds until the steam valve opening is triggered by the rising temperature, and the valve is kept open for 1.1 seconds, it was still open for 0.56 seconds into the RPV blow down. Thus, steam was still flowing from the steam accumulator to the RPV and was blown

out into the cavity. More steam was ejected, i.e. 49 moles vs. about 32 moles in comparable tests (Table 4-1, Table 4-2).

Due to the open steam valve the pressure curve still rises after the start of the blowdown (Fig. 4-161) and the blowdown lasts much longer than usually. At the time of the closing of the valve the pressure curve shows an inflection point.

The pressure in the lower pit shows some peaks at early times (t < 0.2 s) as could be seen in other tests before (Fig. 4-164). However, a sharp high pressure peak occurs at t = 0.23 s, both, behind the bio-shield and in the lower pit. This should be the instant when melt reaches the water behind the bio-shield. At the same time the positive pressure gradient in the adjacent compartments and containment vessel decreases (Fig. 4-163). The maximum pressure increase in the containment vessel is only 0.14 MPa, which is quite low compared to 0.29 MPa in KH02 (Fig. 4-165).

The maximum temperatures in SC1 on average are 200 K lower than in KH02 (Fig. 4-166). In the containment vessel maximum temperatures are between 250 and 300°C (Fig. 4-167), while in KH02 they were between 300 and 500°C.

4.7.2 Gas analysis

Although the amount of pre-existing hydrogen was similar as in other tests much less hydrogen was produced (Fig. 4-174). Also little hydrogen burnt (Fig. 4-173) and consequently the pressure increase in the containment is low (Fig. 4-175, Table 4-29). The reason for this differing result probably is the additional large flow path leading partially through water into the subdivided subcompartment 1. As can be seen from the melt distribution, a large part of melt went this way.

4.7.3 Debris recovery data

Compared to test KH02, only half the amount of melt was ejected to SC1 via the flow path along the main cooling lines. About the same amount went through the pressure venting holes behind the bio-shield (Fig. 4-1). There, melt was quenched in the water. More of the smaller particles were entrained behind the bio-shield and through the venting holes. Thus the median diameter is only 0.7 mm vs. 3 mm diameter in SC1 (Fig. 4-169).

4.7.4 Video observation results

The cameras looking down from the containment vessel ceiling recorded flames in SC1 between 20 and 280 ms, with two peaks, at 60 ms and 240 ms, respectively; afterward smoke obscured the view. The endoscope camera looking directly into SC1 observed flames and later moving hot debris particles up to 700 ms. The camera looking from the side into the containment vessel registered flames between 220 ms and 440 ms, and moving hot debris particles thereafter until 700 ms.

Table 4-1 Pre-test data

		KH01	KH02	KH03	KH04	KH05	KH06	KH07	KH08
Atmosphere pressure	mbar	1005	998	1004	995	1002	1009	1011	1008
Pre-test accumulator pressure	MPa	3.69	3.48	3.49	3.46	1.94	1.53	3.58	3.53
Pre-test accumulator temperature	°C	265	268	242	242	211	222	243	244
Pre-test water in accumulator	g	1500	1500	1500	1500	954	623	1500	1500
Post-test water in accumulator	g	991	899	920	997	626	379	935	616
Difference (water/steam in RCS/RPV)	g	509	601	580	503	328	244	565	884
Pre-test pressure in RCS/RPV vessel (N_2)	MPa	0.101	0.100	0.100	0.099	0.100	0.116	0.106	0.098
Pre-test temperature in RCS/RPV vessel	°C	189 /219	175 /215	160/- -	136	158	146	151	170
Containment temp. at closing valves	°C	25	20	24	24	34	25	24	21
Pre-test pressure in containment vessel	MPa	0.21	0.211	0.209	0.203	0.210	0.213	0.219	0.208
Pre-test temperature in containment vessel	°C	102	103	104	101	100	102	102	104
Hydrogen in containment vessel	g	103.5	101.7	124.9	103.9	98.1	123.3	170.5	100.4

Table 4-2 Initial conditions in RPV/RCS vessel

		KH01	KH02	KH03	KH04	KH05	KH06	KH07	KH08
Thermite mass	kg	10.665	10.640	10.638	10.400	10.635	10.637	10.640	10.633
RCS/RPV pressure (t = 0 s)	MPa	2.57	1.99	1.98	1.97	1.18	1.04	1.80	2.12
RCS/RPV steam / water	g moles	28.3	33.3	32.2	27.9	18.2	13.56	31.4	49.1*
RCS/RPV nitrogen	g moles	2.1	2.1	2.2	2.4	2.2	2.3	2.3	2.2
Exit hole diameter	cm	5.6	5.6	2.8	5.6	5.6	5.6	5.6	5.6

***** steam valve not closed at t = 0, valve closed at t = 0.564 s and p_{RPV} = 1.42 MPa

Table 4-3 Initial conditions in the containment vessel (incl. subcompartments)

			KH01	KH02	KH03	KH04	KH05	KH06	KH07	KH08
Initial air temperature	T_0	K	298	294	297	297	307	298	297	294
Atmospheric pressure	P_0	MPa	0.1005	0.0998	0.1004	0.0995	0.1004	0.1009	0.1011	0.1006
Temperature at start (average)	T_1	K	376.4	372.1	377.0	374.0	371.0	375.0	375.0	376.0
Pressure at start	P_1	MPa	0.2135	0.210	0.210	0.203	0.21	0.213	0.219	0.208
Added hydrogen	m_{H2}	kg	0.1053	0.1017	0,1249	0.1039	0.0981	0.1233	0.1705	0.1004
Air mass	m_{air}	kg	16.304	16.411	16.343	16.196	15.811	16.369	16.457	16.543
Steam mass	m_{steam}	kg	5.994	5.852	5.284	5.3198	6.3111	5.7974	5.8023	5.4488
Partial pressure air	P_{1air}	MPa	0.127	0.126	0.128	0.125	0.121	0.127	0.128	0.129
Partial pressure H_2	p_{1H2}	MPa	0.0115	0.0113	0.0141	0.01155	0.01081	0.01374	0.01900	0.01122
Partial pressure H_2O	P_{steam}	MPa	0.0750	0.0724	0.0667	0.06616	0.07786	0.07229	0.07235	0.06812
Added hydrogen	N_{H2}	kmol	0.0512	0.0506	0.0620	0.0515	0.0487	0.0612	0.0846	0.0498
Steam moles	N_{H2O}	kmol	0.3327	0.3249	0.2933	0.2953	0.3503	0.3218	0.3221	0.3026
Air moles	N_{air}	kmol	0.5630	0.5667	0.5643	0.5593	0.5459	0.5652	0.5683	0.5712
Total gas moles	N_{total}	kmol	0.9469	0.9421	0.9196	0.9061	0.9449	0.9482	0.9749	0.9235
Nitrogen moles	N_{N2}	kmol	0.4393	0.4422	0.4403	0.4364	0.4260	0.4411	0.4434	0.4457
Oxygen moles	N_{O2}	kmol	0.1182	0.1189	0.1185	0.1174	0.1146	0.1186	0.1193	0.1199
Argon etc. moles	$N_{Ar\ etc.}$	kmol	0.0054	0.0055	0.0054	0.0054	0.0053	0.0054	0.0055	0.0055
Mol% of hydrogen	N_{H2}/N_{tot}	%	5.41	5.37	6.74	5.69	5.15	6.45	8.67	5.39
Mol% of steam	N_{H2O}/N_{tot}	%	35.14	34.48	31.89	32.59	37.07	33.94	33.04	32.75
Mol% of air	N_{air}/N_{tot}	%	59.45	60.15	61.37	61.72	57.78	59.61	58.29	61.86
Mol% of nitrogen	N_{N2}/N_{tot}	%	46.39	46.93	47.89	48.16	45.08	46.51	45.48	48.27
Mol% of oxygen	N_{O2}/N_{tot}	%	12.48	12.63	12.88	12.96	12.13	12.51	12.23	12.98
Mol% of argon	N_{Ar}/N_{tot}	%	0.57	0.58	0.59	0.59	0.56	0.57	0.56	0.60
Data determined from gas samples:										
Mol% of hydrogen	N_{H2}/N_{tot}	%	*6.34*	*7.33*	*5.79*	-	***5.19***	***5.48***	***9.15***	***5.59***
Mol% of oxygen	N_{O2}/N_{tot}	%	*11.01*	*11.04*	*13.18*	-	***12.08***	***12.36***	***12.16***	***12.16***

Table 4-4 Characteristics of the blow down process

No.	d (mm)	Δp (MPa)	u_{liquid} (m/s)	t_L (s)	t_{2ph} (s)	t_{end} (s)	t_s (s)	ε	t_s/t_L -
KH01	0.056	2.37	35.0	0.050	0.18	0.43	0.053	0.6	1.06
KH02	0.056	1.78	30.3	0.064	0.23	0.42	0.061	0.6	0.95
KH03	0.028	1.76	30.1	0.250	0.60	1.38	0.246	0.6	0.98
KH04	0.056	1.77	30.2	0.057	0.21	0.43	0.061	0.6	1.07
KH05	0.056	0.97	22.3	0.110	0.30	0.70	0.083	0.6	0.76
KH06	0.056	0.83	20.6	0.120	0.25	0.60	0.090	0.6	0.75
KH07	0.056	1.58	28.6	0.090	0.28	0.44	0.065	0.6	0.72
KH08	0.056	1.91	31.4	-	0.25	0.71	0.059	0.6	-

Δp = $p_{RPV} - p_{cont.}$

$\mathbf{u}_{Liquid} = (2\,\Delta p/\rho_M)^{1/2}$ (Eq. 4.1), theoretical velocity of liquid jet

$\mathbf{t}_L$ end of single-phase liquid jet (liquid discharge time) (from Fig.4-5)

$\mathbf{t}_{2ph}$ end of 2-phase jet (from pressure gradient, e.g. Fig.4-5)

$\mathbf{t}_{end}$ end of blow down (from pressure gradient, e.g. Fig.4-5)

$\mathbf{t}_s = V_M / (\varepsilon\,\pi\,d^2/4\,u_L)$, (Eq.4.2) theoretical liquid discharge time

Table 4-5 Characteristic times of the thermite burning process

		KH01	KH02	KH03	KH04	KH05	KH06	KH07	KH08
Ignition to plug failure	[s]	3.70	3.25	***9.20***	2.67	3.70	4.20	3.10	***1.78***
Ignition to valve opening	[s]	2.18	1.50	1.20	1.27	1.22	1.40	1.40	1.23
Valve closed to plug failure	[s]	0.32	0.55	6.80	0.30	1.38	1.70	0.60	**-0.55**

Table 4-6 Gas concentrations determined from gas samples in test KH01

Time	Location	Species (mole %)			
		N2	O2	H2	CO_2/CO/CH_4
pretest	containment	73.15	16.93	9.93	n.n.
	subcompartment 1	73.48	17.16	9.35	
	subcompartment 2	76.87	17.19	6.61	
2 s	subcompartment 2	42.65	3.69	46.06	2.0/5.2/0.4
5 s	containment	77.66	14.68	7.66	n.n.
	subcompartment 1	81.10	11.28	5.74	1.9/ 0 / 0
	subcompartment 2	44.85	4.22	42.98	1.9/5.6/0.5
5 min	containment	78.77	13.53	7.69	n.n.
	subcompartment 1	78.42	14.01	7.56	
	subcompartment 2	77.66	13.01	9.34	

Table 4-7 Gas concentrations determined from gas samples in test KH02

Time	Location	Species (mole %)			
		N2	O2	H2	CO_2/CO/CH_4
pretest	containment	72.48	16.53	10.99	n.n.
	subcompartment 1	69.86	18.09	12.05	
	subcompartment 2	72.53	17.96	9.51	
2 s	subcompartment 2	81.89	12.53	5.57	n.n.
5 s	containment	80.76	13.33	5.92	n.n.
	subcompartment 1	87.79	6.62	5.58	
	subcompartment 2	80.99	13.21	5.80	
5 min	containment	81.14	12.74	6.12	n.n.
	subcompartment 1	81.30	12.63	6.07	
	subcompartment 2	81.28	12.13	6.60	

Table 4-8 Gas concentrations determined from gas samples in test KH03

Time	Location	Species (mole %)			
		N2	O2	H2	CO_2/CO/CH_4
pretest	containment	71.94	19.37	8.6	0.1/n.n.
	subcompartment 1	72.51	19.30	8.1	
	subcompartment 2	72.12	19.34	8.4	
0.5 s	subcompartment 2	-	-	-	n.n.
1.2 s	containment	76.41	17.04	6.1	0.5/n.n.
	subcompartment 1	90.13	6.82	0.2	2.85/n.n.
	subcompartment 2	-	-	-	-
5 min	containment	*79.3*	*20.3*	*0.3*	n.n.
	subcompartment 1	-	-	-	
	subcompartment 2	-	-	-	

Gas sampling was imperfect

Table 4-9 Gas concentrations determined from gas samples in test KH04

Time	Location	Species (mole %)			
		N2	O2	H2	CO_2/CO/CH_4
pretest	containment	76.22	15.84	6.60	0.57/0.08/-
	subcompartment 1	77.74	15.24	6.35	0.59/0.08/-
	subcompartment 2	78.61	16.11	5.28	n.n.
0.5 s	subcompartment 2	-	-	-	n.n.
1.2 s	containment	77.21	16.92	5.88	-
	subcompartment 1	90.27	7.49	1.21	1.03/-/-
	subcompartment 2	83.13	15.22	1.65	-
5 min	containment	-	-	-	n.n.
	subcompartment 1	-	-	-	
	subcompartment 2	-	-	-	

Gas sampling was imperfect

Table 4-10 Gas concentrations determined from gas samples in test KH05

Time	Location	Species (mole %)			
		N2	O2	H2	CO_2/CO/CH_4
pretest	containment	72.40	19.22	8.39	n.n.
	subcompartment 1	73.18	19.09	7.73	
	subcompartment 2	72.46	19.30	8.24	
0.5 s	subcompartment 1	83.28	13.63	1.63	n.n.
1.2 s	containment	73.76	17.89	7.86	0.49
	subcompartment 1	85.92	9.21	2.79	2.00
	subcompartment 2	73.81	18.28	7.91	-
5 min	containment	74.44	17.45	7.41	0.70
	subcompartment 1	75.41	17.03	7.13	0.43
	subcompartment 2	75.25	17.09	7.66	-

Table 4-11 Gas concentrations determined from gas samples in test KH06

Time	Location	Species (mole %)			
		N2	O2	H2	CO_2/CO/CH_4
pretest	containment	73.10	18.67	8.23	n.n.
	subcompartment 1	72.56	18.85	8.59	
	subcompartment 2	72.80	18.94	8.26	
0.5 s	subcompartment 1	81.09	18.38	0.53	n.n.
1.2 s	containment	74.49	17.76	7.75	-
	subcompartment 1	84.22	14.96	0.82	n.n.
	subcompartment 2	74.03	17.81	8.15	-
5 min	containment	76.19	16.25	7.56	-
	subcompartment 1	77.07	20.13	2.81	n.n.
	subcompartment 2	75.74	16.43	7.83	-

Table 4-12 Gas concentrations determined from gas samples in test KH07

Time	Location	Species (mole %)			
		N2	O2	H2	CO_2/CO/CH_4
pretest	containment	68.15	18.13	13.73	n.n.
	subcompartment 1	68.24	18.31	13.44	
	subcompartment 2	68.23	17.99	13.78	
0.5 s	subcompartment 1	86.94	7.56	4.01	1.49/-/-
1.2 s	containment	83.88	14.76	1.35	-
	subcompartment 1	92.63	4.00	1.60	1.77/-/-
	subcompartment 2	87.95	9.00	1.93	1.11/-/-
5 min	containment	85.45	12.41	2.14	-
	subcompartment 1	85.37	12.14	2.12	0.37/-/-
	subcompartment 2	85.65	11.90	2.45	-

Table 4-13 Gas concentrations determined from gas samples in test KH08

Time	Location	Species (mole %)			
		N2	O2	H2	CO_2/CO/CH_4
pretest	containment	73.11	17.93	8.95	n.n.
	subcompartment 1	74.47	18.72	5.81	
	subcompartment 2	73.48	17.89	8.62	
0.5 s	subcompartment 1	79.70	20.30	-	-/-/-
1.2 s	containment	76.19	16.92	6.90	-
	subcompartment 1	79.37	20.63	-	-/-/-
	subcompartment 2	76.45	17.03	6.51	-/-/-
5 min	containment	76.50	15.97	7.52	-
	subcompartment 1	79.72	18.96	1.32	-/-/-
	subcompartment 2	76.20	16.09	7.72	-

Table 4-14 Results of gas sampling and gas analysis by the nitrogen method

containment vessel		KH01	KH02	KH03	KH04	KH05	KH06	KH07	KH08
preexisting gas	N_2 mol	354	353	355	*375*	340	361	351	358
	O_2 mol	82	80	96	*76*	90	92	93	88
	H_2 mol	48	54	42	*31*	39	41	71	44
posttest gas moles	O_2 mol	61	55	79	-	80	77	51	75
	H_2 mol	35	27	28	-	34	36	9	35
hydrogen burned	H_2 mol	42	50	33	-	21	30	85	26
hydrogen produced	H_2 mol	29	23	19	-	16	26	23	18
Fraction of available hydrogen that burned $N_{burn}/(N_{pre}+N_{prod})$		0.55	0.65	0.54	-	0.38	0.46	0.91	0.43
sub-compartment 1									
preexisting gas	N_2 mol	90	86	91	*96*	87	91	89	93
	O_2 mol	21	22	24	*19*	23	24	24	23
	H_2 mol	12	15	10	*8*	9	11	18	7
posttest gas	O_2 mol	16	13	7	-	20	16	13	22
	H_2 mol	9	6	0	-	8	1	2	2
hydrogen burned	H_2 mol	10	18	35	-	6	15	23	3
hydrogen produced	H_2 mol	7	9	25	-	5	5	7	*-3*
Fraction of available hydrogen that burned $N_{burn}/(N_{pre}+N_{prod})$		0.53	0.74	0.99	-	0.43	0.94	0.91	*0.62*
sub-compartment 2									
preexisting gas	N_2 mol	5.0	4.7	4.8	*5.1*	4.5	4.8	4.7	4.8
	O_2 mol	1.1	1.2	1.3	*1.0*	1.2	1.2	1.2	1.2
	H_2 mol	0.4	0.6	0.6	*0.3*	0.5	0.5	0.9	0.6
posttest gas	O_2 mol	0.8	0.7	1.3	-	1.0	1.0	0.7	1.0
	H_2 mol	0.6	0.4	0.0	-	0.5	0.5	0.1	0.5
hydrogen burned	H_2 mol	0.6	0.9	-	-	0.4	0.4	1.2	0.3
hydrogen produced	H_2 mol	0.7	0.7	-	-	0.3	0.4	0.4	0.2
Fraction of available hydrogen that burned $N_{burn}/(N_{pre}+N_{prod})$		0.48	0.71	-	-	0.44	0.46	0.90	0.39
Total									
Initial	H_2 mol	60	69	53	*40*	49	52	89	52
Produced	H_2 mol	37	33	43	-	21	31	30	15
Burned	H_2 mol	53	69	67	-	28	46	109	29
Post test	H_2 mol	44	33	29	-	42	37	10	38
Fraction burned	-	0.55	0.67	0.70	-	0.39	0.55	0.91	0.44

Table 4-15 Detailed debris recovery results

Location	KH01	KH02	KH03	KH04	KH05	KH06	KH07	KH08
Containment								
Hoses Containment	0.0	13.4	0.0	10.5	0.2	3.9	25.9	13.9
SC2 cover top side	426.8	42.2	34.9	184.2	37.0	13.0	19.2	18.2
Containment wall and floor	356.6	188.8	247.7	97.5	79.2	101.6	80.3	59.80
containment dome	5.2	0.0	0.0	0.0	0.0	0.0	0.0	0.0
Containment total	**788.6**	**244.4**	**282.6**	**292.2**	**116.4**	**118.5**	**125.4**	**91.9**
Subcompartment 1								
Cover plates underside 0-1	14.9	63.0	11.4	24.9	2.7	0	11.1	11.8
Cover plates underside 1-2	16.6	35.8	2.1	12.9	4.8	0	3.5	12.5
Cover plates underside 2-3	24.0	41.5	19.3	17.9	1.8	0	9.3	25.0
Cover plates underside 3-0	11.4	26.6	8.2	27.8	4.2	0	18.5	9.6
subtotal cover plates	***66.9***	***166.9***	***41.0***	***83.5***	***13.5***	***0***	***42.4***	***58.9***
Plates below 300 mm opening								
Plate 1	77.7	44.5	78.0	59.5	68.6	28.0	47.2	28.1
Plate 2	84.8	42.5	99.6	27.9	53.8	32.0	47.1	88.7
Plate 3	50.6	94.7	83.9	27.2	33.3	52.0	47.2	52.5
Plate 4	130.9	162.1	91.1	89.6	63.8	92.0	47.1	89.7
Equivalent area beside plates	369.4	510.3	472.3	331.4	291.4	176.1	373.5	250.0
subtotal plates	***713.4***	***854.1***	***824.9***	***535.6***	***510.9***	***380.1***	***562.1***	***509.0***
subtotal hoses	31.0	0.0	5.2	1.6	1.0	1.8	1.8	5.5
Particles Subcompartment 1								
Main cooling lines (8)	20.3	468.5	293.5	104.0	140.2	563.3	42.5	-16.5
wall and floor / sump	2057.4	2541.5	1833.2	1336.8	1746.3	1641.4	2196.7	1052.4 /2020.0
cover of nuts M20	24.4	-	28.3	24.5	22.6	-	33.9	21.3
crusts at subcompartment wall	512.0	720.9	902.6	464.8	375.9	383.3	182.2	613.6
HKM, collected particles	837.3						1047.1	
subtotal Subcompartment 1	***3451.4***	***3730.9***	***3057.6***	***1930.1***	***2285.0***	***2588.0***	***3502.2***	***3690.8***
Subcompartment 1 total	**4262.7**	**4751.9**	**3928.7**	**2550.8**	**2810.4**	**2969.9**	**4108.5**	**4288.3**
Subcompartment 2								
cover of nuts M56	67.1	0.0	0.0	48.1	0	0	0	0
Nuts M56	0.0	0.0	0.0	0.0	0	0	0	0
SC2 Part 1	216.6	0.0	0.0	67.0	0	0	0	0
SC2 Part 2	405.7	0.0	0.0	72.4	0	0	0	0
Sub 2 particles	2627.3	0.0	25.8	3828.6	0	0	0	0
Subcompartment 2 total	**3316.7**	**0.0**	**25.8**	**4040.1**	**0**	**0**	**0**	**0**
Pit (weight difference)	9658.2	2640.0	4720.0	2100.00	3826.5	2261.6	3534.0	3283.5
biological shield	551.6					1067.2	346.4	870.9
Collected crust	107.6	518.2	334.0	283.2	945.6		109.7	0.0
crust at RPV outside	707.8	571.0	1366.5		898.0	2726.1	855.5	1410.5
8x flow path	47.6	253.9	93.4	133.3	198.5	0.21	-10.4	-276.4
Melt below pit							1146.0	
Pit total	***1414.6***	**4562.1**	**6513.9**	**2847.0**	**5868.6**	**6055.1**	**5981.2**	**5288.5**
Total recovered melt	**9782.6**	**9558.4**	**10751.0**	**9731.2**	**8795.4**	**9143.5**	**10215.1**	**9668.7**
Initial thermite charge	**10665.0**	**10640.0**	**10638.0**	**10640.0**	**10635.0**	**10637.0**	**10640.0**	**10633.3**
Ejected melt	**9658.2**	**9962.4**	**10942.0**	**10062.0**	**8809.0**	**8776.4**	**10241.0**	**8979.6**
Remaining in RPV / RCS	**1006.8**	**656.3**	**-660.0**	**568.0**	**1235.0**	**1860.6**	**399.0**	**1653.4**
Difference recovered-ejected	**124.4**	**-404.0**	**-191.0**	**-331.2**	**-13.6**	**367.1**	**-25.9**	**689.1**

Table 4-16 Debris recovery summary

Mass Balance (kg)	**KH01**	**KH02**	**KH03**	**KH04**	**KH05**	**KH06**	**KH07**	**KH08**
Initial thermite charge	10.665	10.640	10.638	10.640	10.635	10.637	10.640	10.633
Total ejected out of RPV	9.658	9.962	*10.942*	10.062	8.809	8.776	10.241	8.980
Total recovered	9.782	9.558	10.747	9.731	8.795	9.144	10.215	9.669
Balance recovered - ejected	+0.124	-0.404	-0.195	-0.331	-0.014	+0.367	-0.026	+0.689
Recovery factor	1.013	0.959	0.982	0.967	0.998	1.042	0.997	1.077
Fraction particles smaller 10 mm, total	*0.477*	*0.351*	*0.278*	*0.442*	*0.241*	*0.210*	*0.269*	*0.344*
Fraction particles smaller 2.5 mm, total	*0.247*	*0.218*	*0.159*	*0.194*	*0.167*	*0.138*	*0.209*	*0.236*
Cavity	1.415	4.562	6.514	2.848	5.869	6.055	5.981	5.289
Subcompartment 1	4.263	4.752	3.929	2.551	2.810	2.970	4.108	4.288*
Fraction smaller 10 mm in SC1	*0.634*	*0.661*	*0.697*	*0.697*	*0.732*	0.456	0.644	*0.753**
Fraction smaller 2.5 mm in SC1	*0.408*	*0.395*	*0.375*	*0.456*	*0.503*	0.291	0.495	*0.510**
Subcompartment 2	3.316	0.0	0.026	4.041	0.0	0.0	0.0	0.0
Fraction smaller 10 mm in SC2	*0.398*	-	*1.000*	*0.568*	-	-	-	-
Fraction smaller 2.5 mm in SC2	*0.081*	-	*0.946*	*0.145*	-	-	-	-
Containment	0.789	0.244	0.283	0.292	0.116	0.119	0.125	0.099
Fraction smaller 10 mm in containment	*0.815*	*0.878*	*0.792*	*0.787*	*0.516*	0.469	0.792	*1.000*
Fraction smaller 2.5 mm in containment	*0.522*	*0.828*	*0.757*	*0.459*	*0.490*	0.457	0.787	*0.988*
Melt transport fractions:								
Remained in cavity	0.145	0.477	0.606	0.293	0.667	0.662	0.586	0.547
Transported to SC 1	0.436	0.497	0.366	0.262	0.320	0.325	0.402	0.444*
Transported to SC 2	0.339	0.000	0.002	0.415	0.000	0.000	0.000	0.000
Transported to containment	0.081	0.026	0.026	0.030	0.013	0.013	0.012	0.010
Particle size of debris smaller 10 mm								
SMMD SC 1 [mm]	2.00	2.15	2.60	2.00	1.55	1.83	1.00	3.00
SMMD SC 2 / *sump* * [mm]	6.30	-	0.27	6.20	-	-	-	*0.75**
SMMD containment [mm]	1.00	0.13	0.25	1.20	0.11	0.09	0.17	0.15
SMMD average [mm]	2.90	2.00	2.30	3.90	1.54	1.80	0.95	1.2

*part of it (2.020 kg) entered SC1 through the pressure venting flaps behind the biological shield, (0.209 fraction)

Note: Differences to earlier published data for tests KH01 and KH02 are due to a re-evaluation of the size distribution data (omitting debris, which remained in the sieve with 10 mm grid, and interpolating particle size for the cumulative percentage plot).

Table 4-17 Results of the sieve analysis of KH01 (mass in gram)

Sieve No.	particle size < [mm]	Subcompartment 1	Subcompartment 2	Containment	Total
1	10	56,7	417,1	74,1	547,9
2	7,1	192,8	294,5	61,9	549,2
3	5	272,2	189,7	44,8	506,7
4	3,55	443,2	148,5	50,1	641,8
5	2,5	306,1	85,7	27,8	419,6
6	1,8	278,4	53,3	26,1	357,8
7	1,25	199,6	29,0	23,5	252,1
8	0,9	186,6	23,5	31,6	241,7
9	0,63	137,1	14,0	27,6	178,7
10	0,45	137,2	12,4	35,7	185,3
11	0,315	108,6	8,7	35,0	152,3
12	0,224	88,6	8,4	34,8	131,8
13	0,16	73,0	7,4	35,7	116,1
14	0,112	56,6	5,5	35,6	97,7
15	0,08	52,5	6,4	36,3	95,2
16	0,056	40,1	4,0	37,9	82,0
17	0,04	72,9	11,3	24,1	108,3
	Total	**2702,2**	**1319,4**	**642,6**	**4664,2**
≤ 2.5 mm		**1737.3**	**269.6**	**411.7**	**2418.6**

Table 4-18 Results of the sieve analysis of KH02 (mass in gram)

Sieve No.	particle size < [mm]	Subcompartment 1	Subcompartment 2	Containment	Total
1	10	174,4	-	4,1	178,5
2	7,1	308,4	-	3,8	312,2
3	5	406,5	-	1,0	407,5
4	3,55	376,1	-	3,5	379,6
5	2,5	321,3	-	4,0	325,3
6	1,8	278,6	-	5,2	283,8
7	1,25	198,7	-	6,8	205,5
8	0,9	194,0	-	9,9	203,9
9	0,63	147,3	-	9,7	157,0
10	0,45	151,6	-	12,2	163,8
11	0,315	121,8	-	13,2	135,0
12	0,224	106,7	-	14,3	121,0
13	0,16	88,7	-	16,2	104,9
14	0,112	73,9	-	17,9	91,8
15	0,08	63,9	-	21,7	85,6
16	0,056	51,1	-	27,4	78,5
17	0,04	79,9	-	43,8	123,7
	Total	3142,9	-	214,7	3357,6
≤ 2.5 mm		1877,5	**-**	202,3	2079,8

Table 4-19 Results of the sieve analysis of KH03 (mass in gram)

Sieve No.	particle size < [mm]	Subcompartment 1	Subcompartment 2	Containment	Total
1	10	270,3	0,0	2,1	272,4
2	7,1	317,3	1,4	2,1	320,8
3	5	346,0	0,0	1,5	347,5
4	3,55	332,9	0,0	4,3	337,2
5	2,5	251,1	1,7	6,6	259,4
6	1,8	200,9	0,9	8,8	210,6
7	1,25	149,1	0,9	9,1	159,1
8	0,9	138,4	1,1	15,5	155,0
9	0,63	112,4	1,6	15,1	129,1
10	0,45	123,6	2,2	20,6	146,4
11	0,315	108,6	3,3	21,5	133,4
12	0,224	92,7	2,5	18,9	114,1
13	0,16	76,0	3,0	20,5	99,5
14	0,112	53,7	1,6	16,6	71,9
15	0,08	52,2	1,5	21,4	75,1
16	0,056	51,2	0,9	20,6	72,7
17	0,04	63,0	3,2	18,7	84,9
	Total	**2739,4**	**25,8**	**223,9**	**2989,1**
≤ 2.5 mm		**1472,9**	**24,4**	**213,9**	**1711,2**

Table 4-20 Results of the sieve analysis of KH04 (mass in gram)

Sieve No.	particle size < [mm]	Subcompartment 1	Subcompartment 2	Containment	Total
1	10	53,8	664,5	22,2	740,5
2	7,1	135,9	527,6	31,5	695,0
3	5	193,6	321,6	27,2	542,4
4	3,55	230,0	196,5	14,8	441,3
5	2,5	210,0	227,4	9,1	446,5
6	1,8	181,5	181,1	6,4	369,0
7	1,25	138,1	47,1	4,4	189,6
8	0,9	116,7	32,3	5,0	154,0
9	0,63	91,6	18,8	5,5	115,9
10	0,45	89,3	20,1	4,3	113,7
11	0,315	71,4	13,7	5,2	90,3
12	0,224	62,4	11,9	13,3	87,6
13	0,16	55,1	8,8	21,7	85,6
14	0,112	48,2	6,1	22,6	76,9
15	0,08	51,2	6,5	21,2	78,9
16	0,056	39,2	5,6	11,0	55,8
17	0,04	9,8	5,1	4,5	19,4
	Total	**1777,8**	**2294,7**	**229,9**	**4302,4**
≤ 2.5 mm		**1164,5**	**584,5**	**134,2**	**1883,2**

Table 4-21 Results of the sieve analysis of KH05 (mass in gram)

Sieve No.	particle size < [mm]	Subcompartment 1	Subcompartment 2	Containment	Total
1	10	84,8	0	0,0	84,8
2	7,1	119,9	0	1,0	120,9
3	5	187,1	0	0,0	187,1
4	3,55	250,7	0	1,9	252,6
5	2,5	218,4	0	0,0	218,4
6	1,8	194,6	0	1,3	195,9
7	1,25	149,4	0	3,6	153,0
8	0,9	133,0	0	0,5	133,5
9	0,63	105,0	0	1,2	106,2
10	0,45	118,2	0	1,4	119,6
11	0,315	100,0	0	5,9	105,9
12	0,224	92,1	0	2,4	94,5
13	0,16	86,9	0	6,0	92,9
14	0,112	78,9	0	7,6	86,5
15	0,08	62,6	0	7,9	70,5
16	0,056	47,7	0	6,6	54,3
17	0,04	26,6	0	12,6	39,2
	Total	**2055,9**	**0**	**59,9**	**2115,8**
≤ 2.5 mm		**1413.4**	**0**	**57,0**	**1470,4**

Table 4-22 Results of the sieve analysis of KH06 (mass in gram)

Sieve No.	particle size < [mm]	Subcompartment 1	Subcompartment 2	Containment	Total
1	10	153,2	0	0	153,2
2	7,1	130,8	0	0	130,8
3	5	166,0	0	0,5	166,5
4	3,55	207,4	0	0,9	208,3
5	2,5	170,2	0	1,7	171,9
6	1,8	149,6	0	0,8	150,4
7	1,25	113,8	0	0,4	114,2
8	0,9	100,2	0	1,1	101,3
9	0,63	82,6	0	2,6	85,2
10	0,45	94,4	0	3,6	98,0
11	0,315	83,2	0	5,6	88,8
12	0,224	75,6	0	7,8	83,4
13	0,16	79,4	0	10,6	90,0
14	0,112	76,2	0	13,6	89,8
15	0,08	71,0	0	19	90,0
16	0,056	52,4	0	20,8	73,2
17	0,04	14,4	0	14,8	29,2
	Total	**1820,4**	**0**	**103,8**	**1924,2**
≤ 2,5 mm		**1163,0**	**0**	**102,4**	**1265,4**

Table 4-23 Results of the sieve analysis of KH07 (mass in gram)

Sieve No.	particle size < [mm]	Subcompartment 1	Subcompartment 2	Containment	Total
1	10	68,4	0	0,0	68.4
2	7,1	124,3	0	0,0	124.3
3	5	187,2	0	0,0	187.2
4	3,55	233,8	0	0,6	234.4
5	2,5	238,4	0	0,4	238.8
6	1,8	240,5	0	1,0	241.5
7	1,25	206,1	0	0,6	206.7
8	0,9	199,3	0	1,3	200.6
9	0,63	187,8	0	6,3	194.1
10	0,45	187,0	0	10,8	197.8
11	0,315	153,2	0	12,2	165.4
12	0,224	135,8	0	11,4	147.2
13	0,16	112,2	0	12,9	125.1
14	0,112	89,8	0	9,2	99.0
15	0,08	80,4	0	9,0	89.4
16	0,056	73,2	0	6,5	79.7
17	0,04	129,0	0	17,1	146.1
	Total	**2646,4**	**0**	**99,3**	**2745.7**
≤ 2,5 mm		**2032.7**	**0**	**98,7**	**2131,4**

Table 4-24 Results of the sieve analysis of KH08 (mass in gram)

Sieve No.	particle size < [mm]	Subcompartment 1	Sump	Containment	Total
1	10	154.9	77.1	1.0	233.0
2	7,1	163.6	92.6	0.0	256.2
3	5	164.6	116.6	0.0	281.2
4	3,55	142.0	130.4	0.2	272.6
5	2,5	112.8	136.0	20.6	269.4
6	1,8	85.0	146.8	0.4	232.2
7	1,25	64.4	137.8	1.2	203.4
8	0,9	61.0	141.0	1.8	203.8
9	0,63	49.2	118.8	2.6	170.6
10	0,45	48.5	132.4	4.0	184.9
11	0,315	47.2	105.0	5.8	158.0
12	0,224	32.0	92.2	7.6	131.8
13	0,16	25.4	80.4	7.4	113.2
14	0,112	22.2	71.0	7.0	100.2
15	0,08	21.8	94.4	9.2	125.4
16	0,056	22.4	232.6	10.8	265.8
17	0,04	45.6	59.2	19..0	123.8
	Total	**1262.6**	**1964.3**	**98.6**	**3325.5**
≤ 2,5 mm		**637.5**	**1547.6**	**97.4**	**2282.5**

Table 4-25 Results of chemical analysis of small particles in containment

	Location	Containment								
	Particle	1			2			3	4	5
	Position	A	B		A	B	C			
	Notation	C-1A	C-1Ba	C-1Bb	C-2A	C-2B	C-2C	C-3	C-4	C-5
Fe	atom%	90,3	92,5	30,5	96,7	4,6	49,0	40,8		33,0
Cr	atom%	6,7				0,3		1,6		
Cu	atom%		7,0		2,3			0,5		
Mg	atom%					0,1				0,2
Al	atom%			10,7		31,3	1,4	1,5	16,5	0,1
Si	atom%			1,5		1,2	1,3	0,3	16,9	
Ca	atom%		0,5	0,9		0,9	0,5			0,2
O	atom%	3,0		56,4	1,0	61,6	47,8	55,3	66,6	66,5

Table 4-26 Results of chemical analysis of small particles in subcompartment 1

	Location	Subcompartment 1						
	Particle	1	2		3	4		
	Position		A	B		A	B	C
	Notation	S1-1	S1-2A	S1-2B	S1-3	S1-4A	S1-4B	S1-4C
Fe	atom%	43,1	40,0	6,0	40,9	31,0	20,4	35,0
Cr	atom%	0,5	0,7	0,2				
Cu	atom%	1,0						
Mg	atom%				0,6	9,0	23,2	1,0
Al	atom%	0,4	1,4	30,1	0,3	0,3	0,2	0,2
Si	atom%	0,3	0,4	2,4	0,2	0,2	0,3	
Ca	atom%	0,3		1,0	0,9	9,3	0,3	0,4
O	atom%	54,4	57,5	60,3	57,1	59,2	55,6	63,4

Table 4-27 Results of chemical analysis of small particles in subcompartment 2

	Location	Subcompartment 2								
	Particle	1	2	3	4	5		6	7	
	Position					A	B		A	B
	Notation	S2-1	S2-2	S2-3	S2-4	S2-5A	S2-5B	S2-6	S2-7A	S2-7B
Fe	atom%	44,0	1,6	94,6	42,1	95,7	1,9	0,3	39,4	6,3
Cr	atom%			1,2	0,3	0,7			0,9	0,5
Cu	atom%			2,2		2,5				
Mg	atom%		4,3				4,2	2,2	0,2	
Al	atom%		7,3		1,5		7,1	5,5	4,9	29,6
Si	atom%		13,3	0,6	1,3		13,5	16,4	0,5	0,9
Ca	atom%		9,5		0,2		9,5	8,3	0,2	0,6
O	atom%	56,0	64,0	1,4	54,6	1,1	63,8	67,3	53,9	62,1

Table 4-28 Results of chemical analysis of large particles in subcompartment 1 and 2

	Location	Subcompartment 1					Subcompartment 2				
	Particle	L1			L2		L3		L4	L5	
	Position	A	B	C	A	B	A	B		A	B
	Notation	L1-A	L1-B	L1-C	L2-A	L2-B	L3-A	L3-B	L4	L5-A	L5-B
Fe	atom%	92,4	17,4	13,4	96,4	15,8	4,4	73,7	97,4	97,7	0,5
Cr	atom%	0,2	0,7	0,4	2,0	1,4	0,9	5,0	0,7	0,4	0,4
Cu	atom%	2,6		0,3				1,7	1,7	1,5	
Mg	atom%		0,2			0,2	0,1				
Al	atom%		19,6	21,6		19,6	28,2				40,1
Si	atom%	0,4	1,6	2,1	0,3	1,1	4,0	1,1	0,2	0,4	0,5
Ca	atom%		0,7	0,9		0,6	0,8	0,4			0,5
O	atom%	4,4	59,8	61,3	1,3	61,3	61,6	18,1			58,0

Table 4-29 Summary of initial conditions and results of all Konvoi experiments

Test		KH01	KH02	KH03	KH04	KH05	KH06	KH07	KH08
Initial conditions									
RPV pressure	MPa	2,57	2,00	1,98	1,97	1,18	1,04	1,80	2,12
RPV steam	g mol	28,3	33,3	32,2	27,9	18,2	13,6	31,4	49,1*
RPV nitrogen	g mol	2,1	2,1	2,2	2,4	2,2	2,3	2,3	2,2
Hole diameter	cm	5,6	5,6	2,8	5,6	5,6	5,6	5,6	5,6
Scaled hole dia,	m	1,0	1,0	0,5	1,0	1,0	1,0	1,0	1,0
Cont, vessel pressure	MPa	0,21	0,21	0,21	0,20	0,21	0,21	0,22	0,21
Cont, vessel temp,	K	376	372	377	374	371	375	375	376
Cont, vessel gas	g mol	947	942	920	906	945	948	975	924
Gas composition in containment vessel									
Steam	mol%	35,1	34,5	31,9	32,6	37,1	33,9	33,0	32,8
N_2	mol%	46,4	46,9	47,9	48,2	45,1	46,5	45,5	48,3
O_2	mol%	12,5	12,6	12,9	13,0	12,1	12,5	12,2	13,0
H_2	mol%	5,4	5,4	6,7	5,7	5,2	6,5	8,7	5,4
other	mol%	0,6	0,6	0,6	0,6	0,6	0,6	0,6	0,6
Experimental results									
Melt transport fractions									
in cavity		0,14	0,48	0,61	0,29	0,67	0,66	0,59	0,55
containment		0,08	0,03	0,03	0,03	0,01	0,01	0,01	0,01
Subcompartment 1		0,44	0,48	0,37	0,26	0,31	0,33	0,40	0,24
Subcompartment 2 /sump		0,34	0,02	0,01	0,42	0,01	0,01	0	/0.20
particle diam, < 2,5 mm		0,25	0,22	0,16	0,19	0,17	0,14	0,21	0,24
Sieve analysis: debris fractions smaller 10 mm in									
Containment		0,82	0,88	0,79	0,79	0,52	0,47	0,79	1,00
Subcompartment 1		0,63	0,66	0,70	0,70	0,73	0,46	0,64	0,75
Sieve mass median diameter (SMMD) of particles < 10 mm in									
containment	mm	1.00	0,13	0,25	1,20	0,11	0,09	0,17	0,15
Subcompartment 1	mm	2,00	2,15	2,60	2,00	1,55	1,83	1,00	3,00
Subcompartment 2	mm	6,30	-	0,27	6,20	-	-	-	-
average	mm	2,90	2,00	2,30	3,90	1,54	1,80	0,95	1,20
Hydrogen									
pretest [1)]	g mol	60	69	*53*	40	49	52	89	52
produced	g mol	37	33	*43*	n.a.	21	31	30	15
burned	g mol	53	69	*67*	n.a.	28	46	109	29
post-test	g mol	44	33	*29*	n.a.	42	37	10	38
Fraction burned		0,55	0,67	*0,70*	n.a.	0,39	0,55	0,91	0,44
$\Delta p_{max\ meas}$ in cont.,	kPa	205	290	192	179	130	124	398	138
Time of p-peak	s	0,93	0,60	1,41	0,97	0,78	0,80	0,80	1,10
Analysis									
Δp_{max} H_2 burn [2)]	kPa	364	462	454	-	209	321	703	217
Δp_{max} HT melt	kPa	217	185	139	-	126	105	154	172
Δp_{max} total	kPa	580	648	594	-	335	426	857	390
DCH-efficiency		0,35	0,45	0,32	-	0,39	0,29	0,46	0,35

[1)] Data determined from gas samples are not consistent with added hydrogen mass

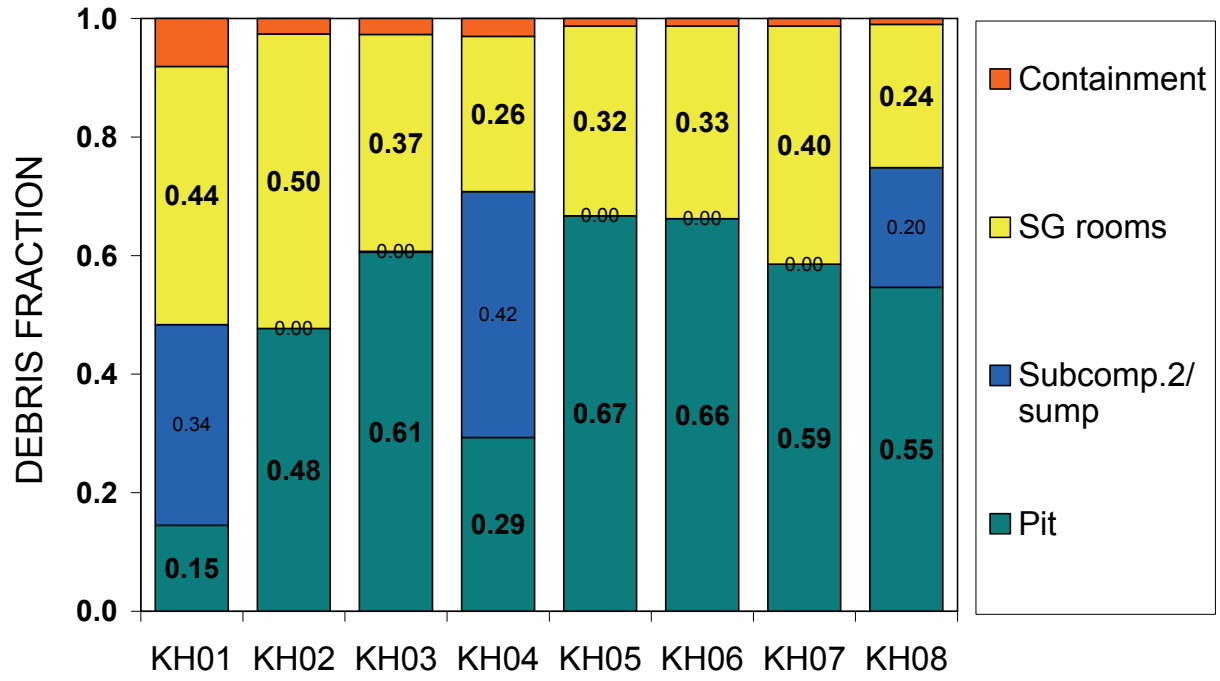

Fig. 4-1. Debris distribution in different locations

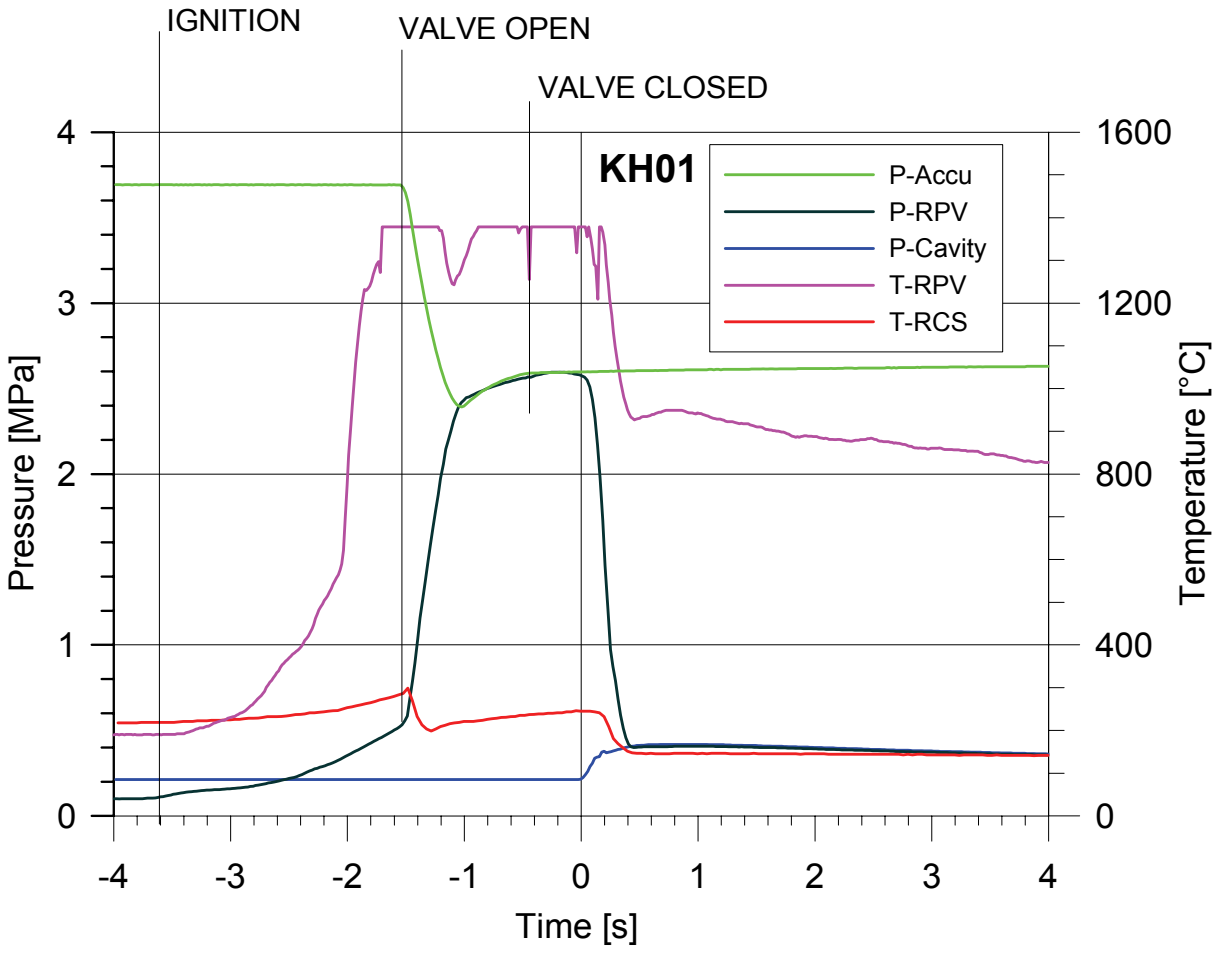

Fig. 4-2. KH01: Pressure, temperature and timing

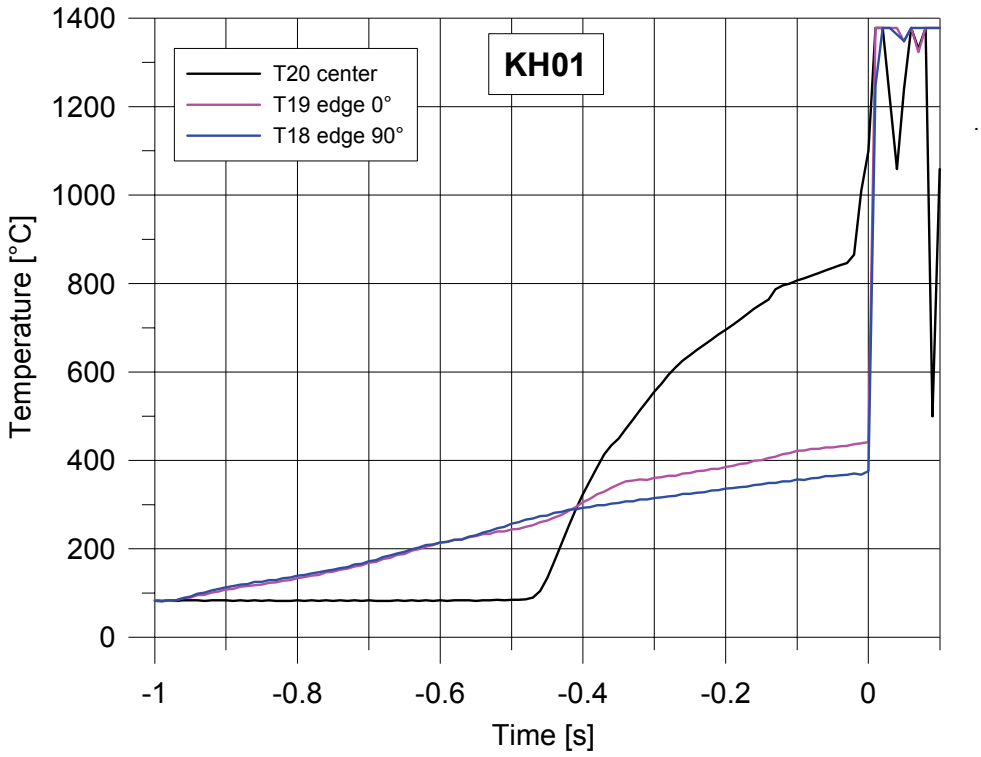

Fig. 4-3. KH01: Thermocouple signals in melt plug

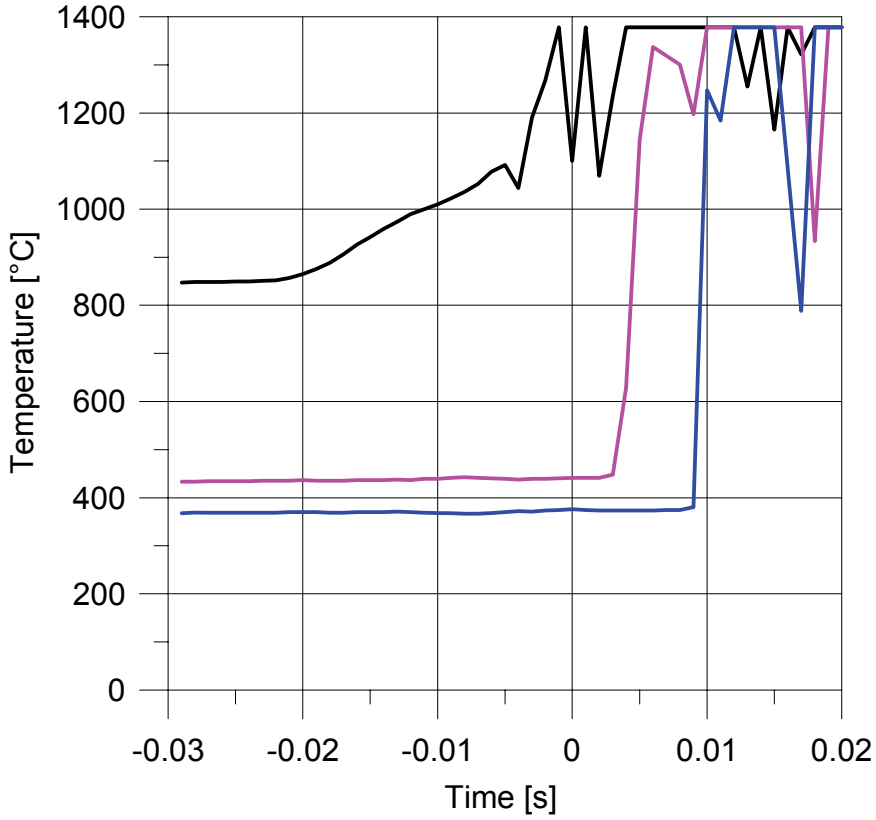

Fig. 4-4. KH01: Thermocouple signals in melt plug, zoom to t = 0 s

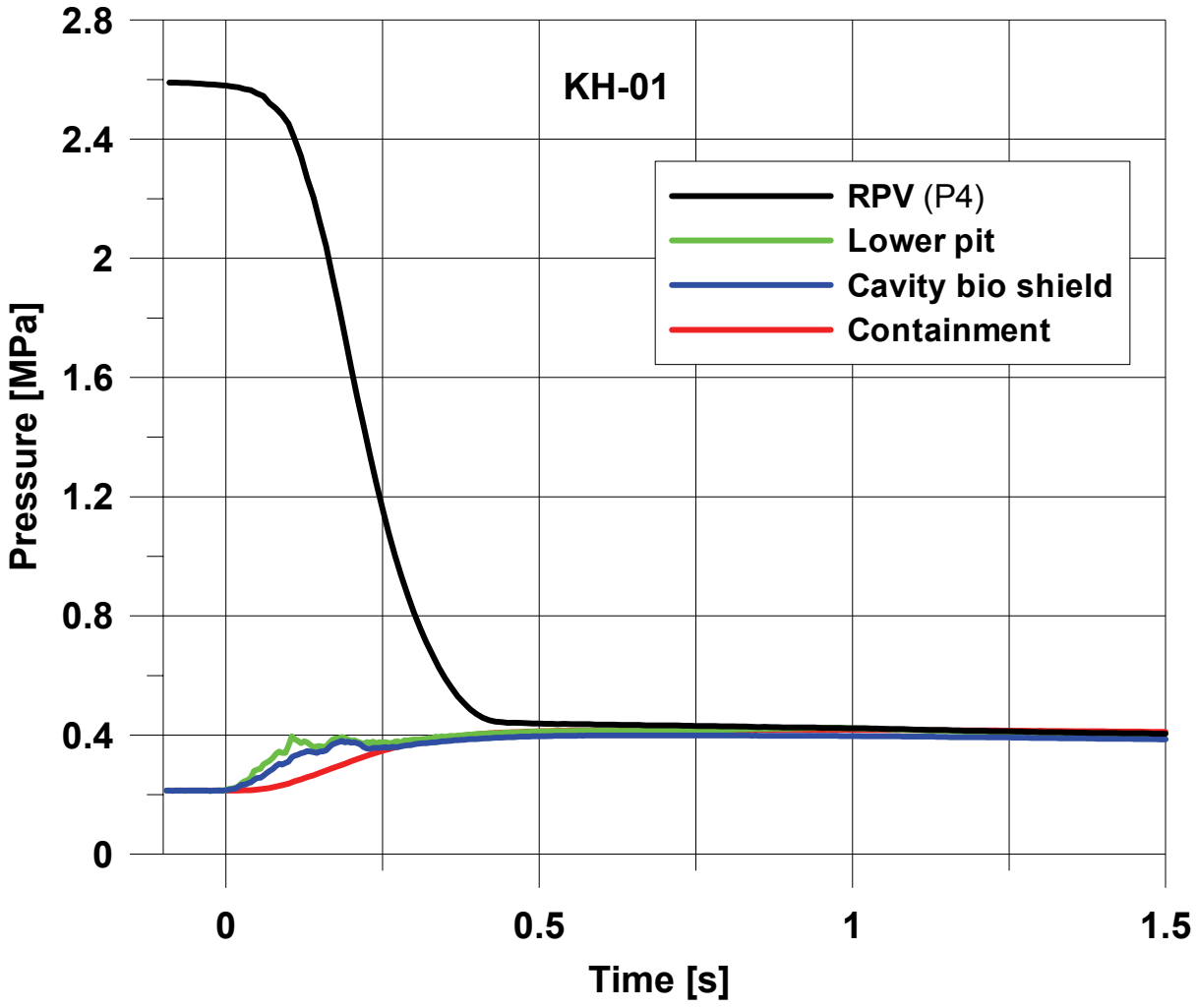

Fig. 4-5. KH01: Pressure in RPV vessel, cavity and containment

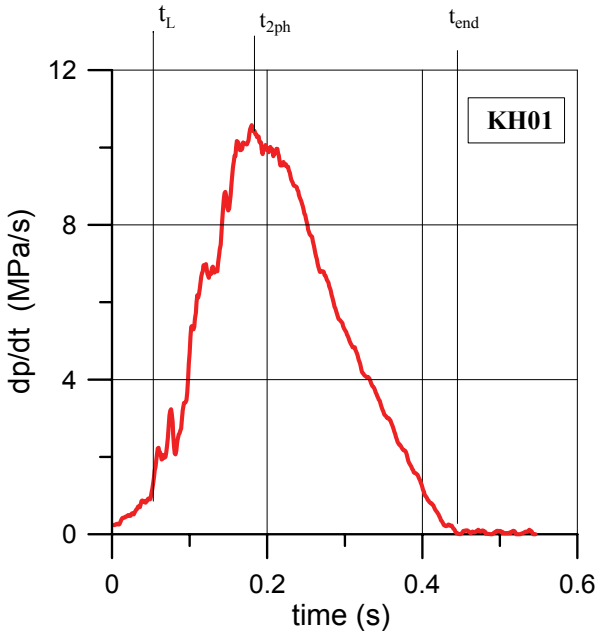

Fig. 4-6. KH01: Pressure gradient in RPV vessel

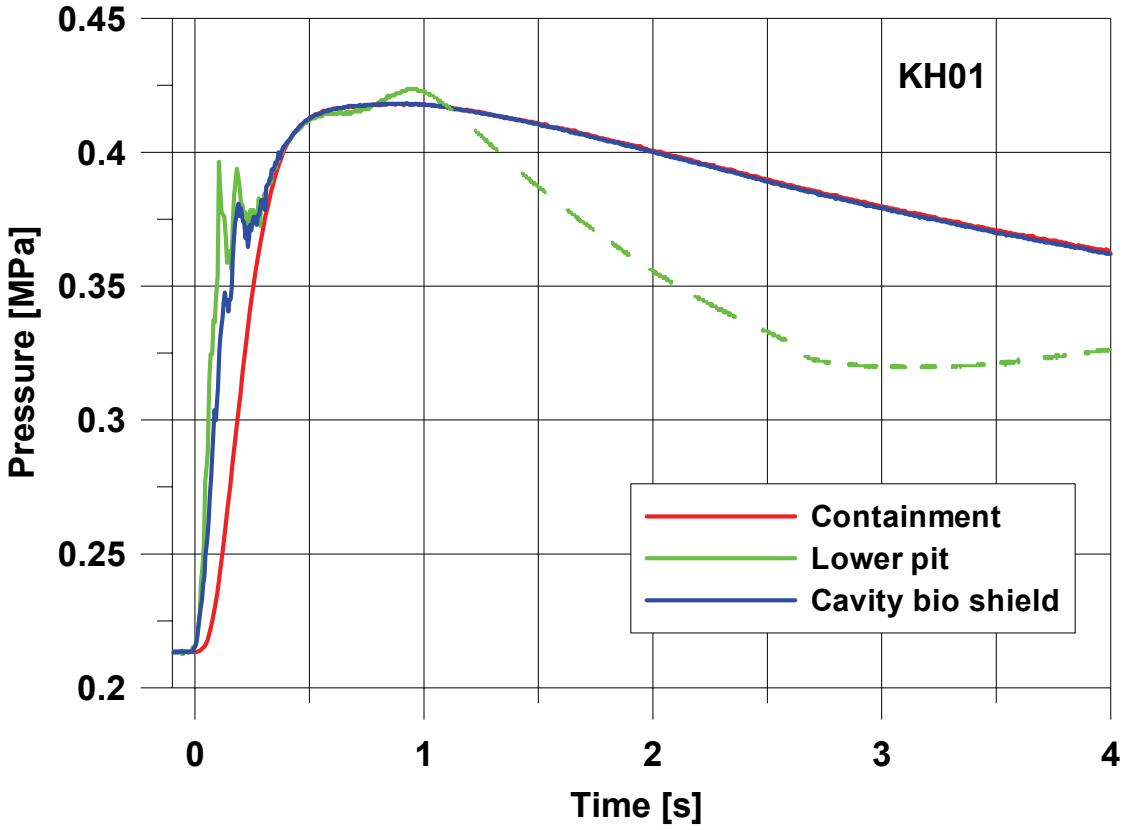

Fig. 4-7. KH01: Pressure in the cavity and containment

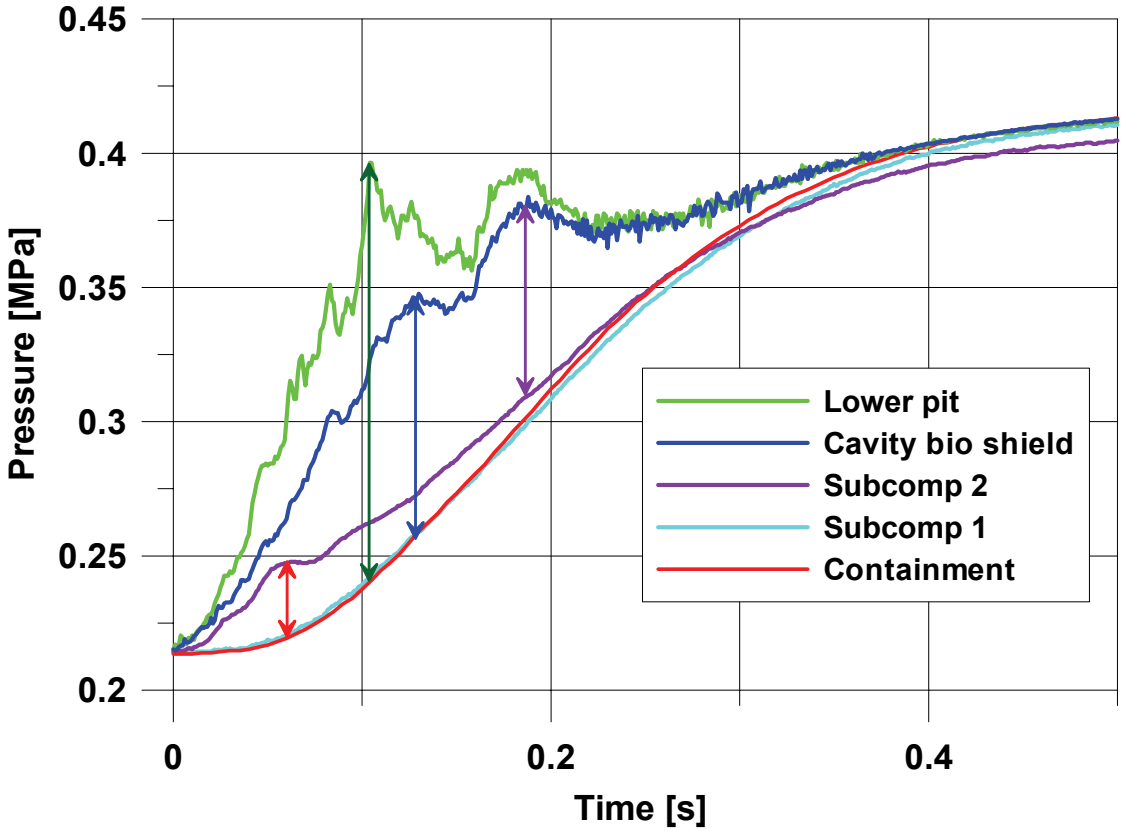

Fig. 4-8. KH01: Pressure in the cavity, subcompartment and containment,

↔ $\Delta p_{sc2\text{-}cont}$ = 0,30 bar, ↔$\Delta p_{lowerpit\text{-}cont}$ = 1,55 bar, ↔ $\Delta p_{cav\text{-}cont}$ = 0,87 bar, ↔ $\Delta p_{cav\text{-}sc2}$ = 0,73 bar

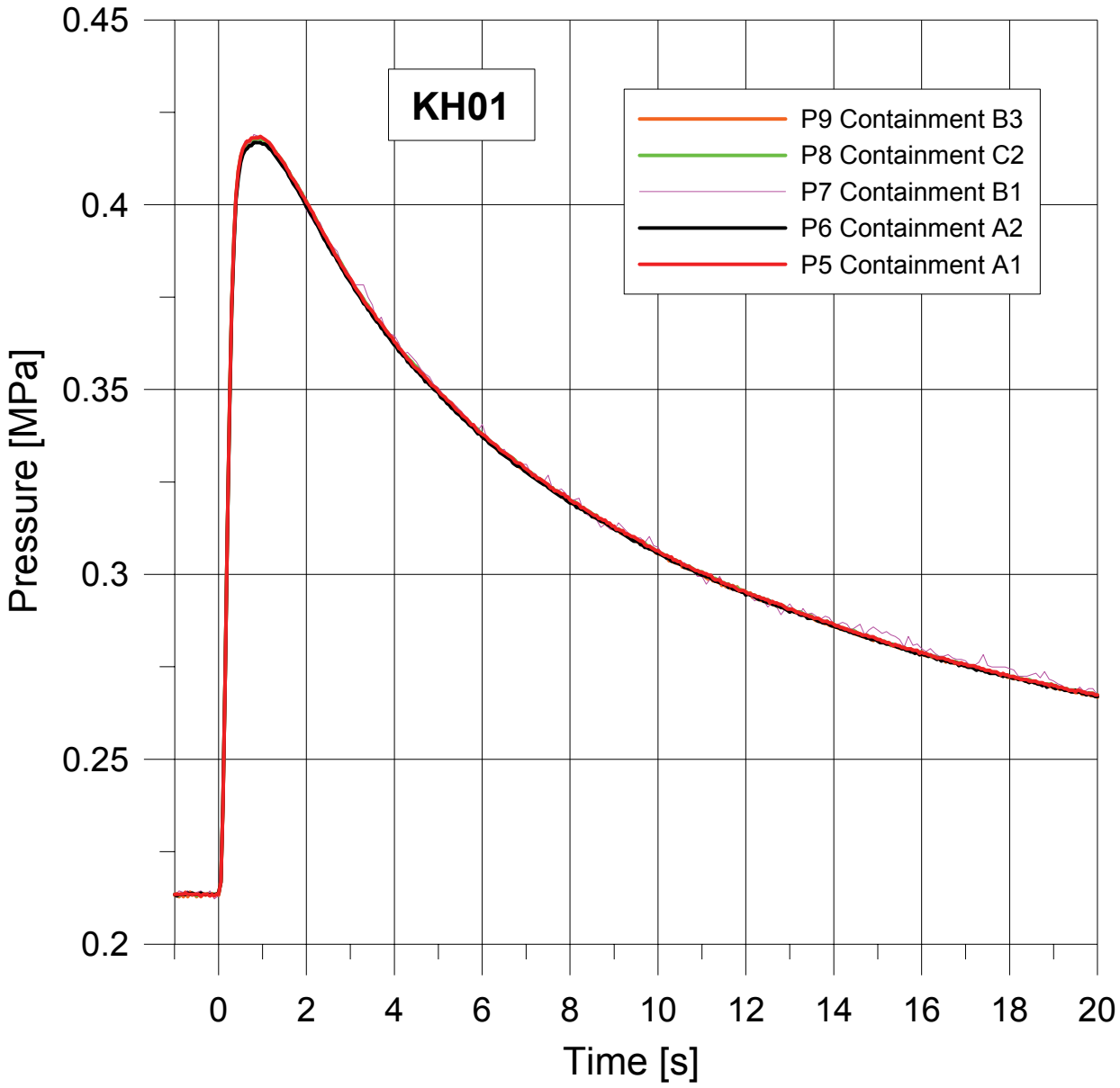

Fig. 4-9. KH01: Long time development of containment pressure

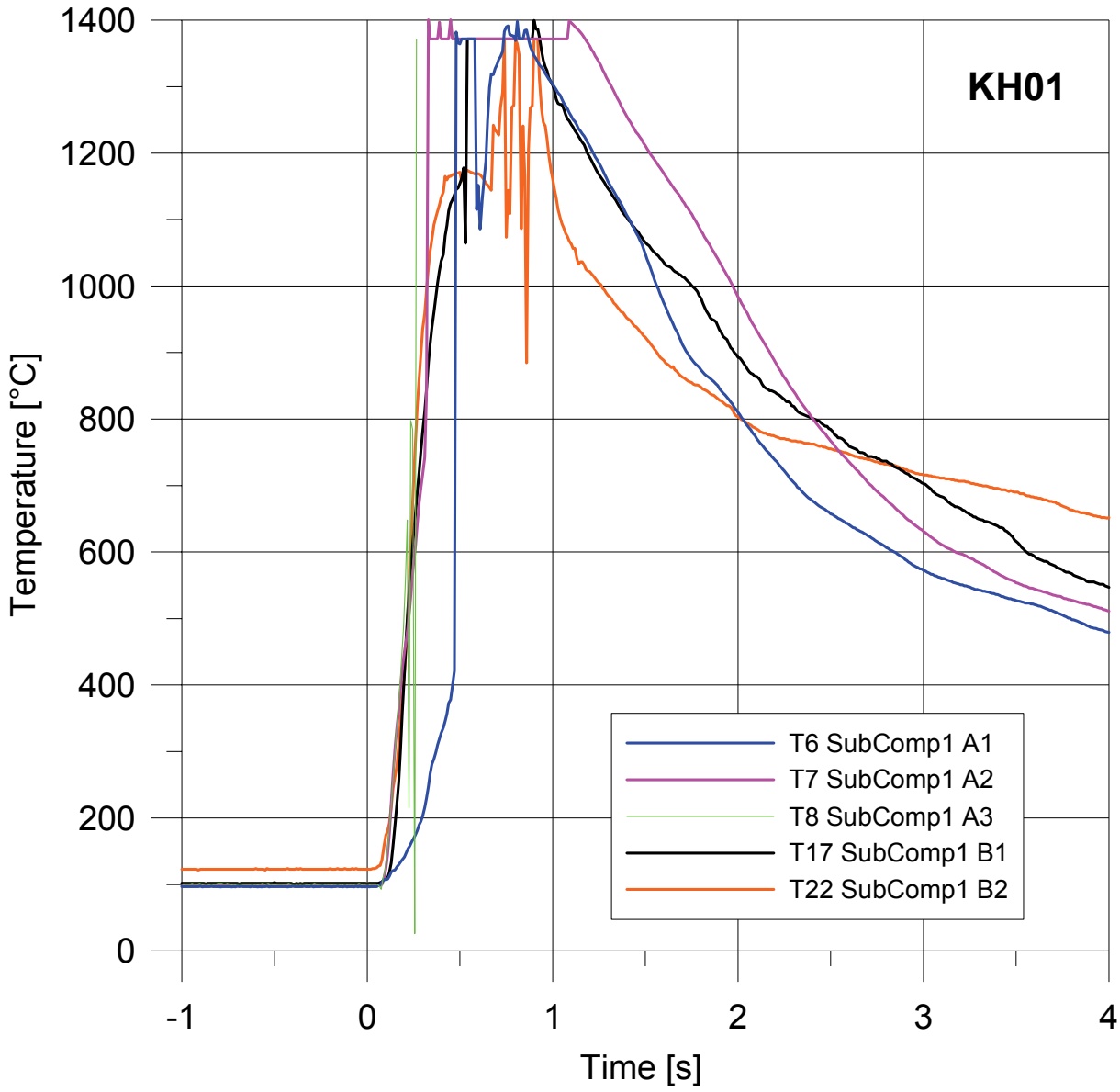

Fig. 4-10. KH01: Gas temperatures in the subcompartment 1

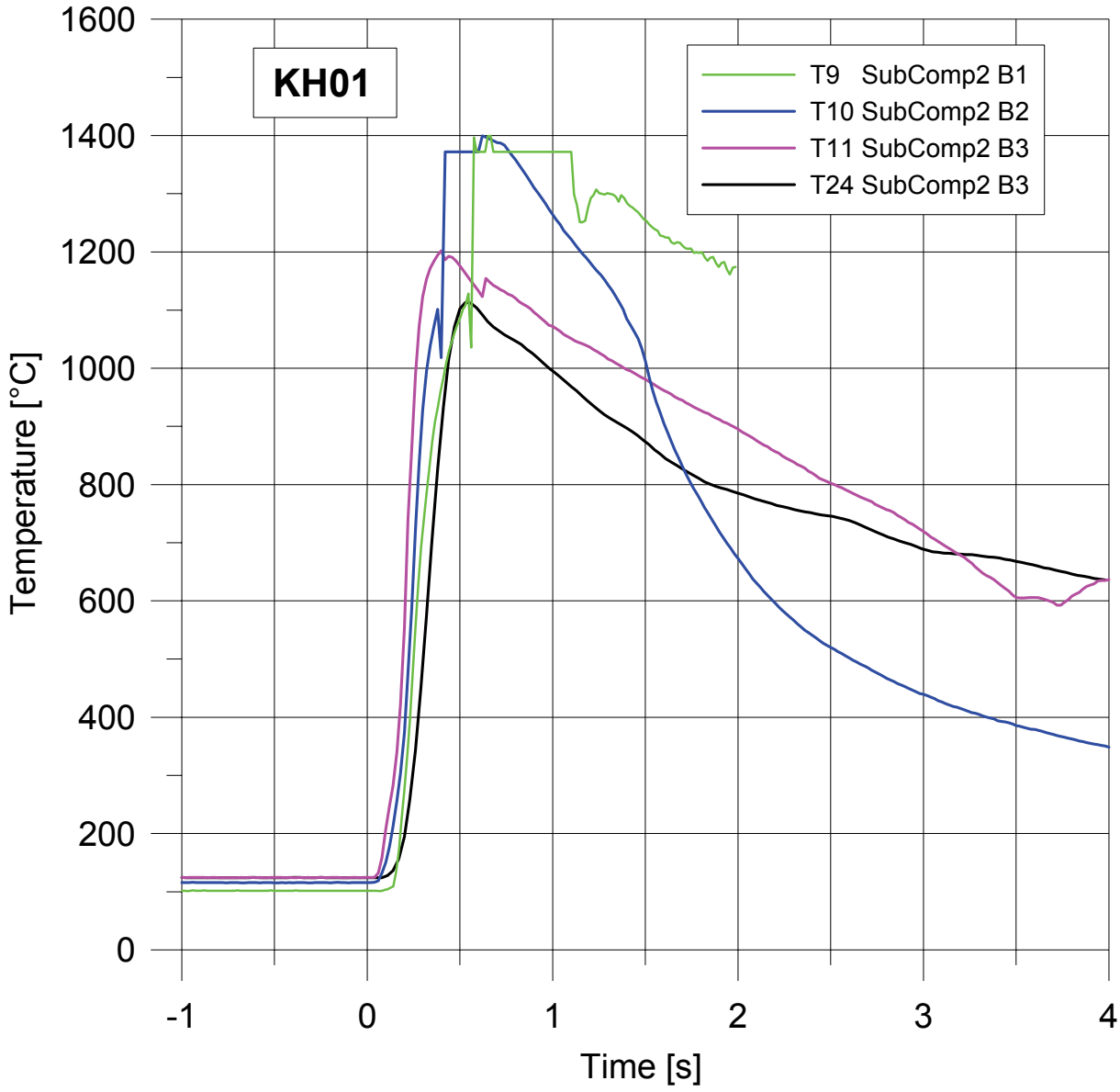

Fig. 4-11. KH01: Gas temperatures in the subcompartment 2

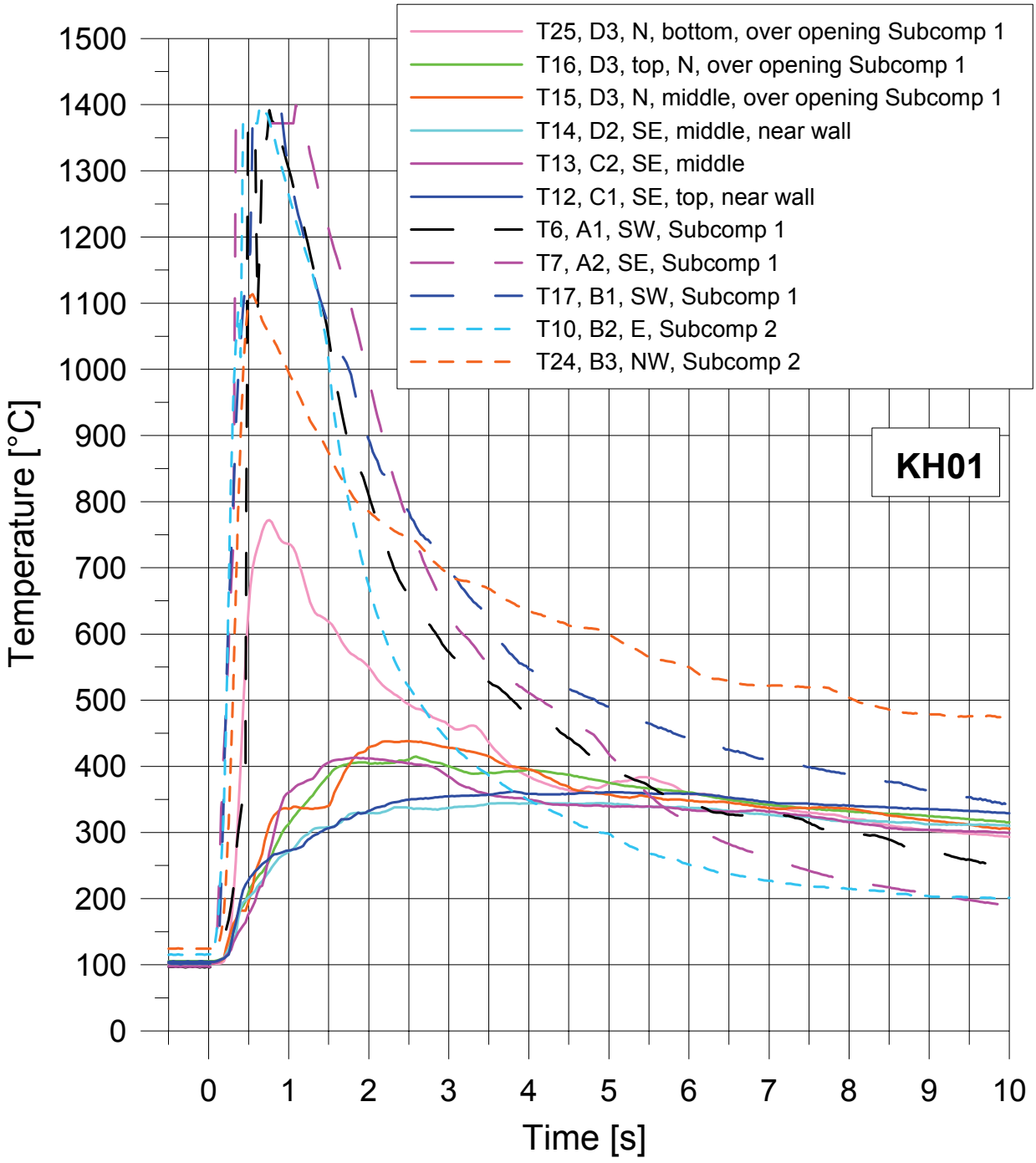

N = north, NW = northwest, E = east, SE = southeast, SW = southwest,

Fig. 4-12. KH01: Gas temperatures in the containment and subcompartments

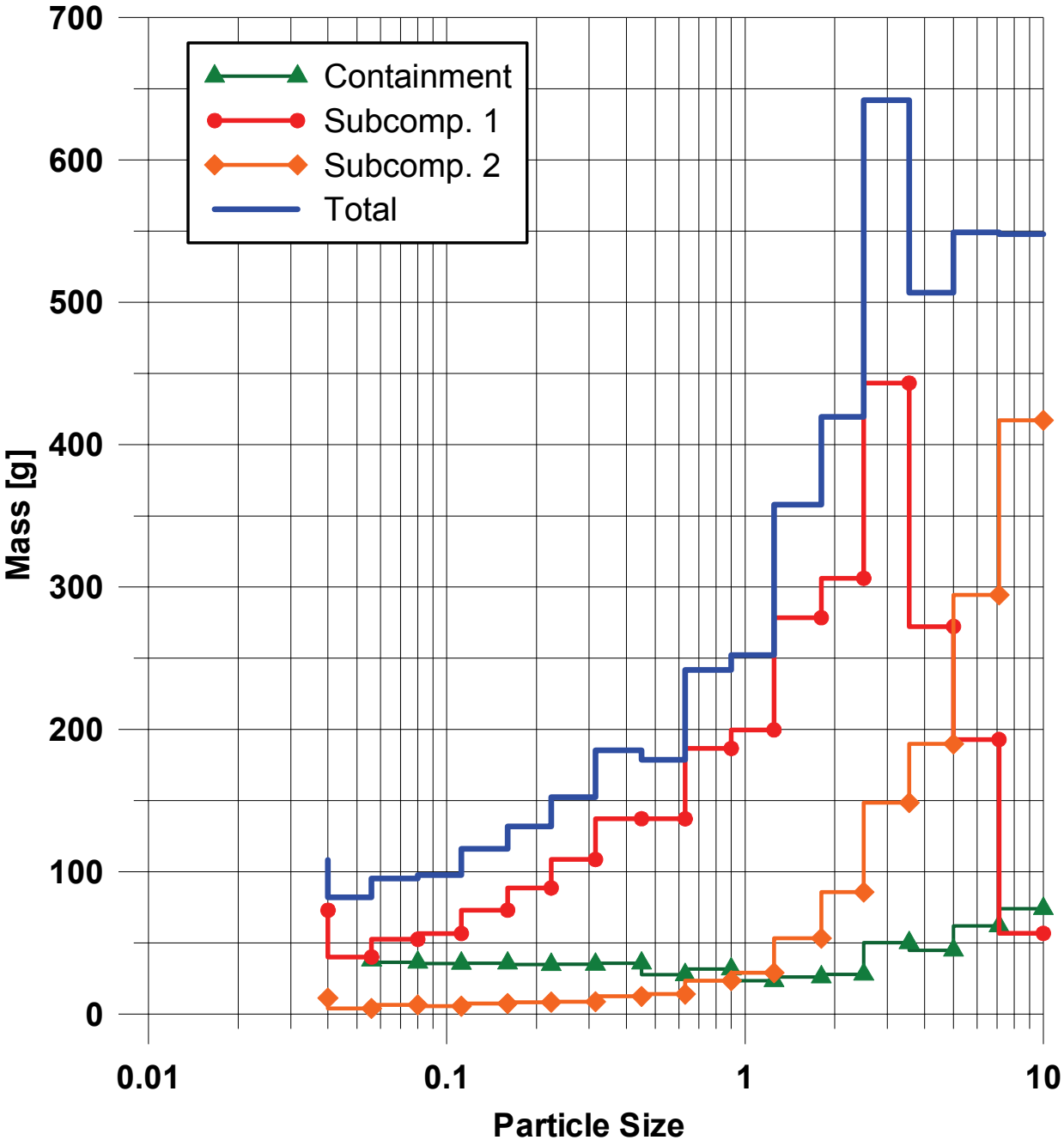

Fig. 4-13. KH01: Size distribution of particles smaller than 10 mm

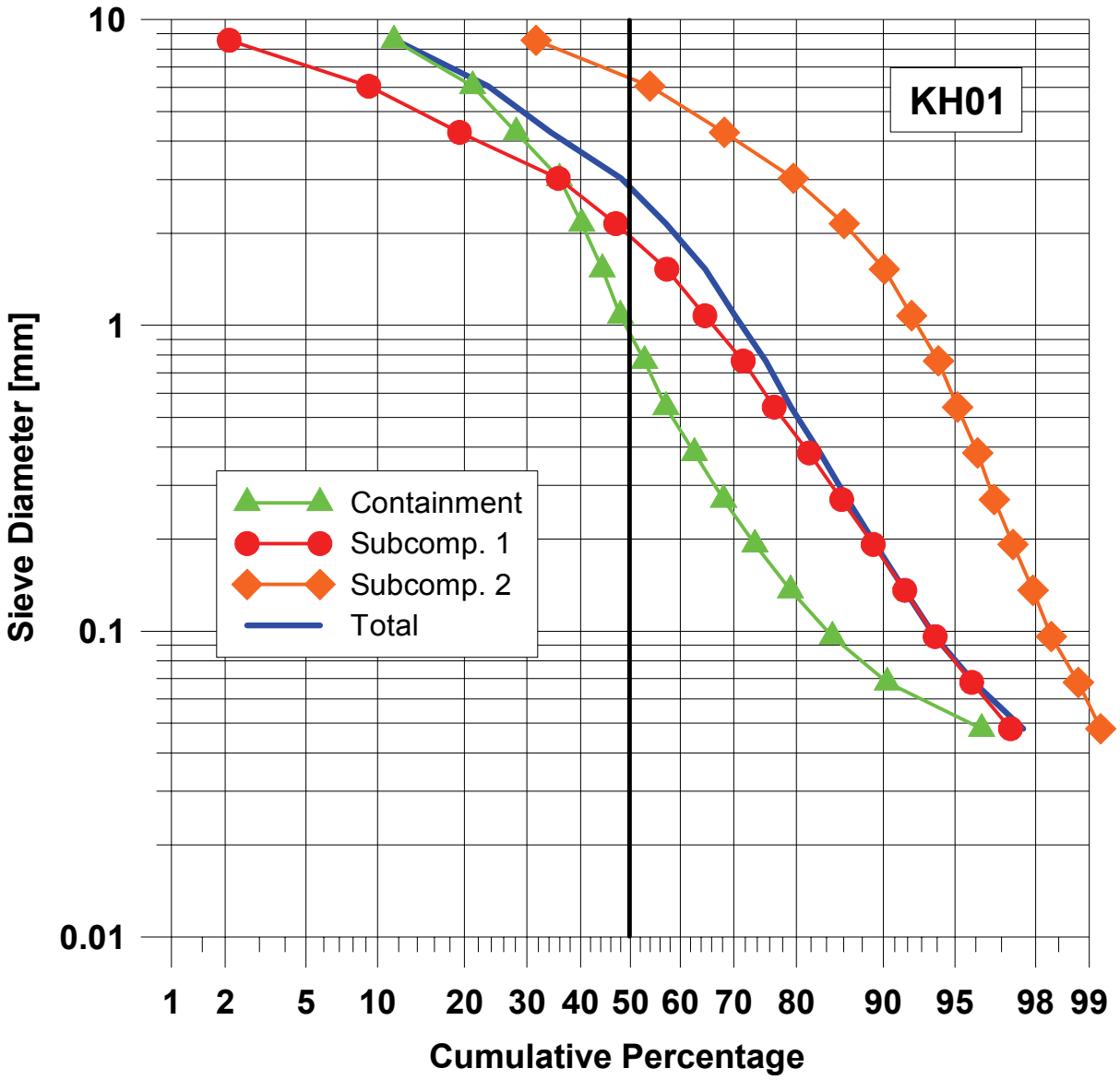

Fig. 4-14. KH01: Cumulative particle size distribution of debris smaller 10 mm

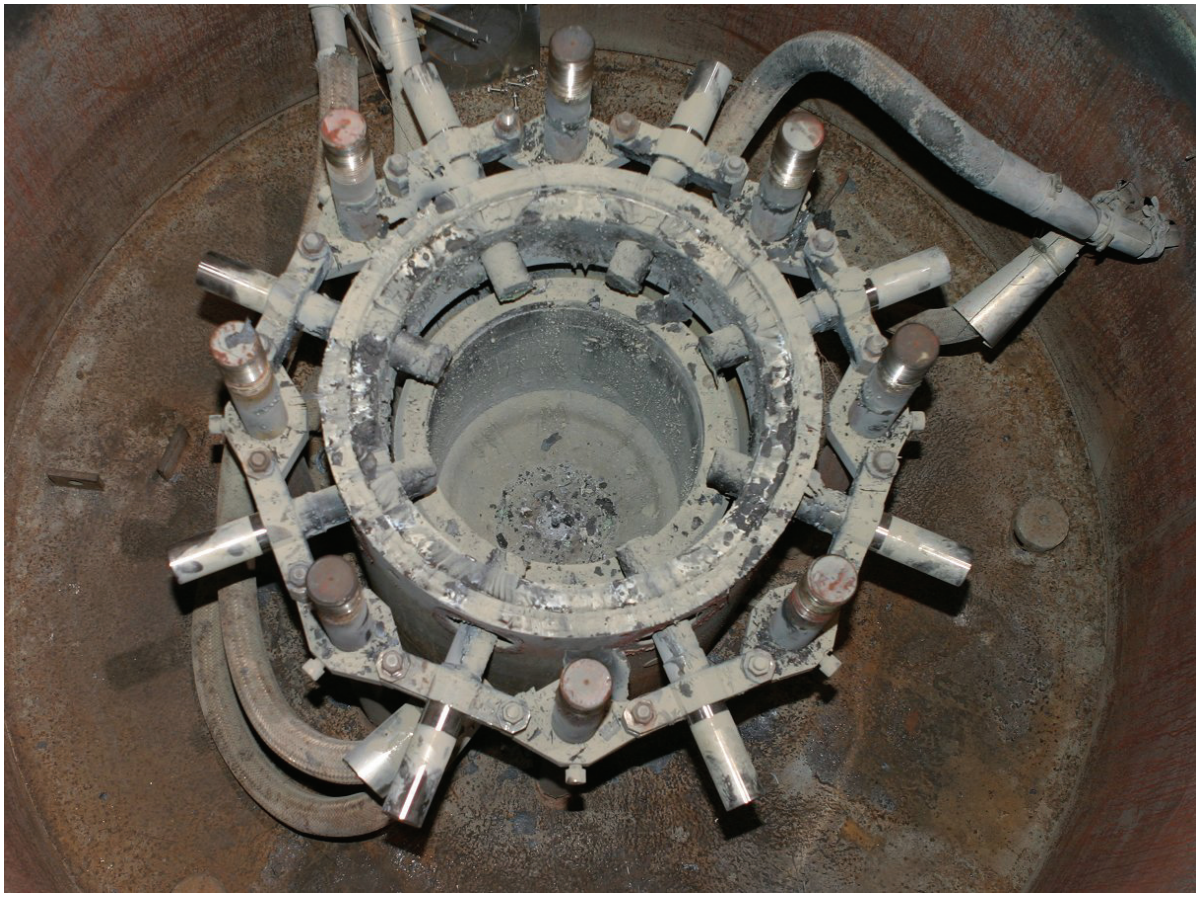

Fig. 4-15. KH01: Post test view of concrete cavity

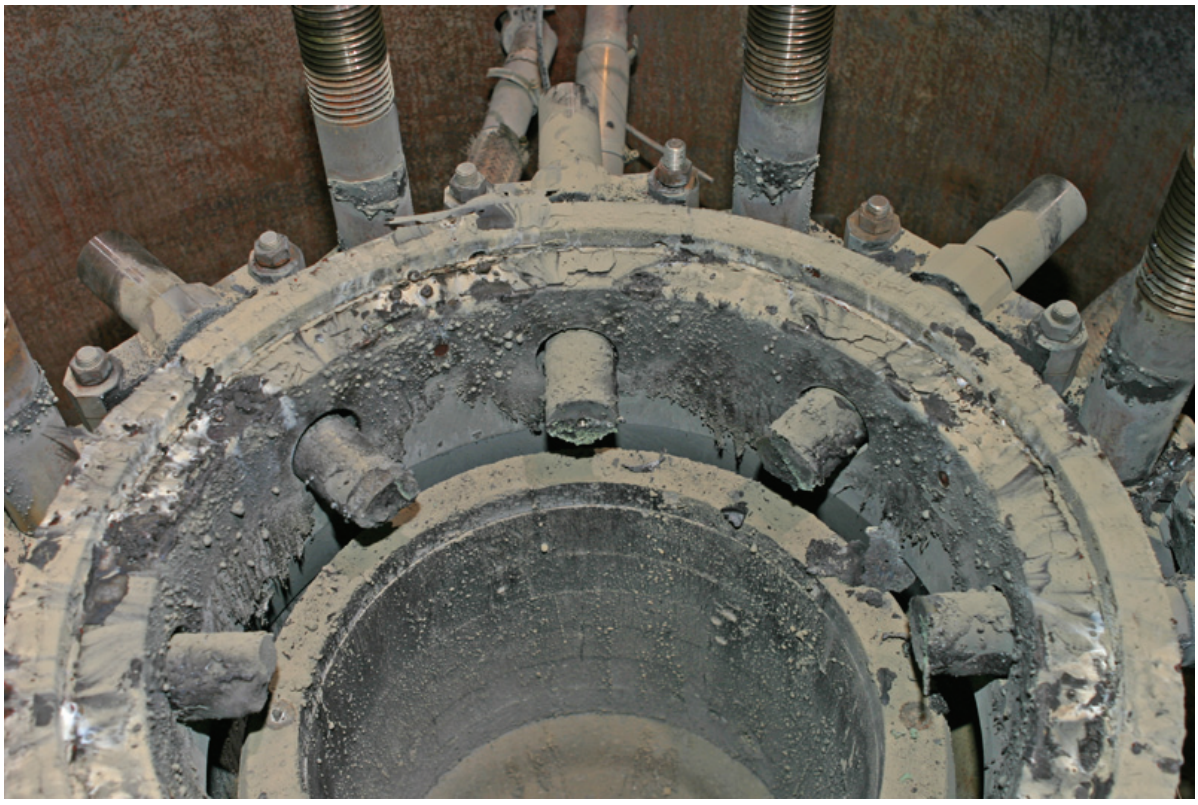

Fig. 4-16. KH01: Post test view into pit

Fig. 4-17. KH01: View at pit exit B leading into subcompartment 2

Fig. 4-18. KH01: Post test view of RPV lower head and hole

Fig. 4-19. KH01: Post test view of subcompartment 1

Fig. 4-20. KH01: Post test view of subcompartment 1 wall

Fig. 4-21. KH01: Crust on the wall of subcompartment 1

Fig. 4-22. KH01: Post test view into subcompartment 2

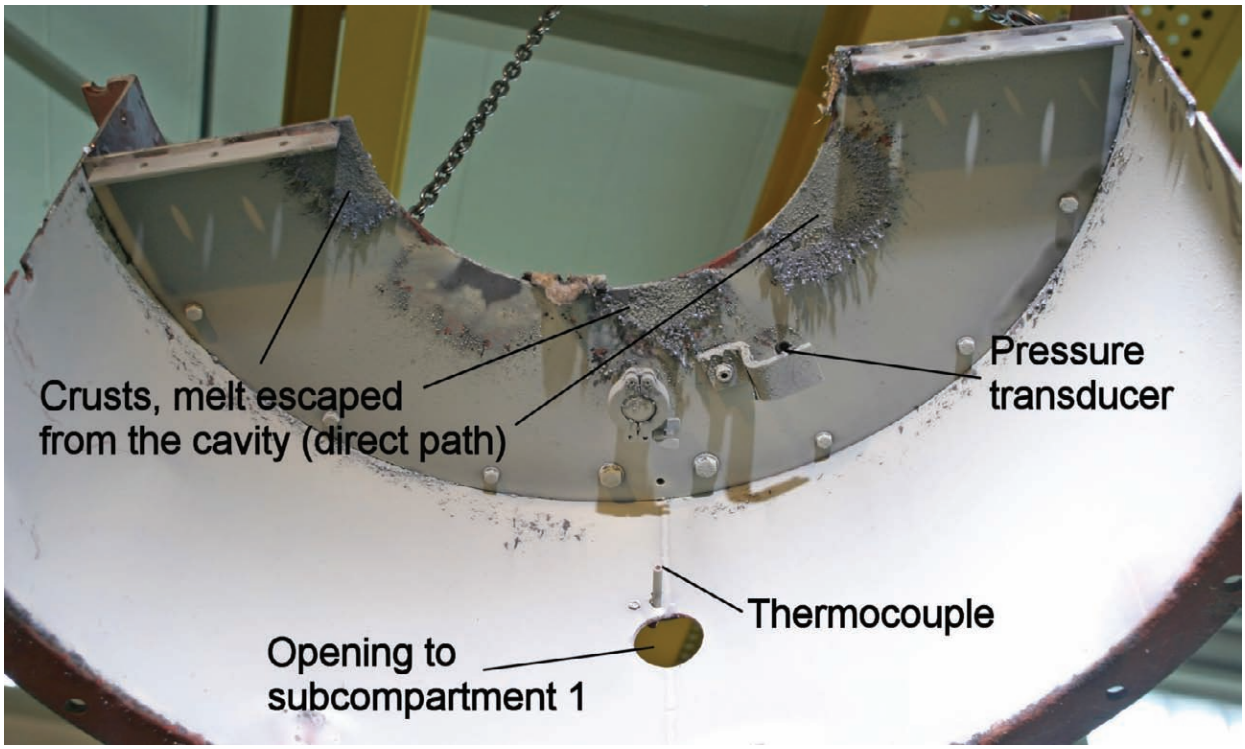

Fig. 4-23. KH01: Post test view to the cap of subcompartment 2

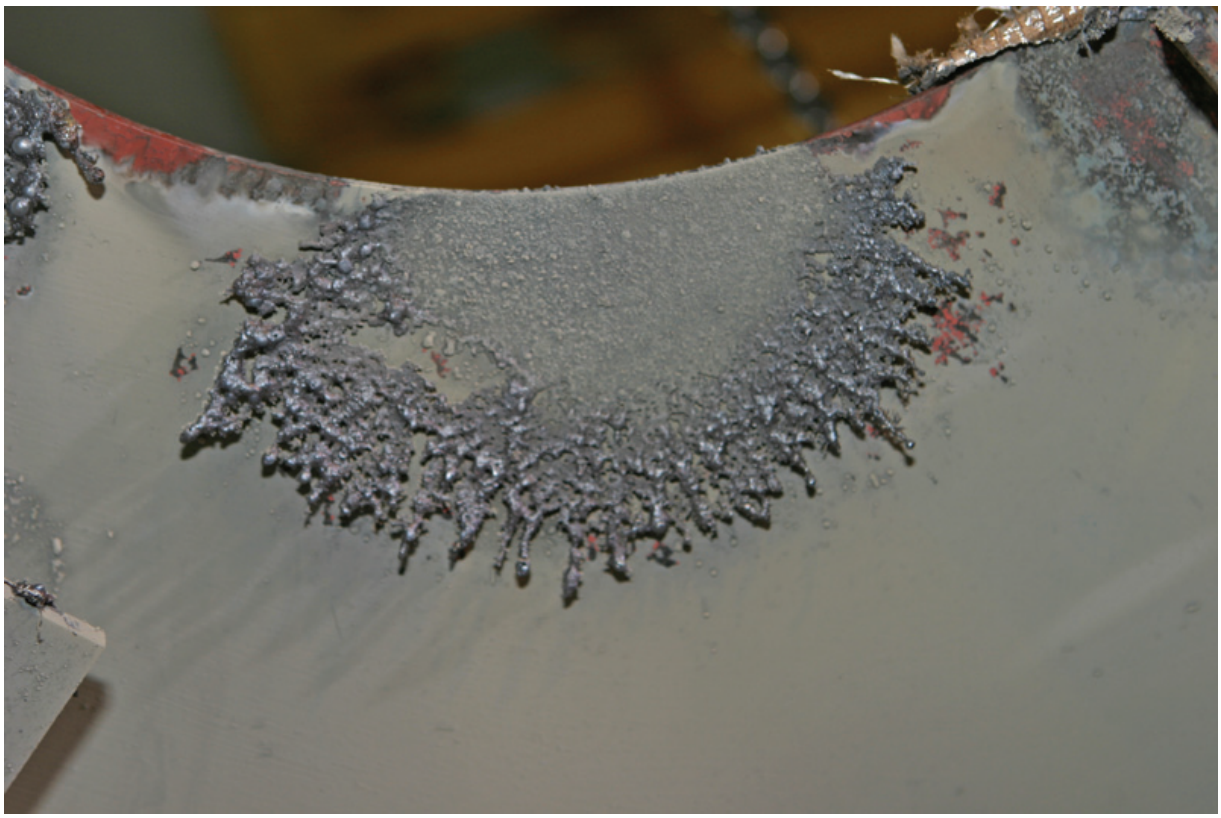

Fig. 4-24. KH01: Close up of the cap of subcompartment 2 with crust from vertical melt jet

Fig. 4-25. KH01: Post test view of containment vessel

Fig. 4-26. KH01: Melt particles at containment wall

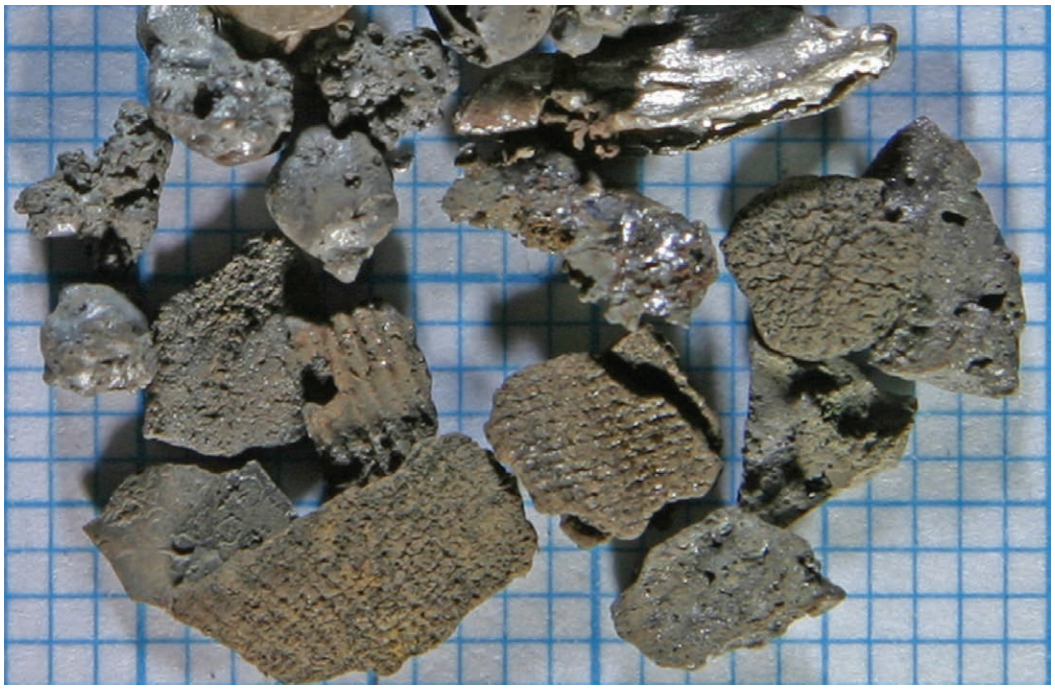

Fig. 4-27. Shape of debris particles, 3,5 – 5,0 mm

Fig. 4-28. Shape of debris particles, 1,8 - 2,5 mm

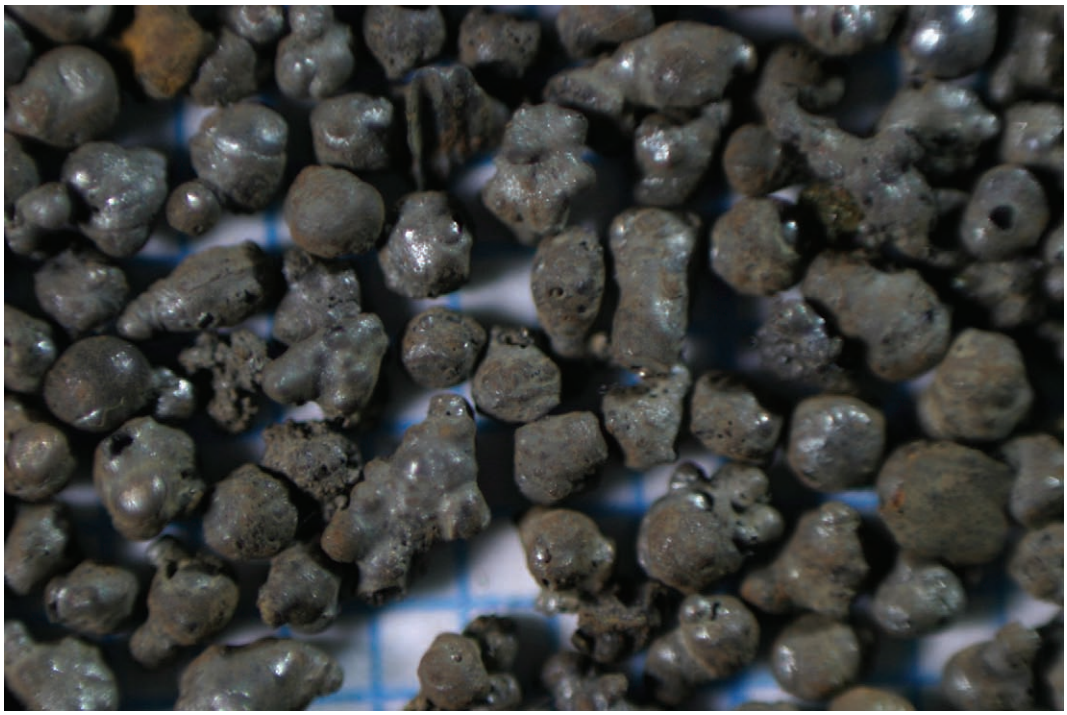

Fig. 4-29. Shape of debris particles, 0,9 – 1,25 mm

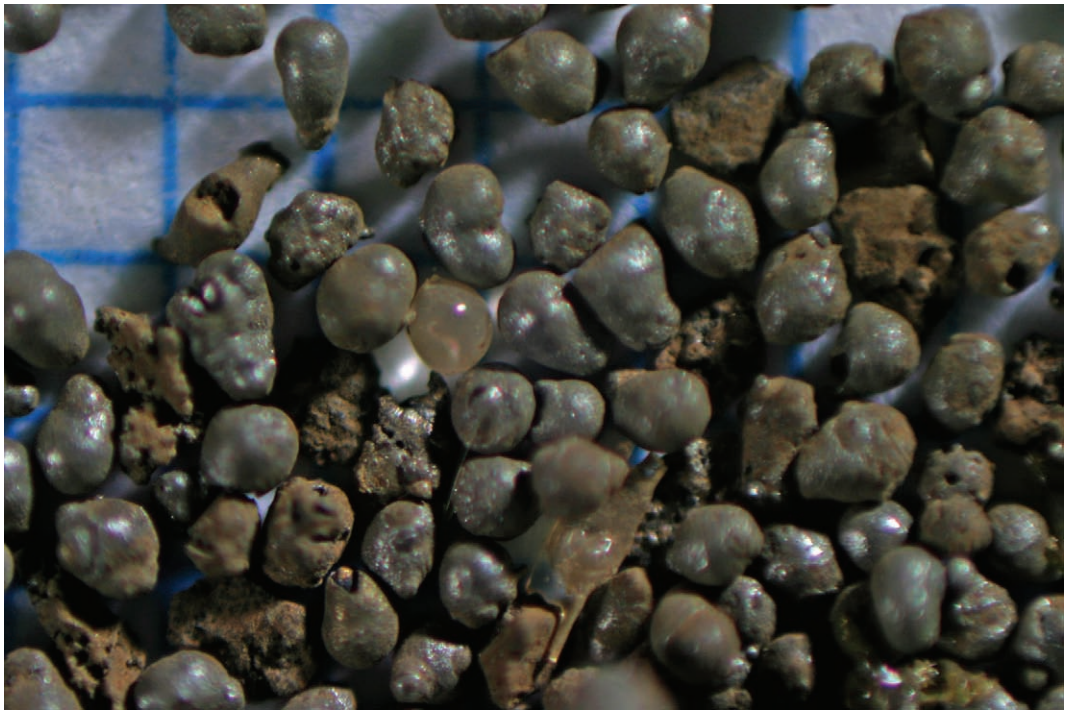

Fig. 4-30. Shape of debris particles, 0,45 – 0,63 mm

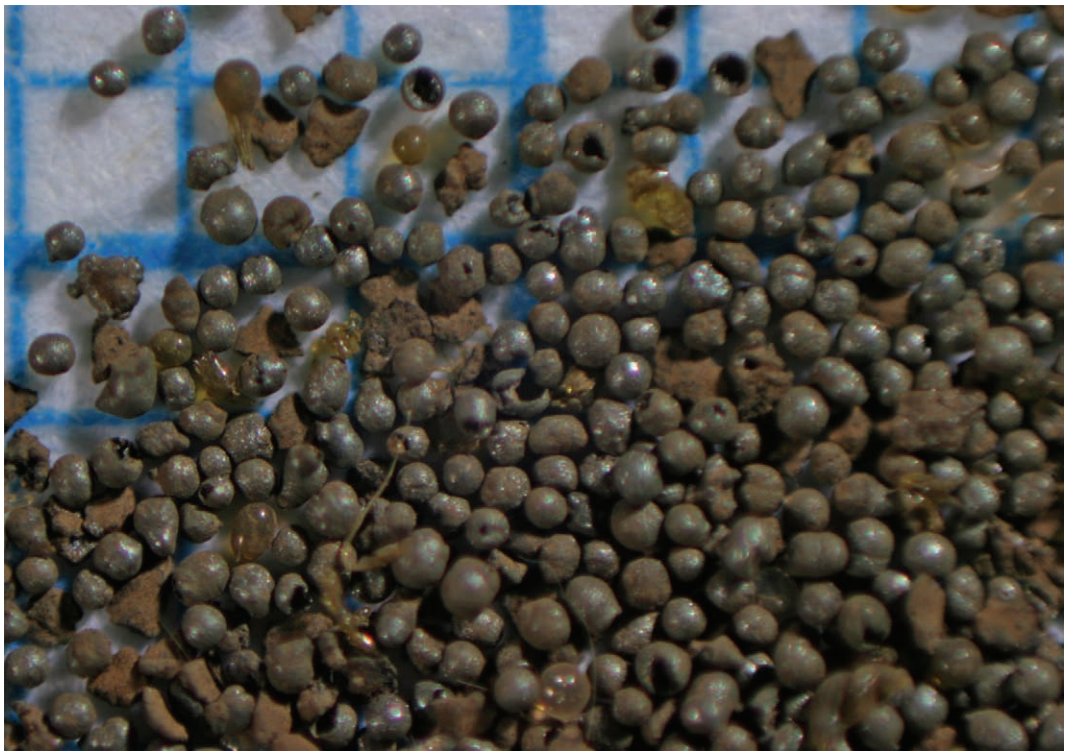

Fig. 4-31. Shape of debris particles, 0,224 – 0,315 mm

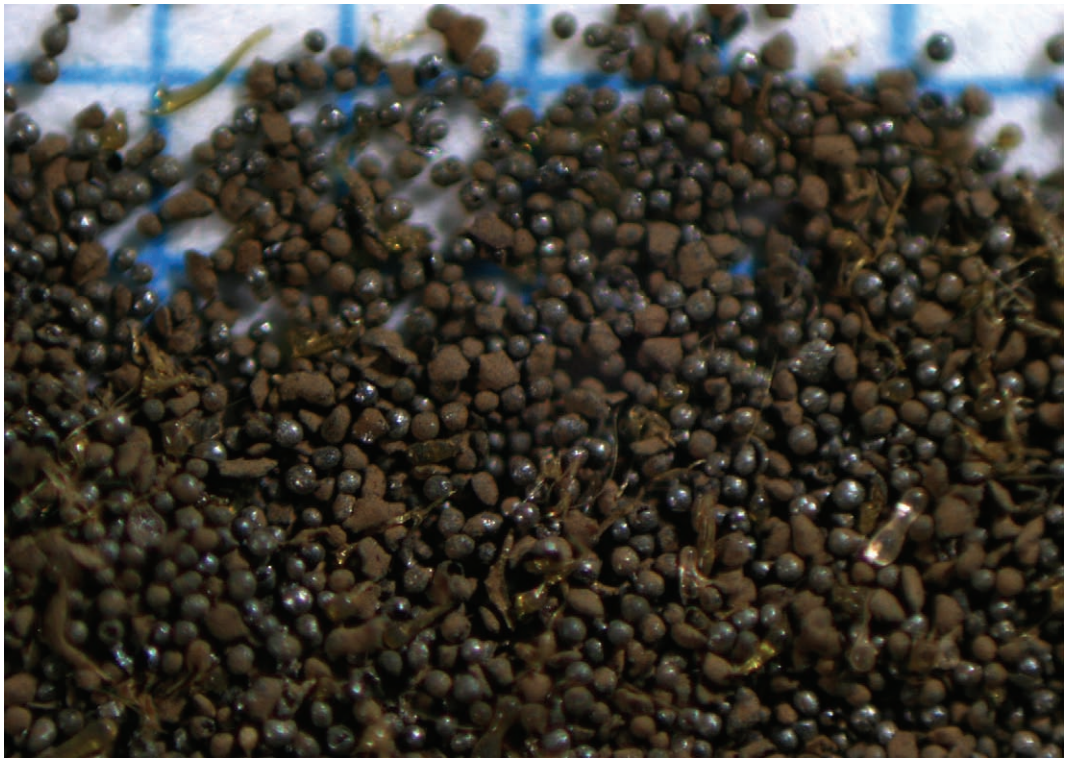

Fig. 4-32. Shape of debris particles, 0,112 – 0,16 mm

Fig. 4-33. Shape of debris particles, 0,056 – 0,08 mm

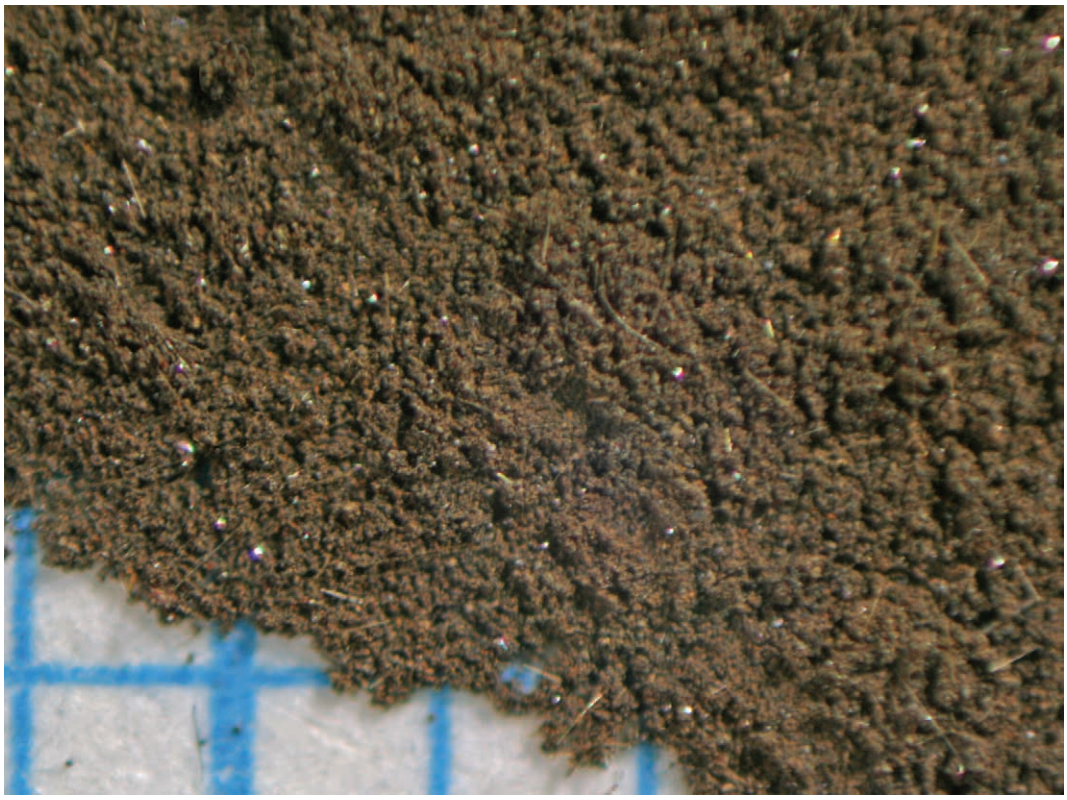

Fig. 4-34. Shape of debris particles, < 0,04 mm

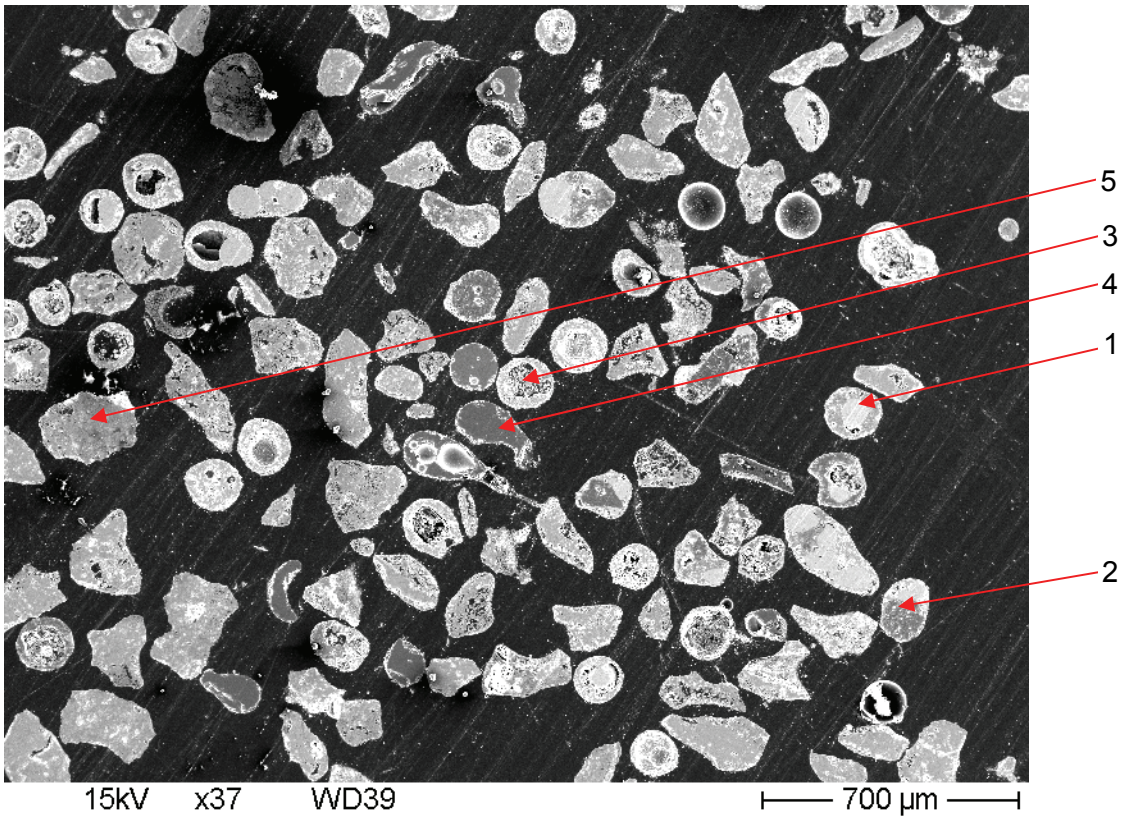

Fig. 4-35. Micrograph of small particles in containment (numbered particles in next figures)

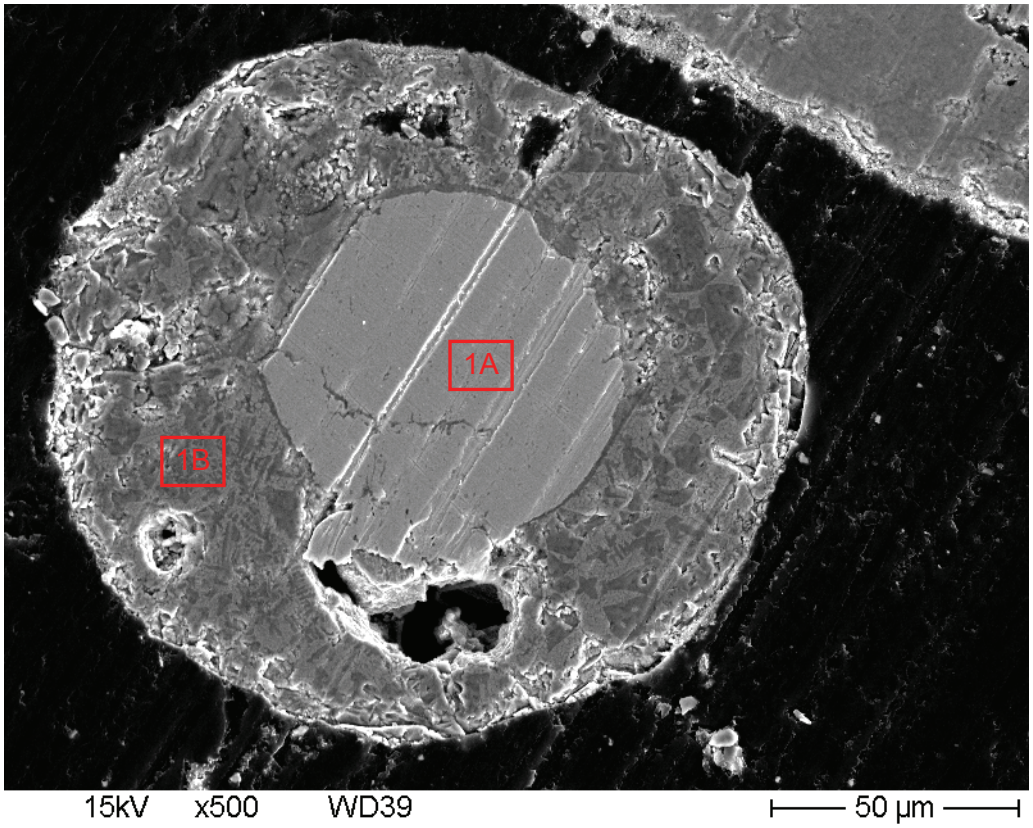

	C-1A
Fe	90,3
Cr	6,7
Cu	
Mg	
Al	
Si	
Ca	
O	3,0

Fig. 4-36. Particle number 1 in containment (section 1B is shown in next figure)

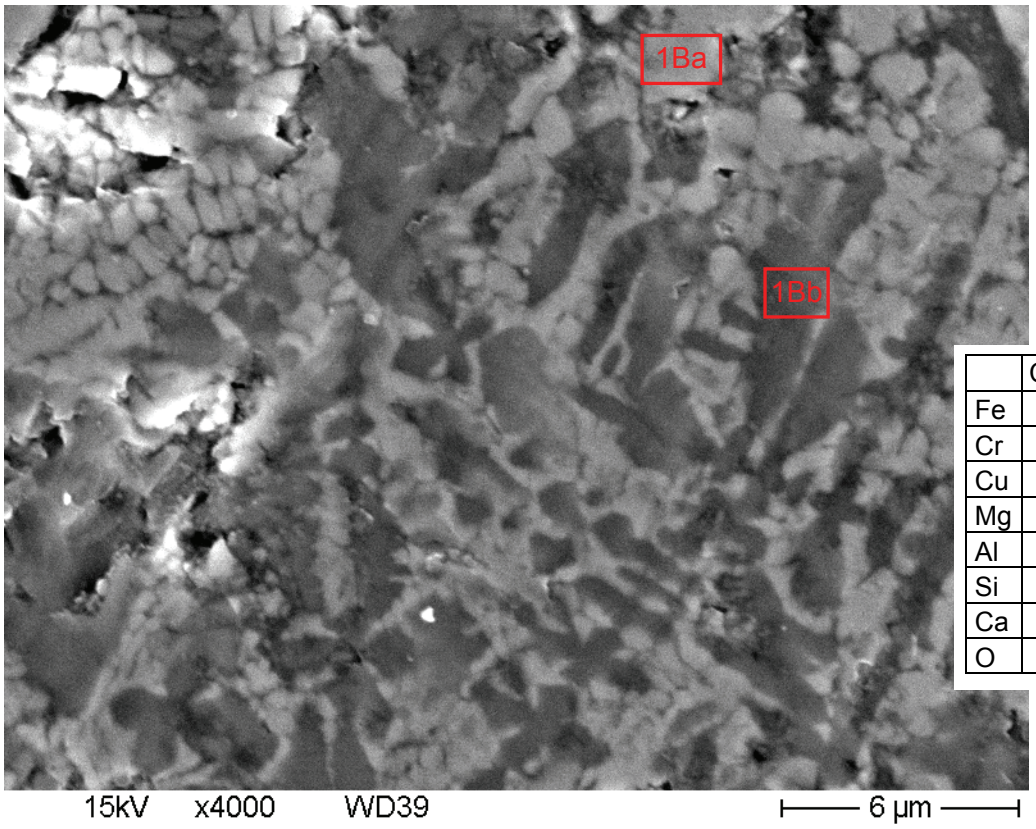

	C-1Ba	C-1Bb
Fe	92,5	30,5
Cr		
Cu	7,0	
Mg		
Al		10,7
Si		1,5
Ca	0,5	0,9
O		56,4

Fig. 4-37. Section 1B from particle 1 in containment

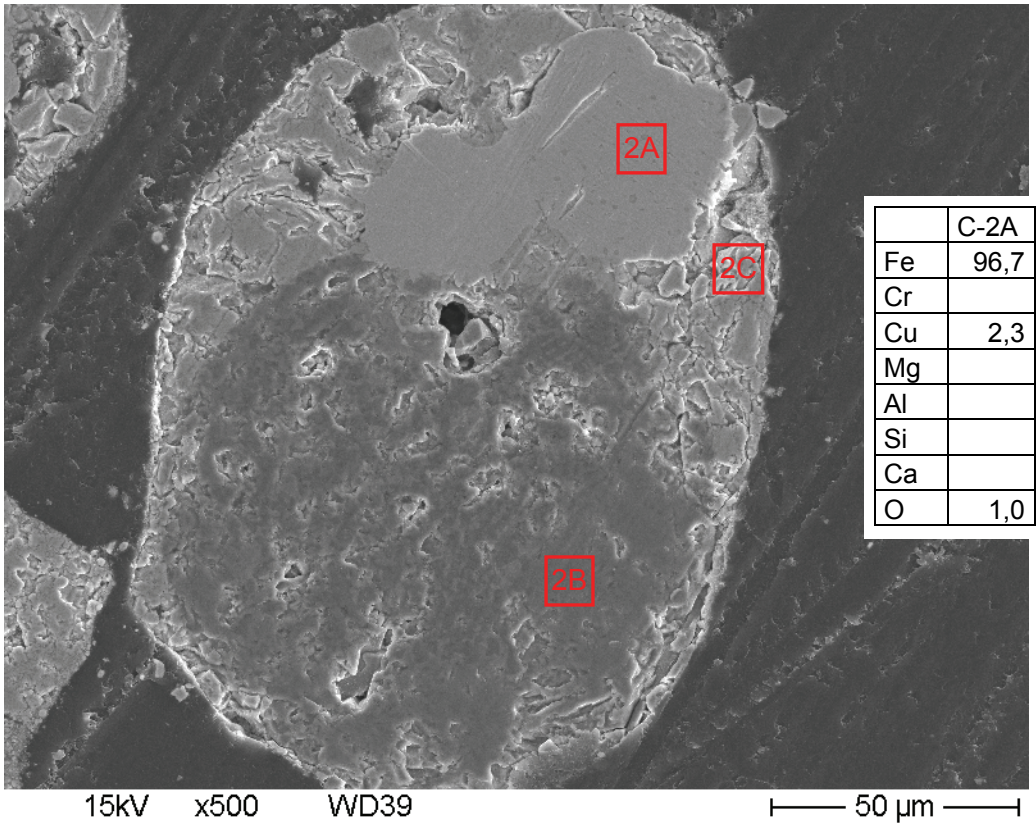

	C-2A	C-2B	C-2C
Fe	96,7	4,6	49,0
Cr		0,3	
Cu	2,3		
Mg		0,1	
Al		31,3	1,4
Si		1,2	1,3
Ca		0,9	0,5
O	1,0	61,6	47,8

Fig. 4-38. Particle number 2 in containment

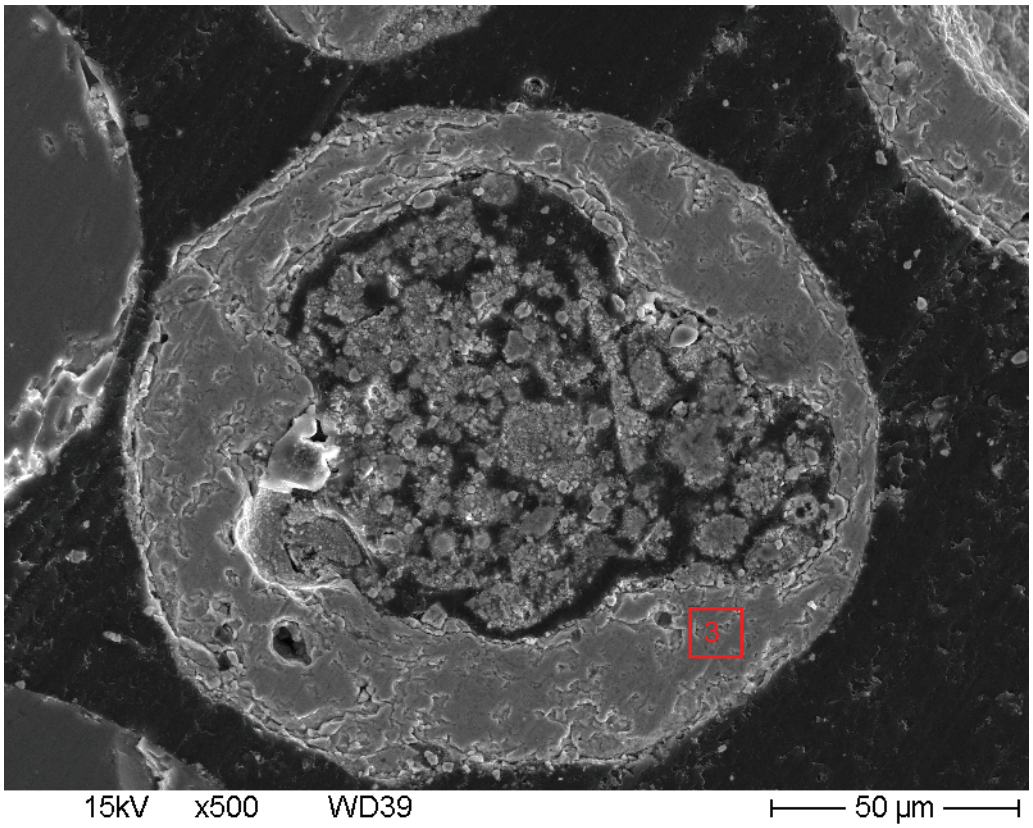

	C-3
Fe	40,8
Cr	1,6
Cu	0,5
Mg	
Al	1,5
Si	0,3
Ca	
O	55,3

Fig. 4-39. Particle number 3 in containment

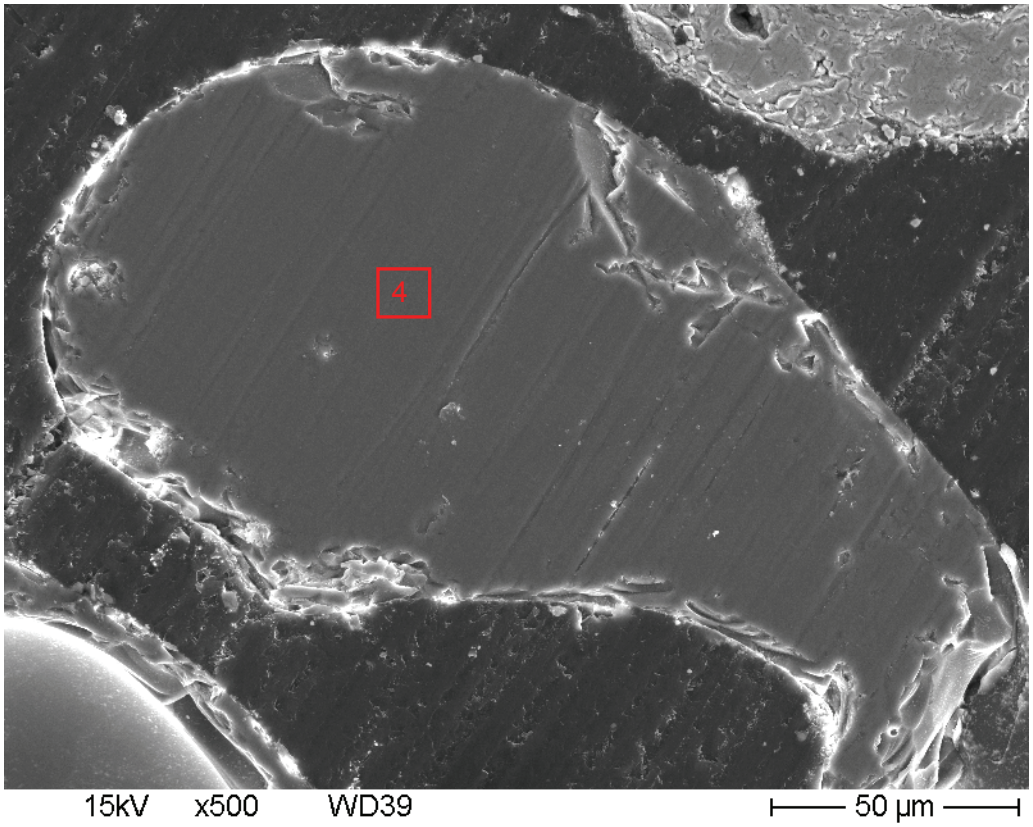

	C-4
Fe	
Cr	
Cu	
Mg	
Al	16,5
Si	16,9
Ca	
O	66.6

Fig. 4-40. Particle number 4 in containment

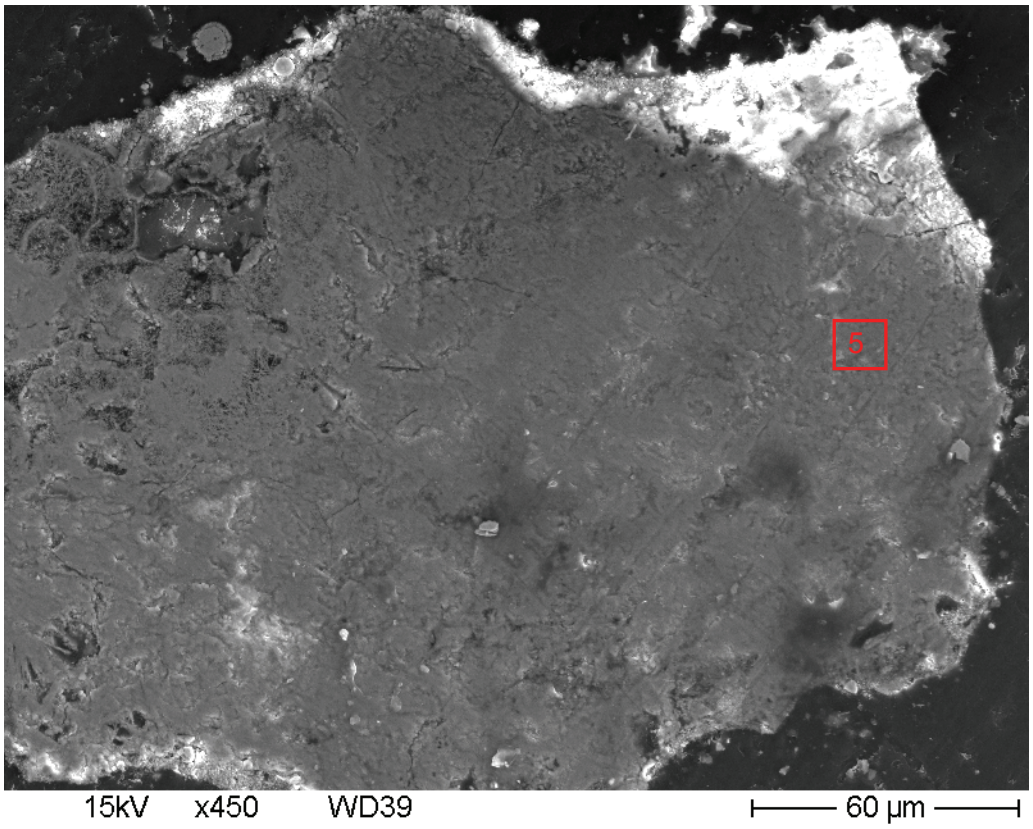

	C-5
Fe	33,0
Cr	
Cu	
Mg	0,2
Al	0,1
Si	
Ca	0,2
O	66.5

Fig. 4-41. Particle number 5 in containment

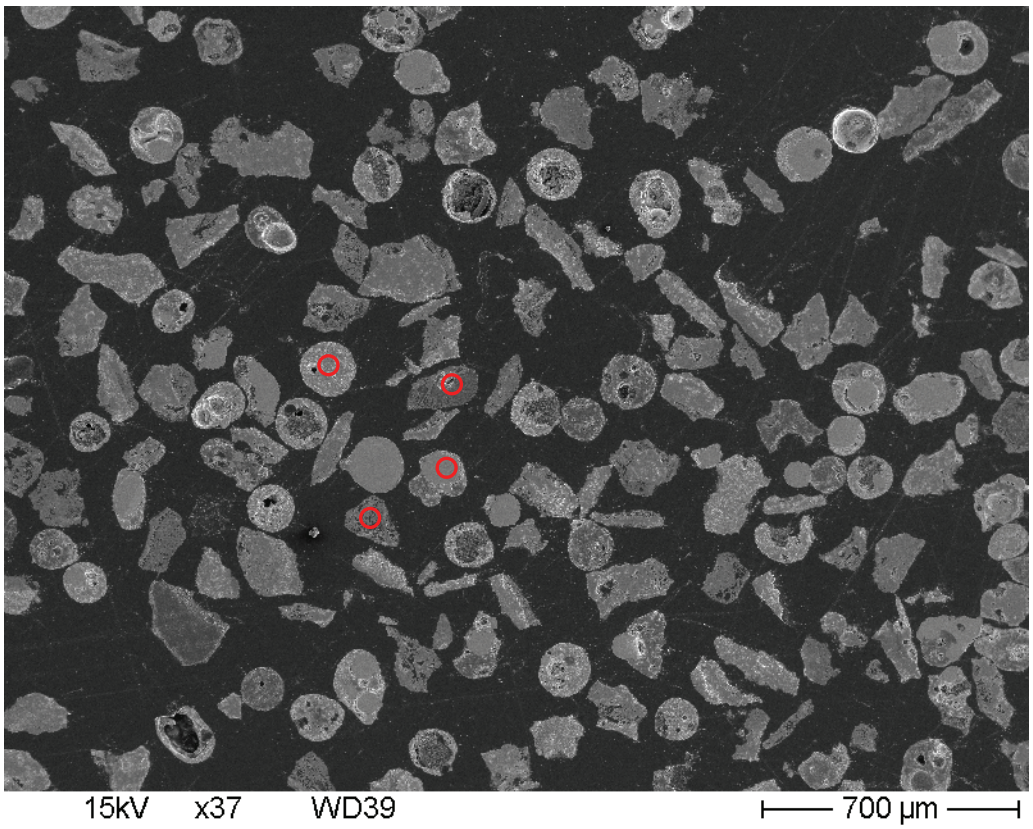

Fig. 4-42. Micrograph of small particles in subcompartment 1 (S1)

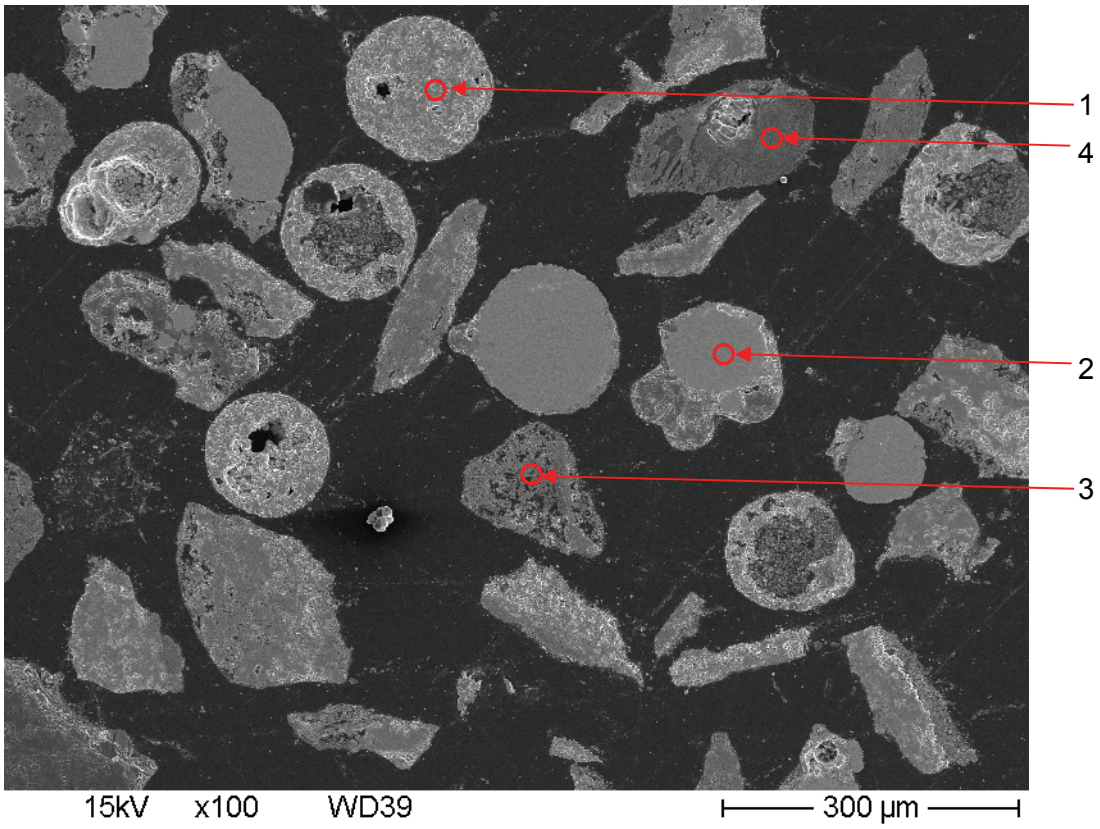

Fig. 4-43. Micrograph of small particles in subcompartment 1, close-up (S1)

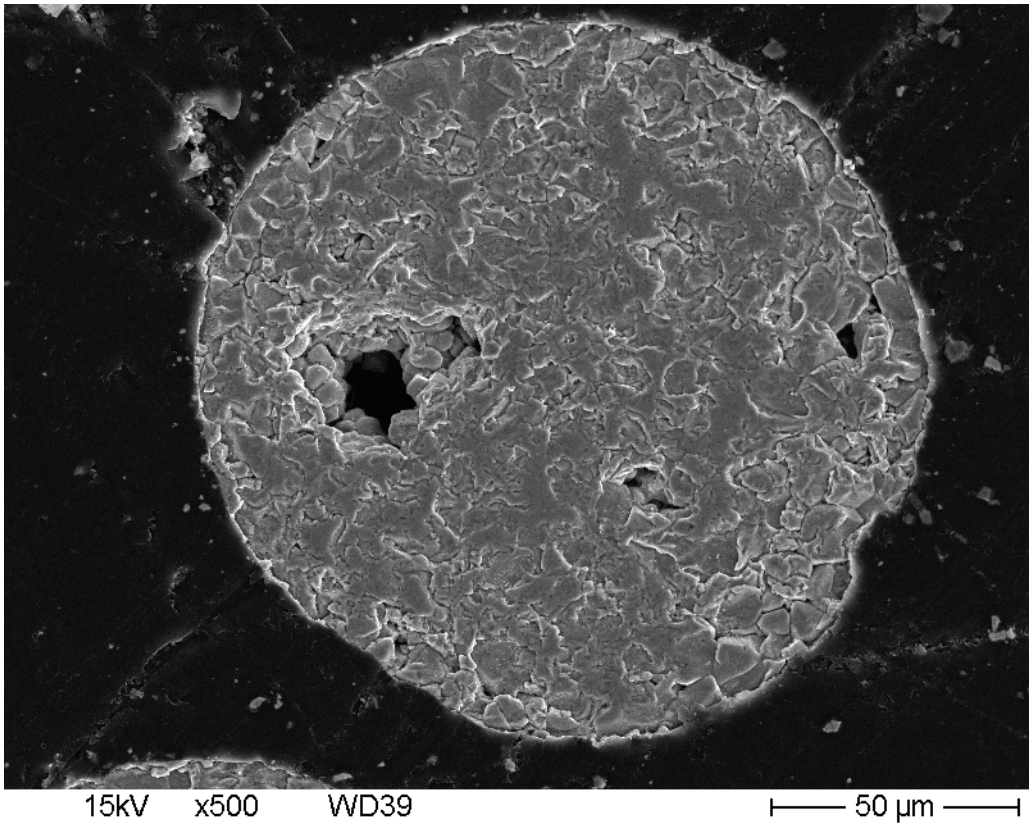

	S1-1
Fe	43,1
Cr	0,5
Cu	1,0
Mg	
Al	0,4
Si	0,3
Ca	0,3
O	54,4

Fig. 4-44. Particle number 1 in subcompartment 1

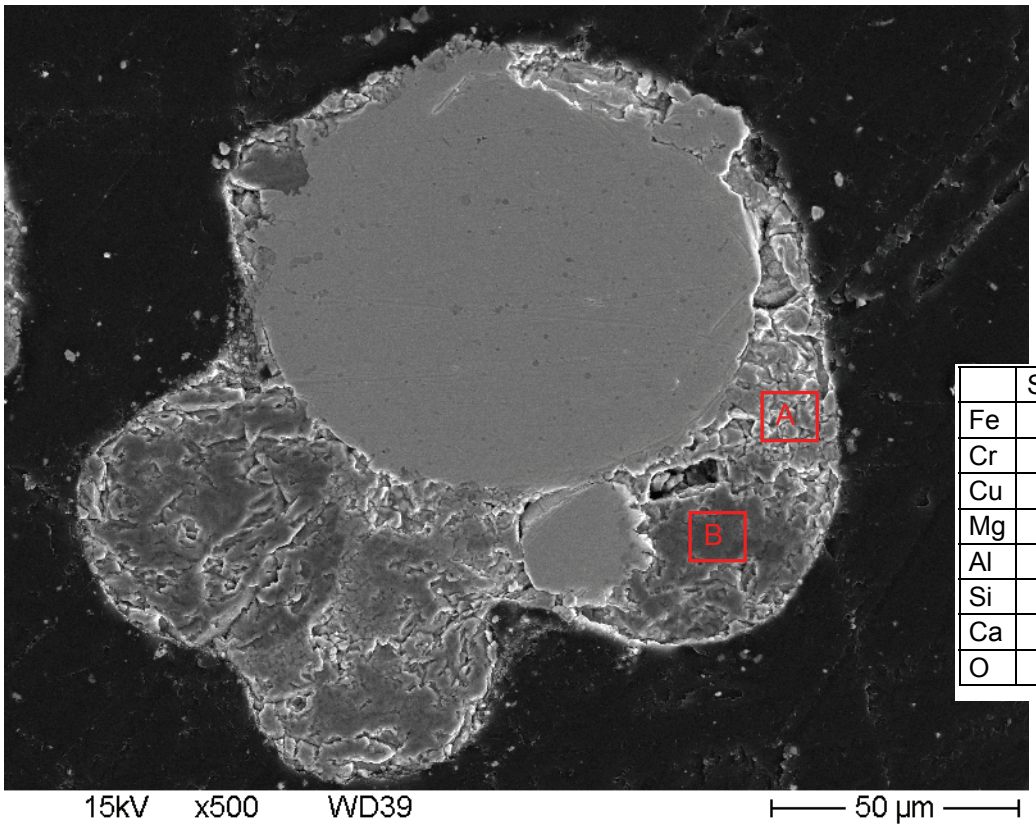

	S1-2A	S1-2B
Fe	40,0	6,0
Cr	0,7	0,2
Cu		
Mg		
Al	1,4	30,1
Si	0,4	2,4
Ca		1,0
O	57,5	60,3

Fig. 4-45. Particle number 2 in subcompartment 1

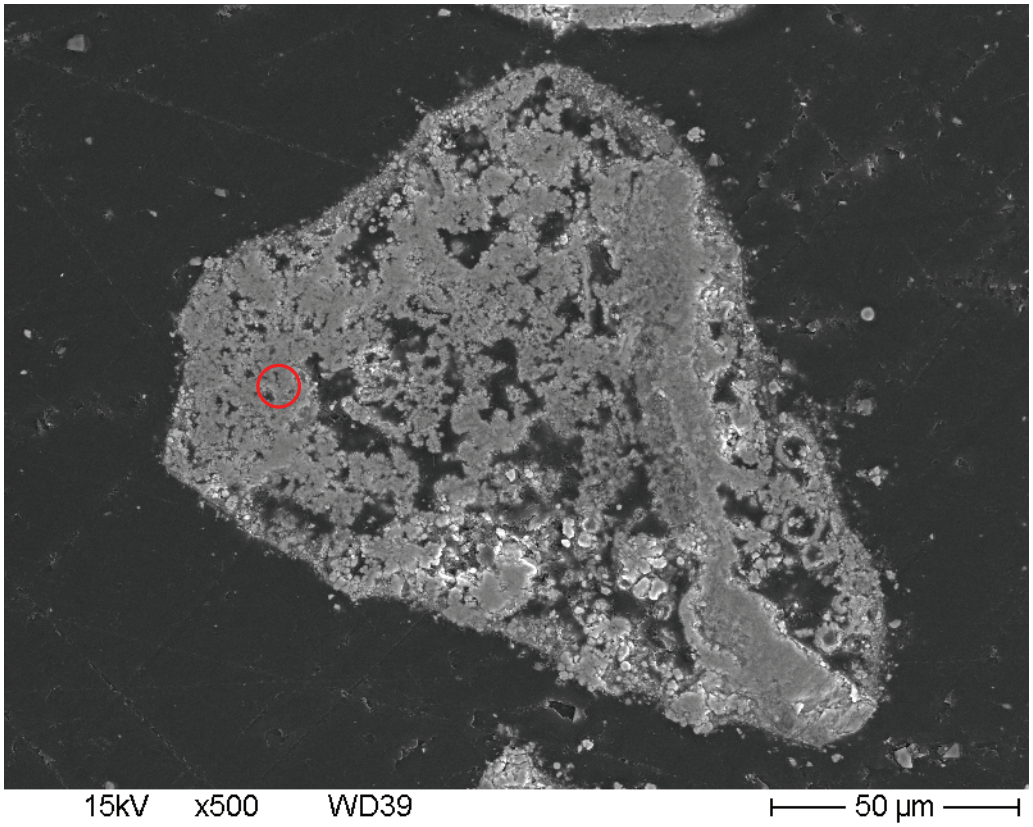

	S1-3
Fe	40,9
Cr	
Cu	
Mg	0,6
Al	0,3
Si	0,2
Ca	0,9
O	57,1

Fig. 4-46. Particle number 3 in subcompartment 1

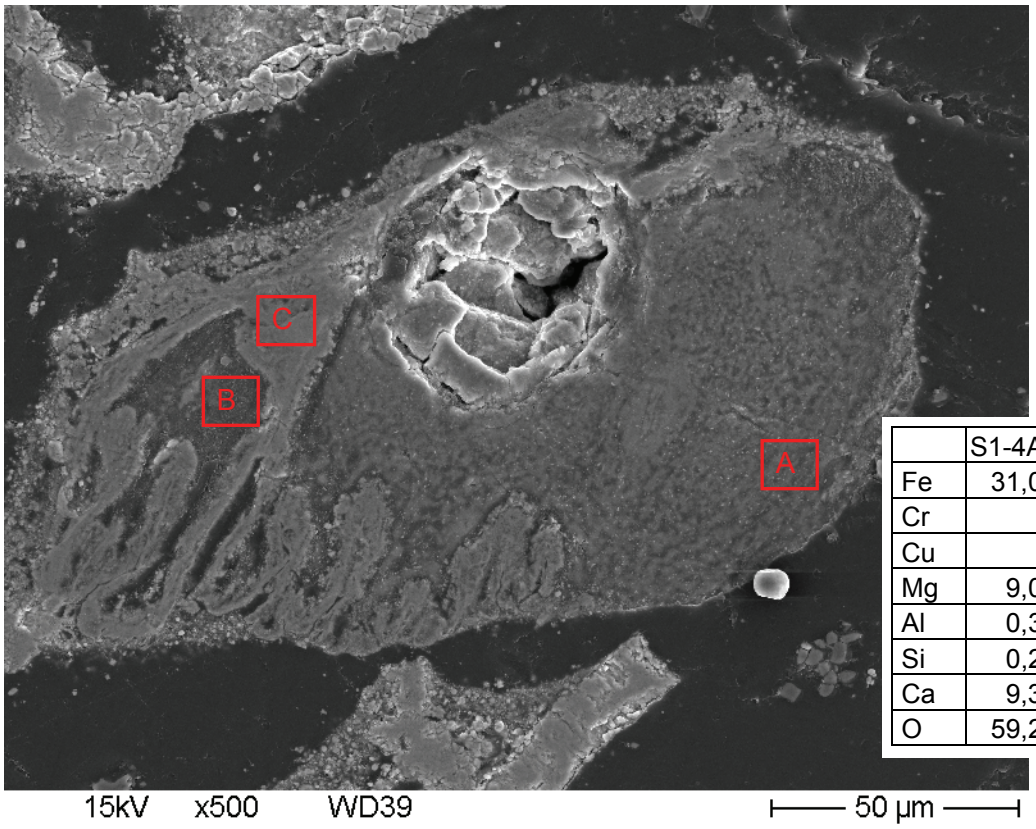

	S1-4A	S1-4B	S1-4C
Fe	31,0	20,4	35,0
Cr			
Cu			
Mg	9,0	23,2	1,0
Al	0,3	0,2	0,2
Si	0,2	0,3	
Ca	9,3	0,3	0,4
O	59,2	55,6	63,4

Fig. 4-47. Particle number 4 in subcompartment 1

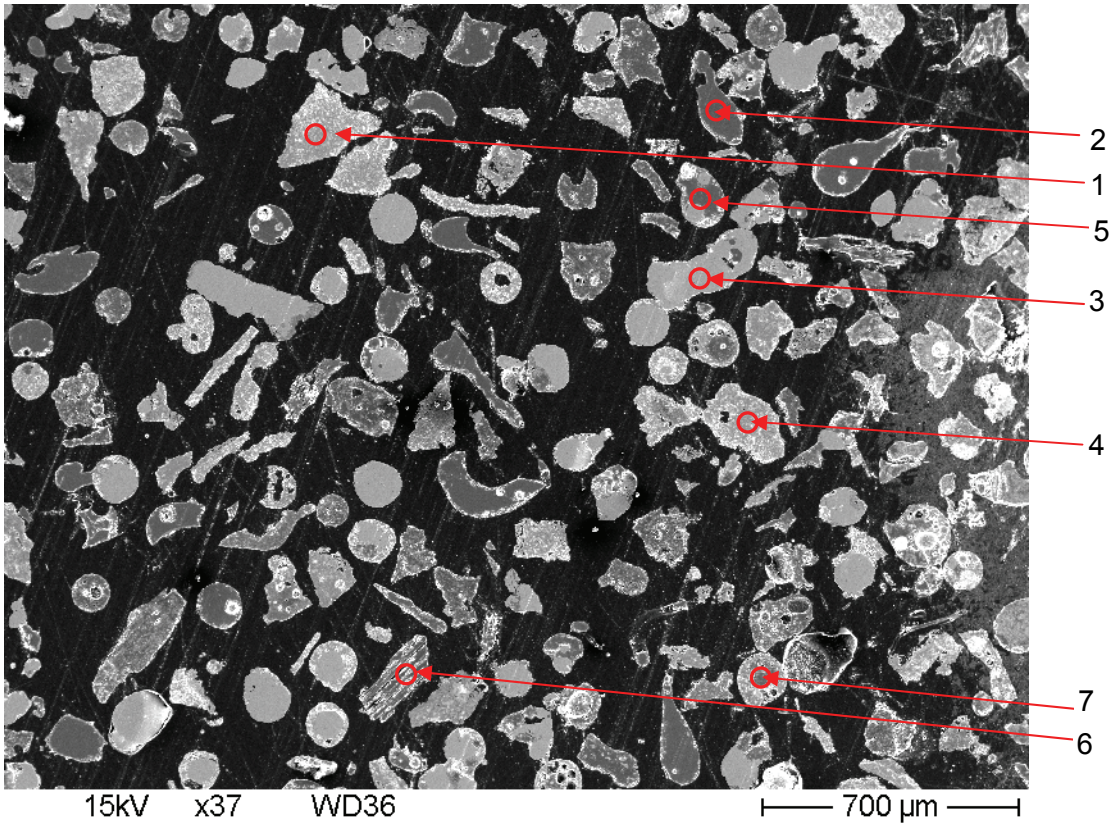

Fig. 4-48. Micrograph of small particles in subcompartment 2 (S2)

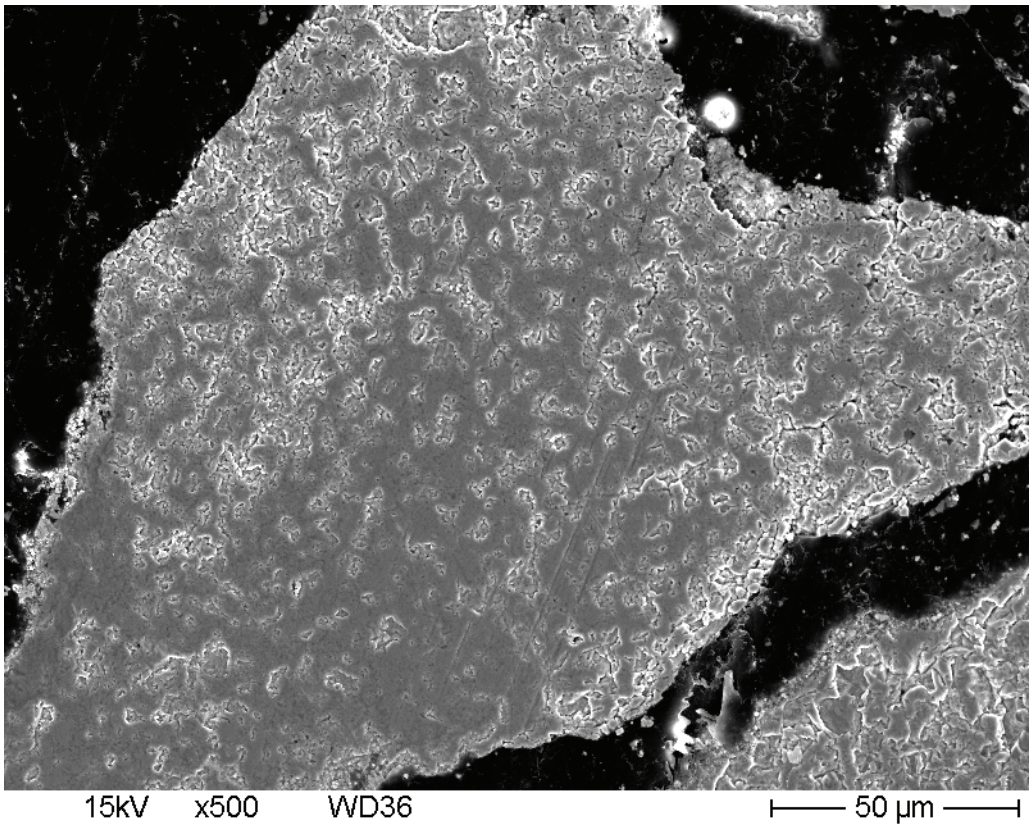

	S2-1
Fe	44,0
Cr	
Cu	
Mg	
Al	
Si	
Ca	
O	56.0

Fig. 4-49. Particle number 1 in subcompartment 2

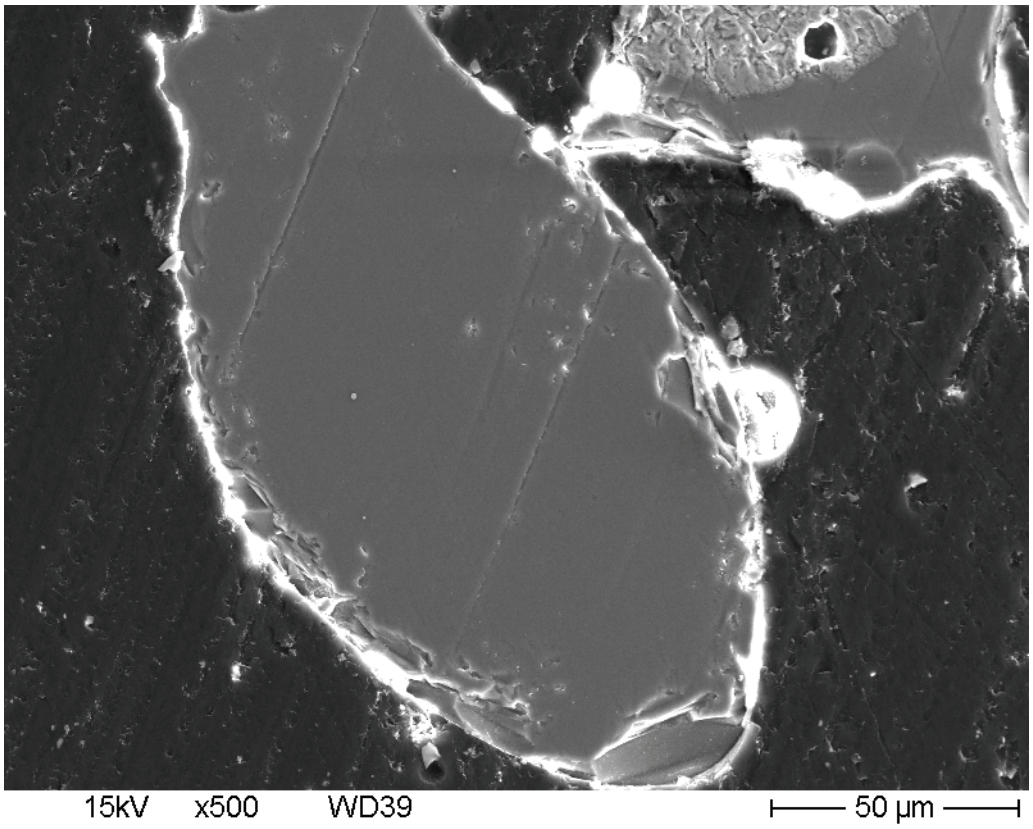

	S2-2
Fe	1,6
Cr	
Cu	
Mg	4,3
Al	7,3
Si	13,3
Ca	9,5
O	64,0

Fig. 4-50. Particle number 2 in subcompartment 2

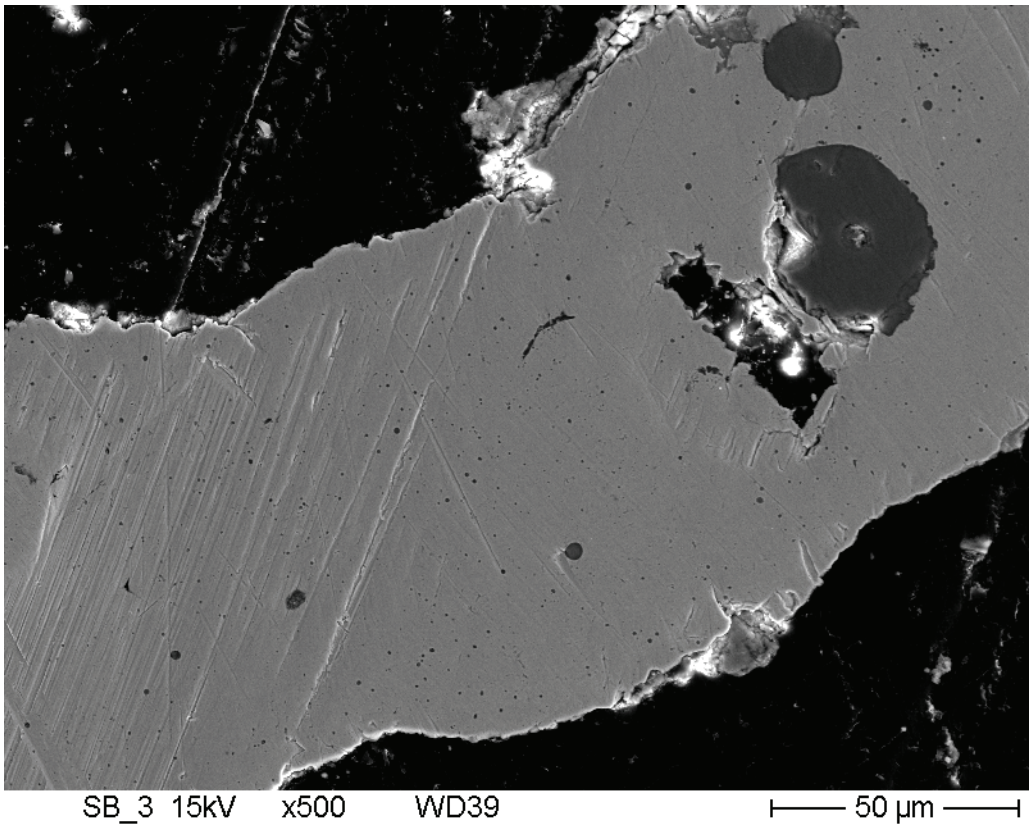

	S2-3
Fe	94,6
Cr	1,2
Cu	2,2
Mg	
Al	
Si	0,6
Ca	
O	1,4

Fig. 4-51. Particle number 3 in subcompartment 2

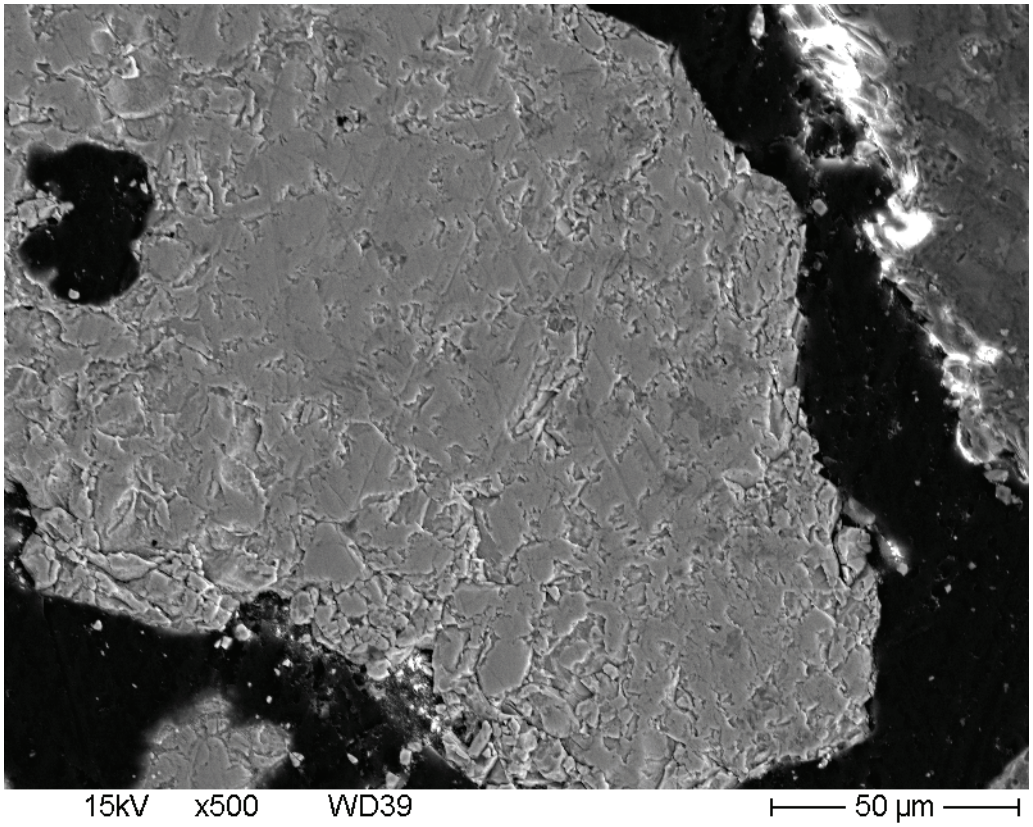

	S2-4
Fe	42,1
Cr	0,3
Cu	
Mg	
Al	1,5
Si	1,3
Ca	0,2
O	54,6

Fig. 4-52. Particle number 4 in subcompartment 2

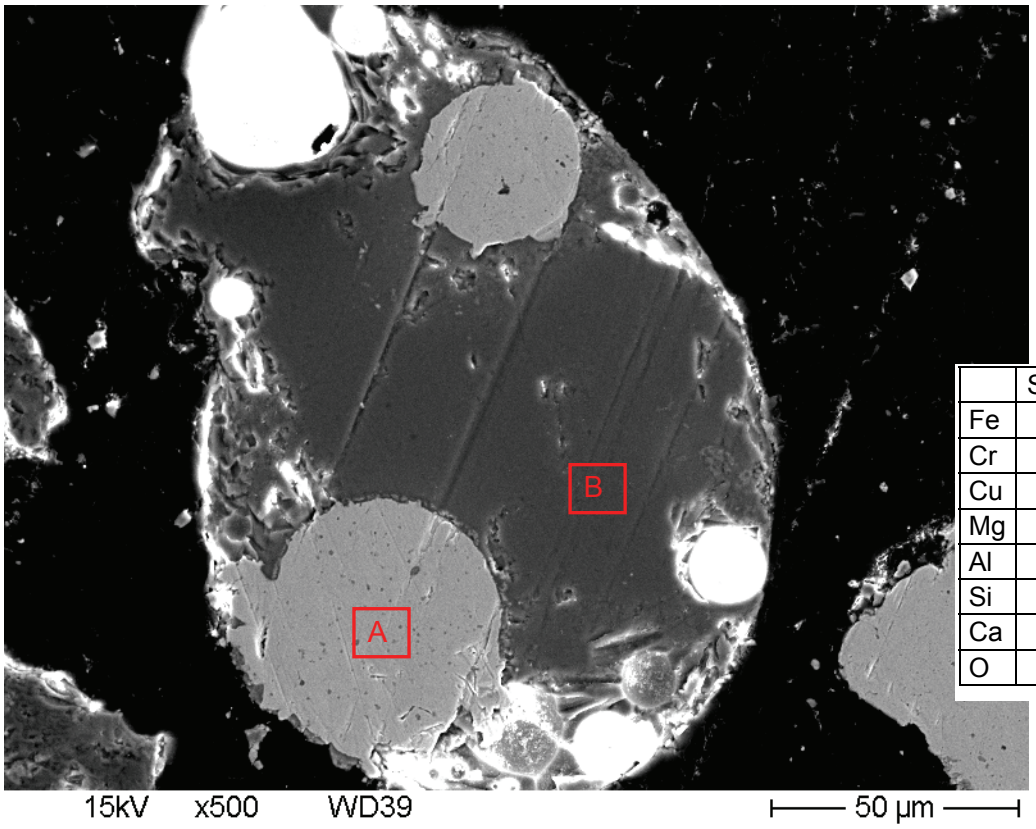

	S2-5A	S2-5B
Fe	95,7	1,9
Cr	0,7	
Cu	2,5	
Mg		4,2
Al		7,1
Si		13,5
Ca		9,5
O	1,1	63,8

Fig. 4-53. Particle number 5 in subcompartment 2

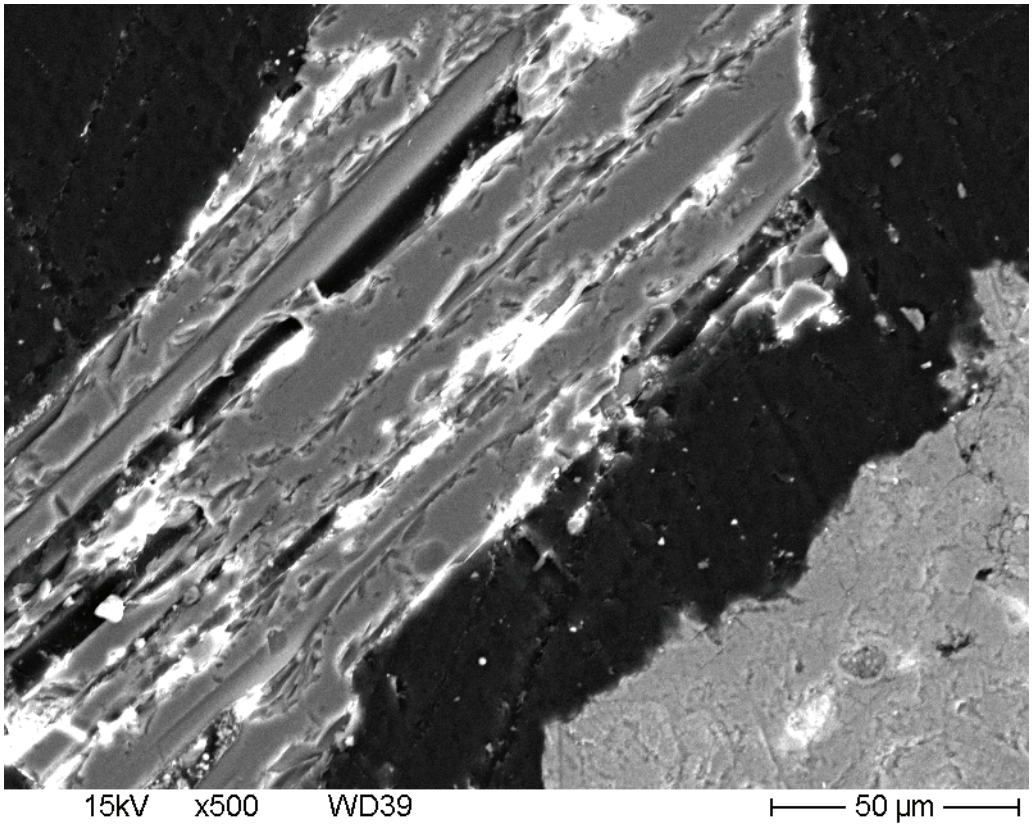

	S2-6
Fe	0,3
Cr	
Cu	
Mg	2,2
Al	5,5
Si	16,4
Ca	8,3
O	67,3

Fig. 4-54. Particle number 6 in subcompartment 2

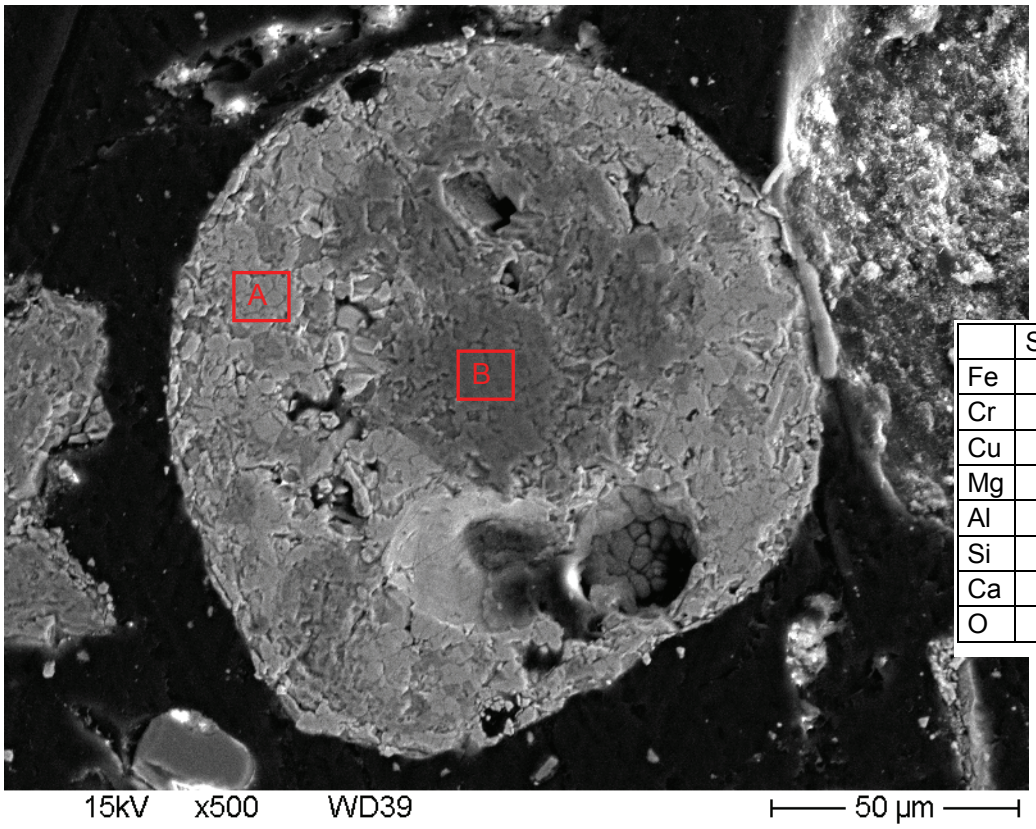

	S2-7A	S2-7B
Fe	39,4	6,3
Cr	0,9	0,5
Cu		
Mg	0,2	
Al	4,9	29,6
Si	0,5	0,9
Ca	0,2	0,6
O	53,9	62,1

Fig. 4-55. Particle number 7 in subcompartment 2

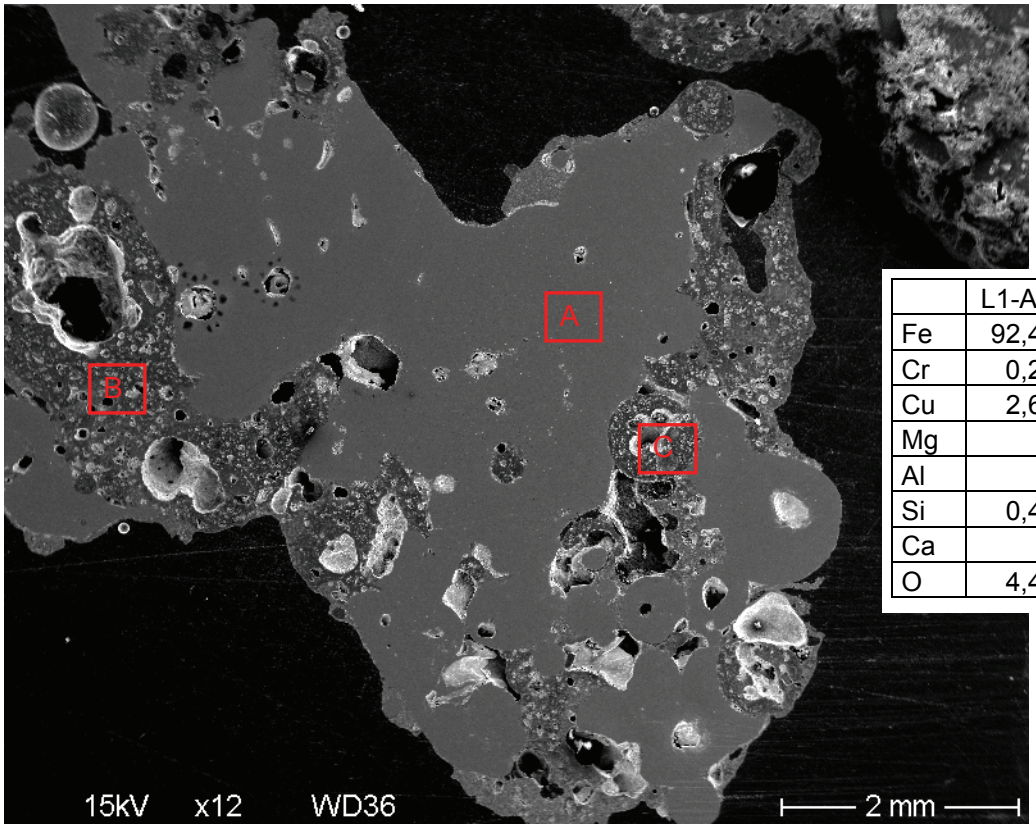

	L1-A	L1-B	L1-C
Fe	92,4	17,4	13,4
Cr	0,2	0,7	0,4
Cu	2,6		0,3
Mg		0,2	
Al		19,6	21,6
Si	0,4	1,6	2,1
Ca		0,7	0,9
O	4,4	59,8	61,3

Fig. 4-56. Large particle number 1 from subcompartment 1

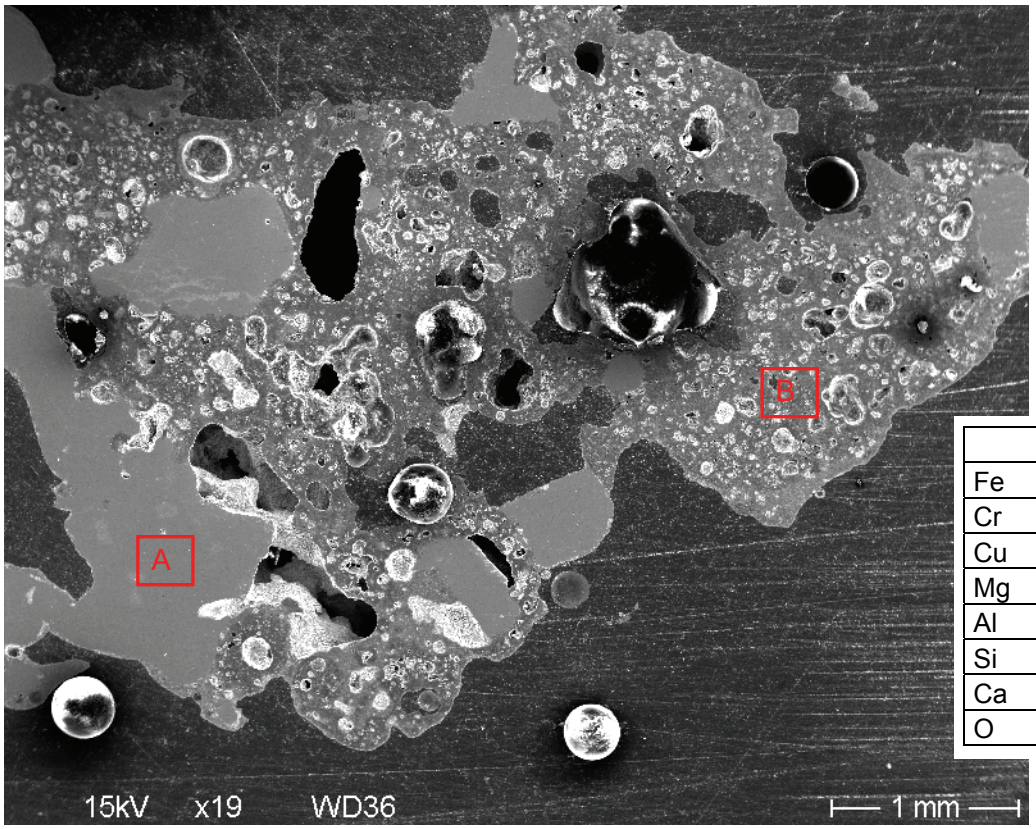

	L2-A	L2-B
Fe	96,4	15,8
Cr	2,0	1,4
Cu		
Mg		0,2
Al		19,6
Si	0,3	1,1
Ca		0,6
O	1,3	61,3

Fig. 4-57. Large particle number 2 from subcompartment 1

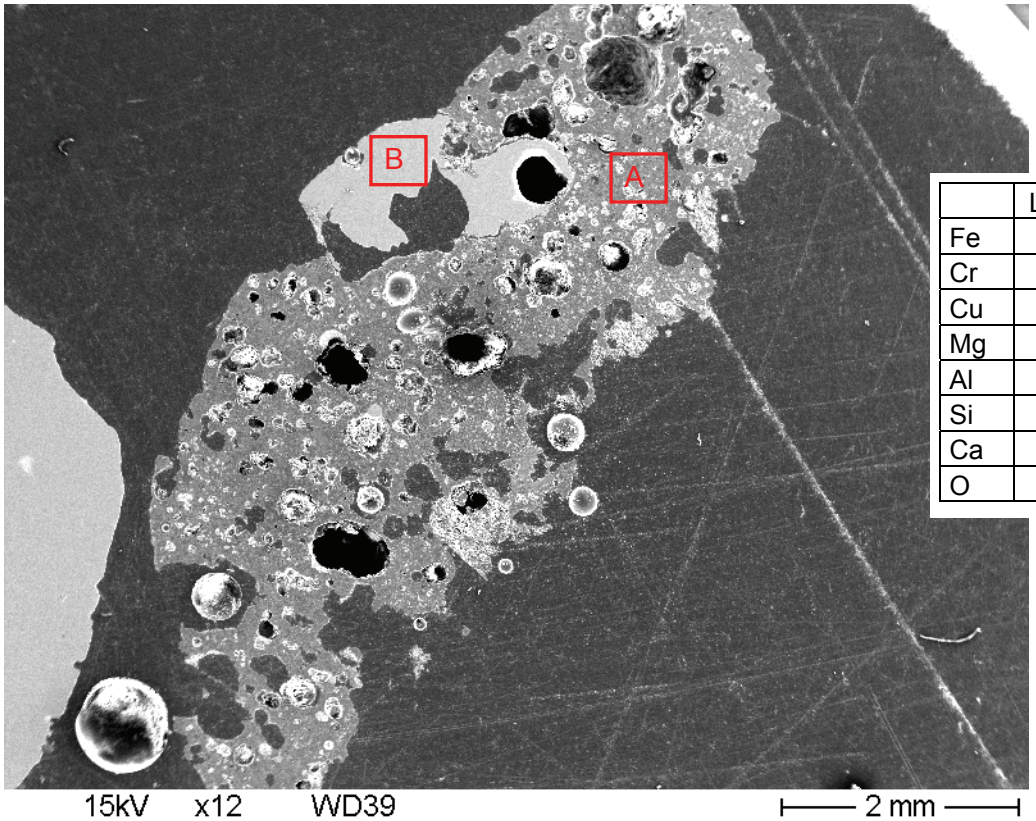

	L3-A	L3-B
Fe	4,4	73,7
Cr	0,9	5,0
Cu		1,7
Mg	0,1	
Al	28,2	
Si	4,0	1,1
Ca	0,8	0,4
O	61,6	18,1

Fig. 4-58. Large particle number 3 from subcompartment 2

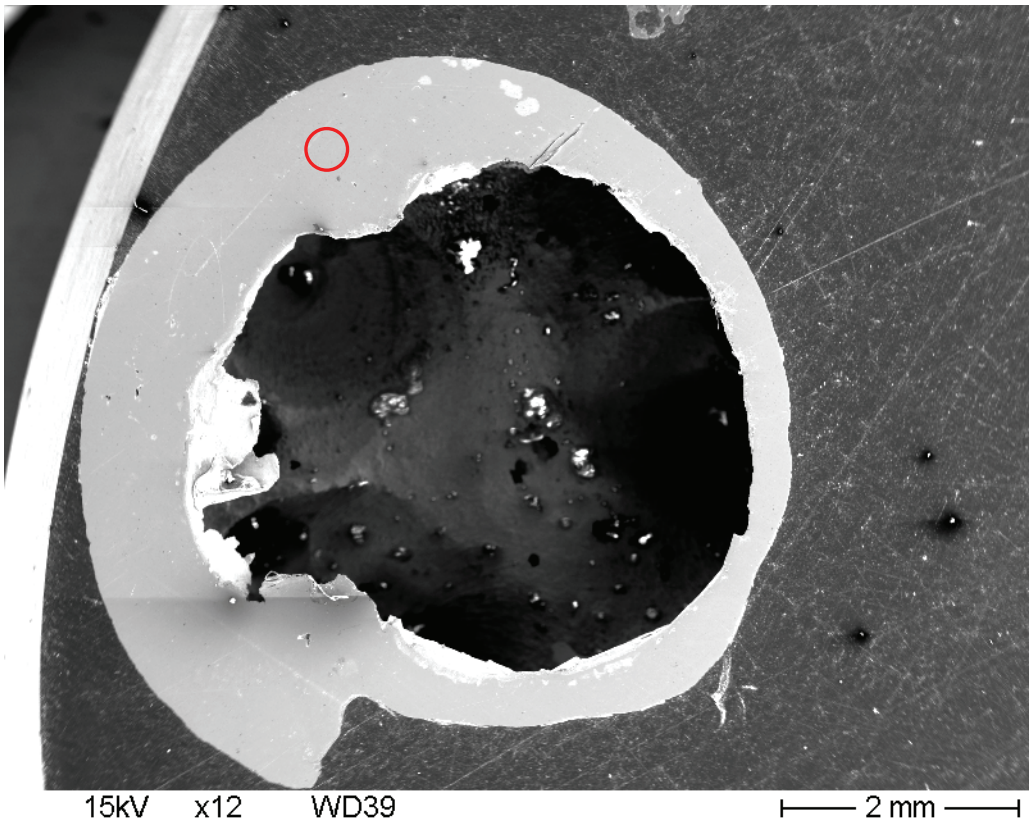

	L4
Fe	97,4
Cr	0,7
Cu	1,7
Mg	
Al	
Si	0,2
Ca	
O	

Fig. 4-59. Large particle number 4 from subcompartment 2

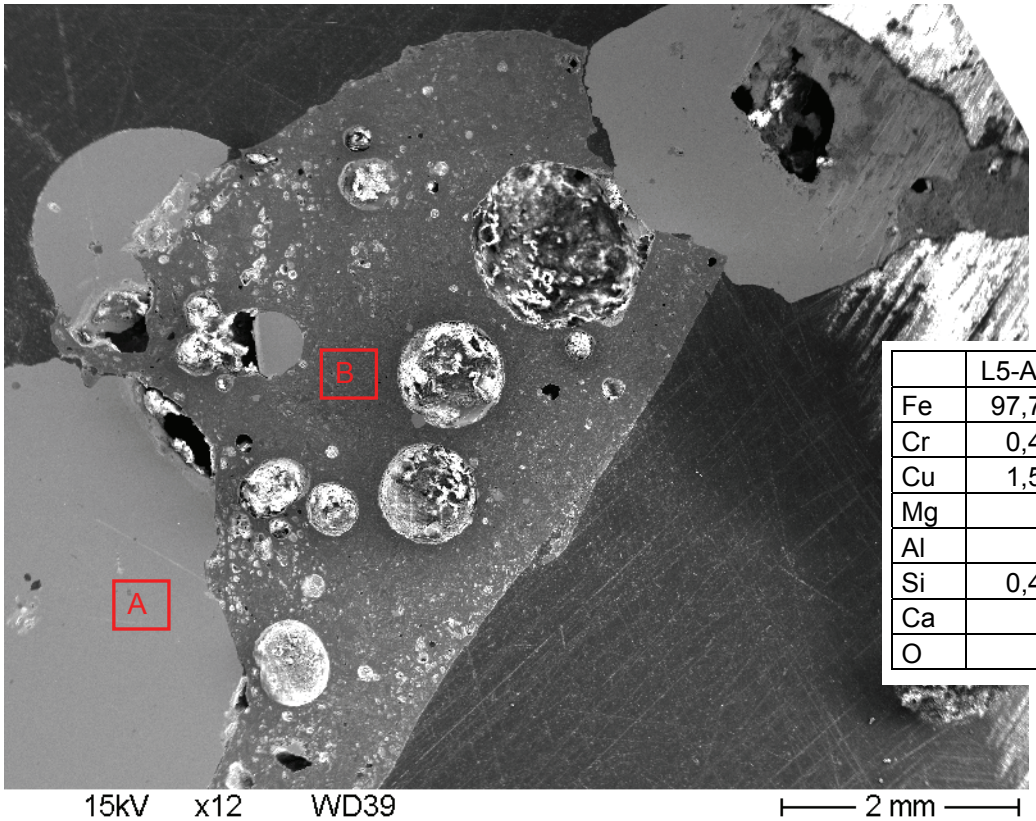

	L5-A	L5-B
Fe	97,7	0,5
Cr	0,4	0,4
Cu	1,5	
Mg		
Al		40,1
Si	0,4	0,5
Ca		0,5
O		58,0

Fig. 4-60. Large particle number 5 from subcompartment 2

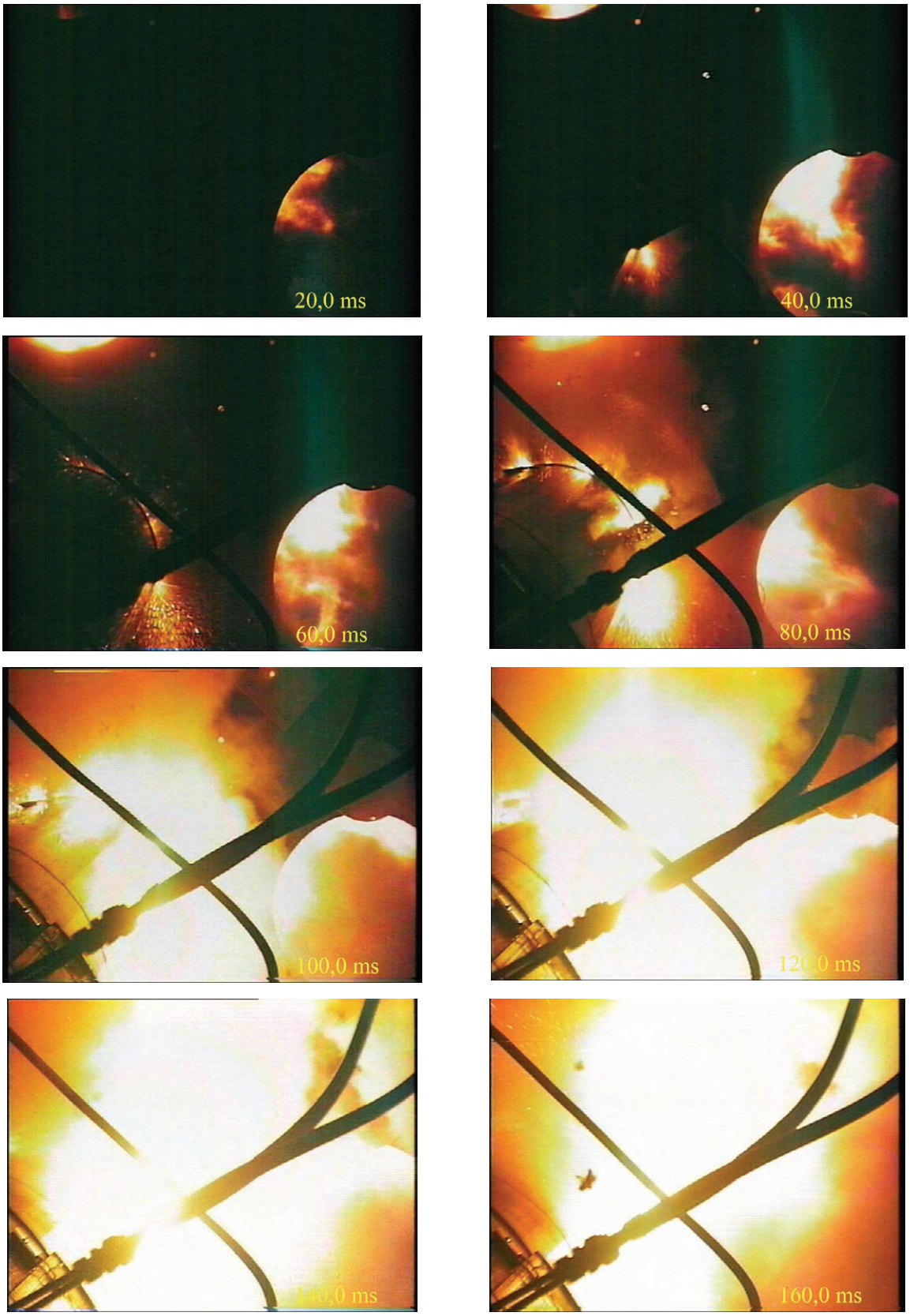

Fig. 4-61. KH01: Top down view at exit of subcompartment 1

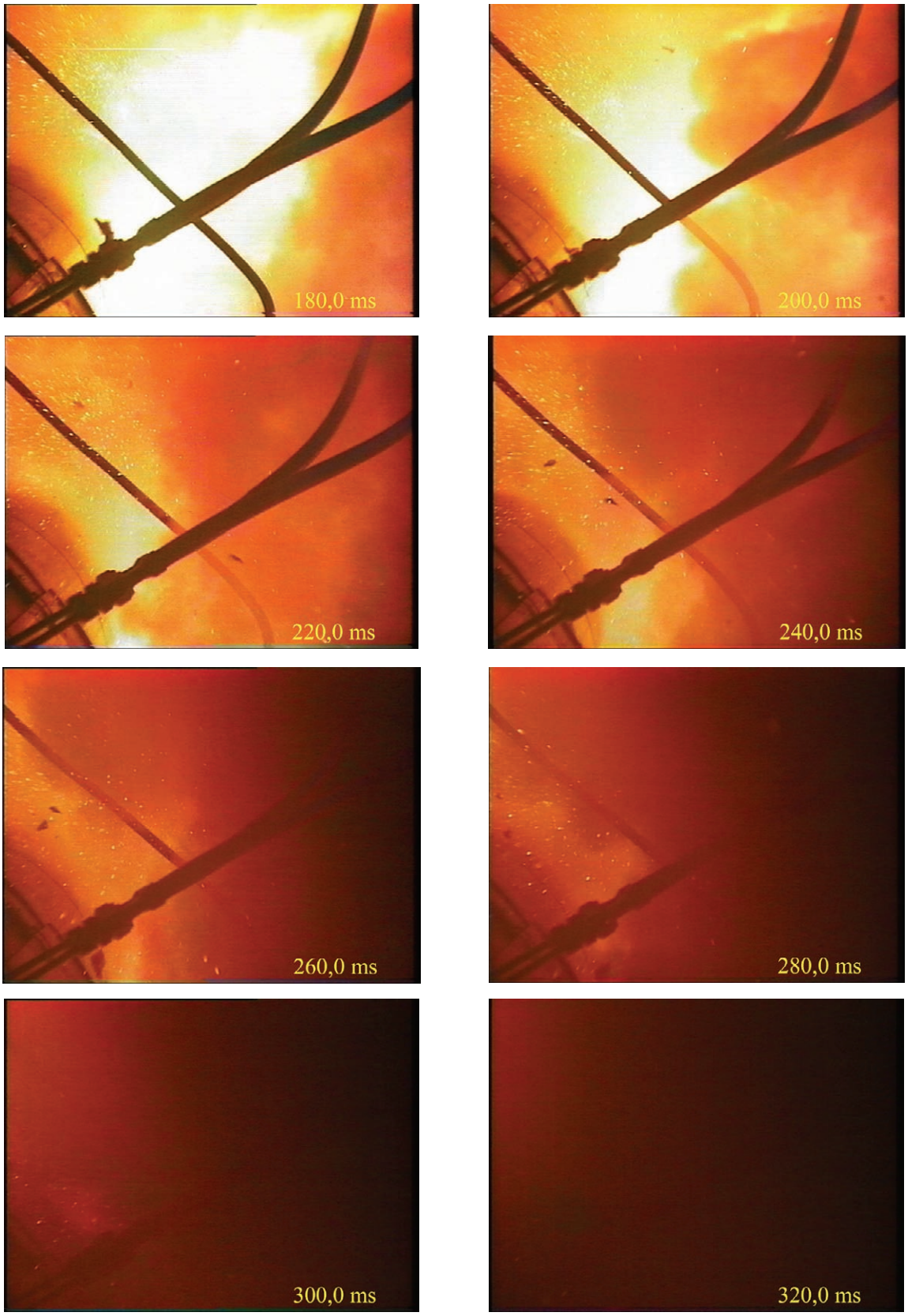

Fig. 4-61. continued

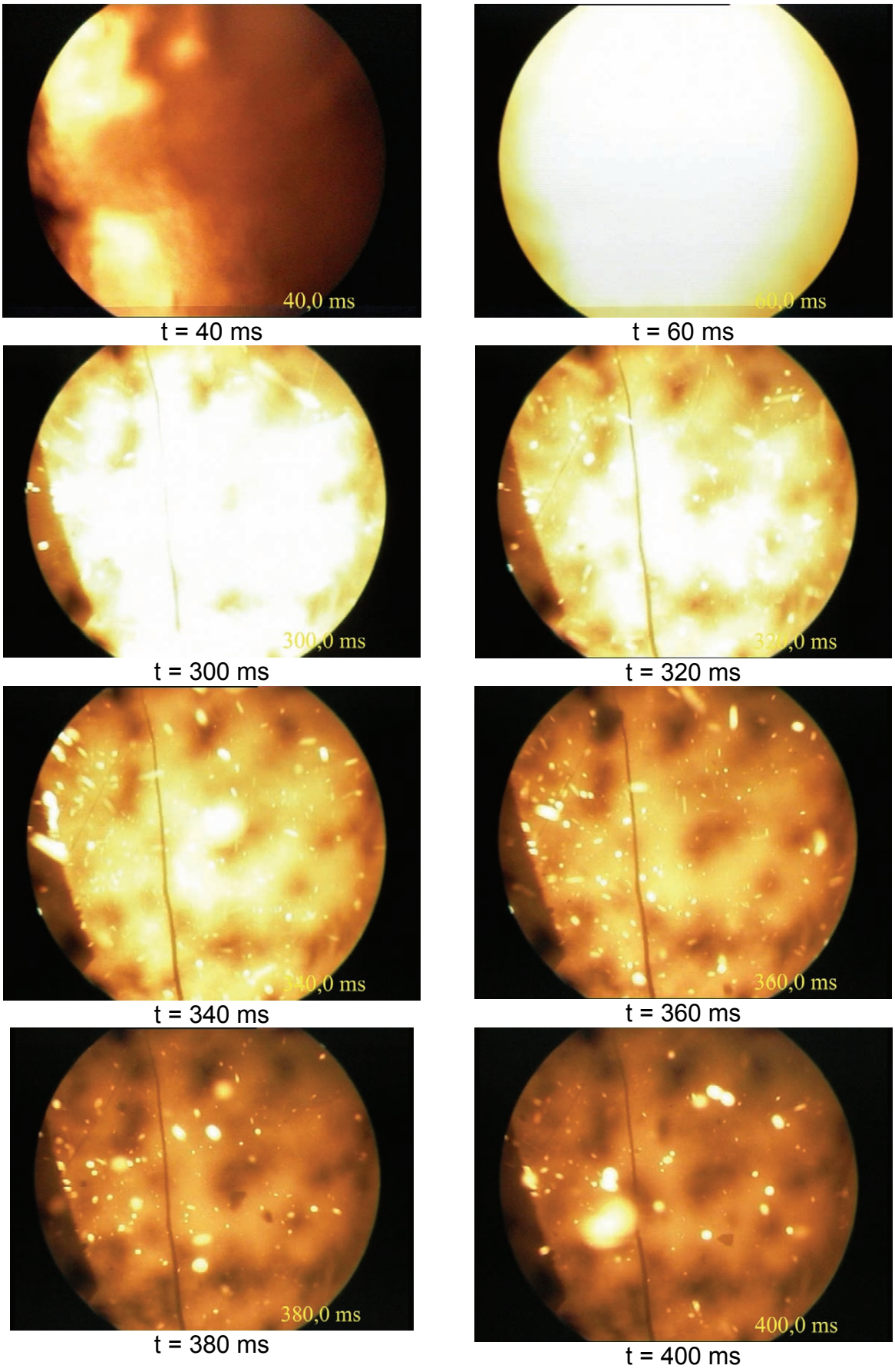

Fig. 4-62. KH01: View with endoscope into subcompartment 1

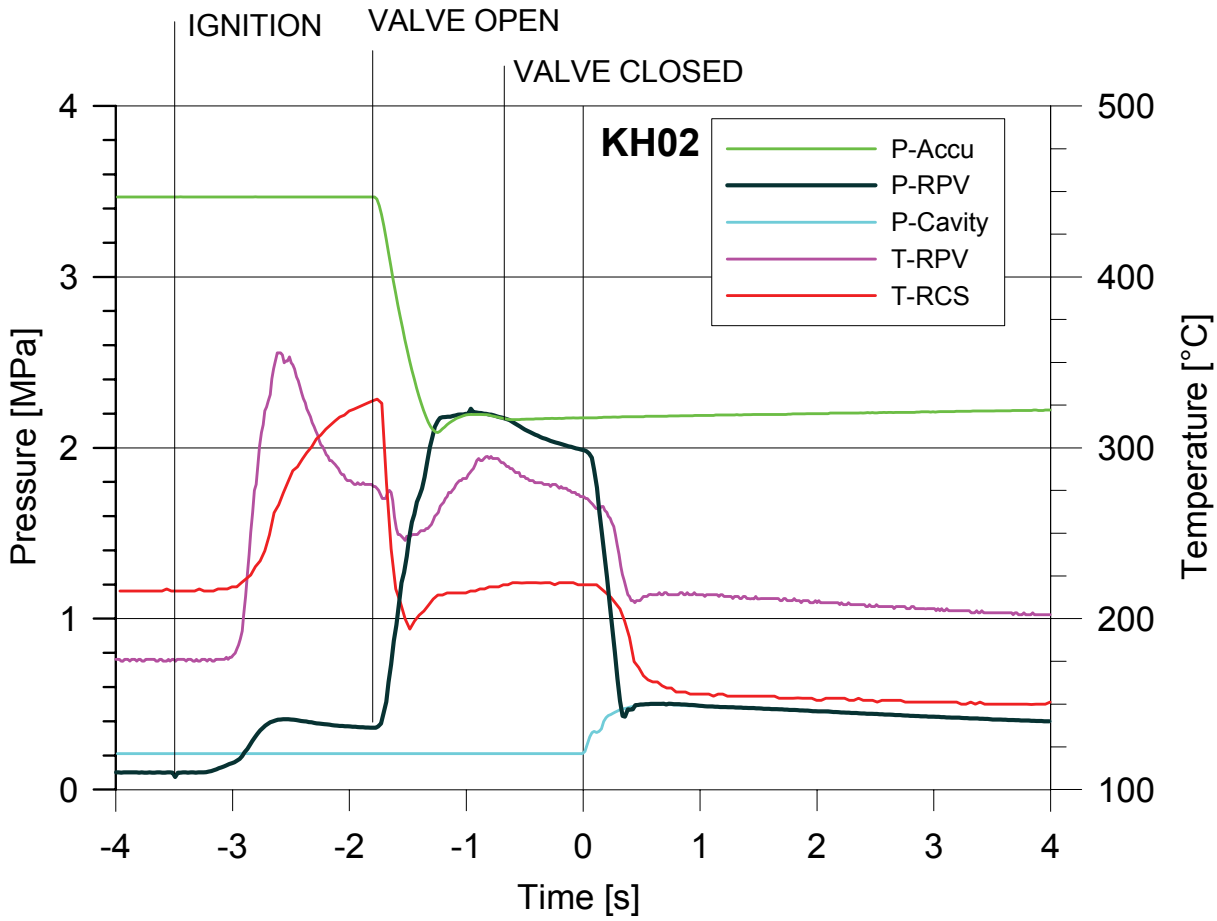

Fig. 4-63. KH02: Pressure, temperature and timing

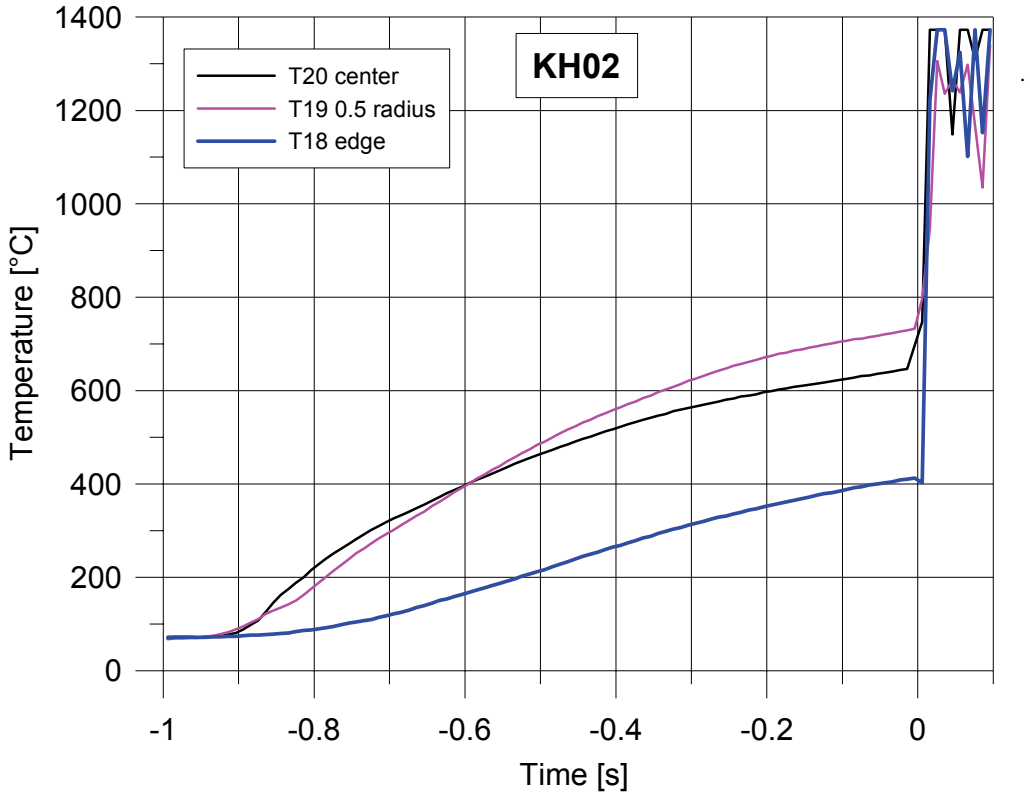

Fig. 4-64. KH02: Thermocouple signals in melt plug

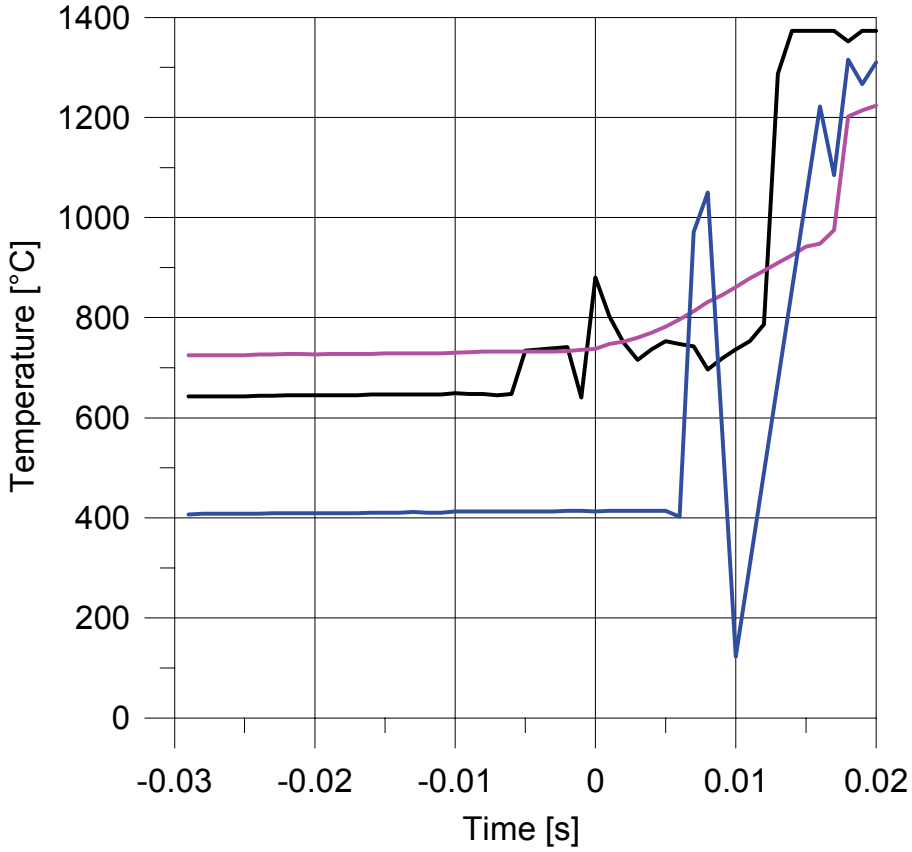

Fig. 4-65. KH02: Thermocouple signals in melt plug, zoom to t = 0 s

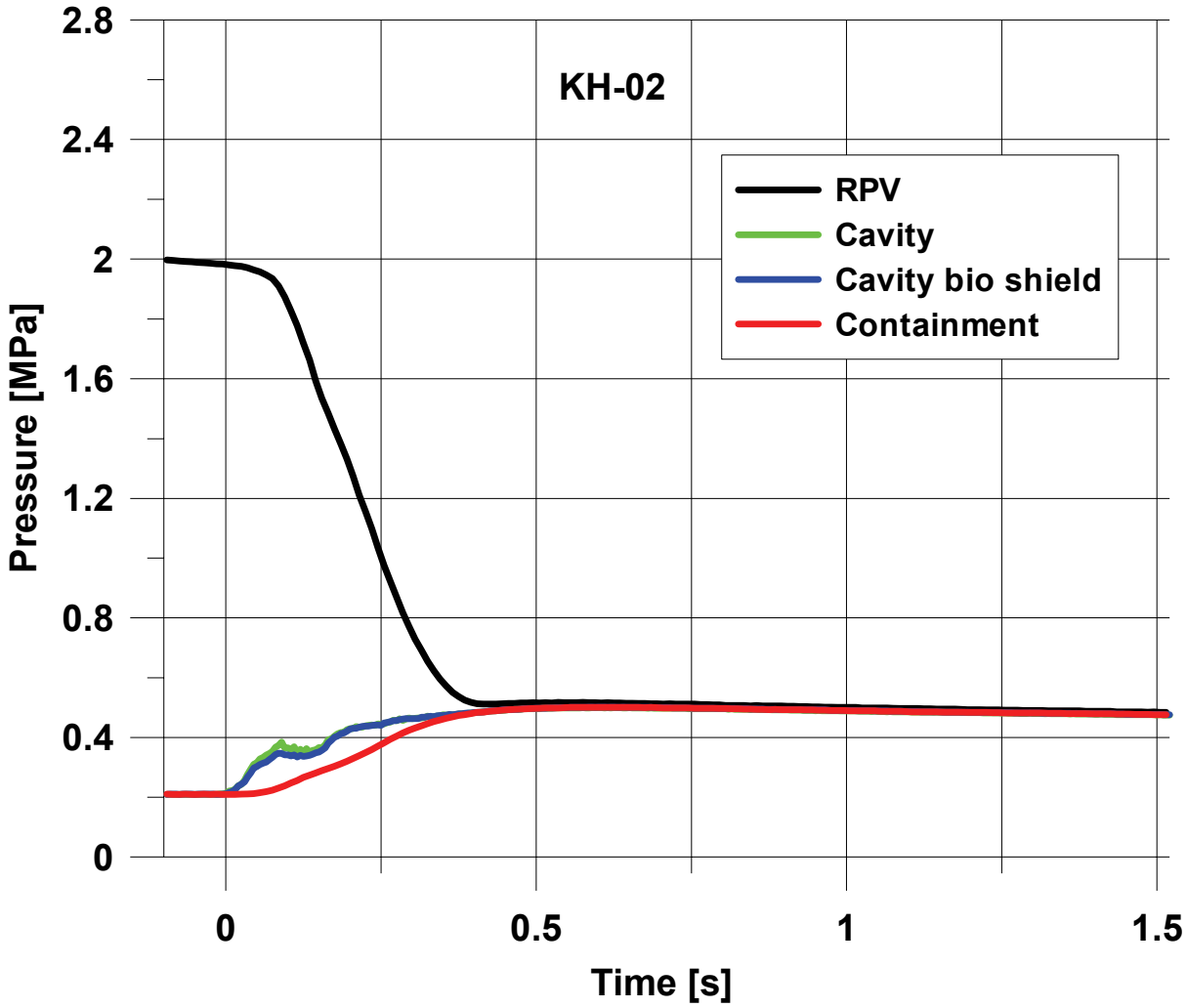

Fig. 4-66. KH02: Pressure in RPV vessel, cavity and containment

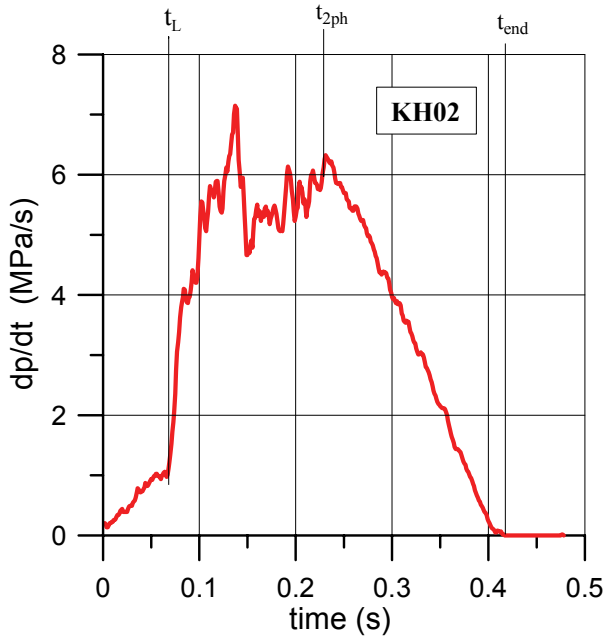

Fig. 4-67. KH02: Pressure gradient in RPV vessel

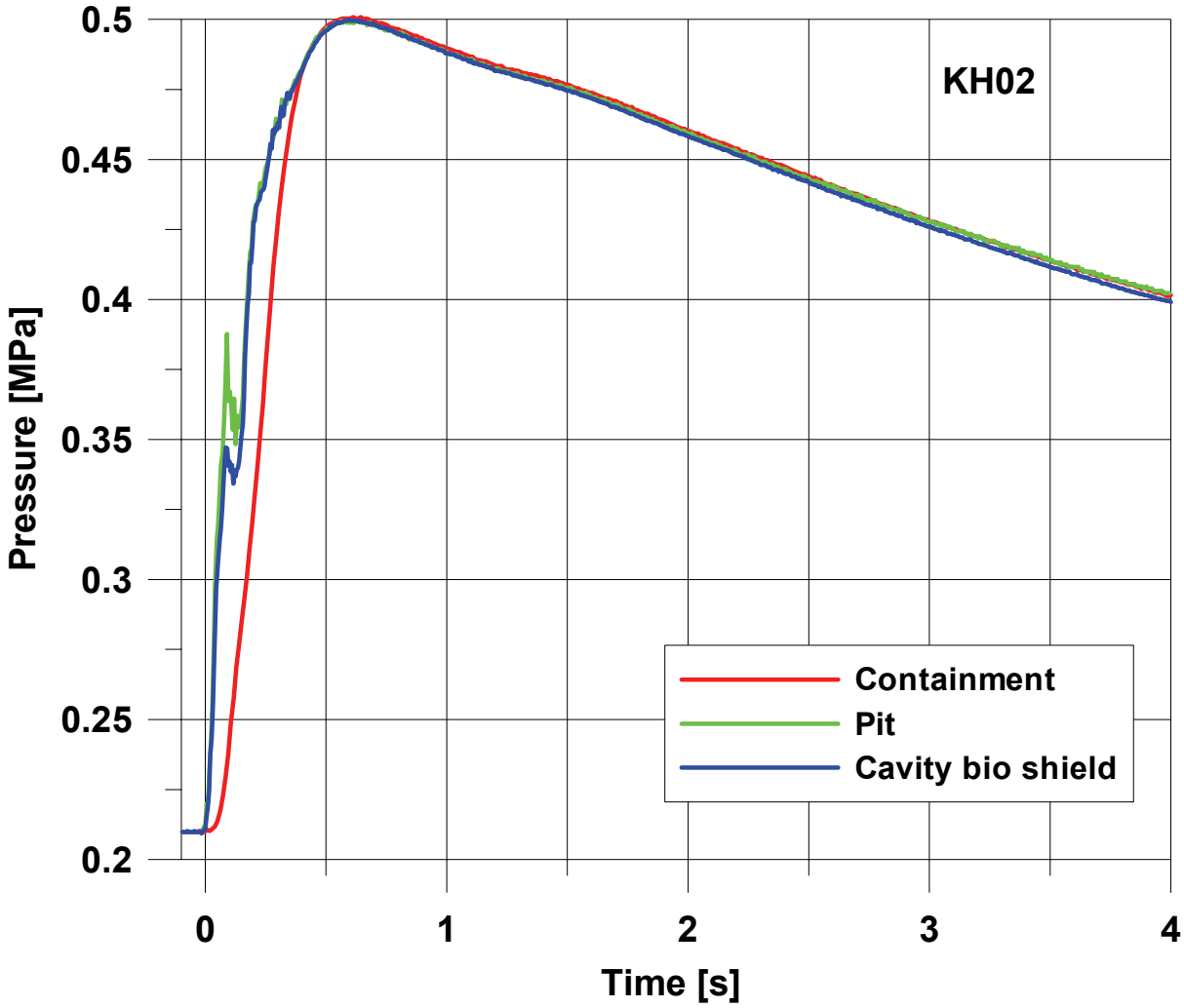

Fig. 4-68. KH02: Pressure in cavity and containment

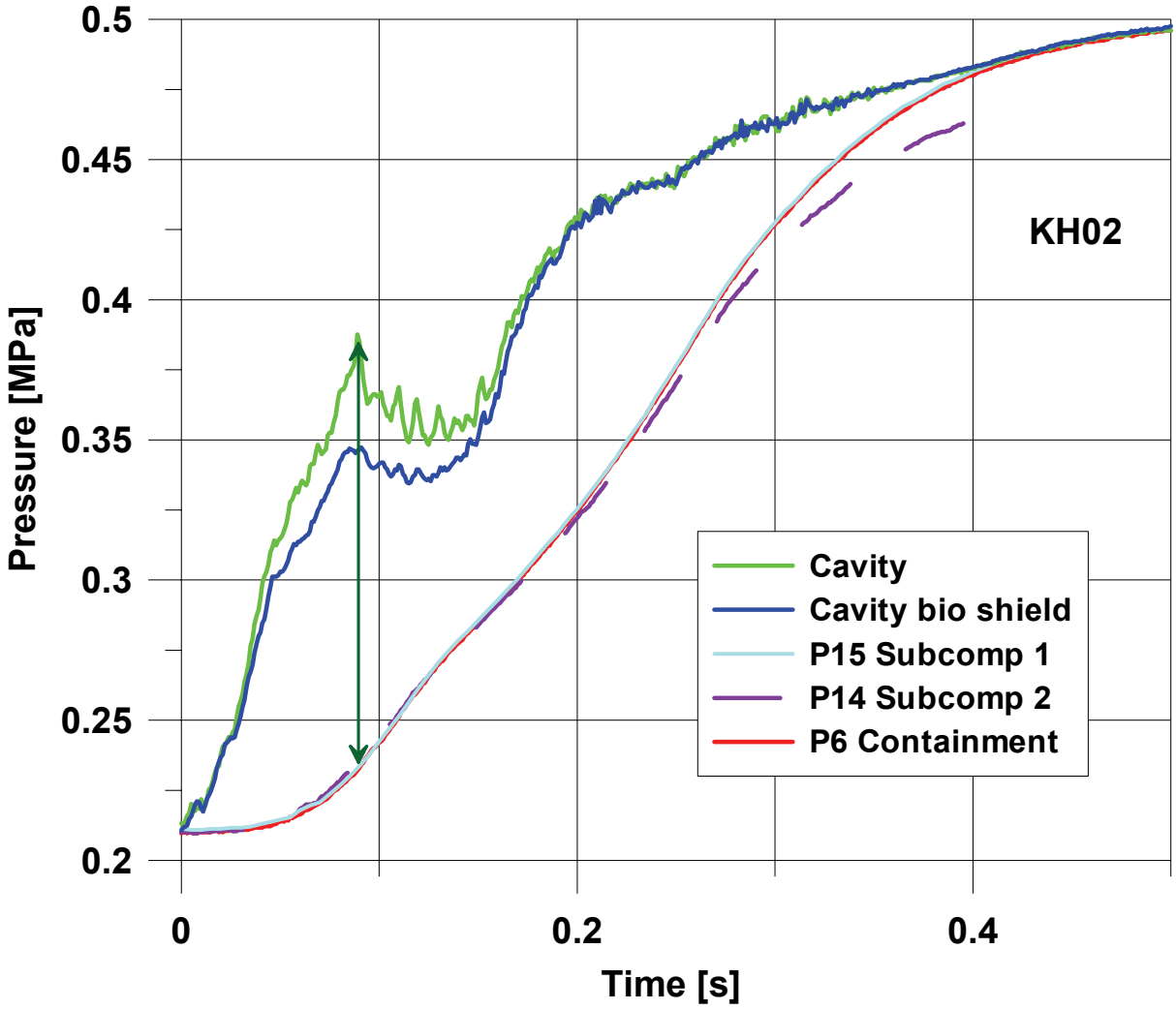

Fig. 4-69. KH02: Pressure in cavity, subcompartment and containment

($\Delta p_{max,\ pit\text{-}cont}$ = 1,53 bar)

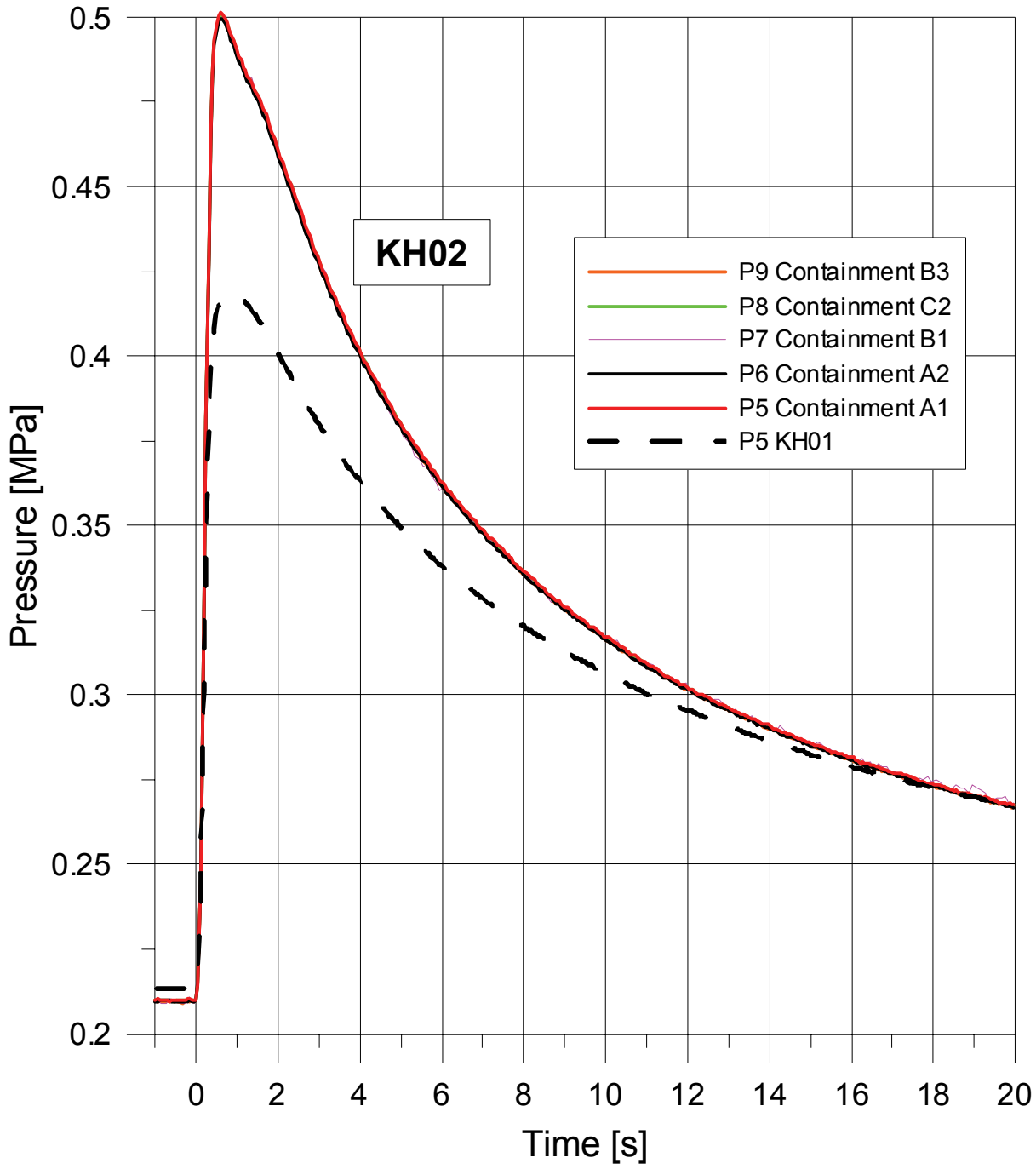

Fig. 4-70. KH02: Pressure in containment, comparison with KH01

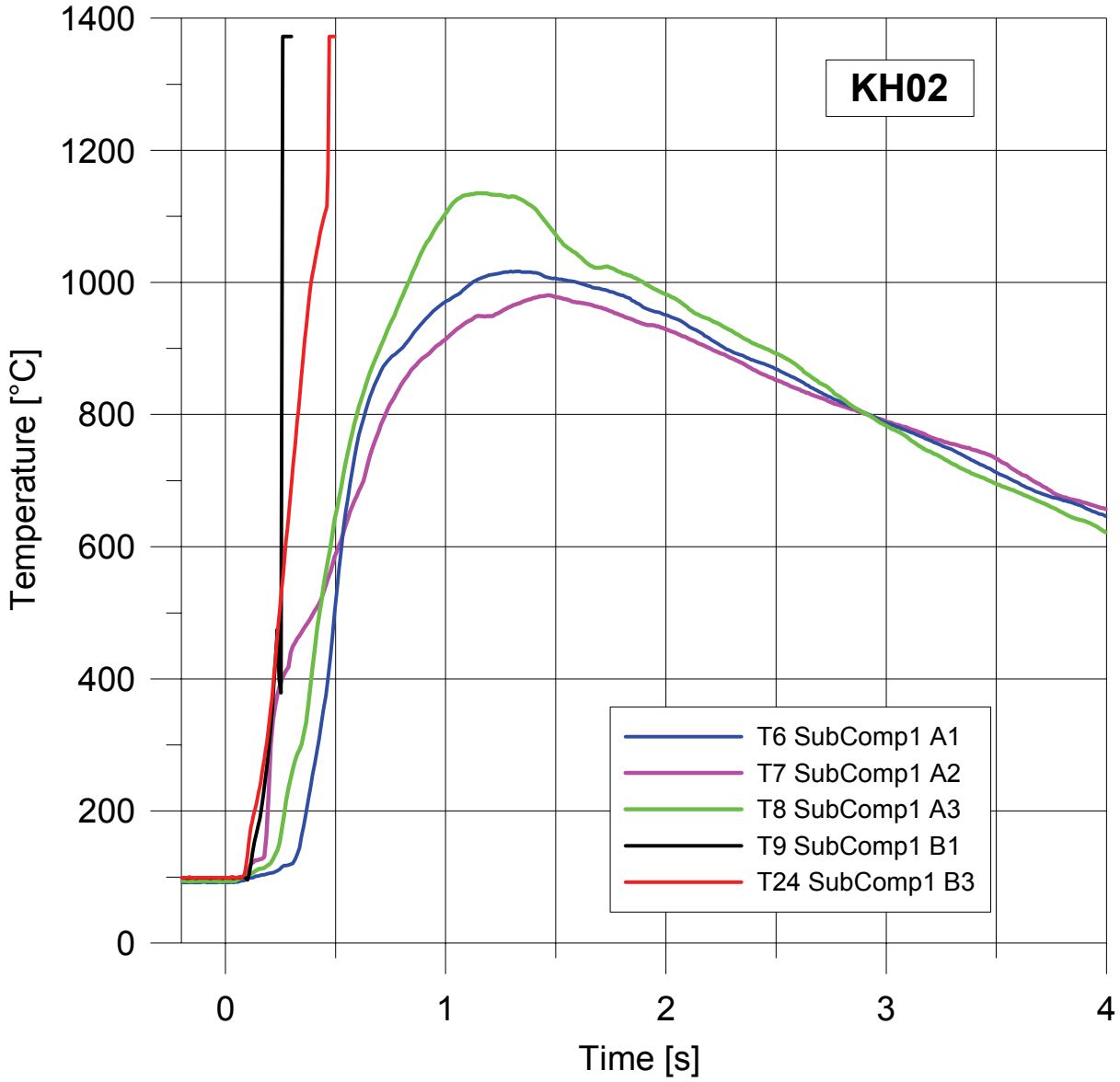

Fig. 4-71. KH02: Temperatures in subcompartment 1

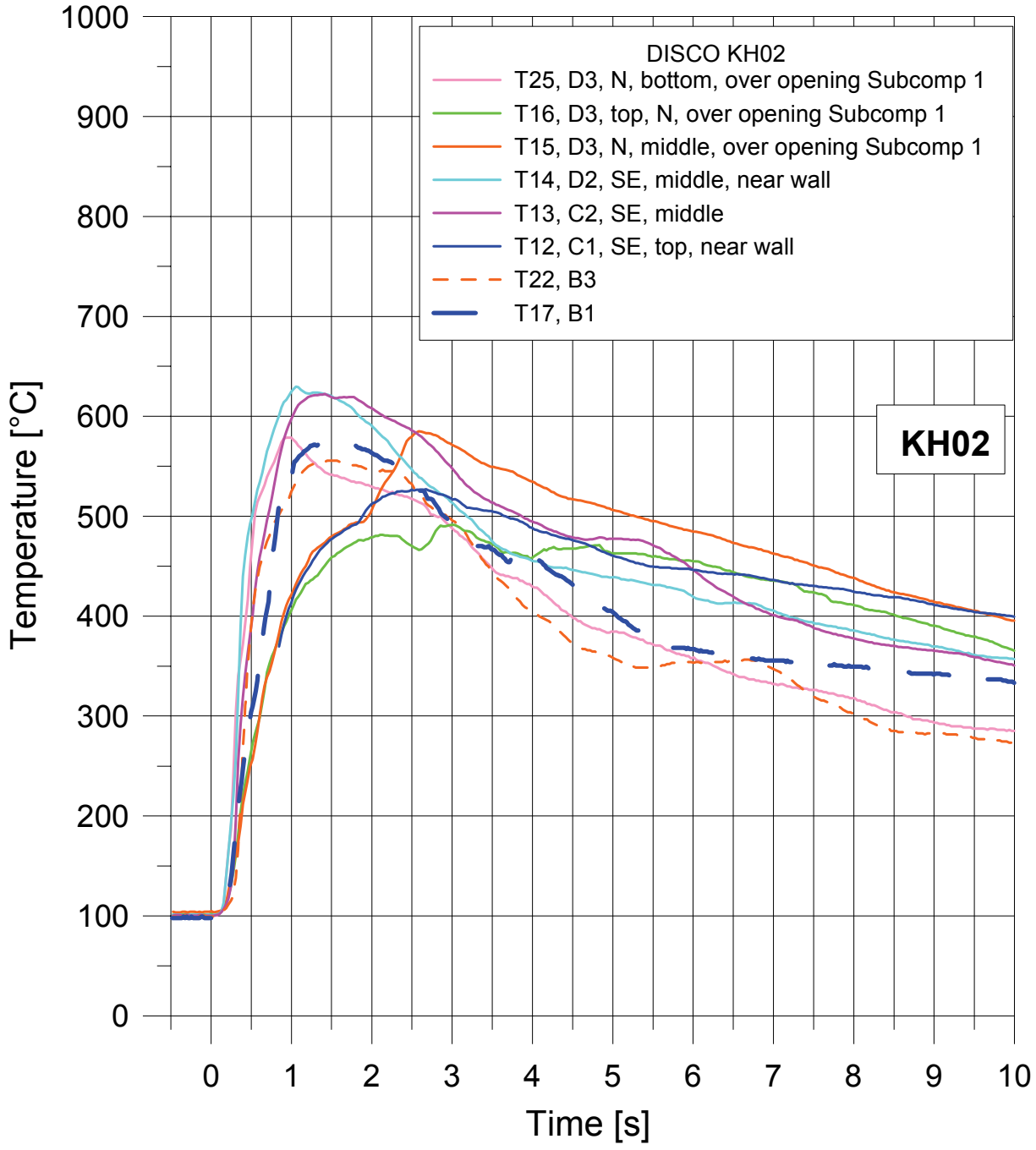

Fig. 4-72. KH02: Temperatures in containment

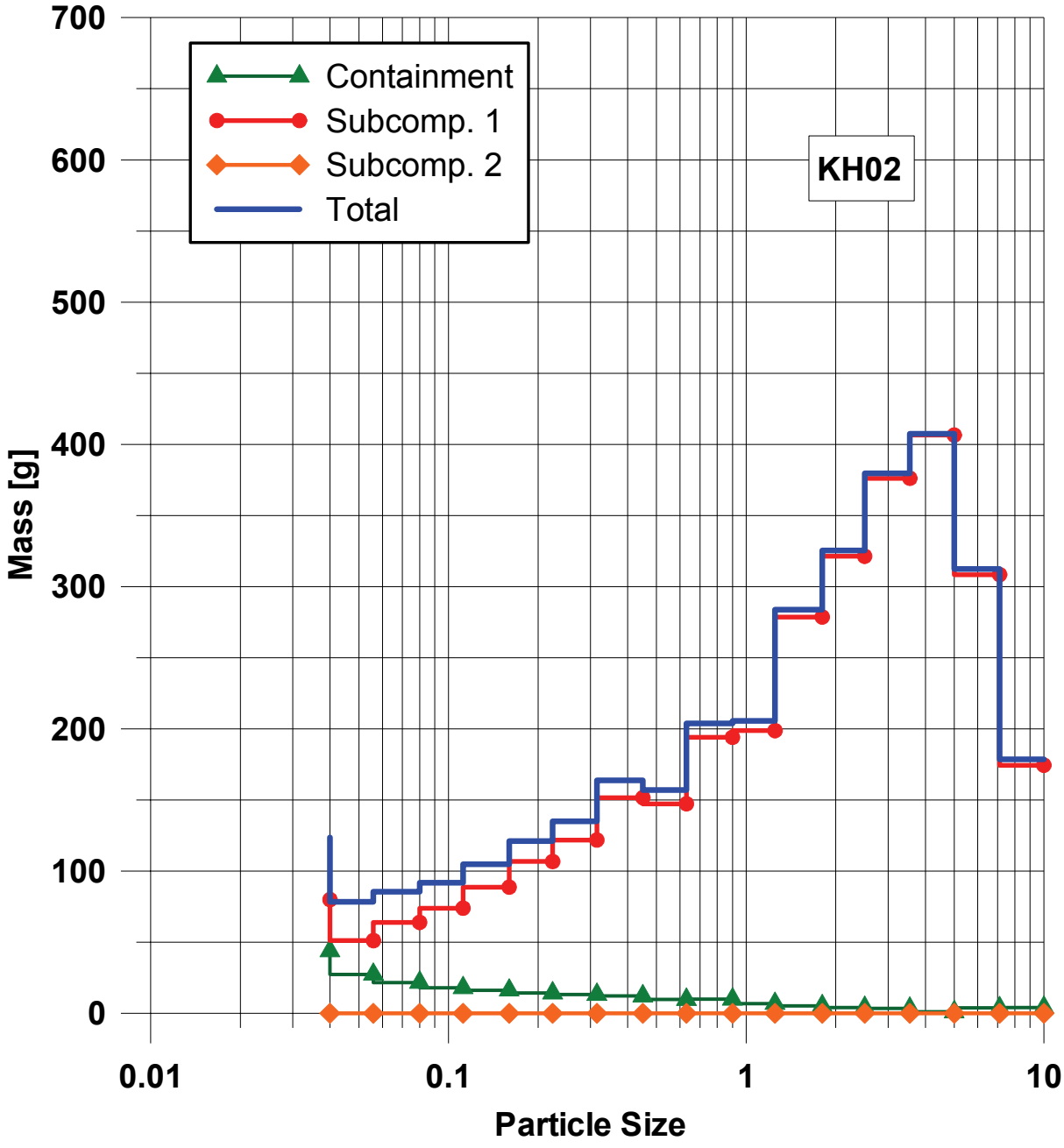

Fig. 4-73. KH02: Size distribution of particles smaller than 10 mm

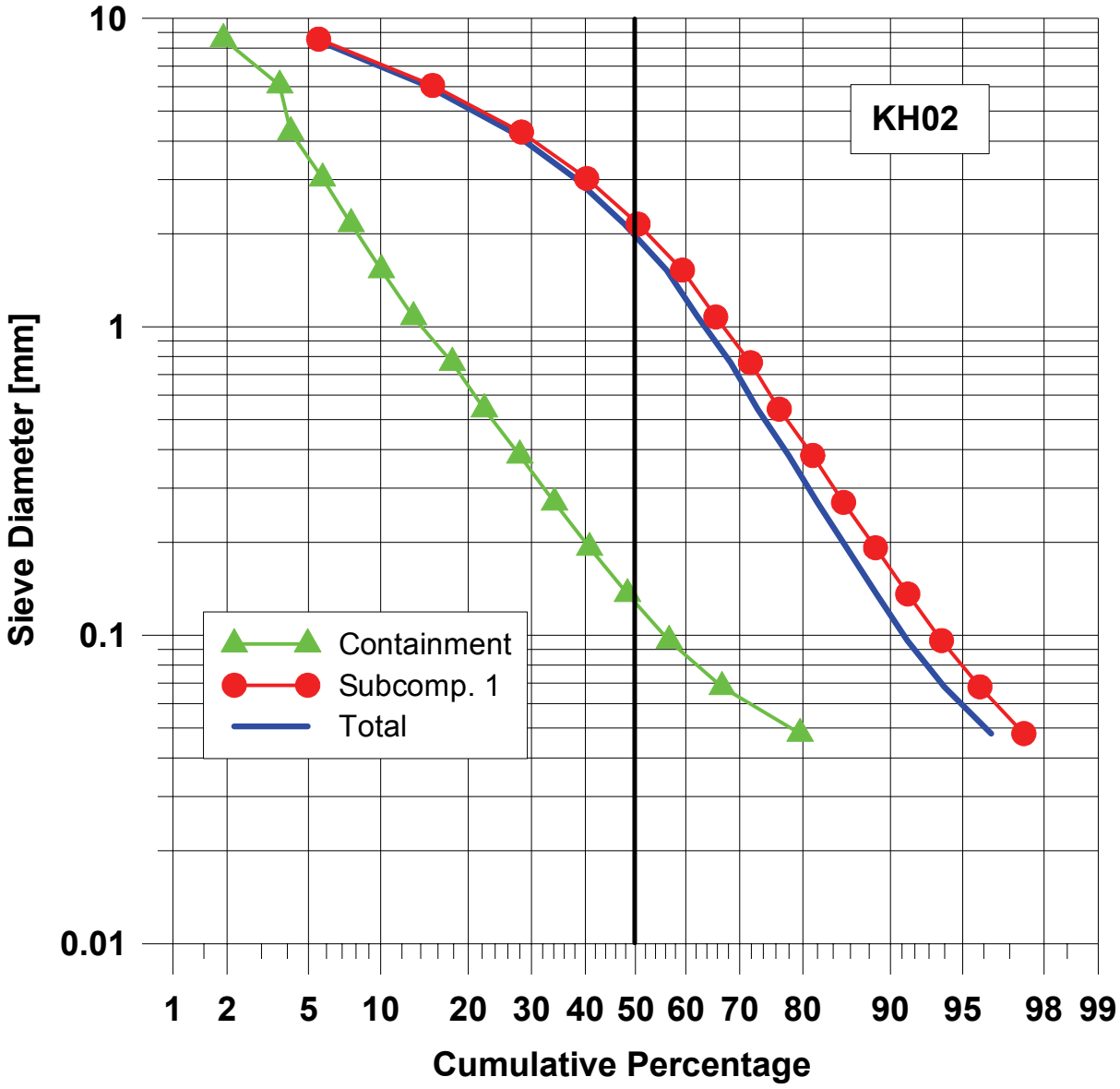

Fig. 4-74. KH02: Cumulative particle size distribution of debris smaller 10 mm

Fig. 4-75. KH02: Post test view of RPV lower head and hole

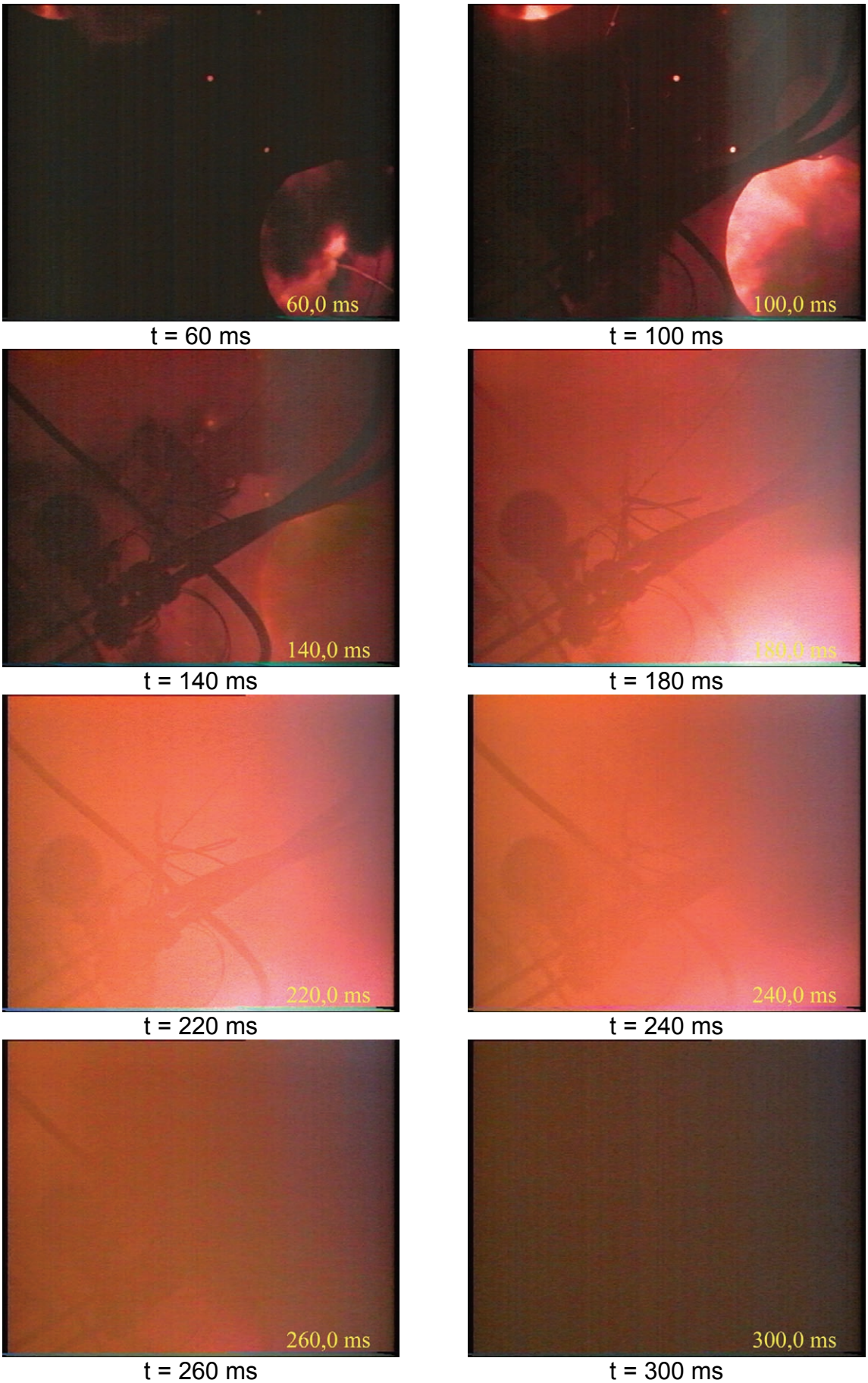

Fig. 4-76. KH02: Top down view at exit of subcompartment 1

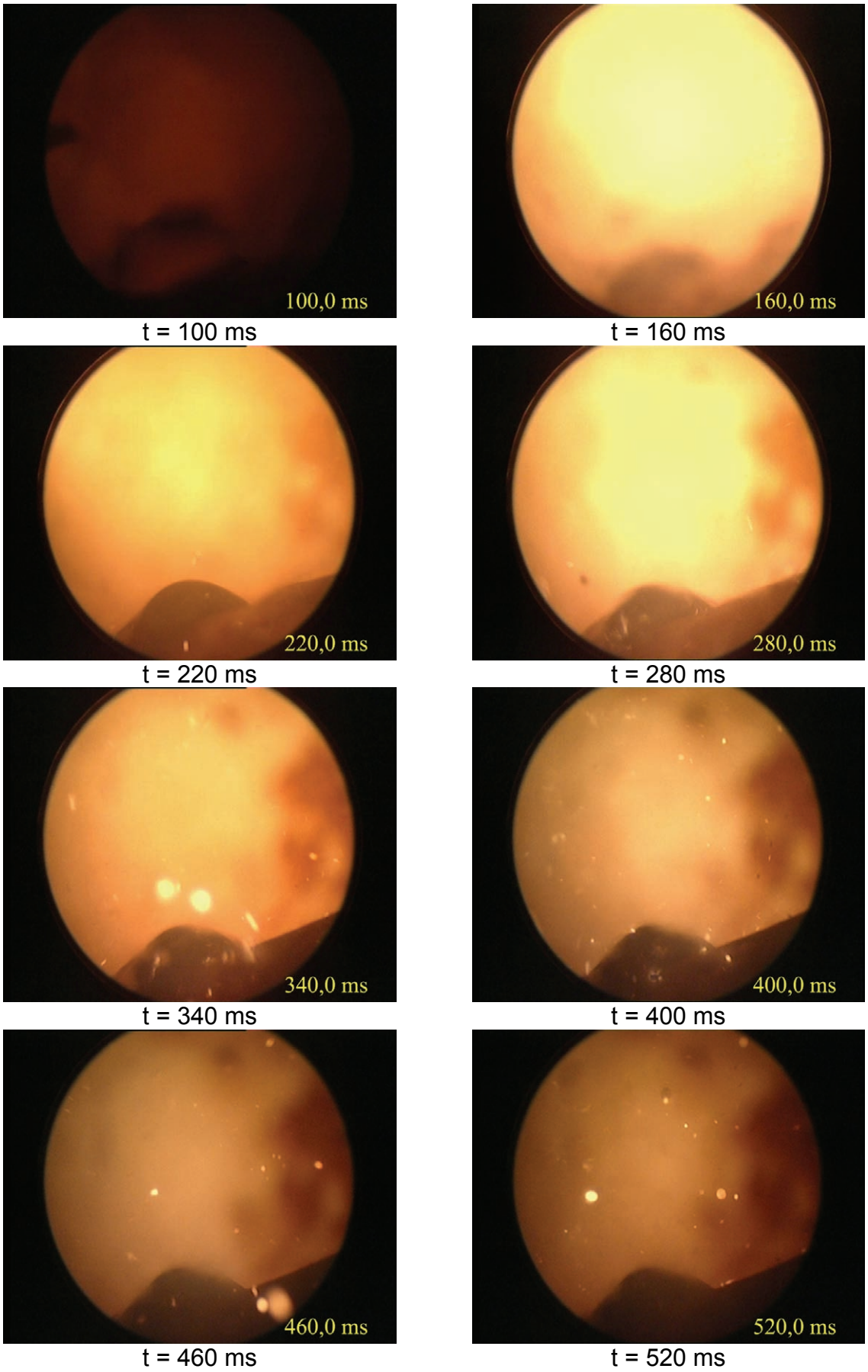

Fig. 4-77. KH02: View with endoscope into subcompartment 1

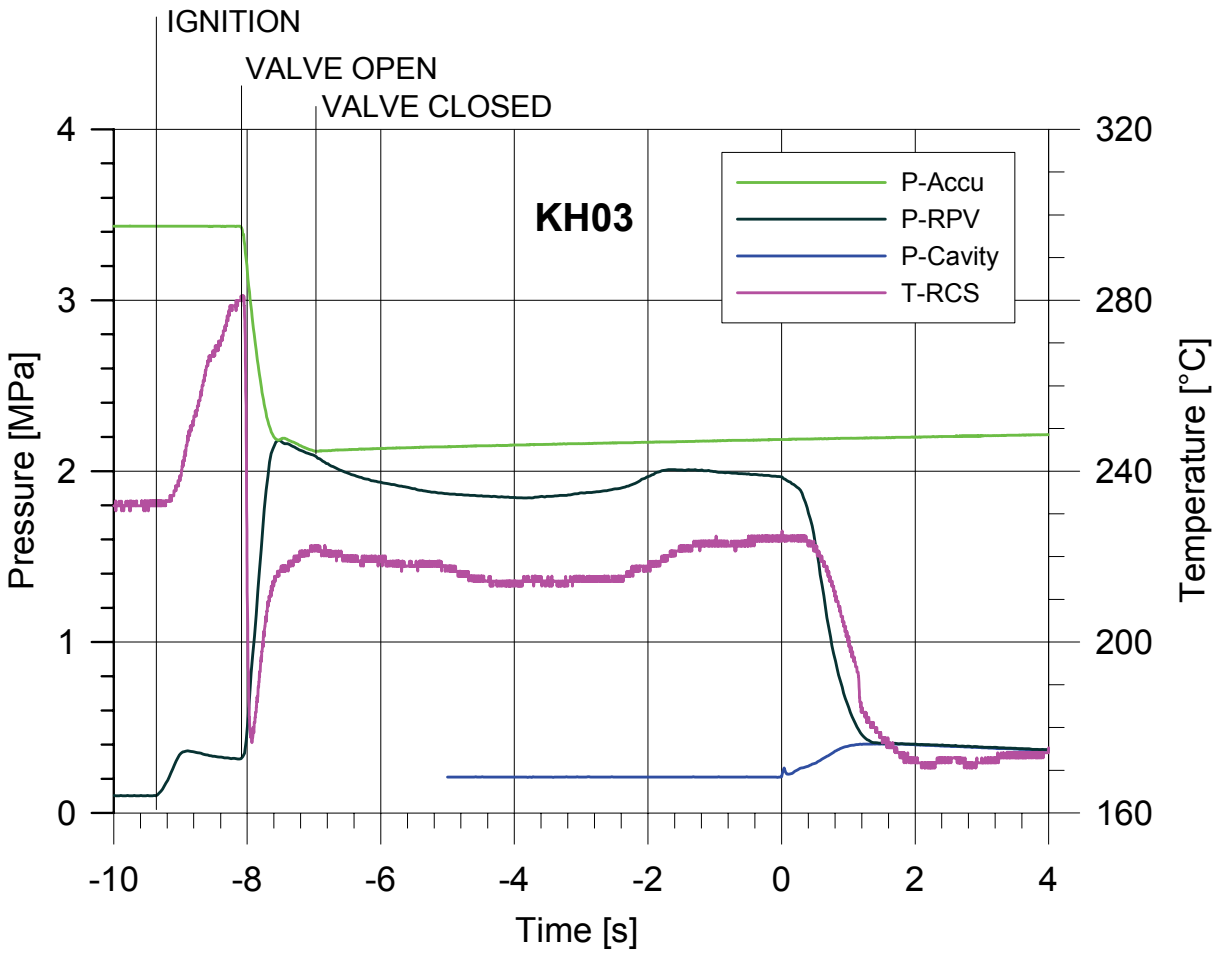

Fig. 4-78. KH03: Pressure, temperature and timing

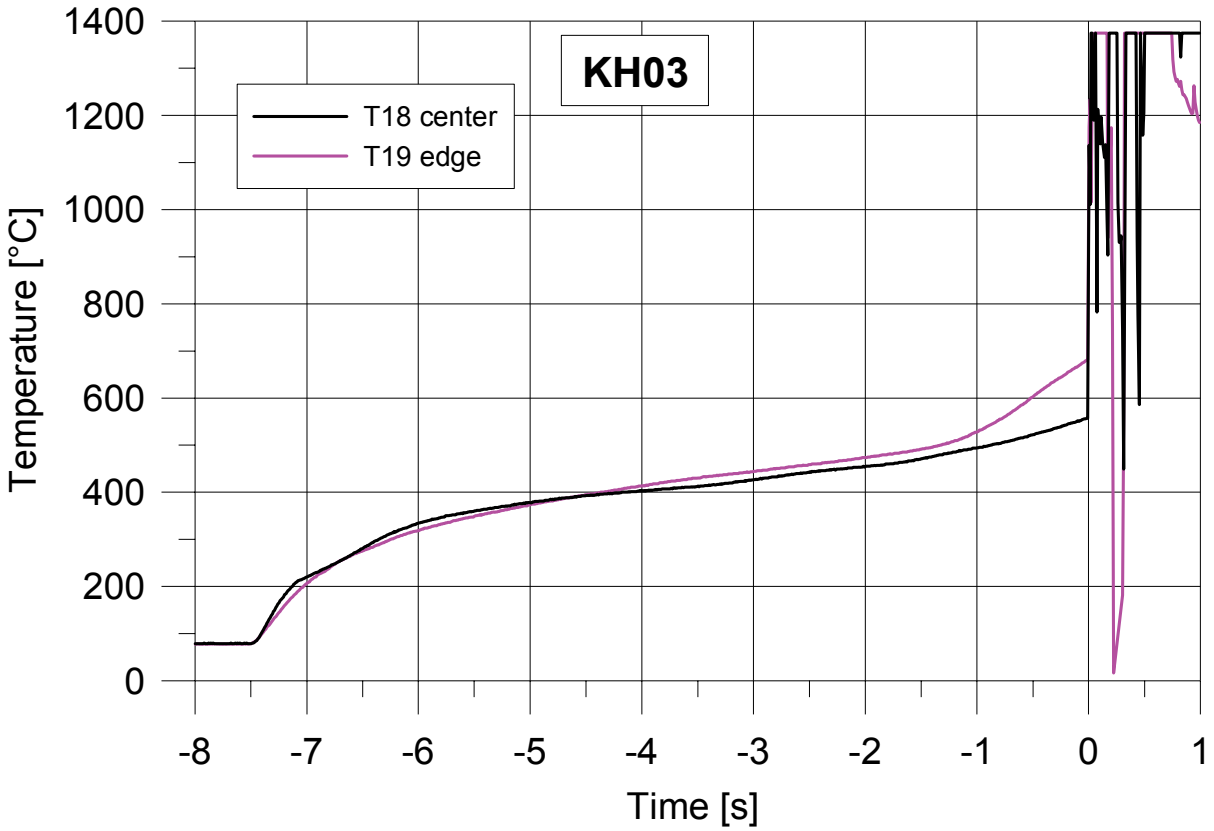

Fig. 4-79. KH03: Thermocouple signals in melt plug

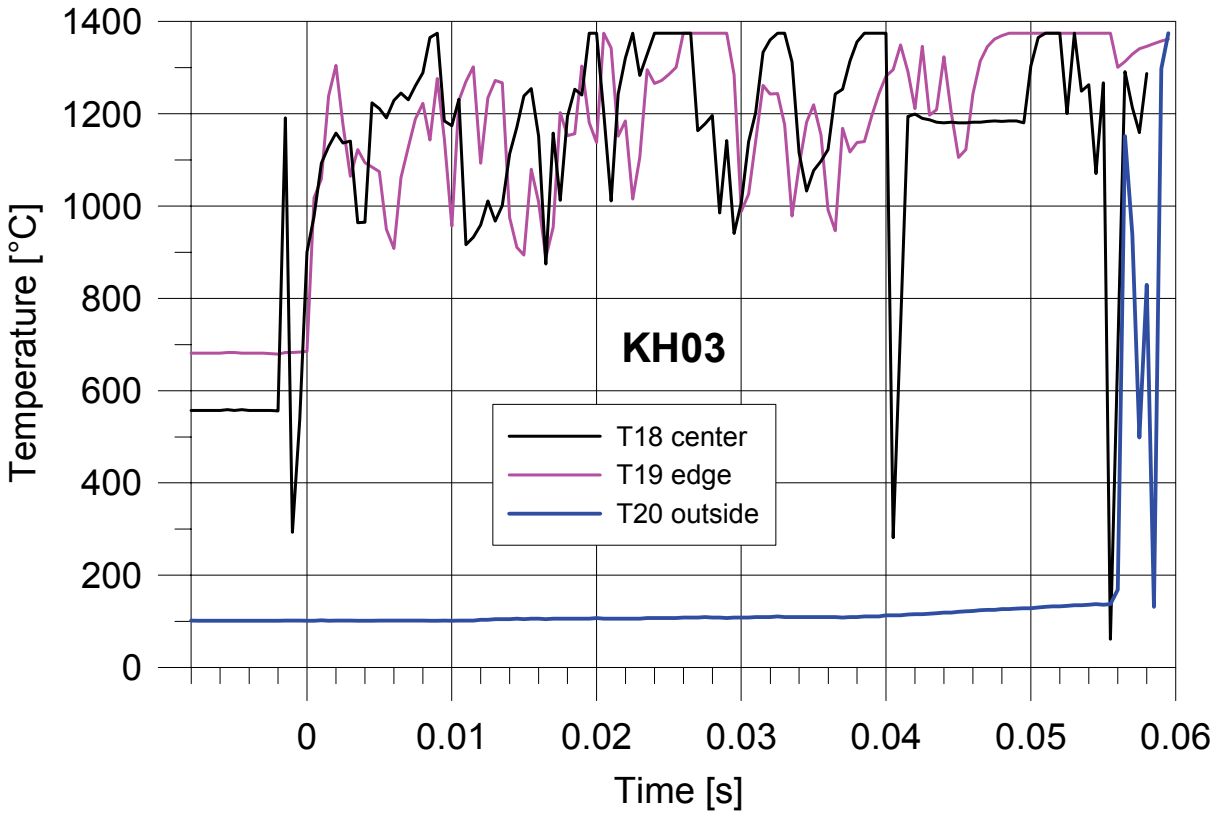

Fig. 4-80. KH03: Thermocouple signals in melt plug, zoom to t = 0 s

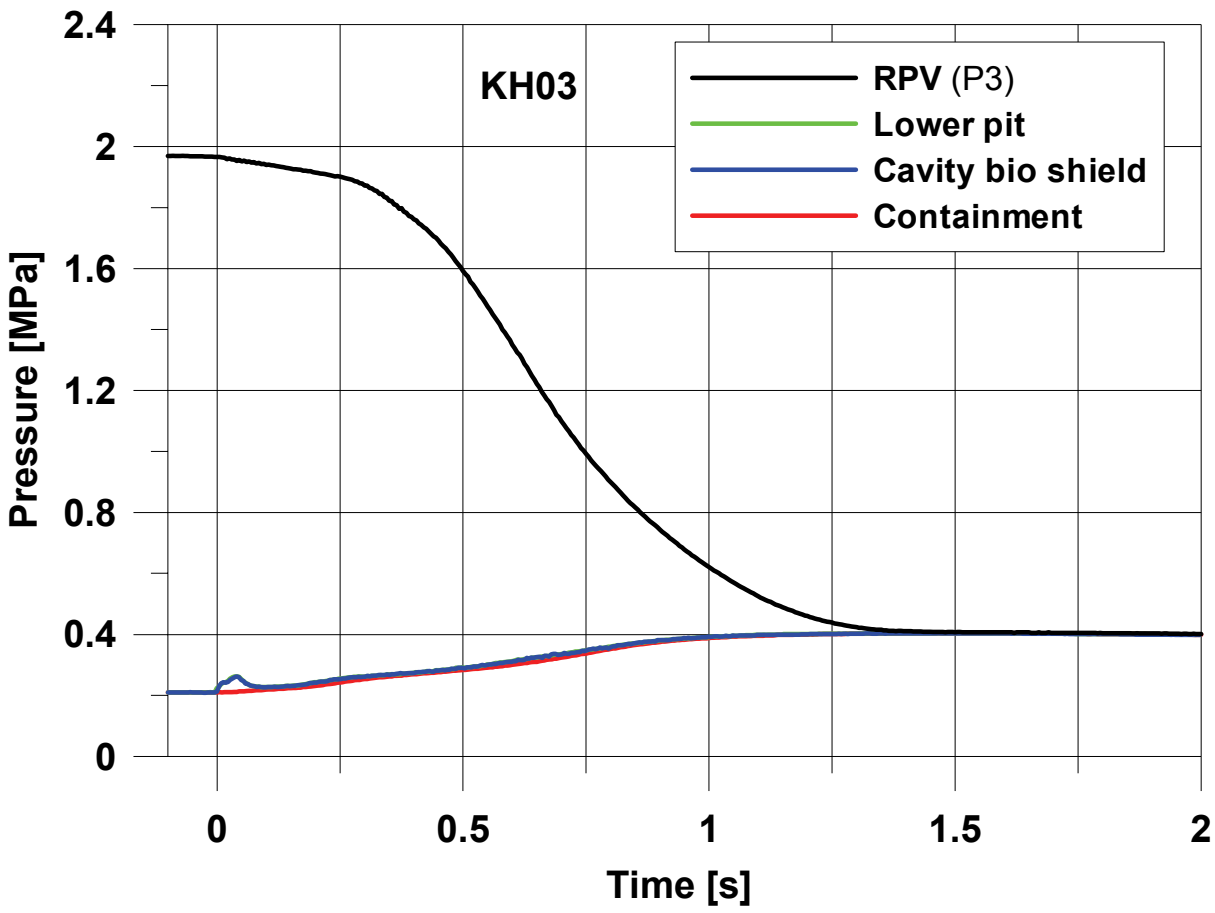

Fig. 4-81. KH03: Pressure in RPV vessel, cavity and containment

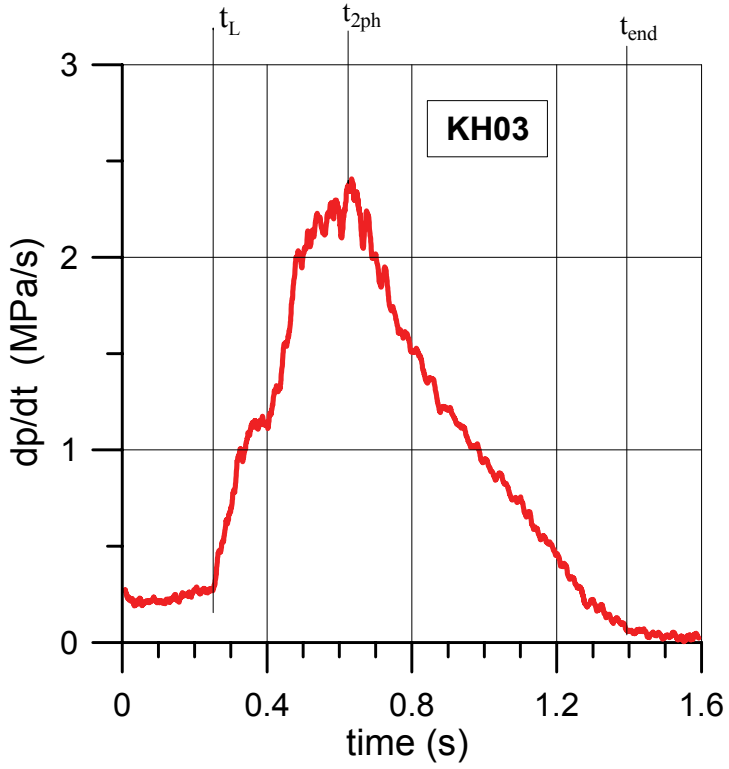

Fig. 4-82. KH03: Pressure gradient in RPV vessel

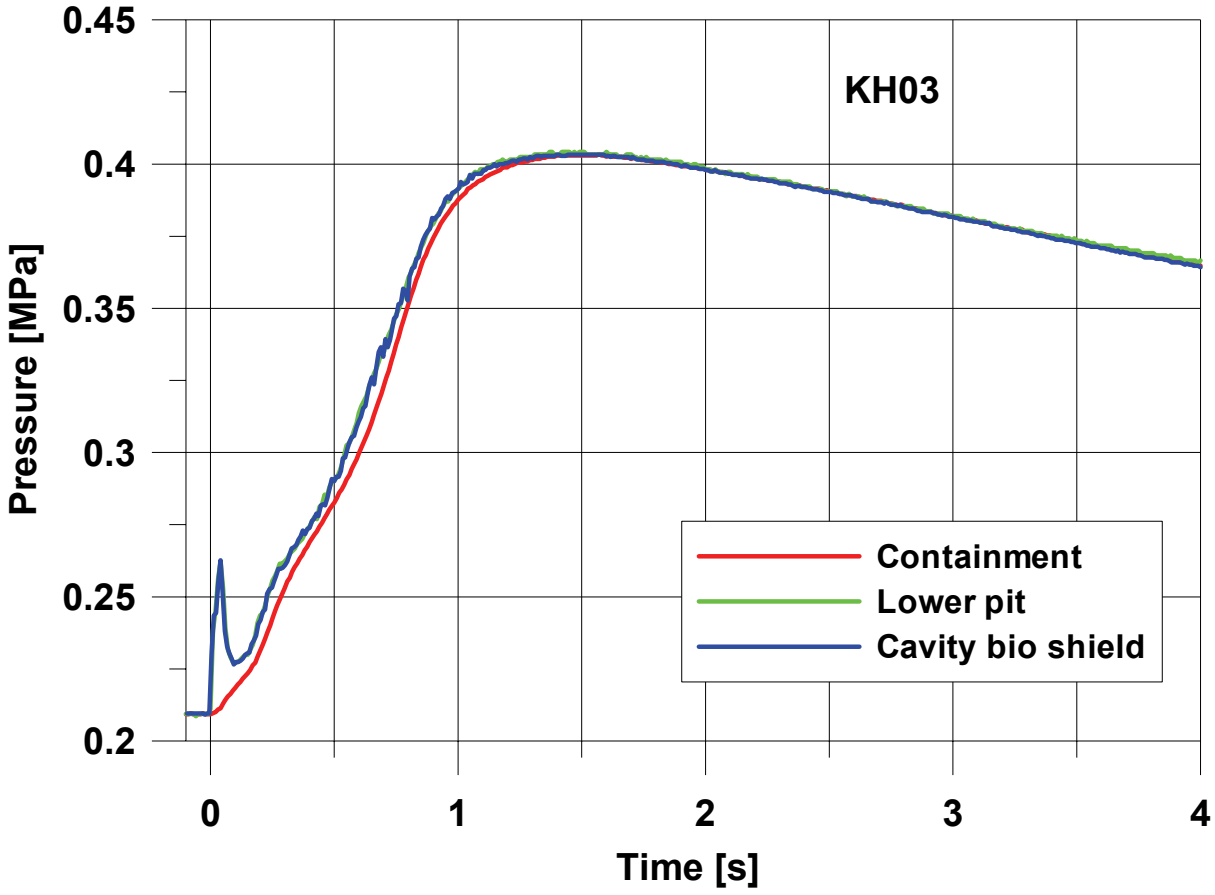

Fig. 4-83. KH03: Pressure in cavity and containment

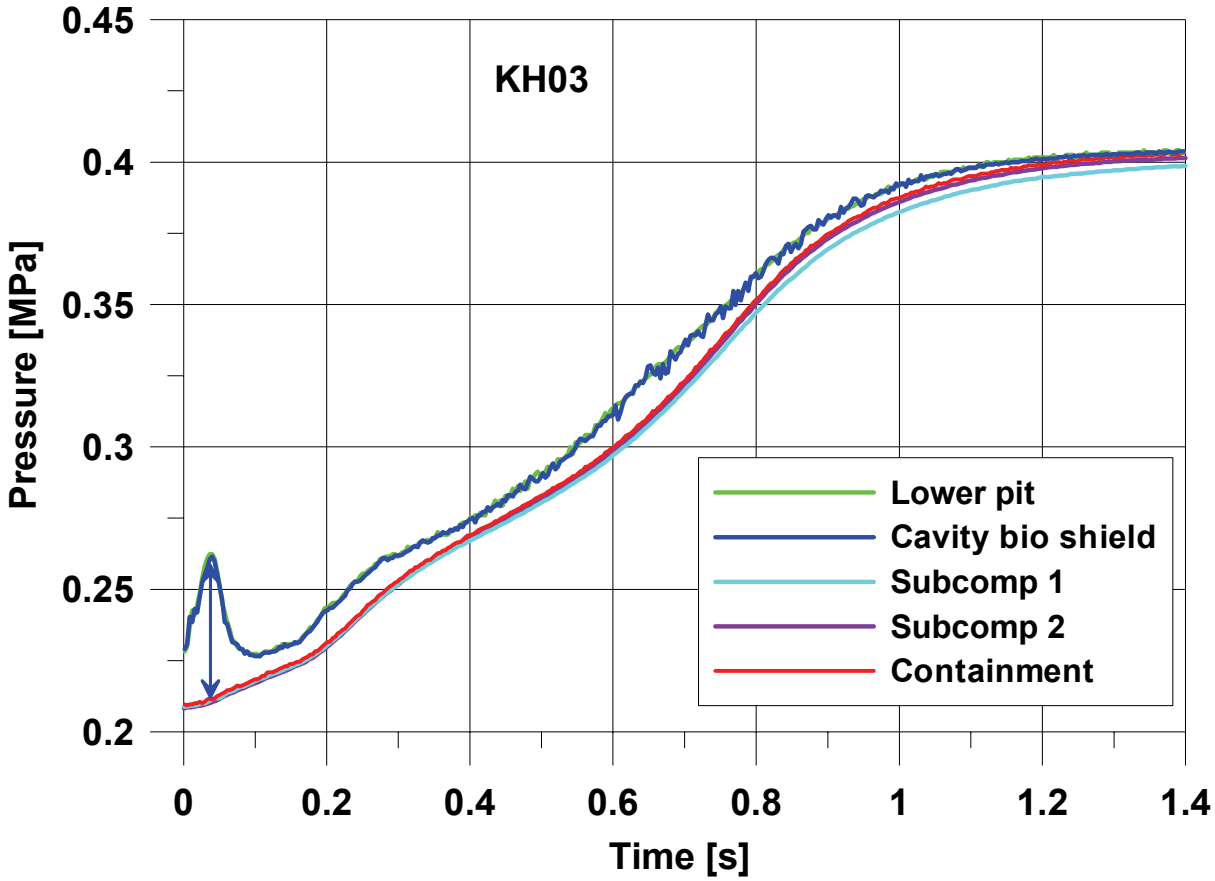

Fig. 4-84. KH03: Pressure in cavity, subcompartment and containment
↔ $\Delta p_{max,\ pit\text{-}cont}$ = 0,52 bar

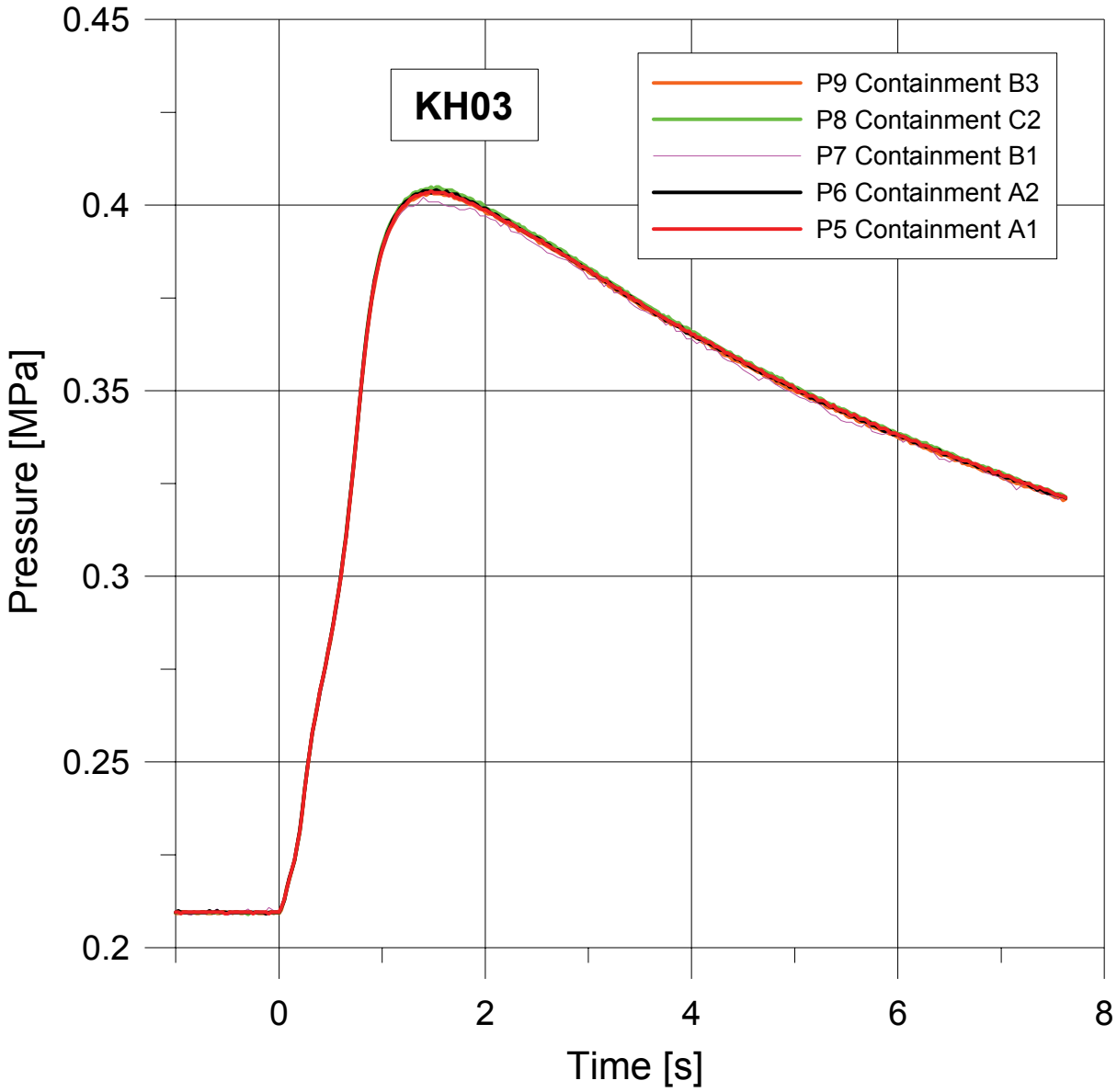

Fig. 4-85. KH03: Pressure in containment

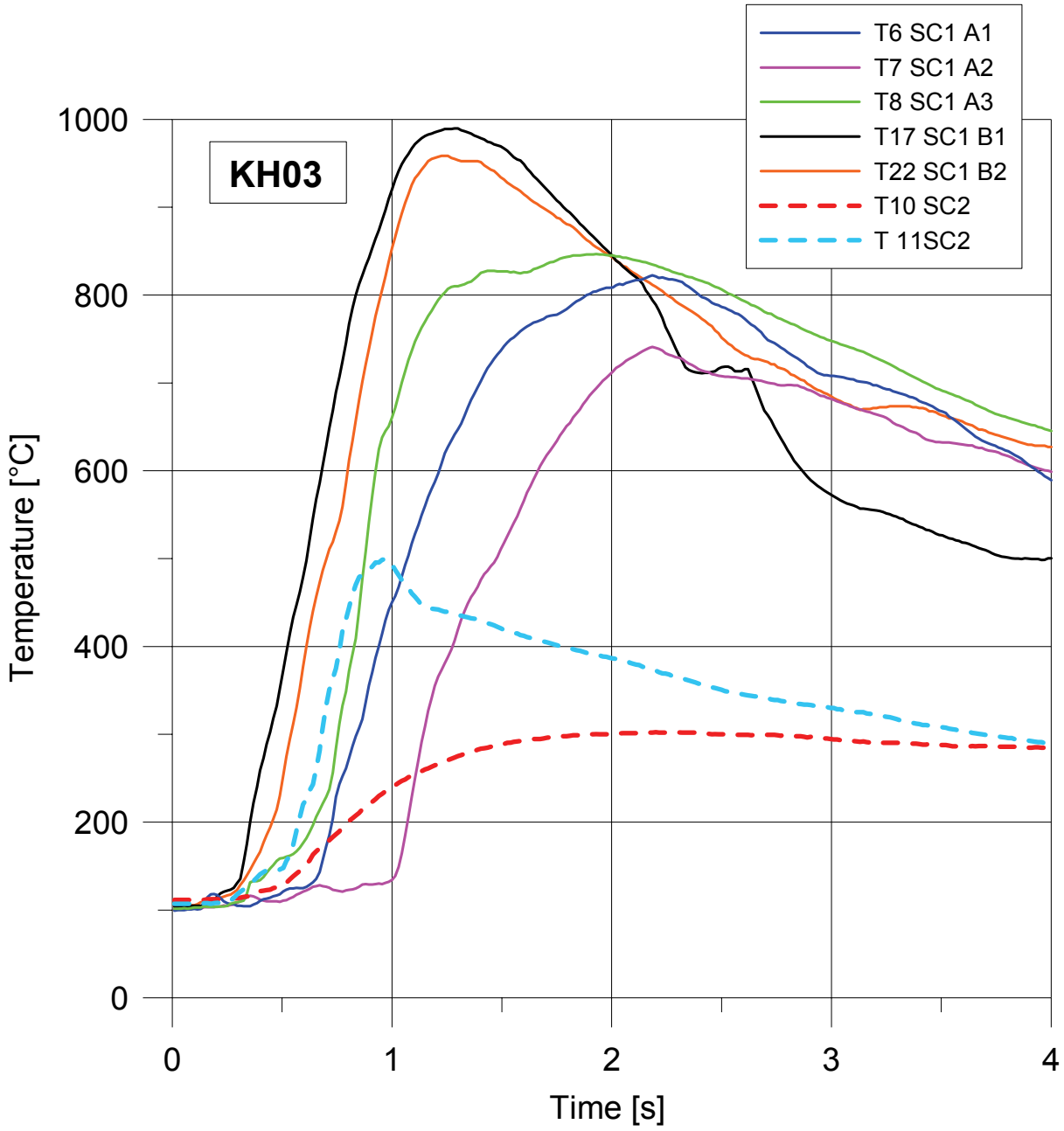

Fig. 4-86. KH03: Temperatures in subcompartments 1 and 2

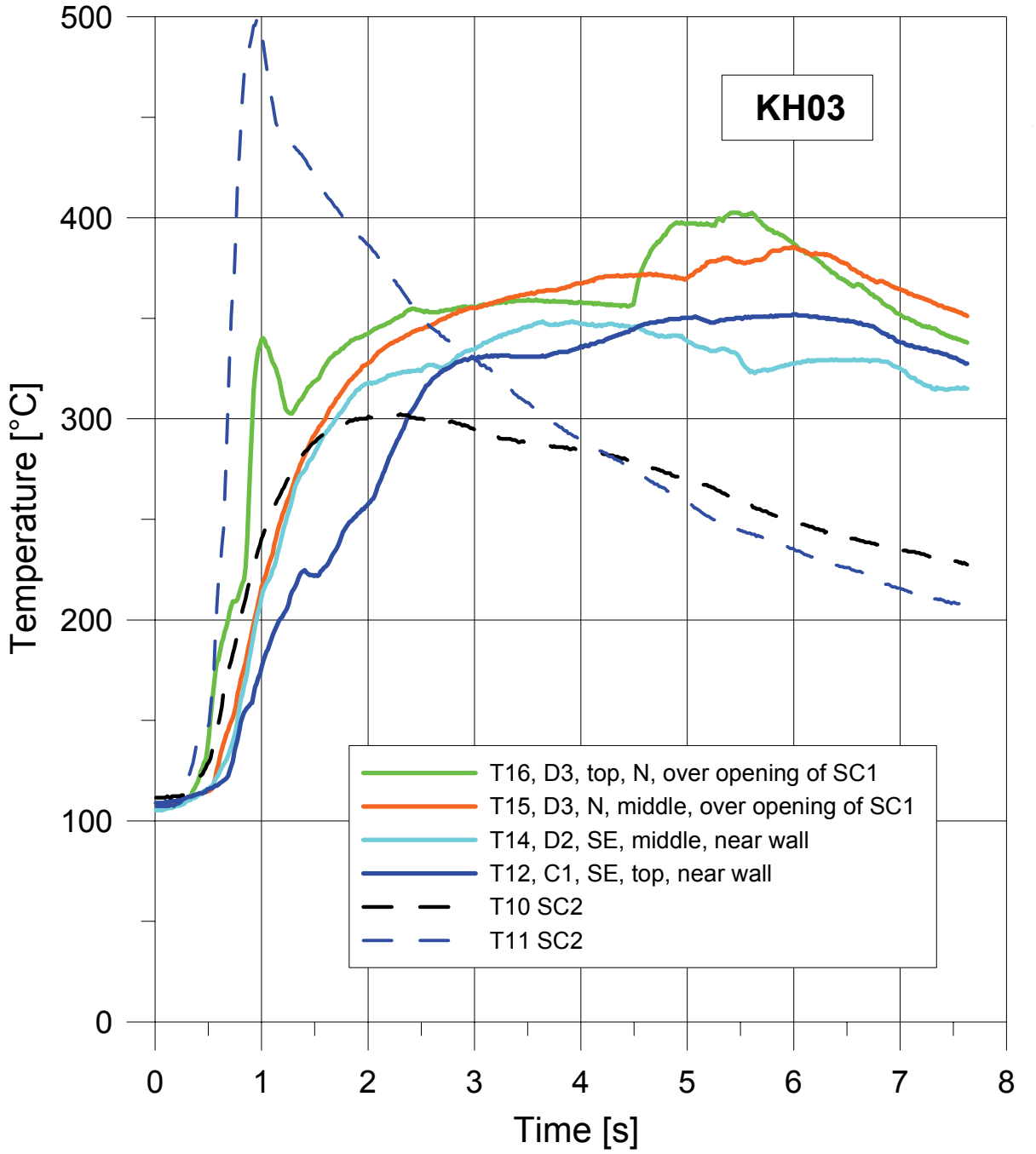

Fig. 4-87. KH03: Temperatures in containment

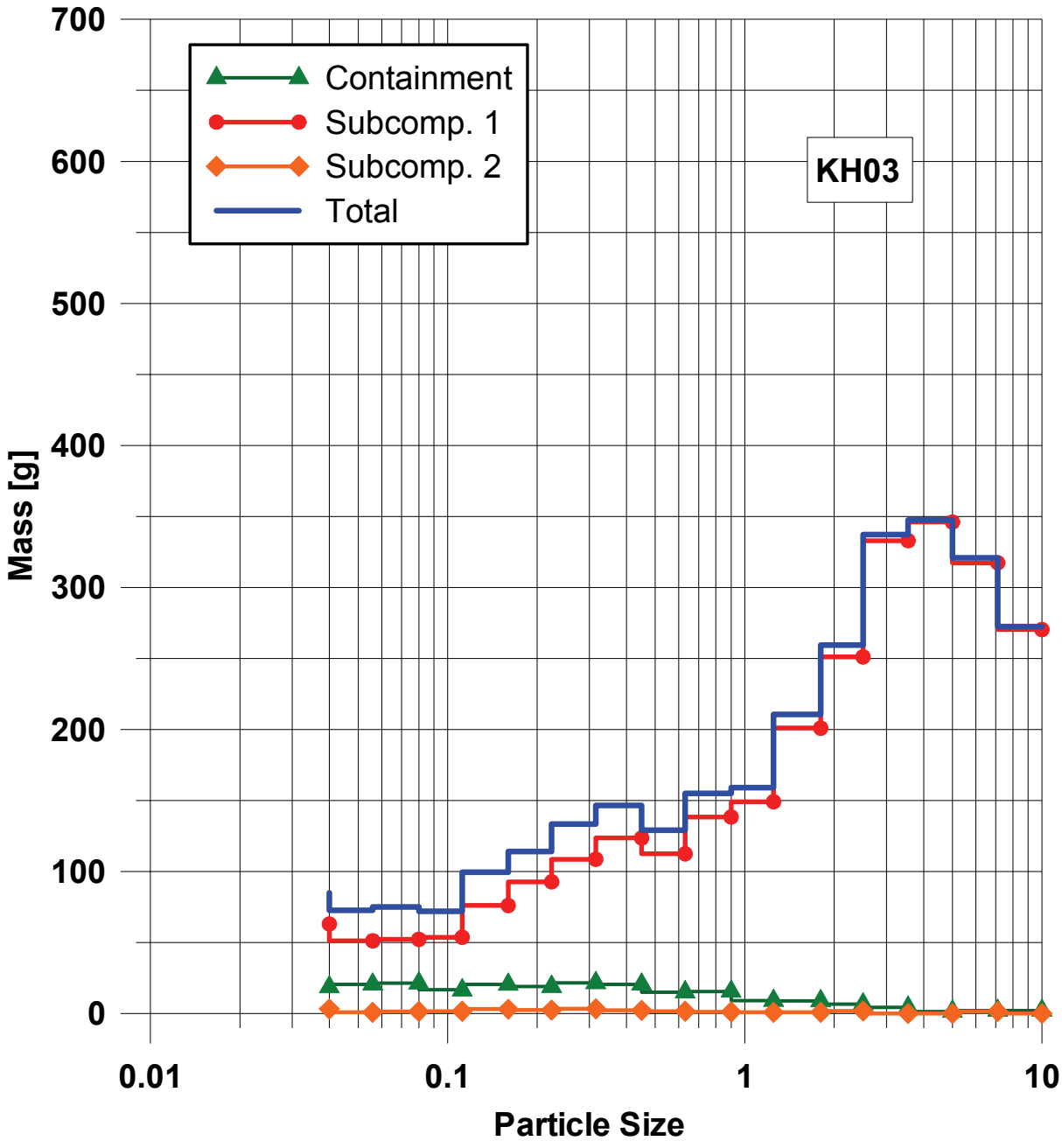

Fig. 4-88. KH03: Size distribution of particles smaller than 10 mm

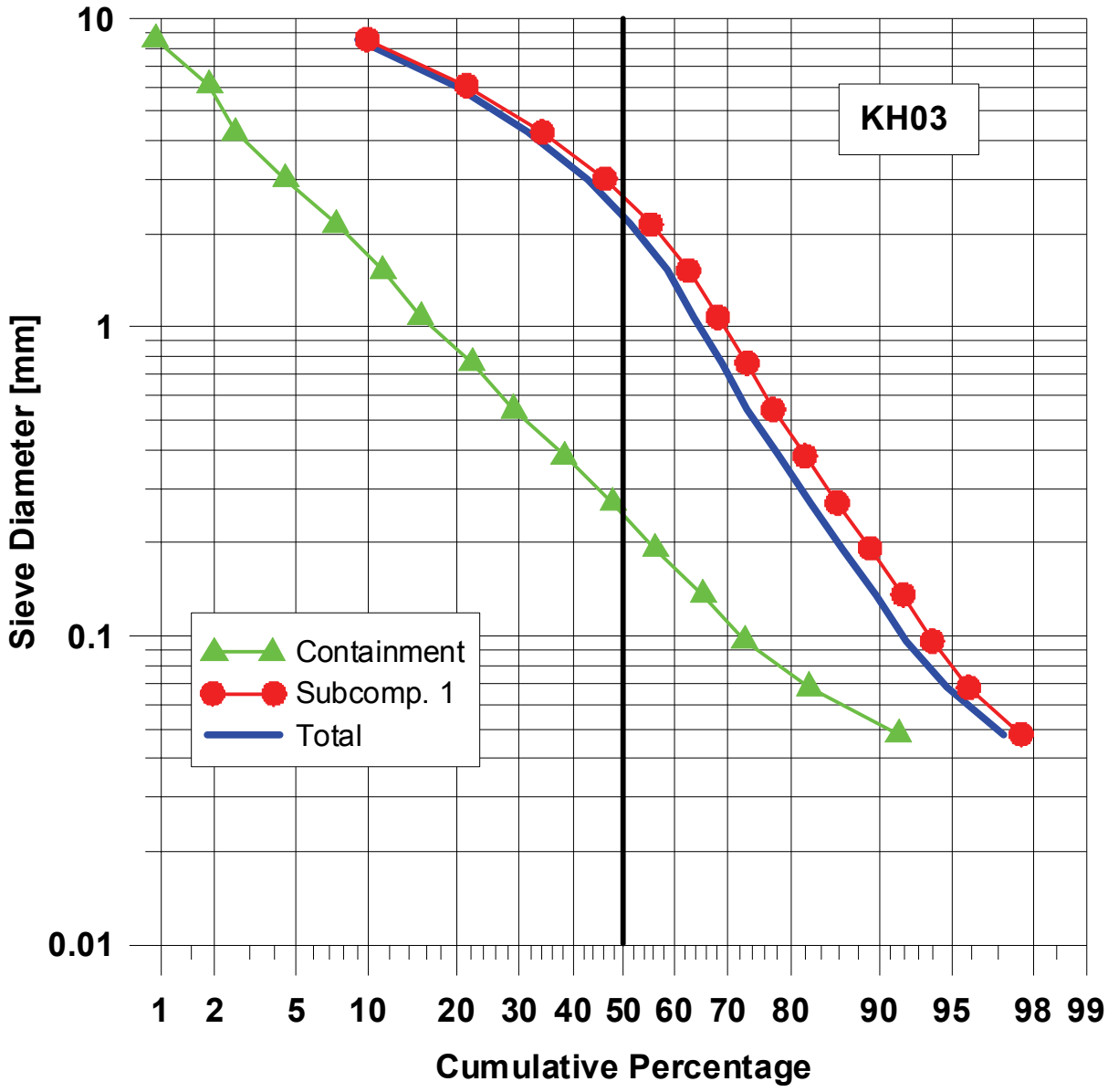

Fig. 4-89. KH03: Cumulative particle size distribution of debris smaller 10 mm

Fig. 4-90. KH03: Post test view of cavity

Fig. 4-91. KH03: View at closed pit exit into subcompartment 2

Fig. 4-92. KH03: Post test view of RPV lower head and hole

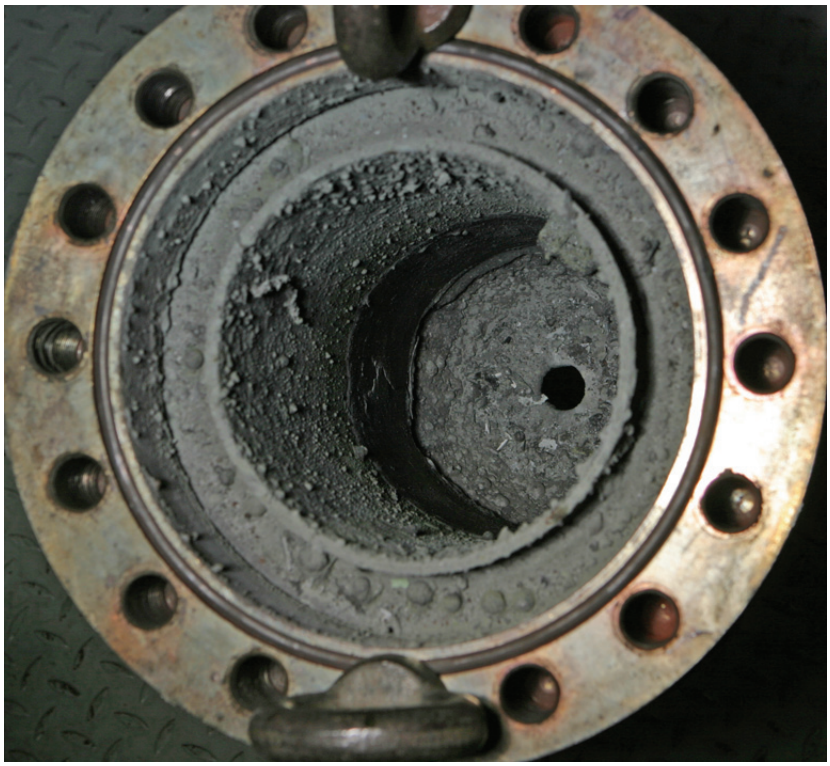

Fig. 4-93. KH03: Post test view into RPV (crucible)

Fig. 4-94. KH03: Post test view into containment

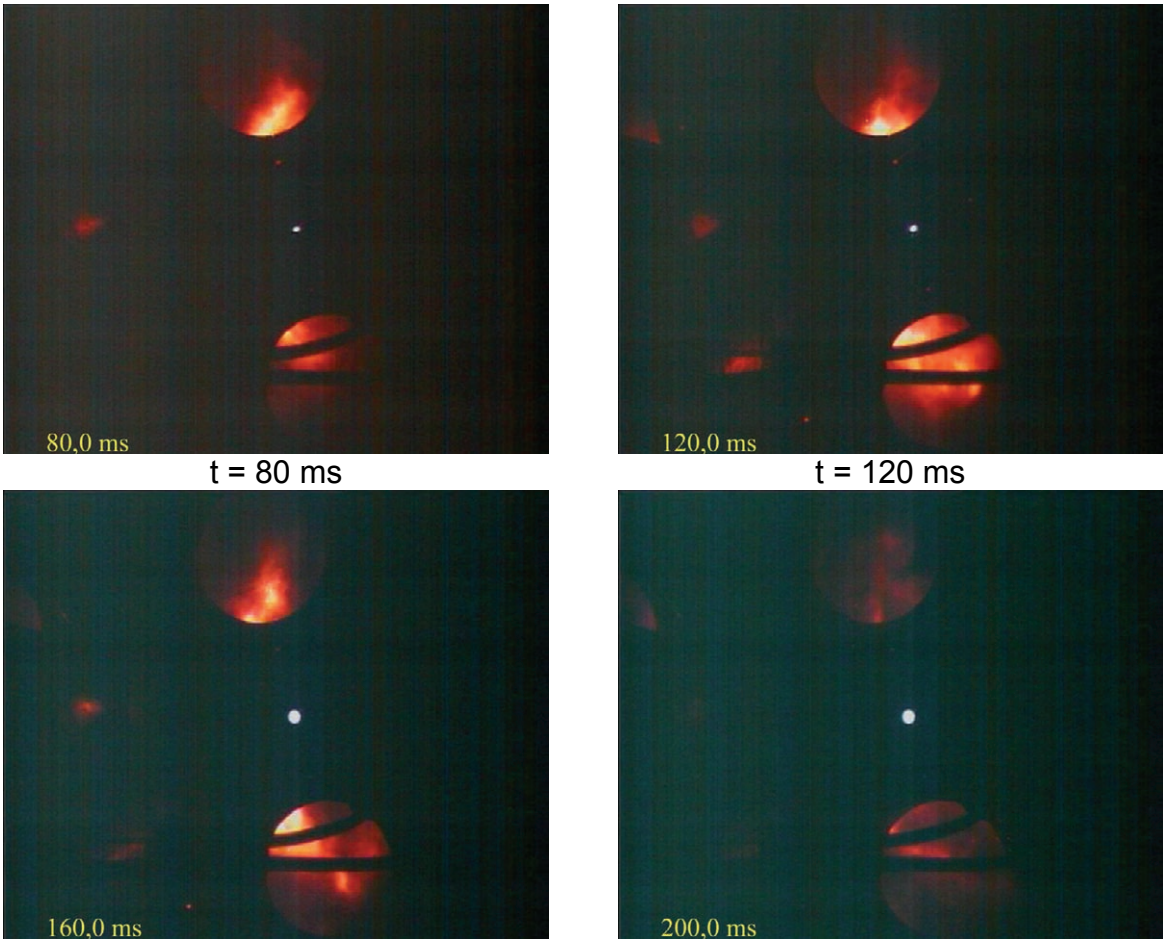

Fig. 4-95. KH03: Top down view at exit of subcompartment 1

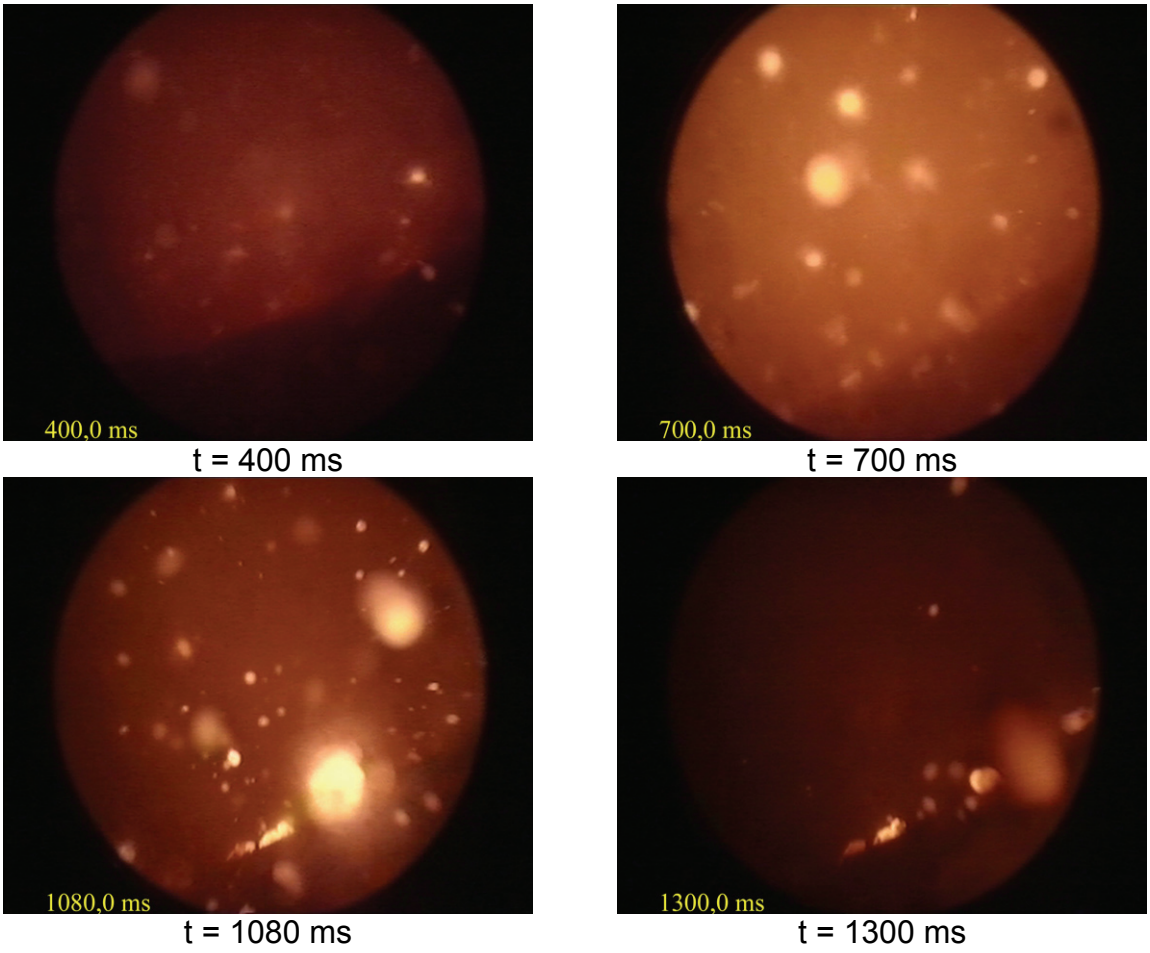

Fig. 4-96. KH03: View into subcompartment 1

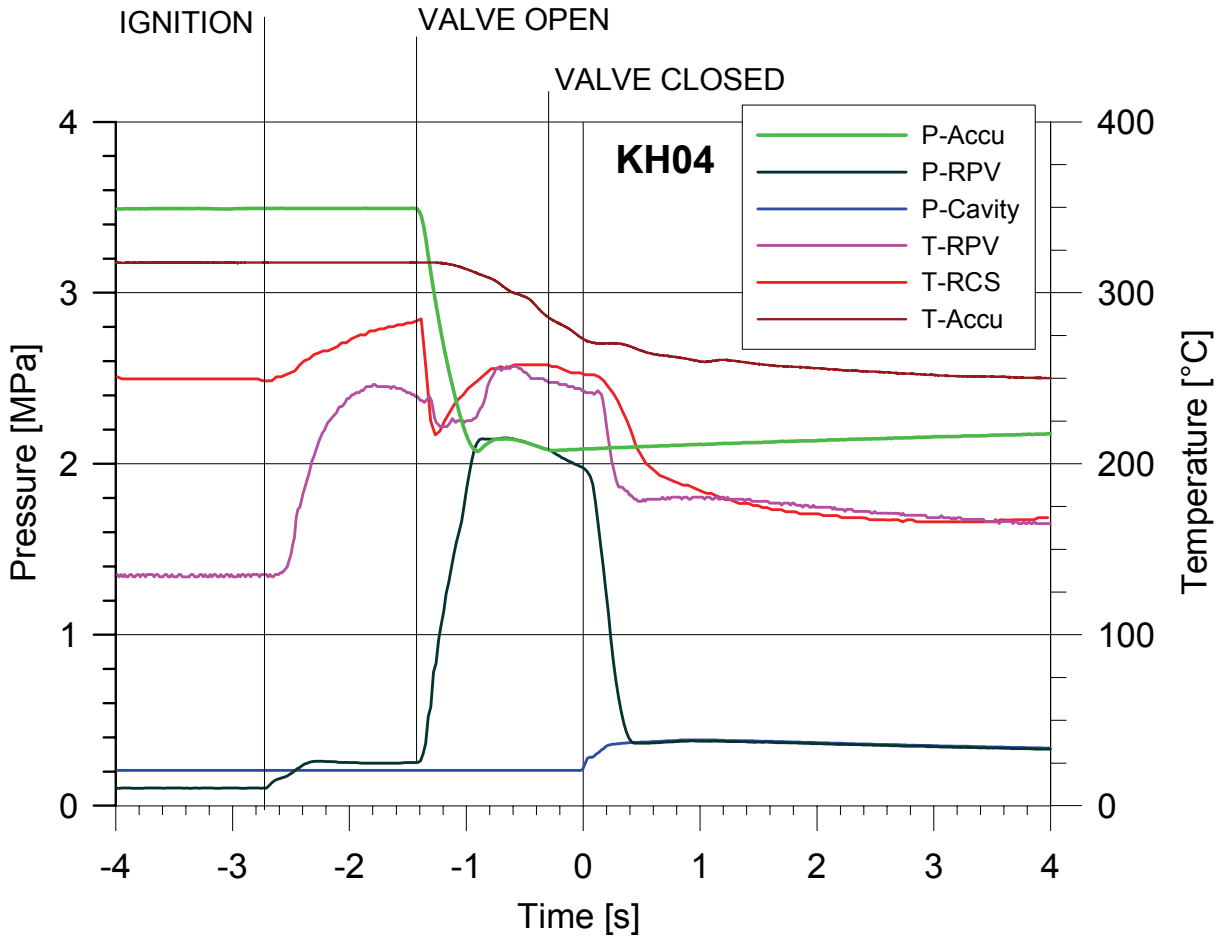

Fig. 4-97. KH04: Pressure, temperature and timing

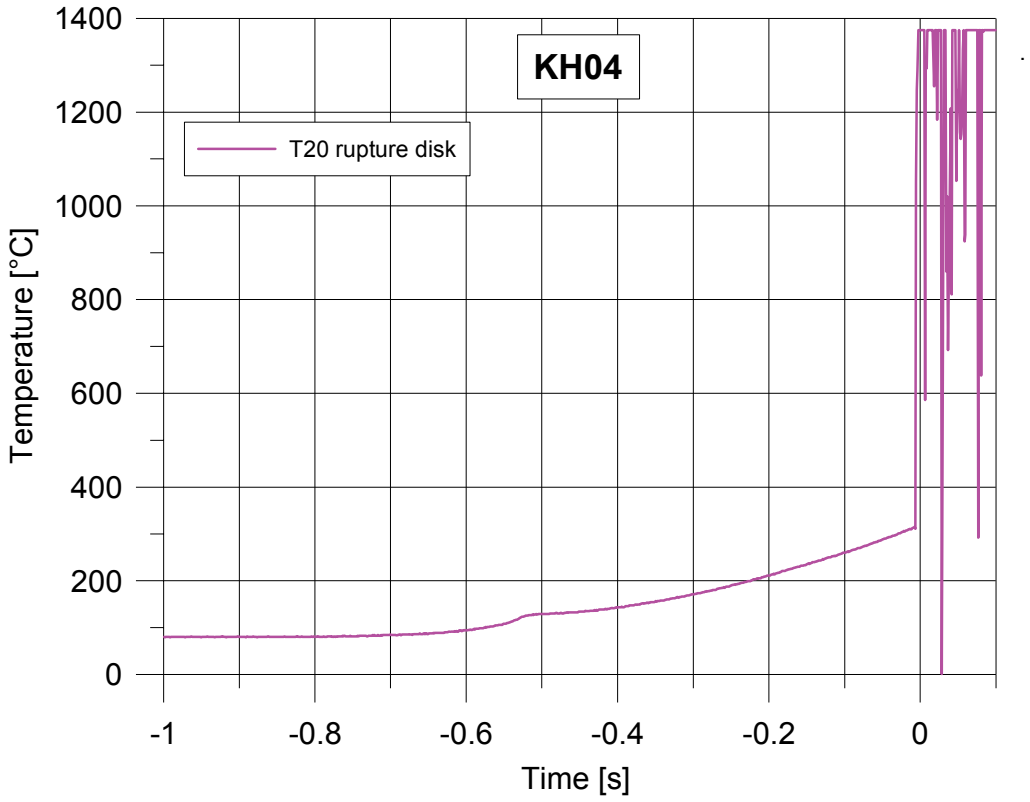

Fig. 4-98. KH04: Thermocouple signals in melt plug

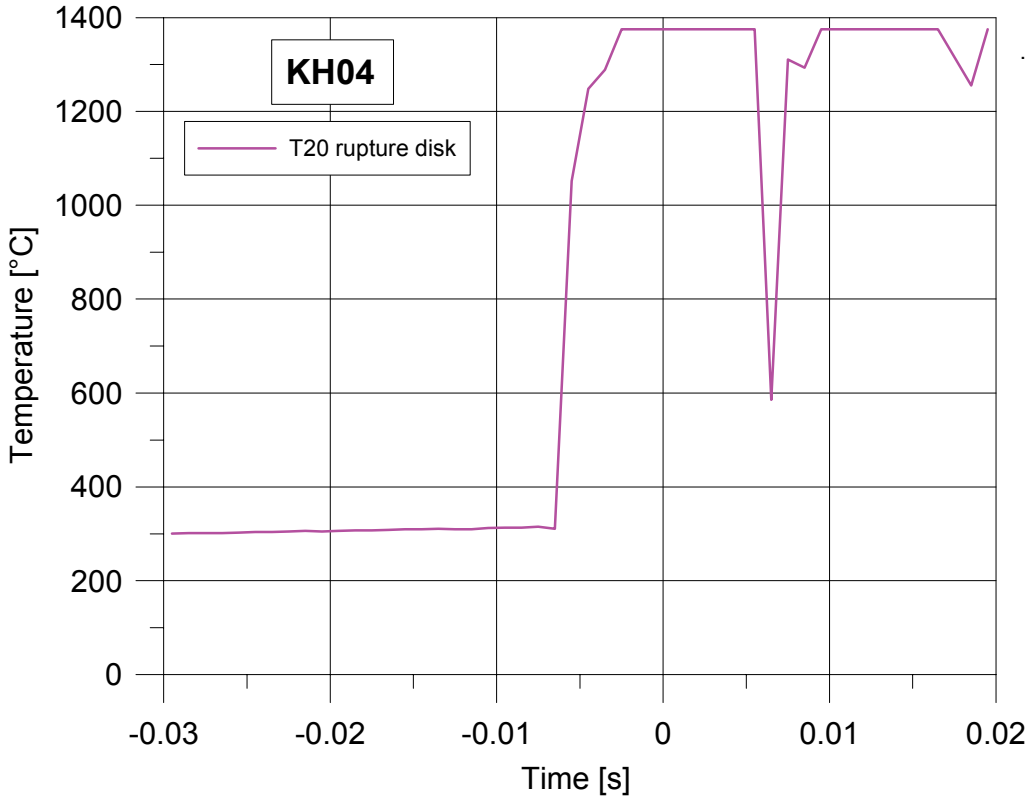

Fig. 4-99. KH04: Thermocouple signals in melt plug, zoom to t = 0 s

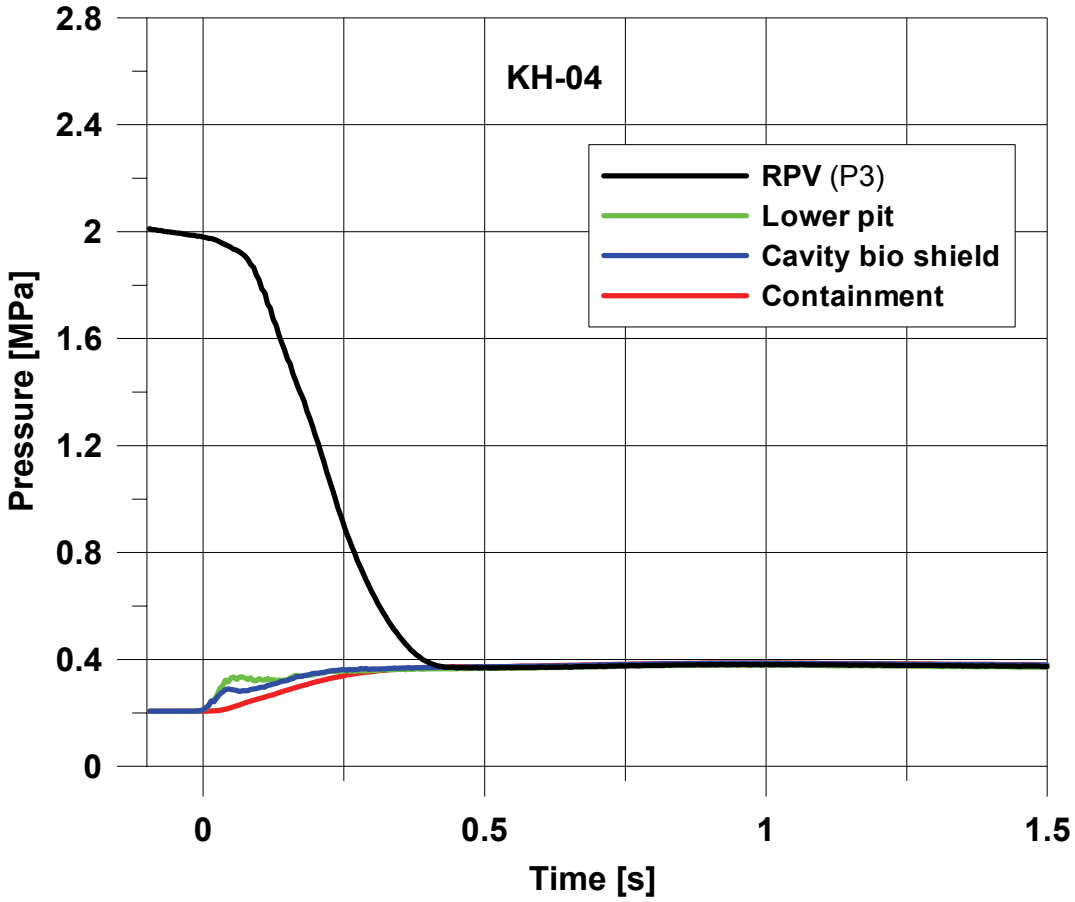

Fig. 4-100. KH04: Pressure in RPV vessel, cavity and containment

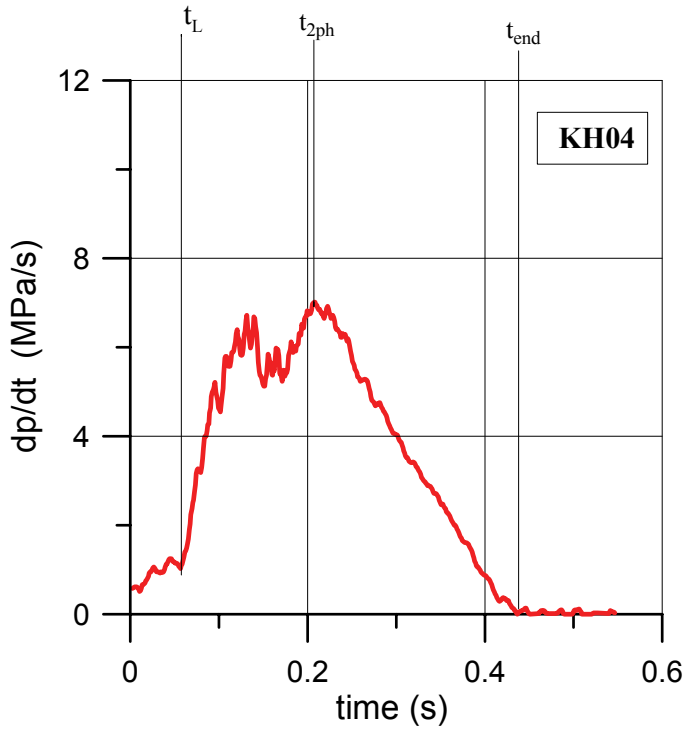

Fig. 4-101. KH04: Pressure gradient in RPV vessel

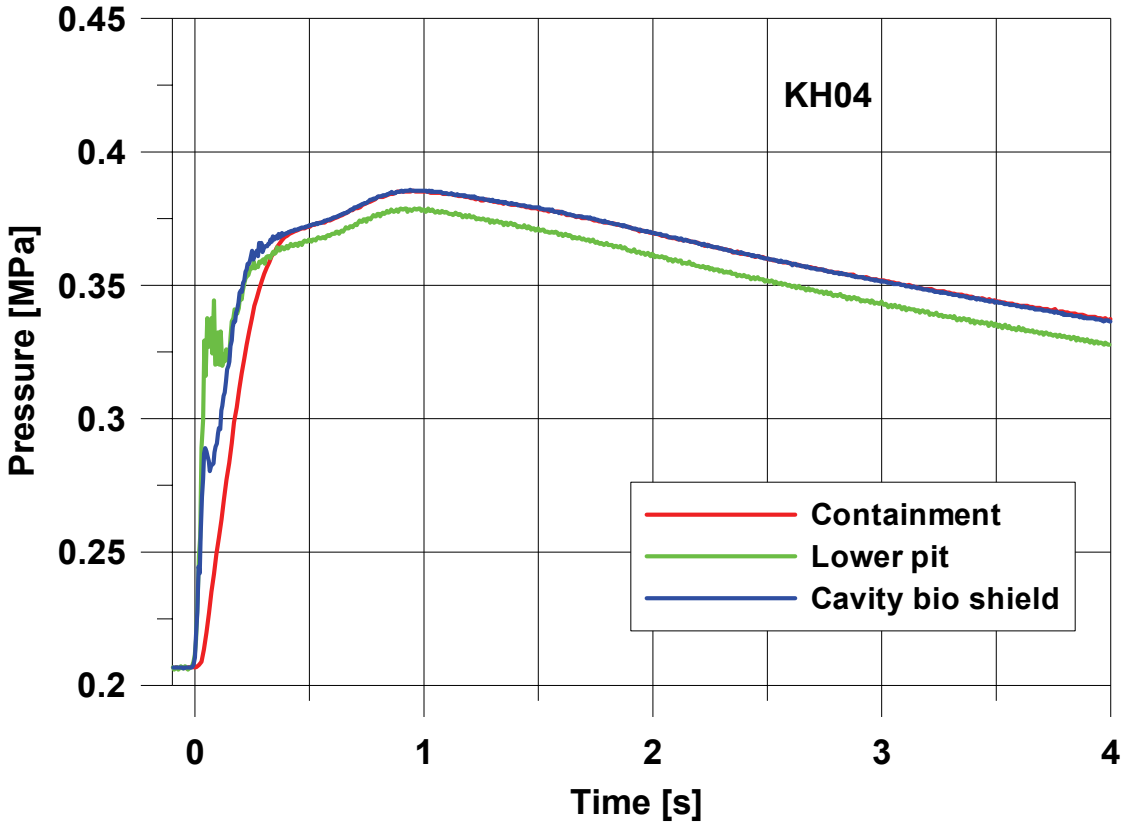

Fig. 4-102. KH04: Pressure in cavity and containment

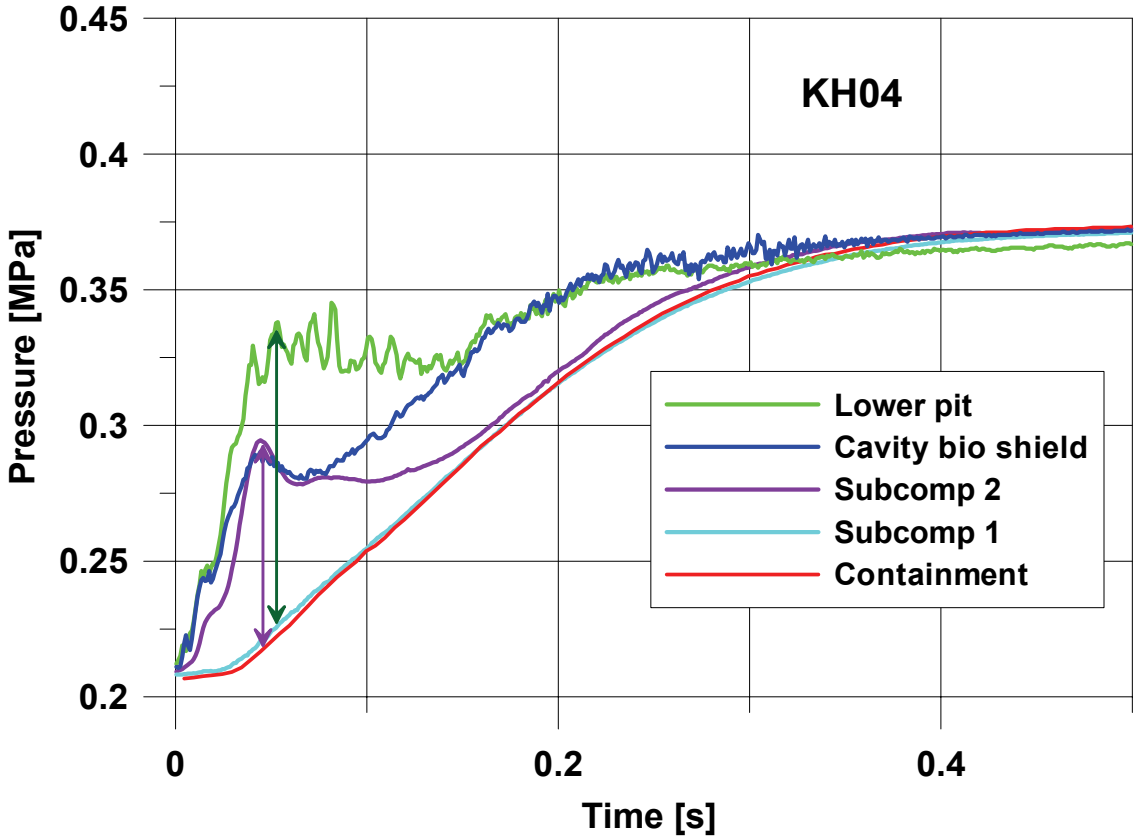

Fig. 4-103. KH04: Pressure in cavity, subcompartment and containment

Δp_{max} : $\leftrightarrow \Delta p_{pit\text{-}cont}$ = 0,11 MPa, $\leftrightarrow \Delta p_{SC2\text{-}cont}$ = 0,075 MPa

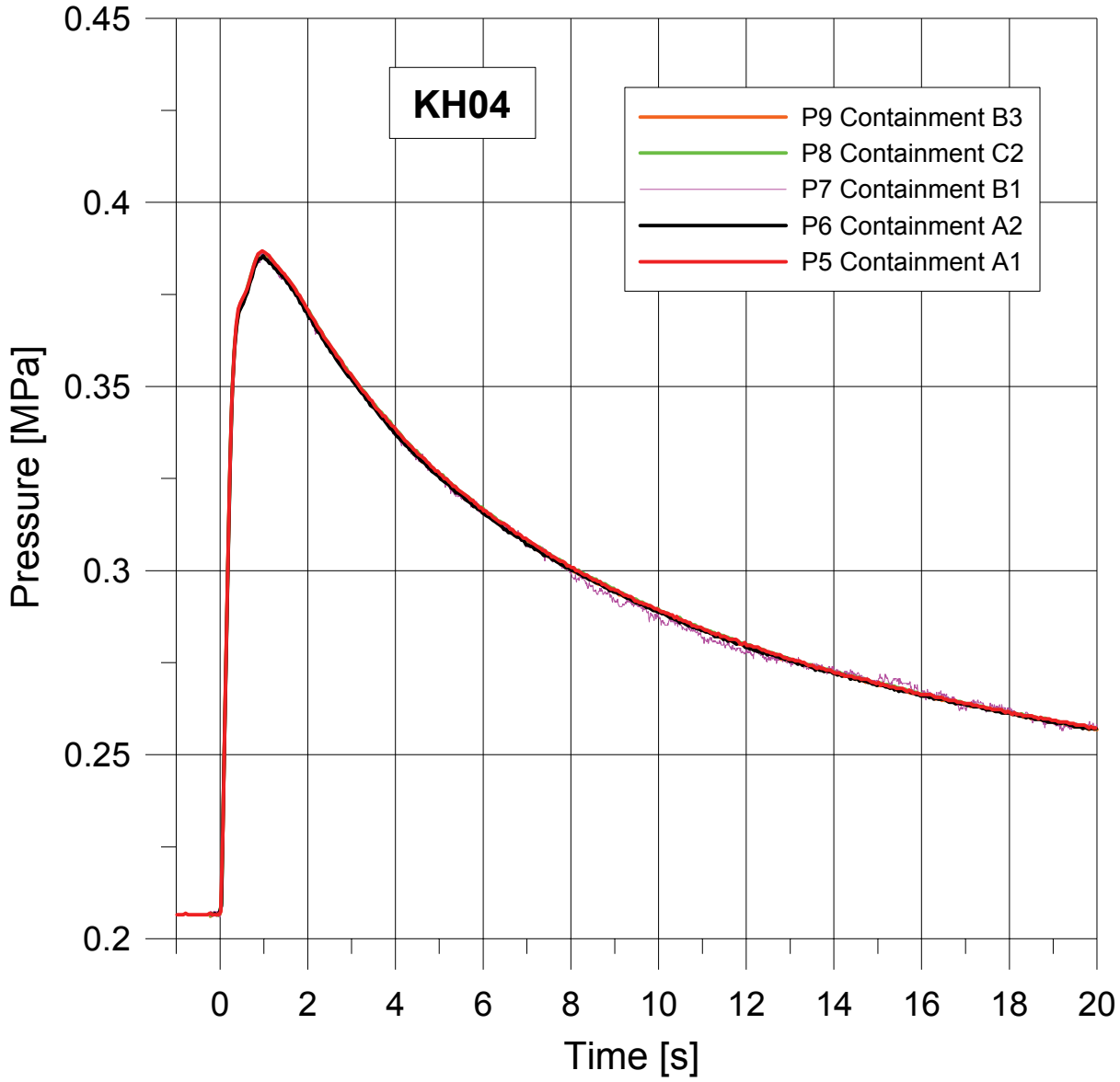

Fig. 4-104. KH04: Pressure in containment

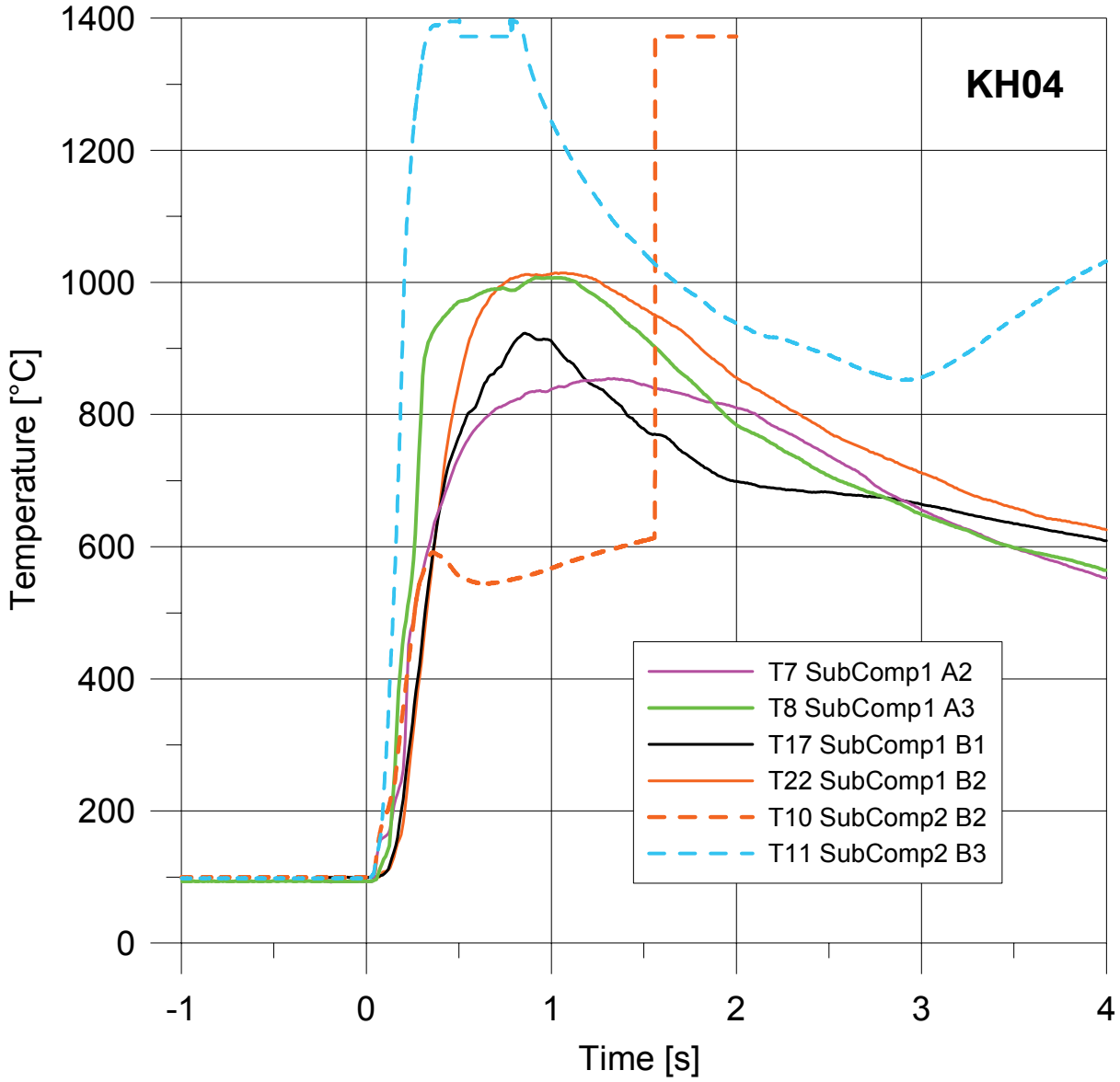

Fig. 4-105. KH04: Temperatures in subcompartments 1 and 2

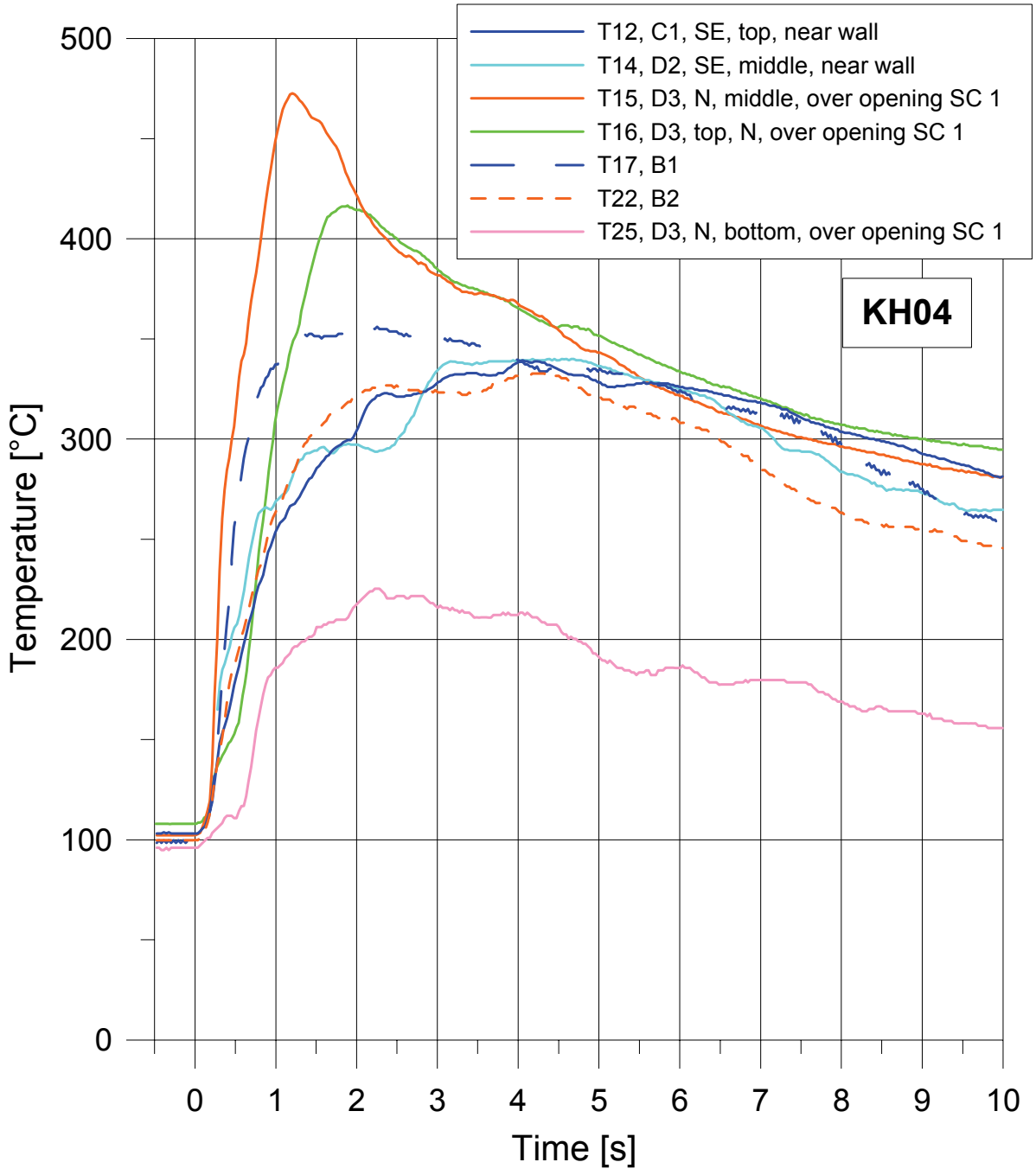

Fig. 4-106. KH04: Temperatures in containment

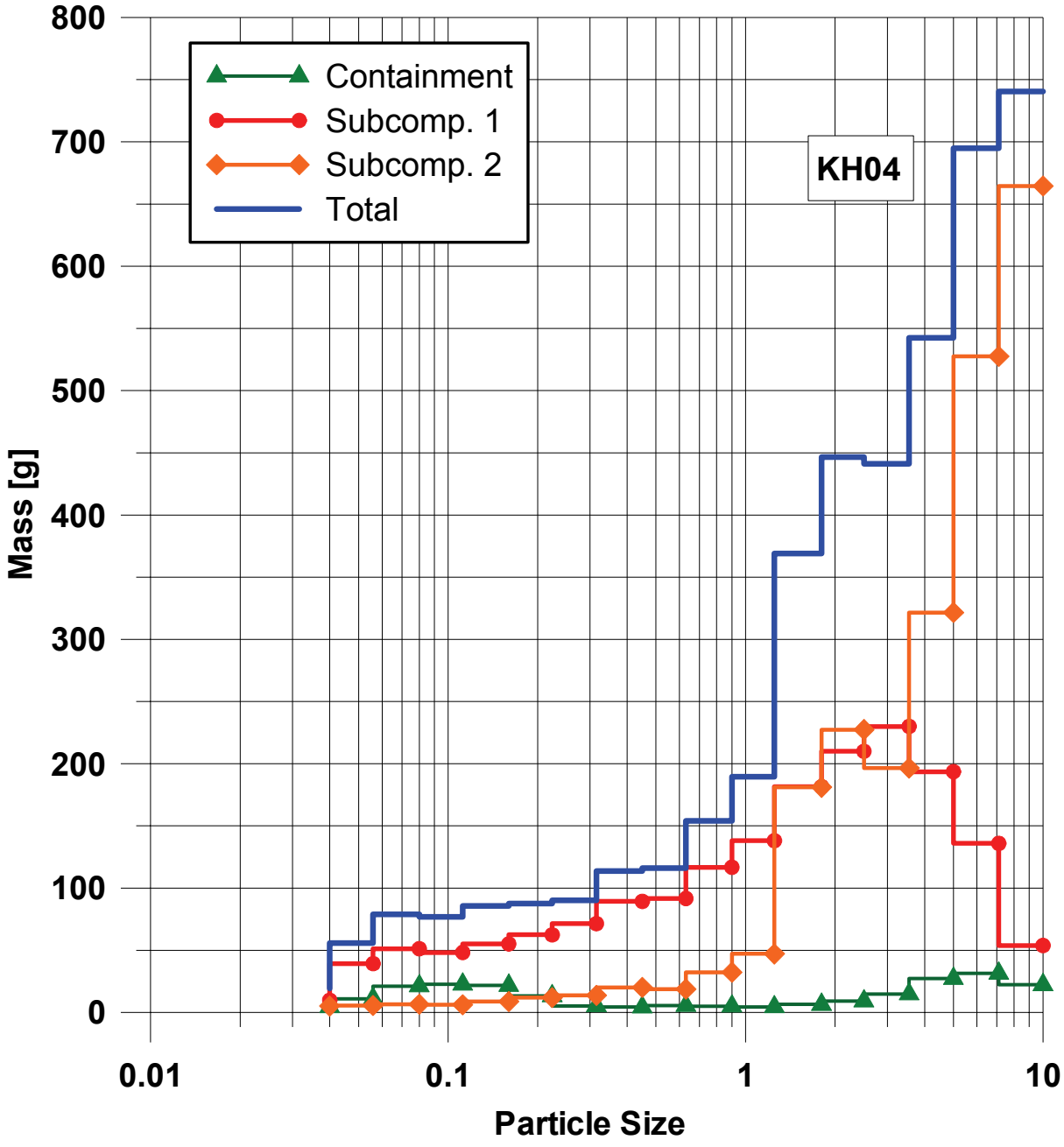

Fig. 4-107. KH04: Size distribution of particles smaller than 10 mm

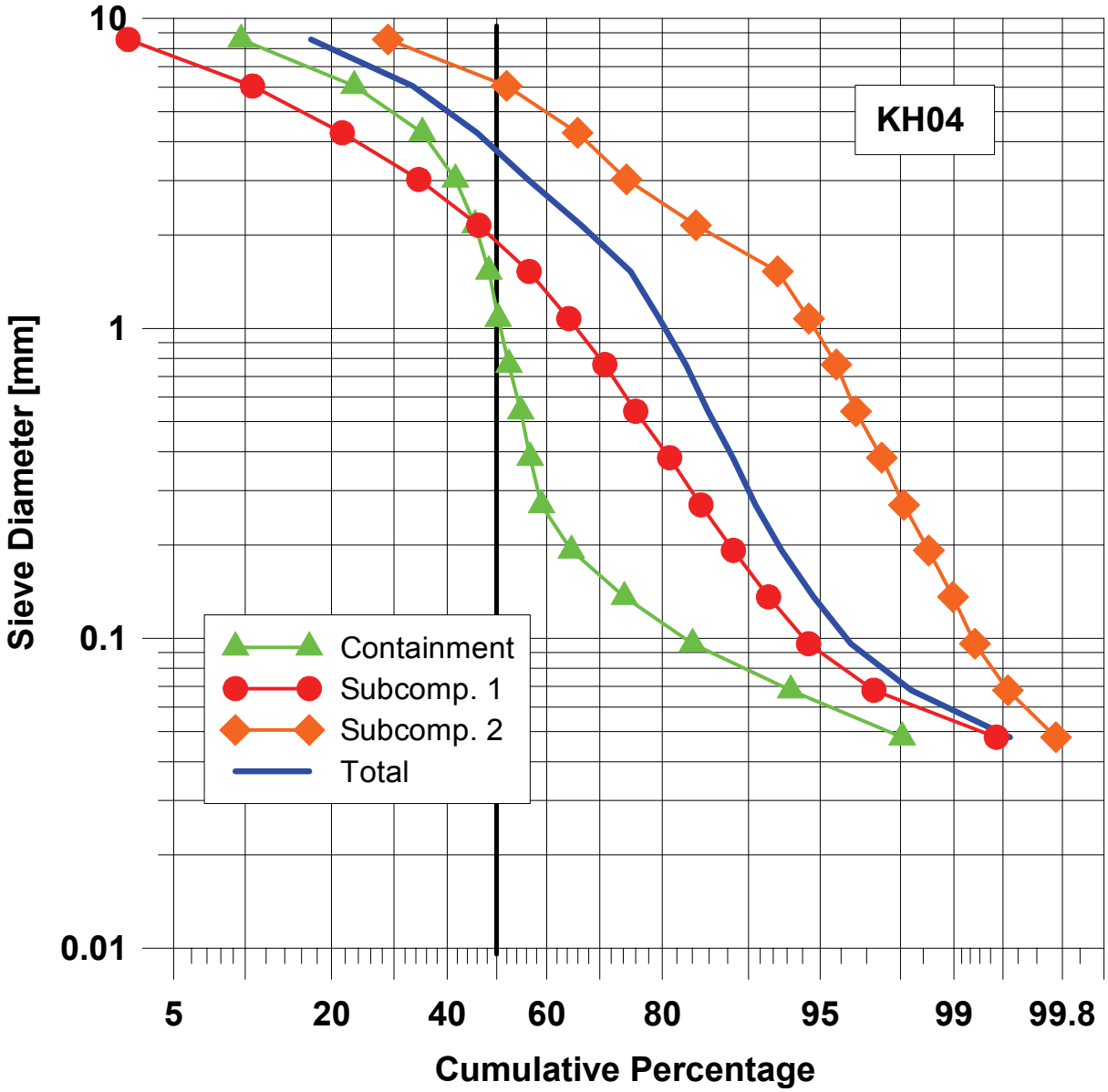

Fig. 4-108. KH04: Cumulative particle size distribution of debris smaller 10 mm

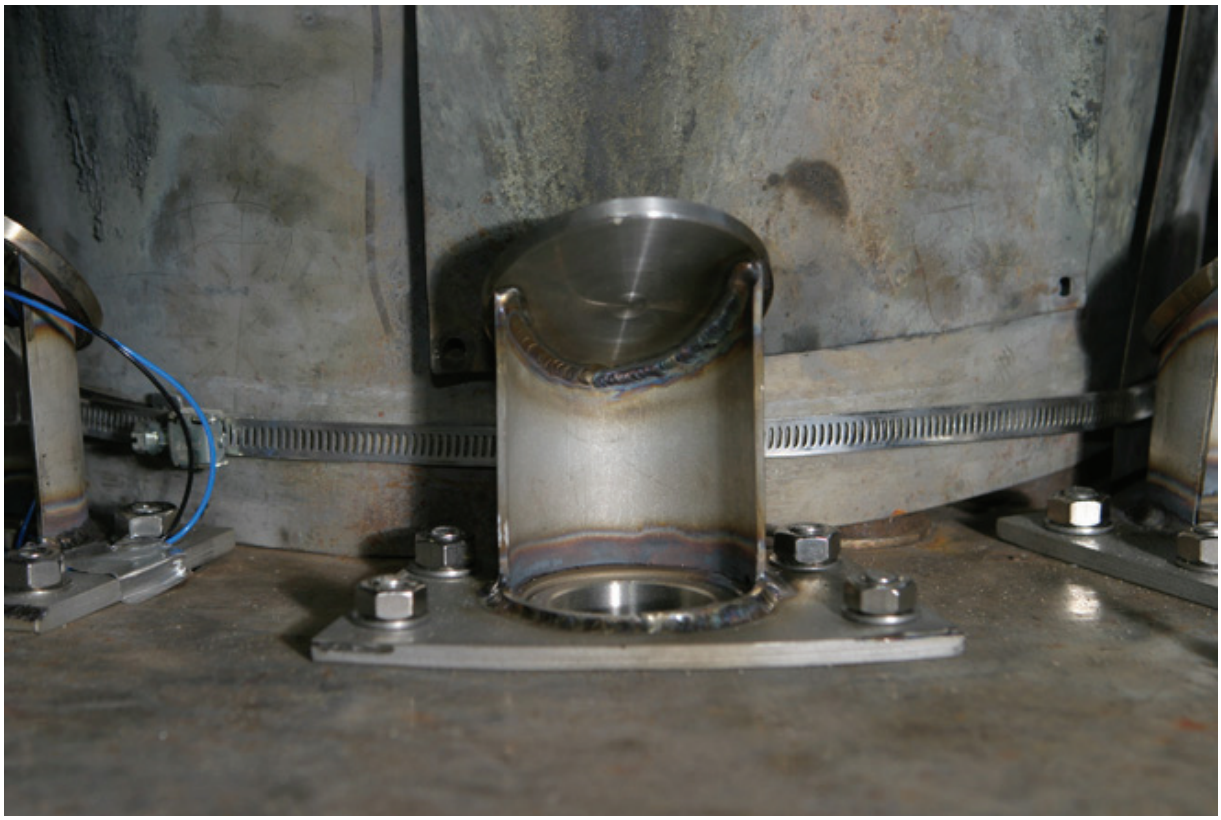

Fig. 4-109. KH04: Exit of path to refueling room (subcompartment 2)

Fig. 4-110. KH04: Post test view of RPV

Fig. 4-111. KH04: Post test view of cavity

Fig. 4-112. KH04: Crust on the wall of subcompartment 1 opposite of main cooling line

Fig. 4-113. KH04: Post test view into subcompartment 2

Fig. 4-114. KH04: Post test view of cover of subcompartment to (belongs to containment)

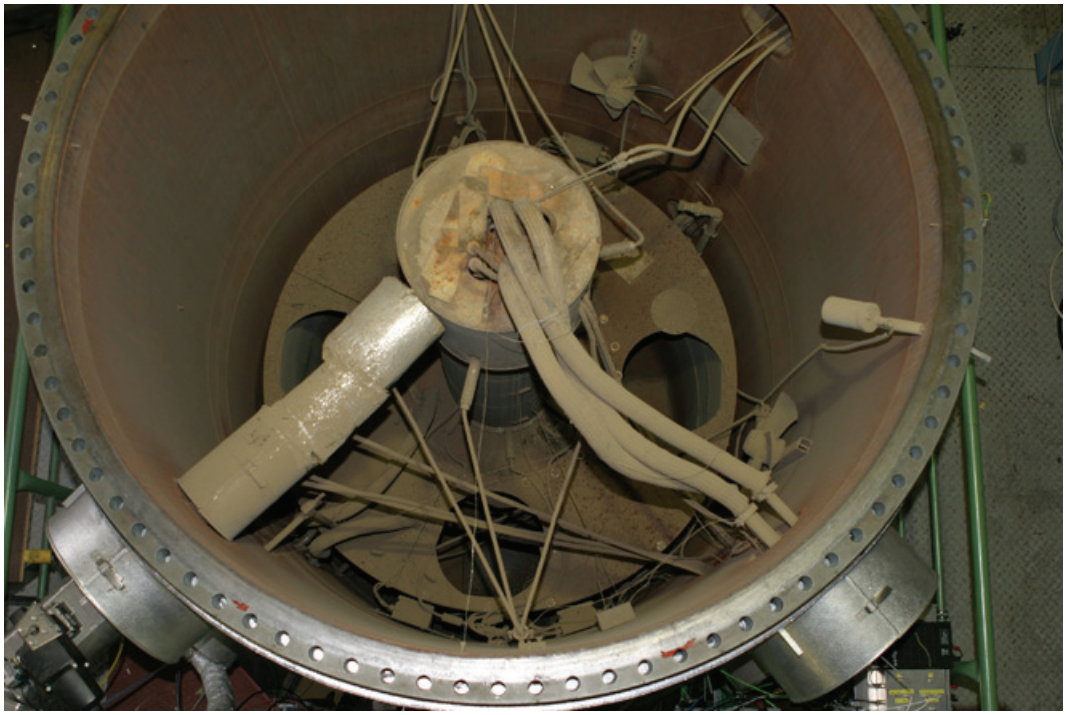

Fig. 4-115. KH04: Post test view of containment vessel

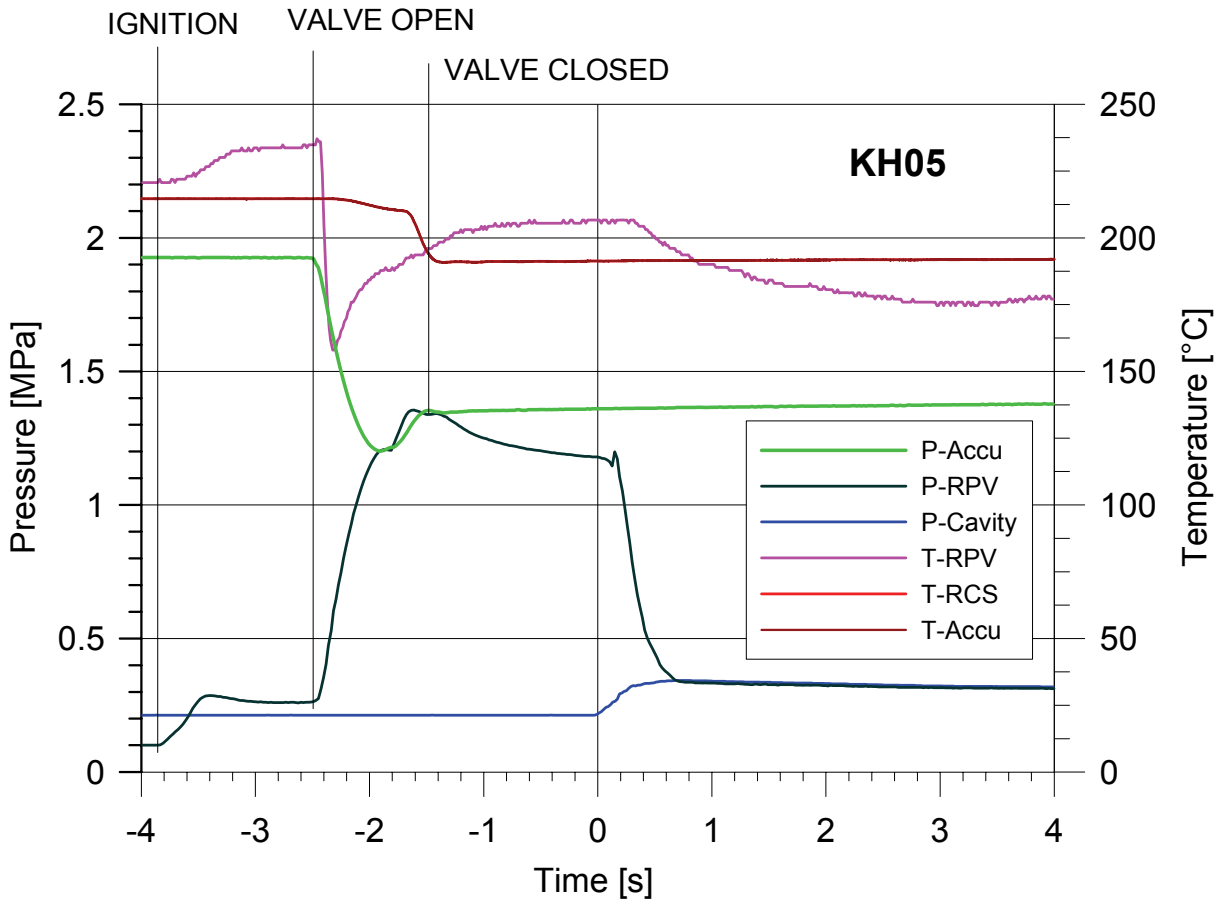

Fig. 4-116. KH05: Pressure, temperature and timing

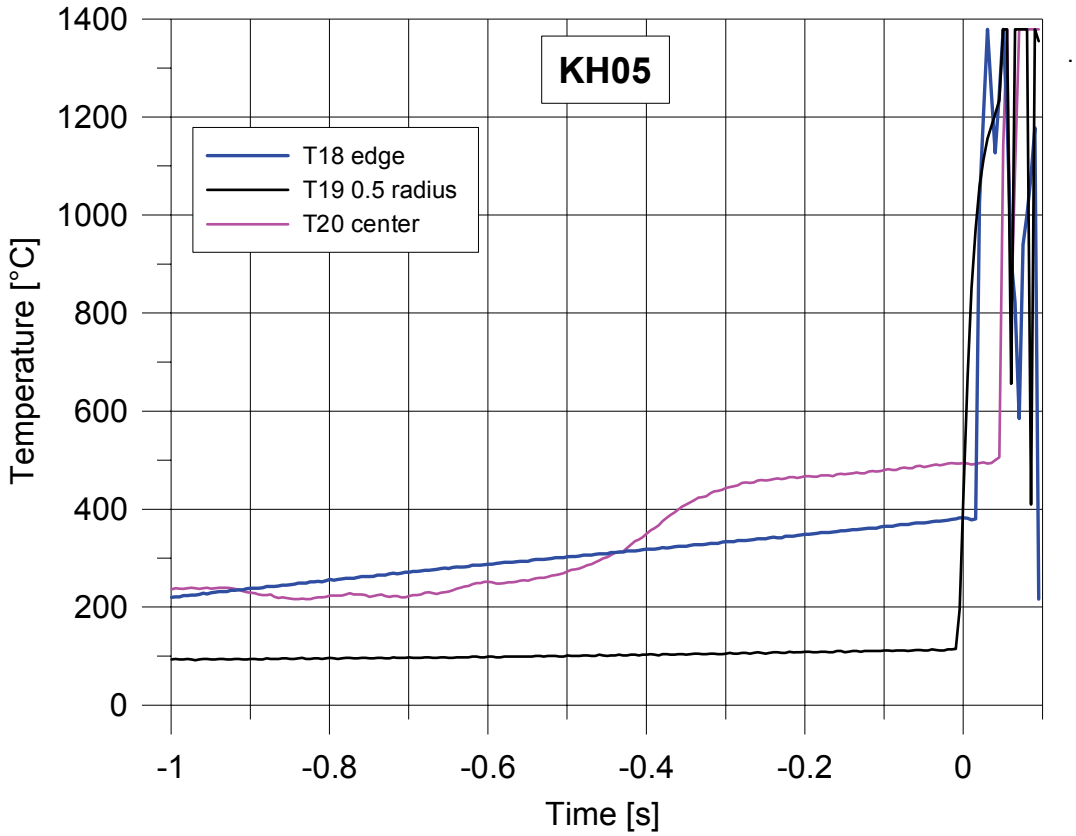

Fig. 4-117. KH05: Thermocouple signals in melt plug

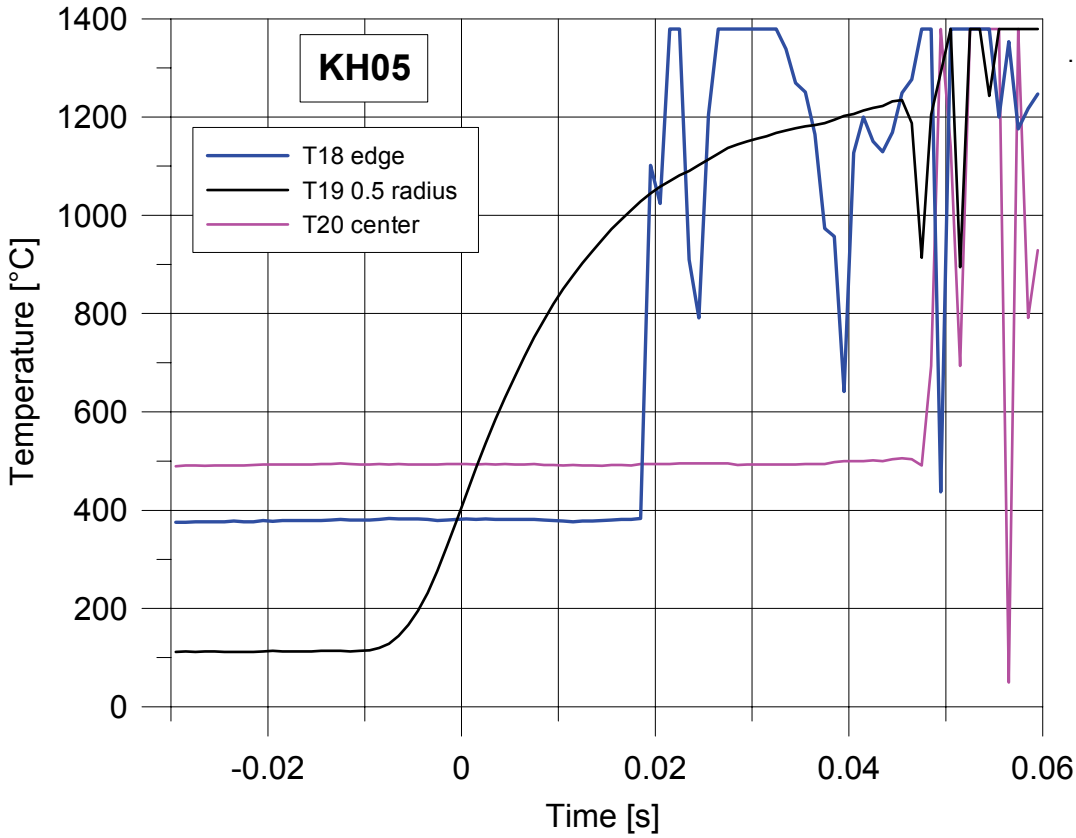

Fig. 4-118. KH05: Thermocouple signals in melt plug, zoom to t = 0 s

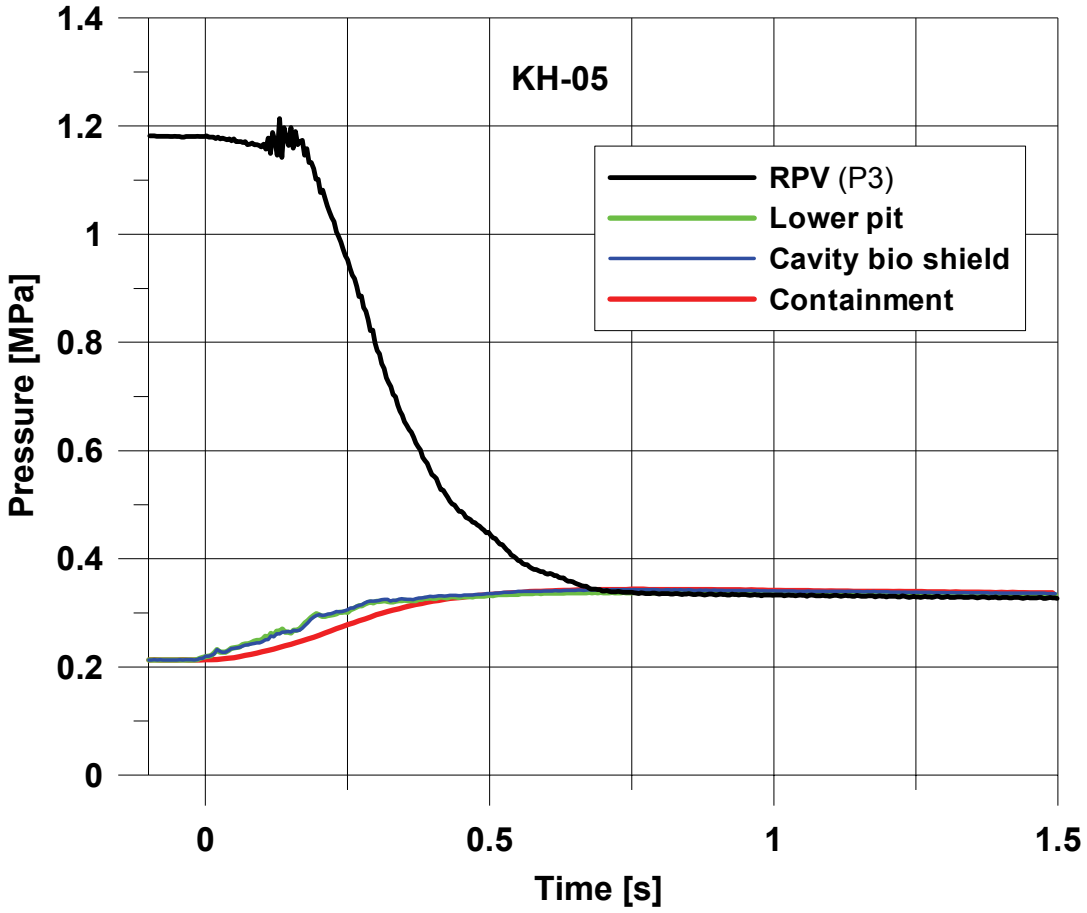

Fig. 4-119. KH05: Pressure in RPV vessel, cavity and containment

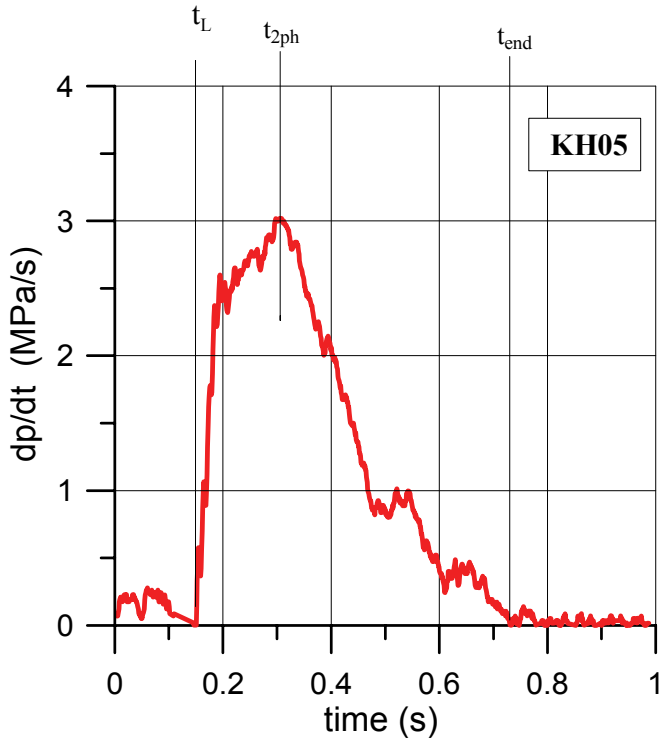

Fig. 4-120. KH05: Pressure gradient in RPV vessel

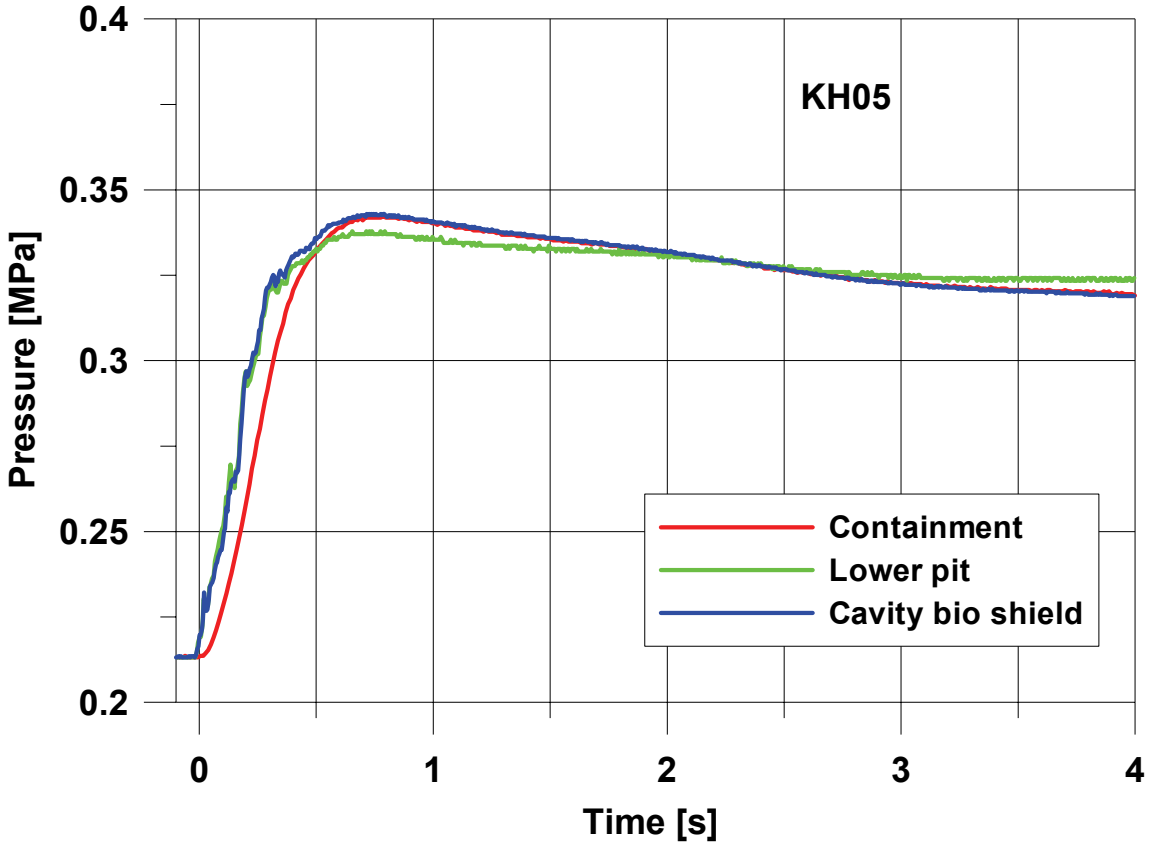

Fig. 4-121. KH05: Pressure in cavity and containment

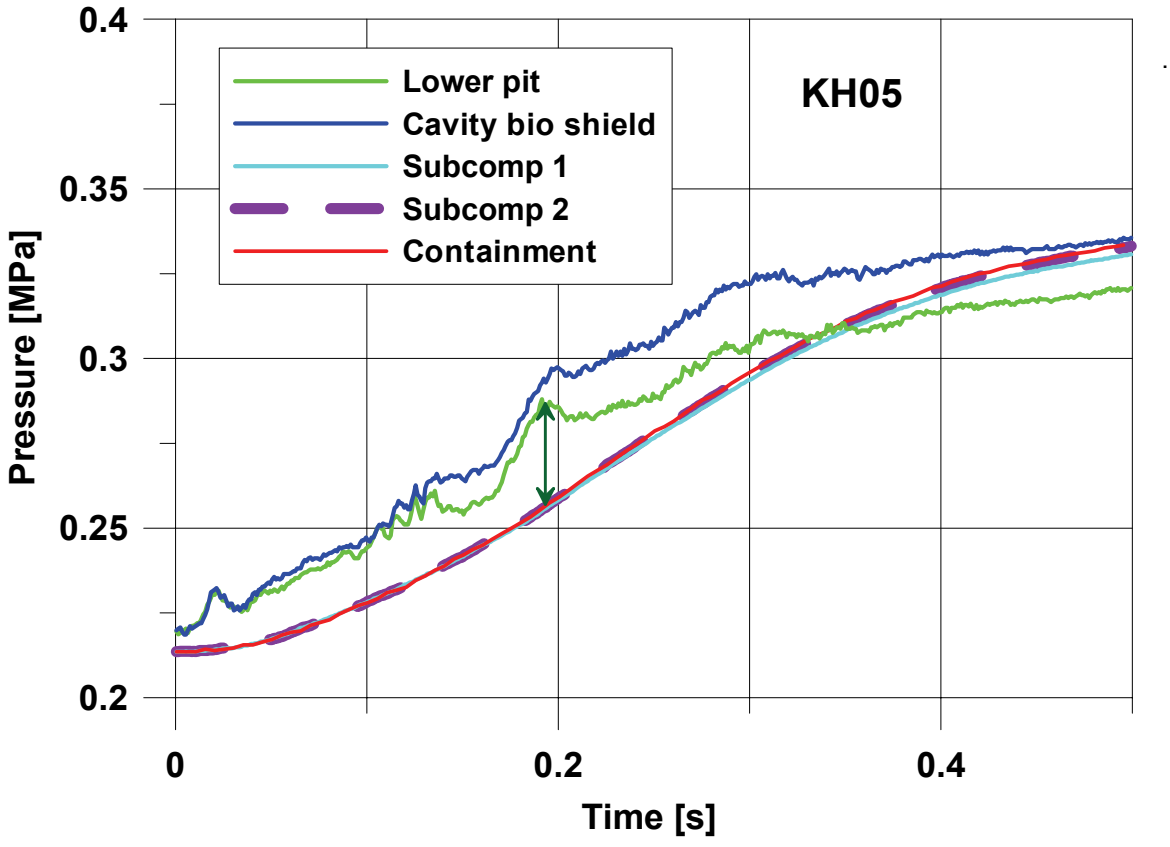

Fig. 4-122. KH05: Pressure in cavity, subcompartment and containment (Δp_{max}= 0.33 bar)

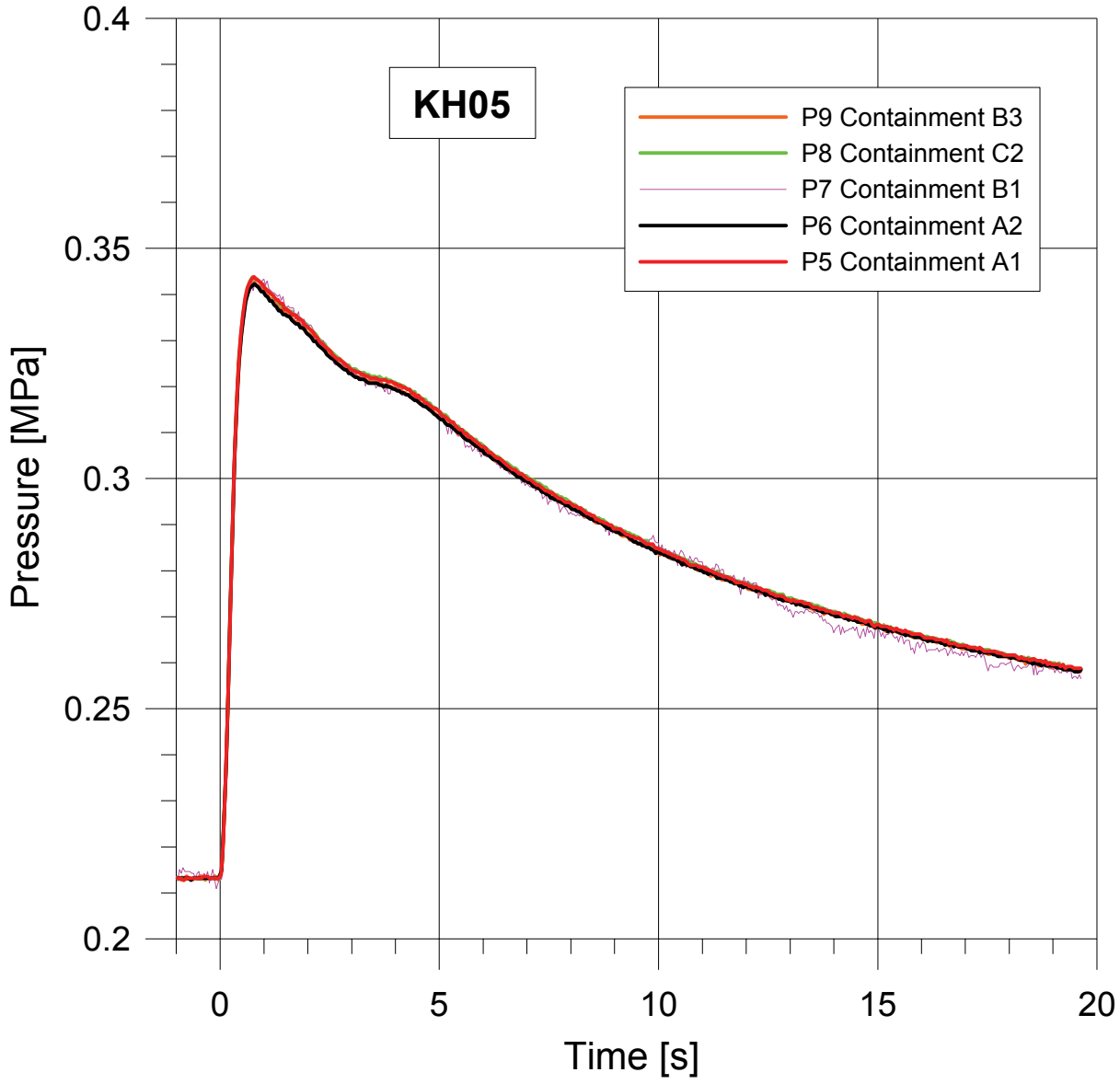

Fig. 4-123. KH05: Pressure in containment

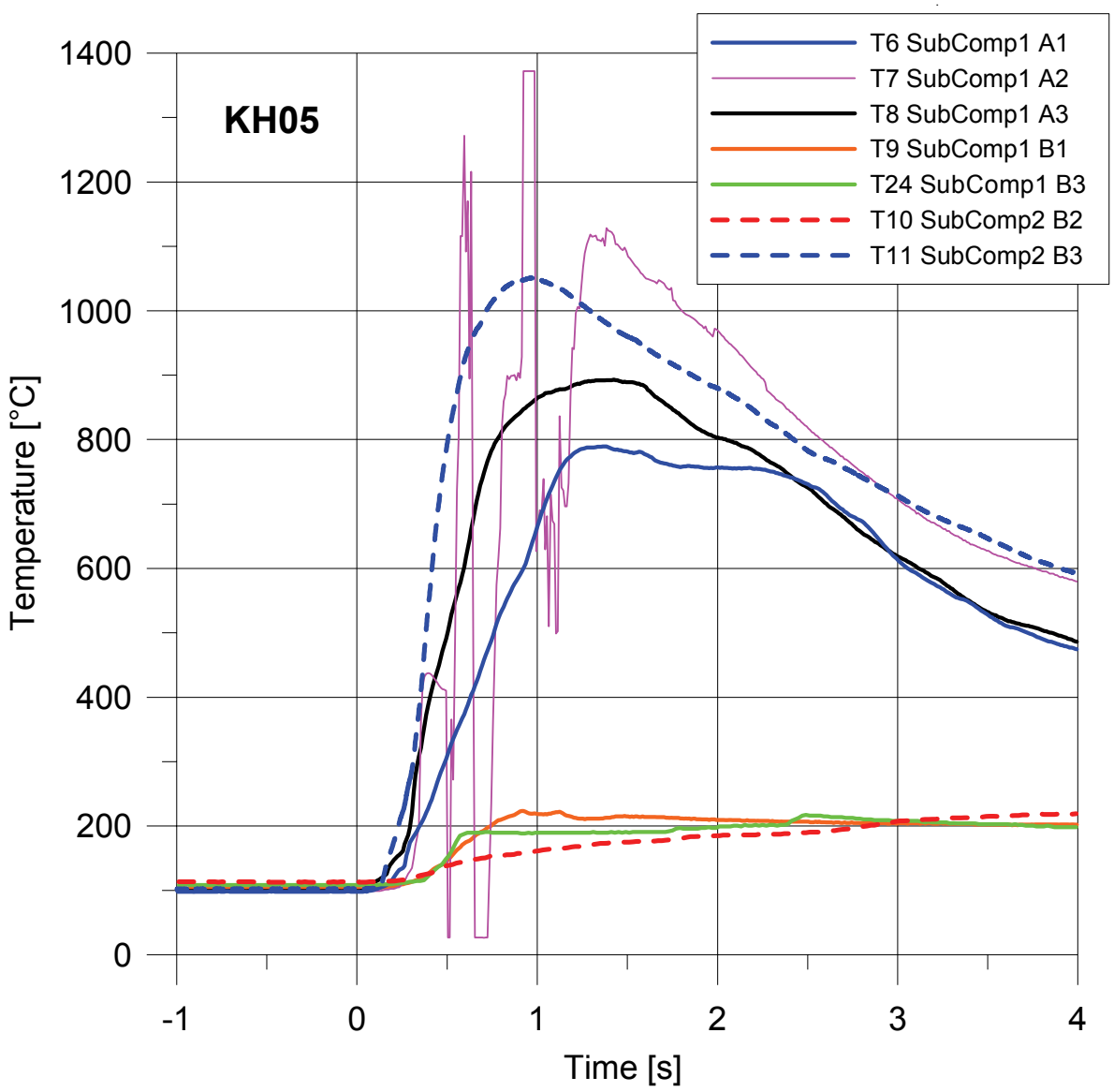

Fig. 4-124. KH05: Temperatures in subcompartments 1 and 2

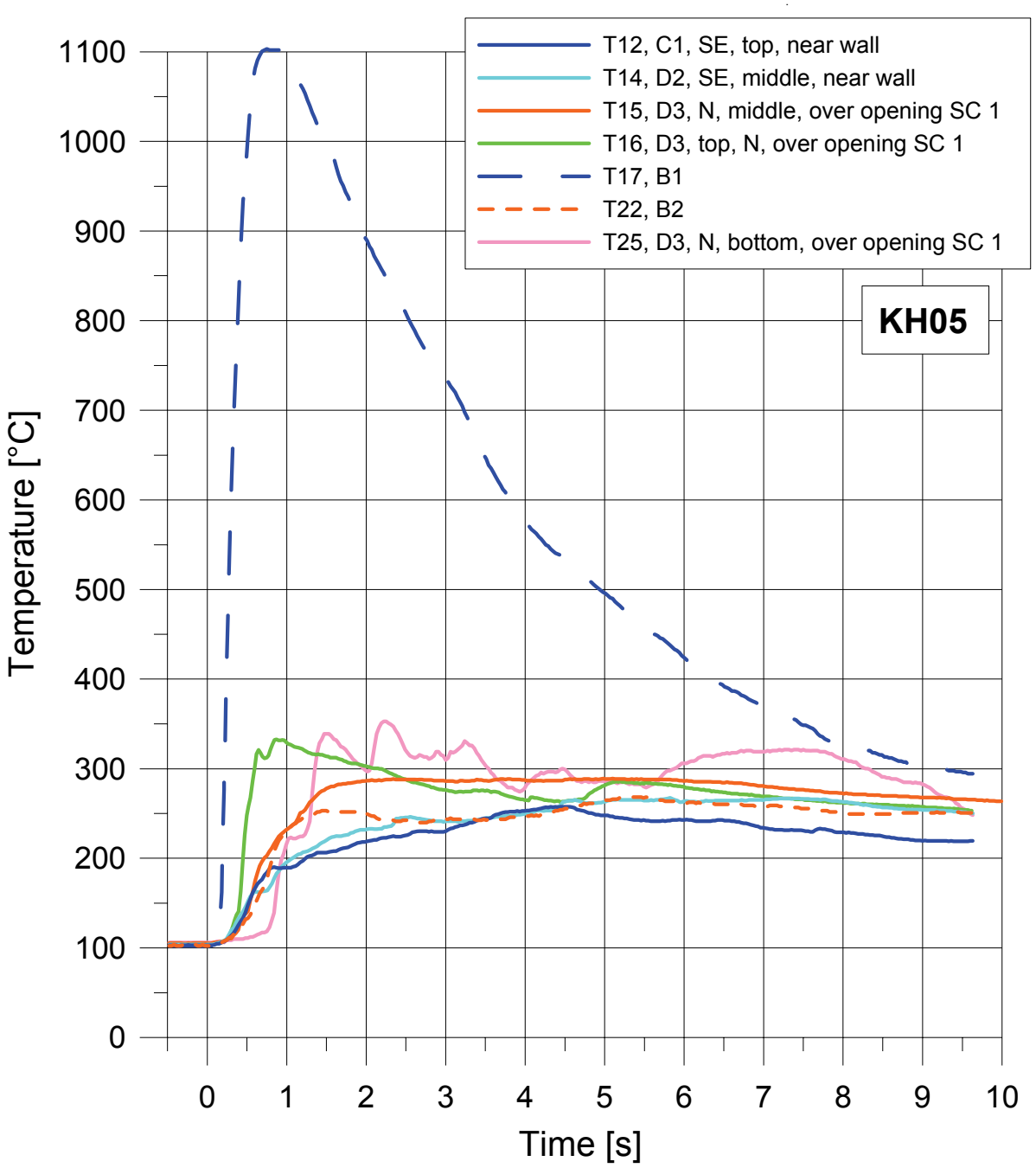

Fig. 4-125. KH05: Temperatures in containment

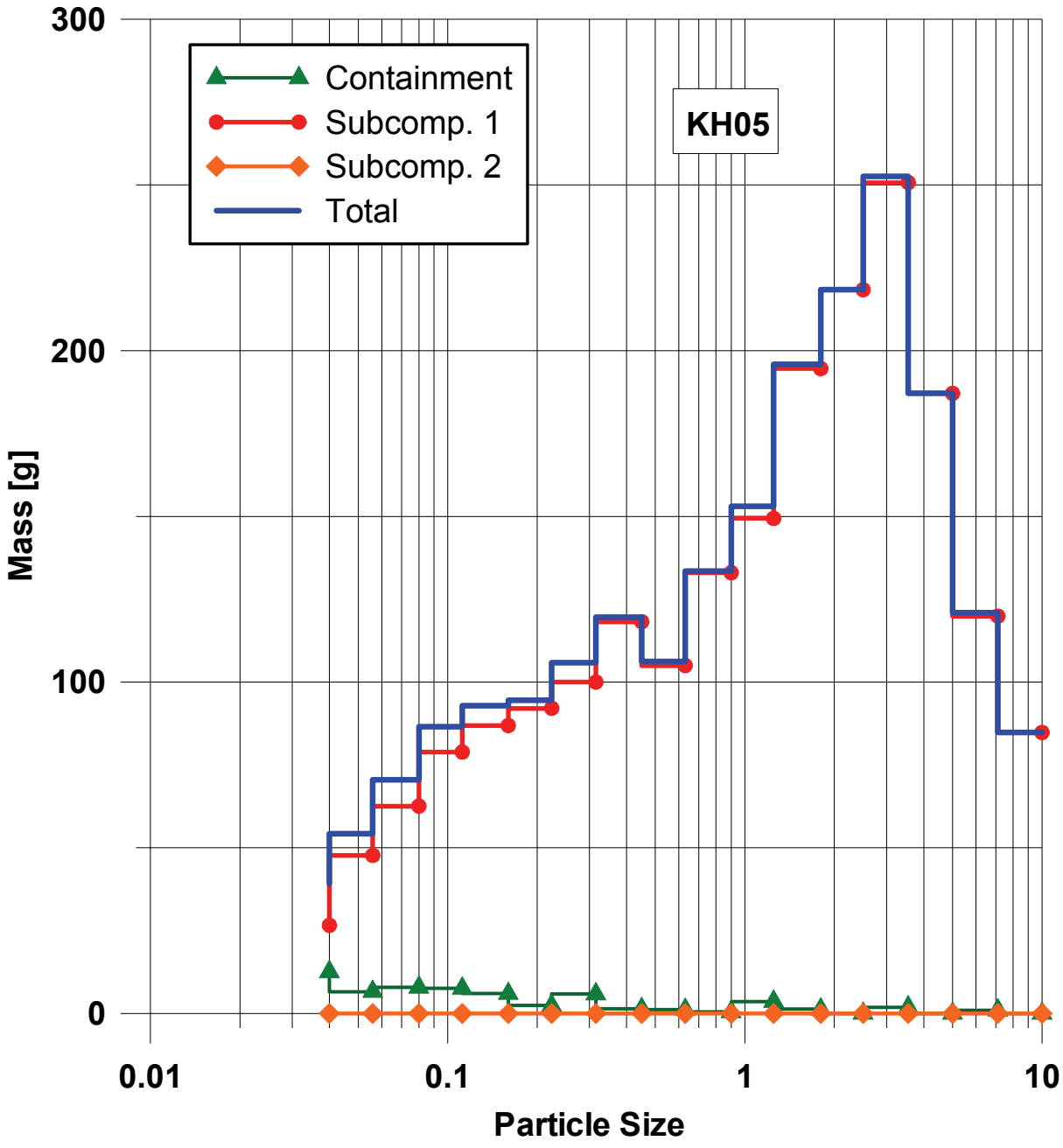

Fig. 4-126. KH05: Size distribution of particles smaller than 10 mm

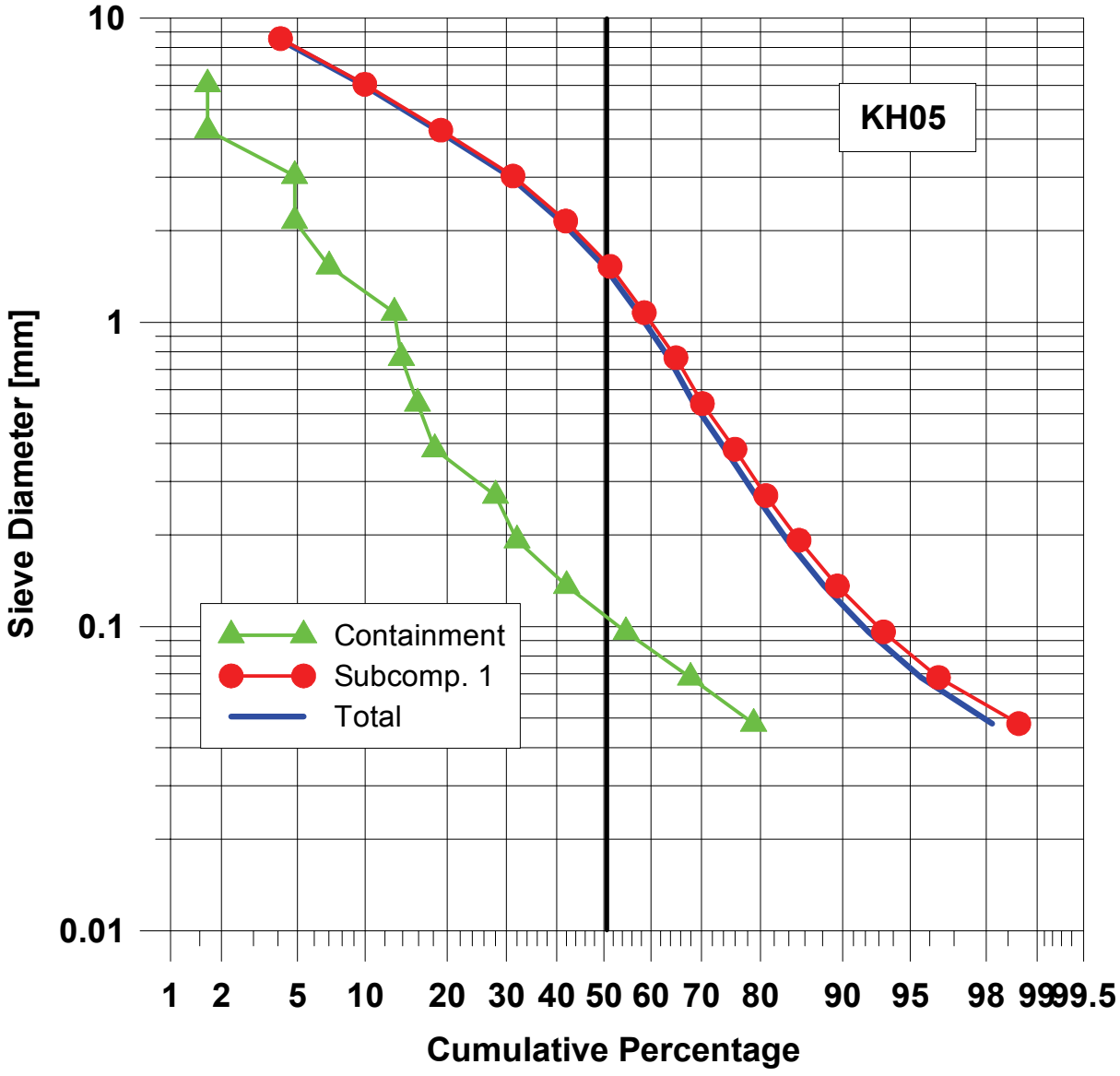

Fig. 4-127. KH05: Cumulative particle size distribution of debris smaller 10 mm

Fig. 4-128. KH05: Post test view of RPV

Fig. 4-129. KH05: Post test view of hole in RPV

Fig. 4-130. KH05: Post test view of inside of RPV

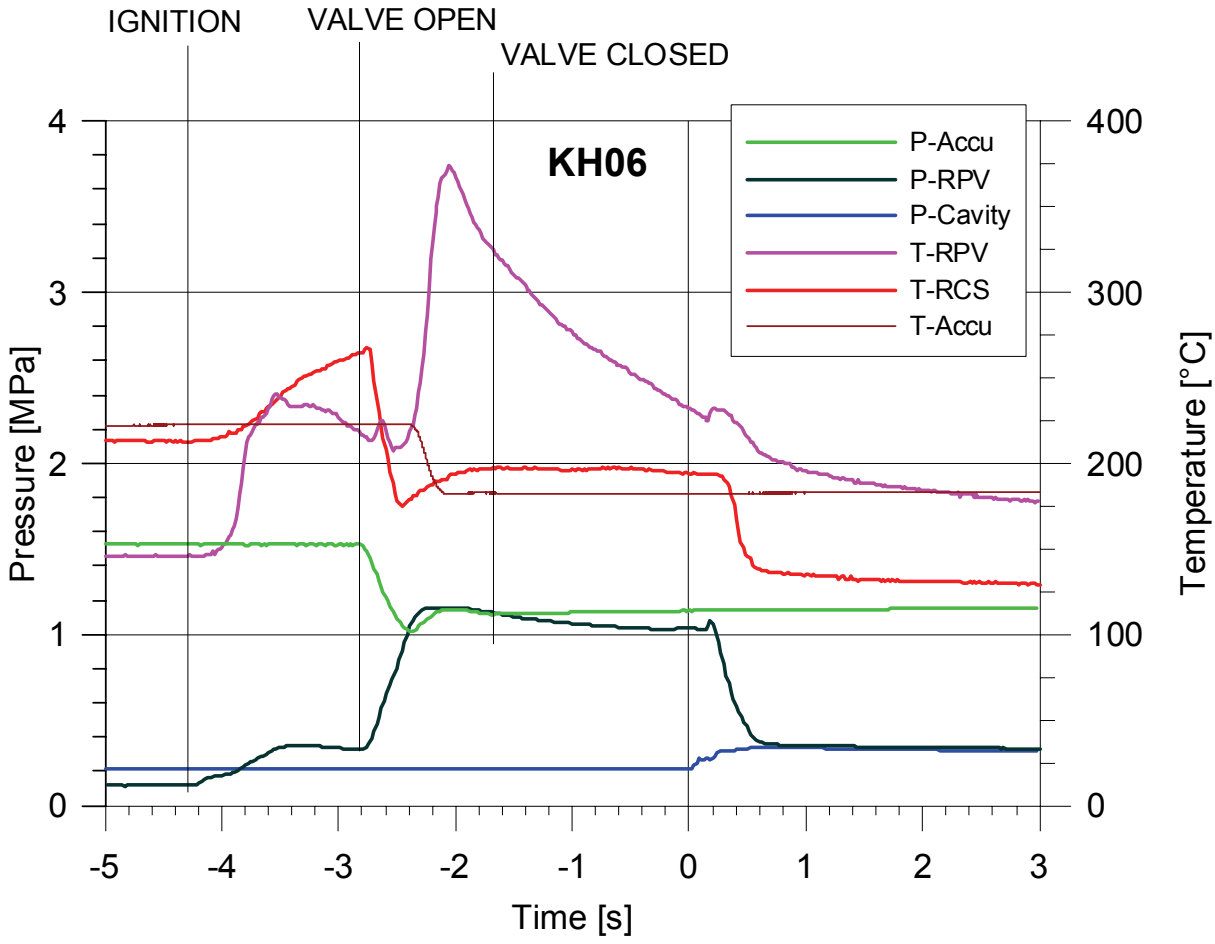

Fig. 4-131. KH06: Pressure, temperature and timing

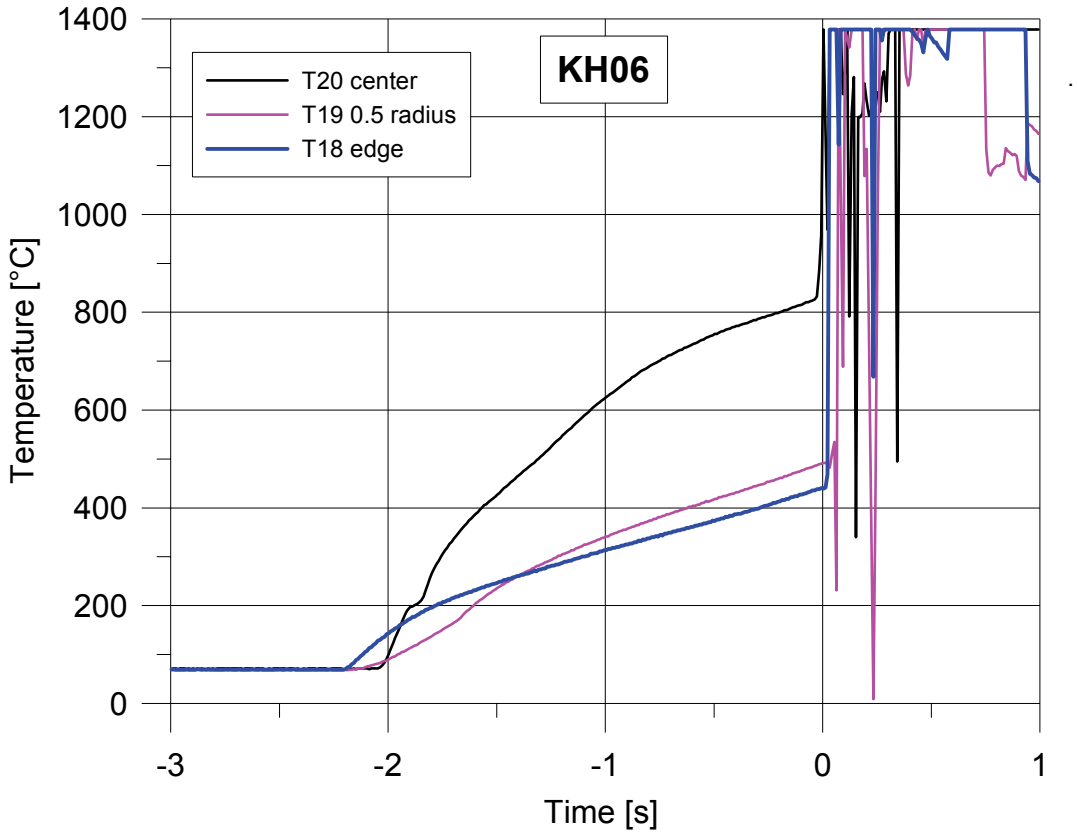

Fig. 4-132. KH06: Thermocouple signals in melt plug

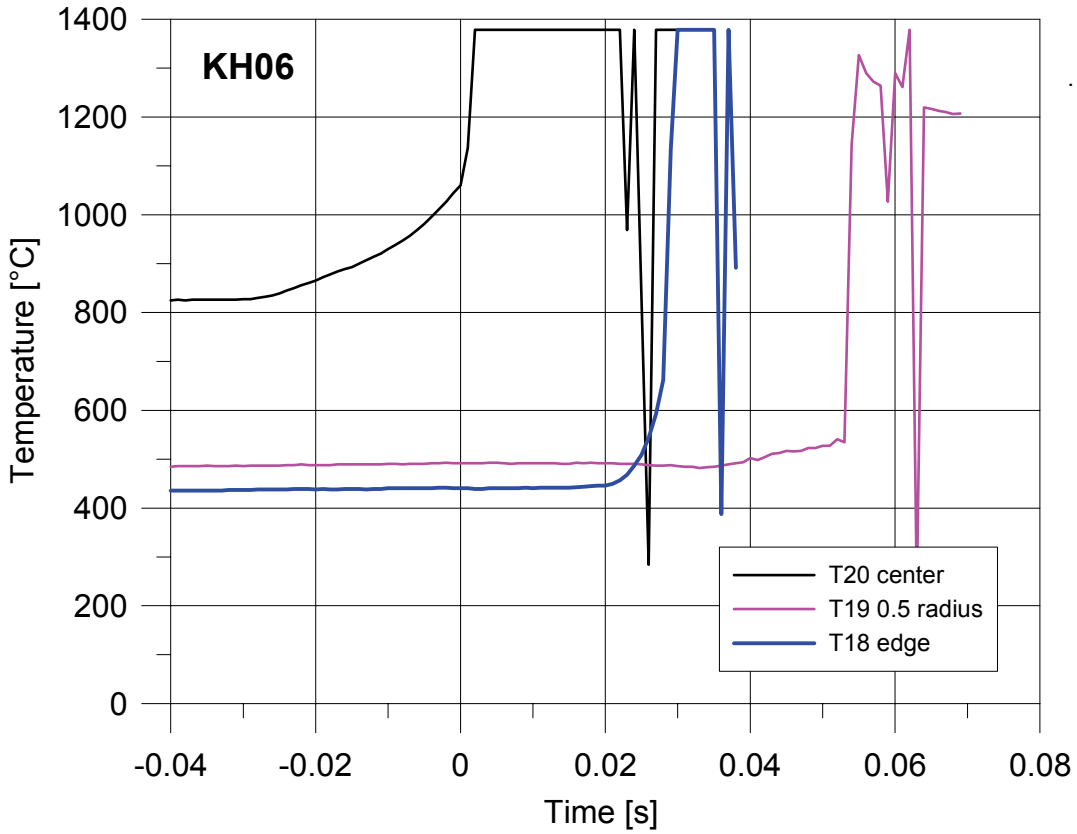

Fig. 4-133. KH06: Thermocouple signals in melt plug, zoom to t = 0 s

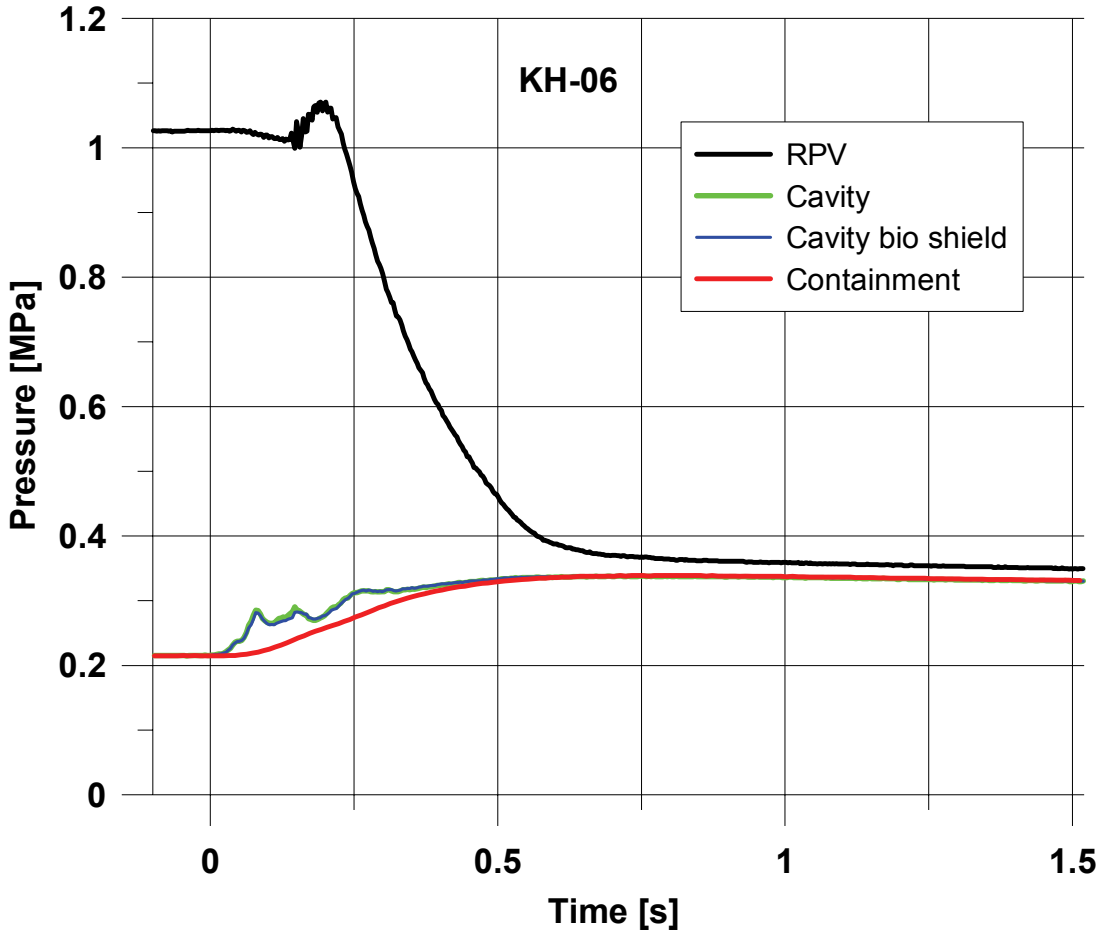

Fig. 4-134. KH06: Pressure in RPV vessel, cavity and containment

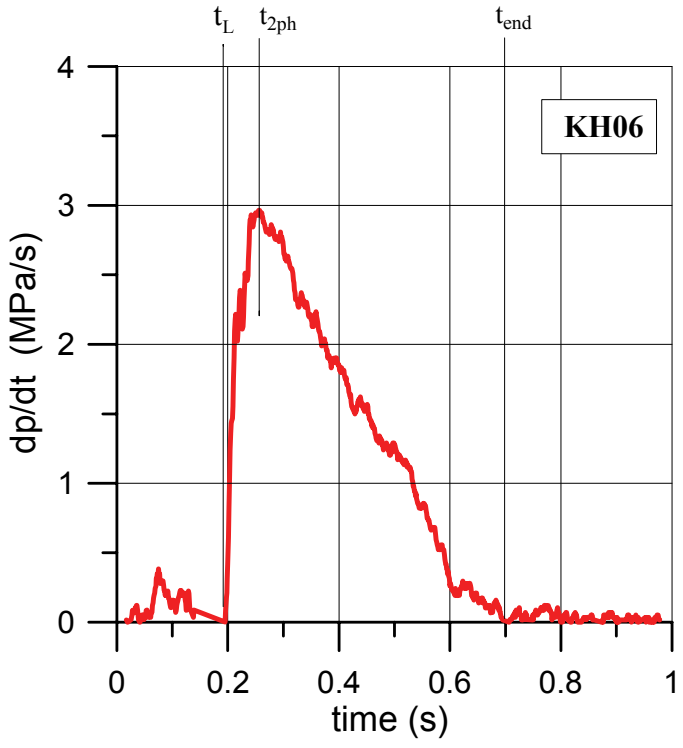

Fig. 4-135. KH06: Pressure gradient in RPV vessel

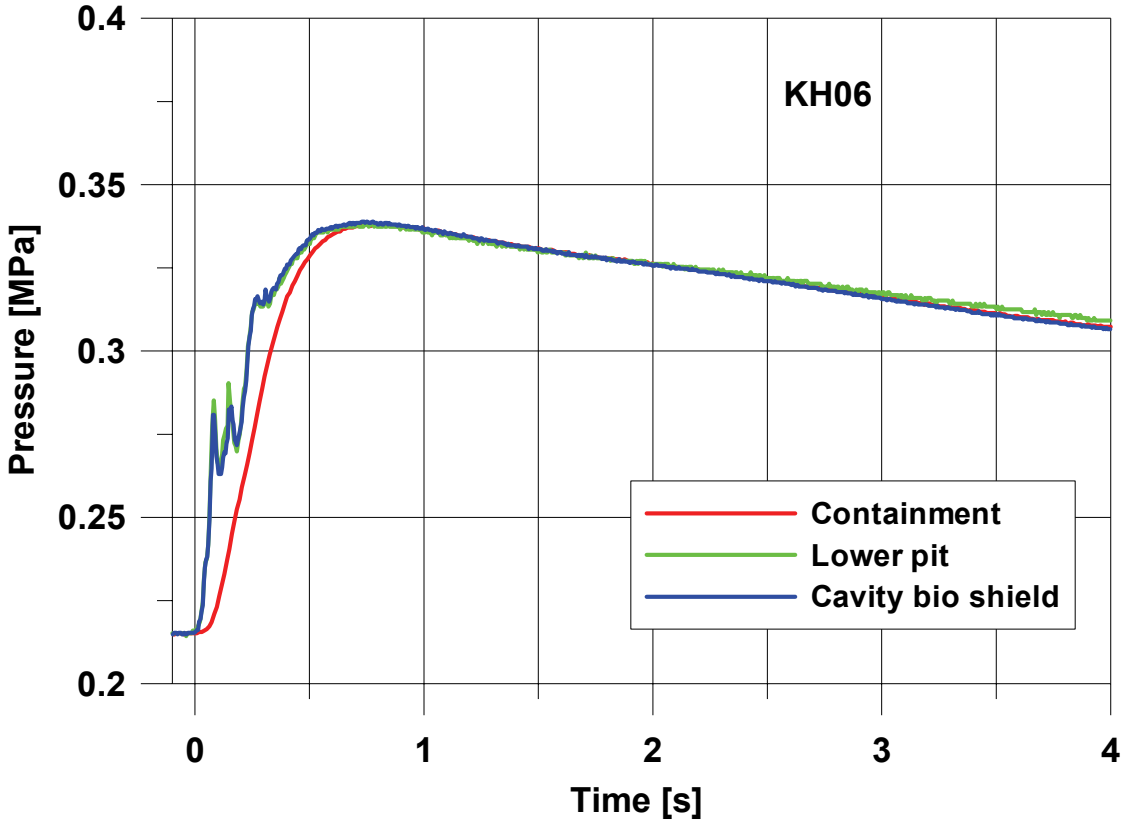

Fig. 4-136. KH06: Pressure in cavity and containment

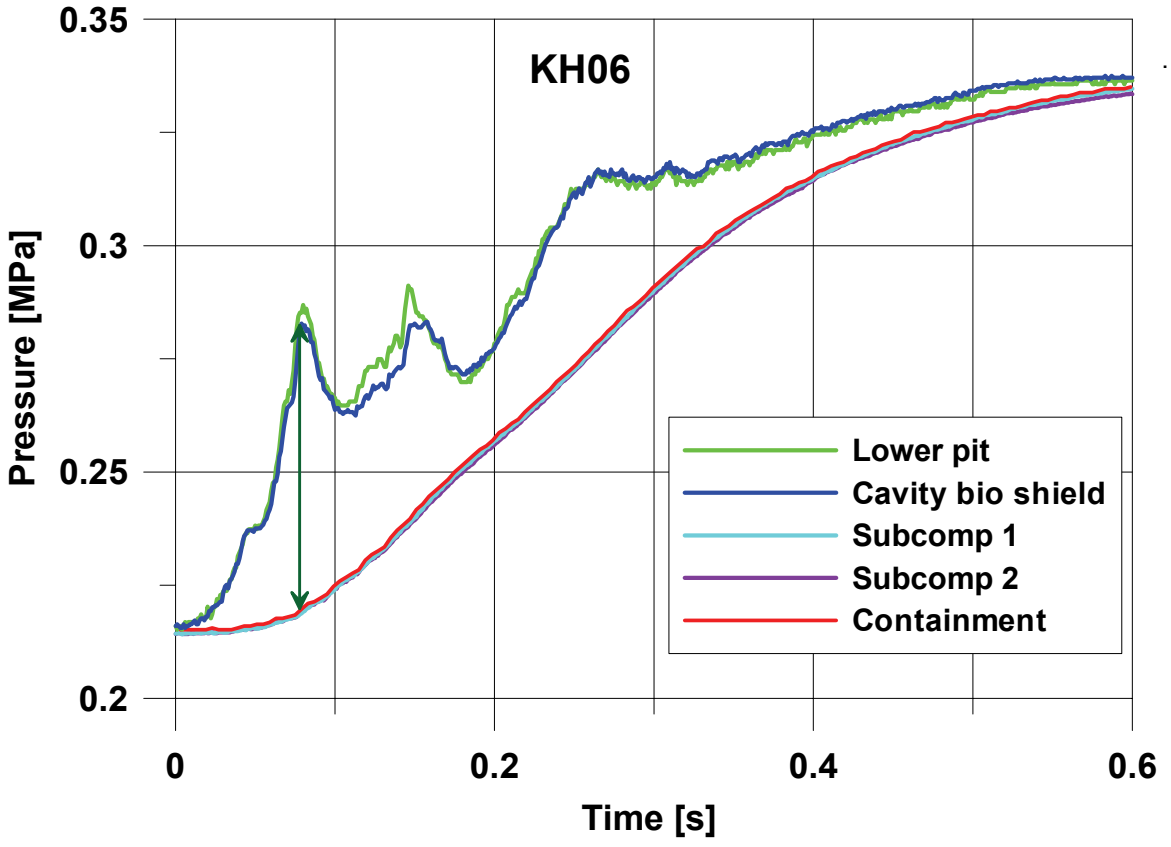

Fig. 4-137. KH06: Pressure in cavity, subcompartment and containment (Δp_{max}= 0.60 bar)

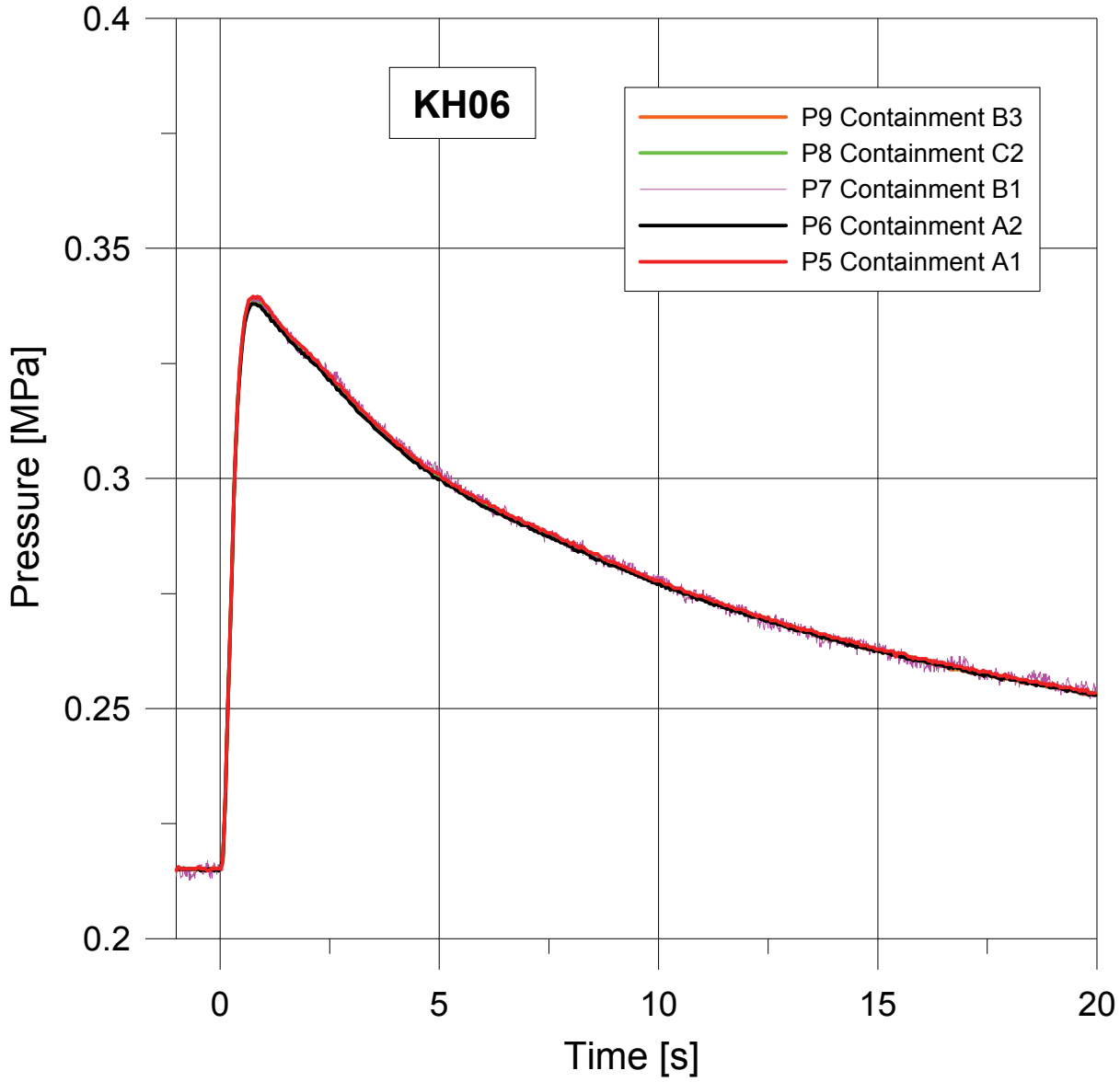

Fig. 4-138. KH06: Pressure in containment

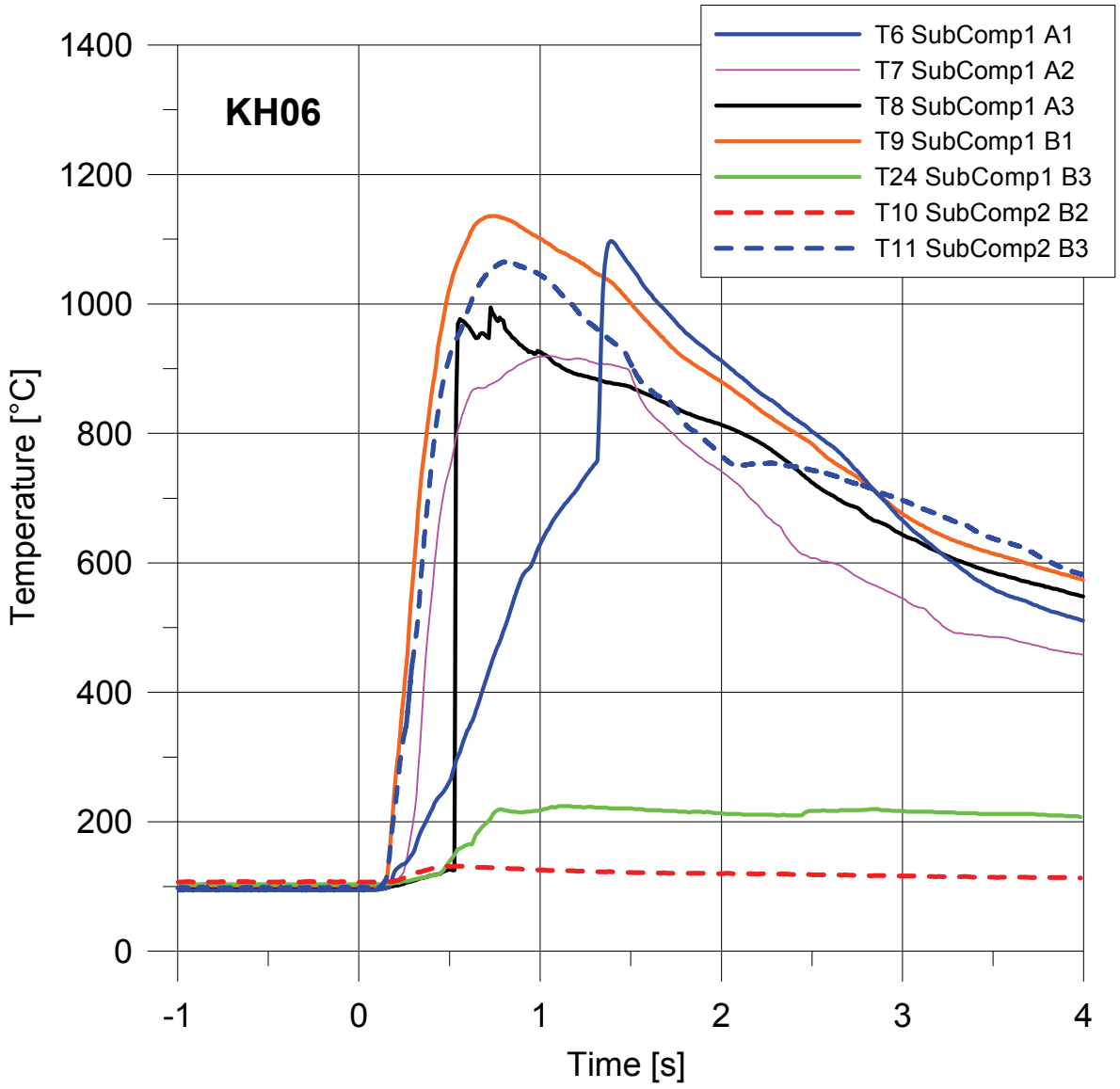

Fig. 4-139. KH06: Temperatures in subcompartments 1 and 2

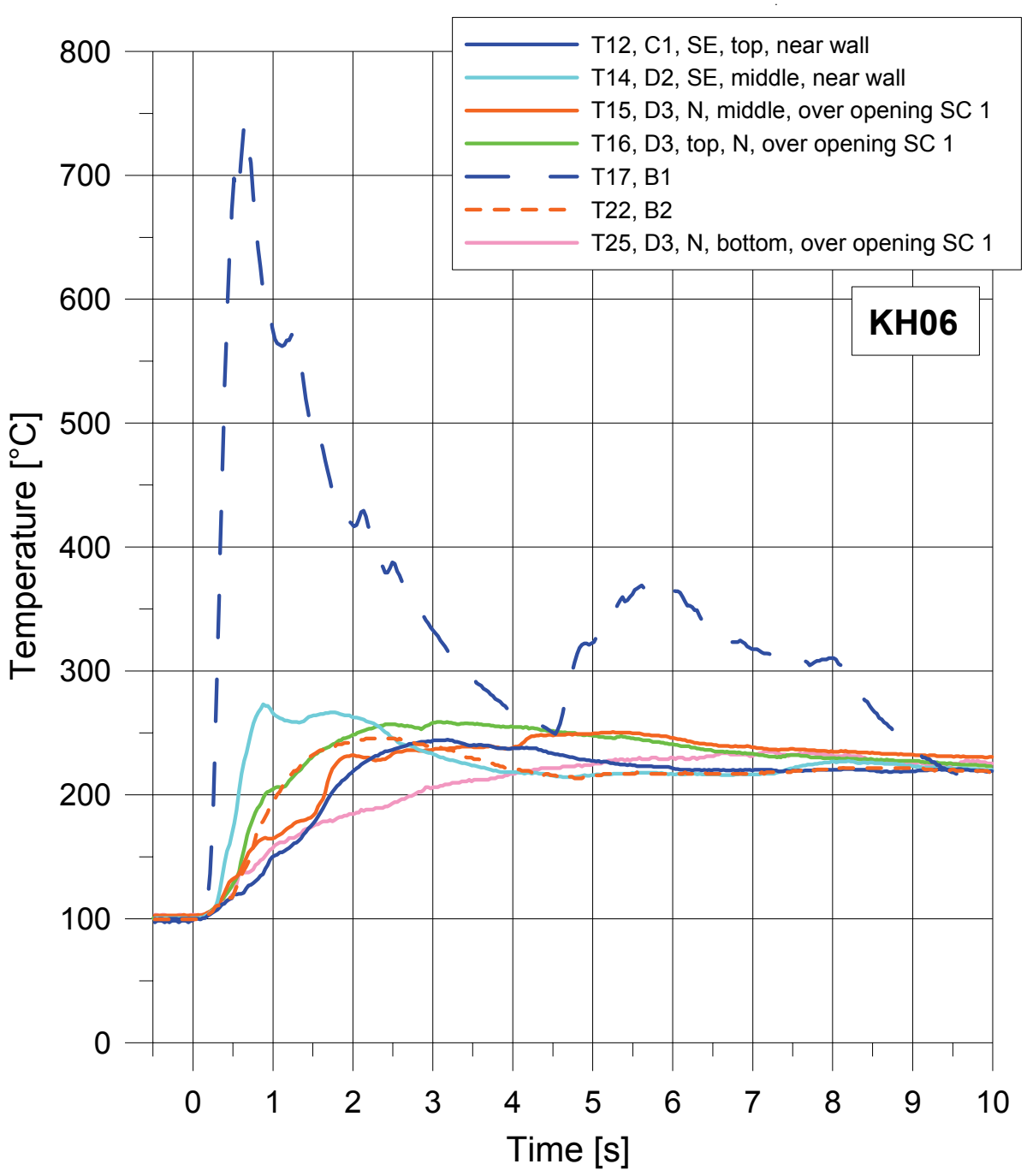

Fig. 4-140. KH06: Temperatures in containment

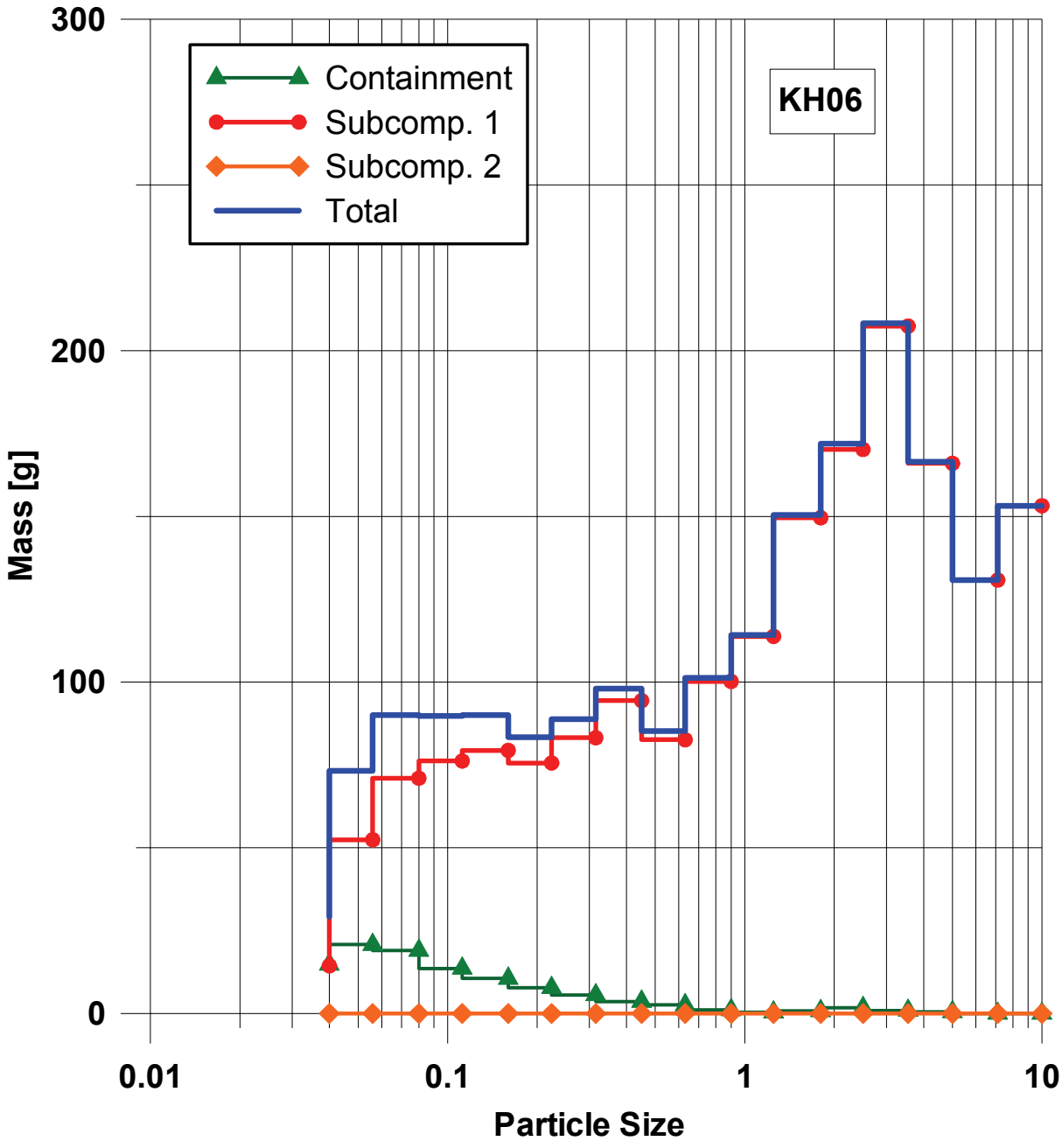

Fig. 4-141. KH06: Size distribution of particles smaller than 10 mm

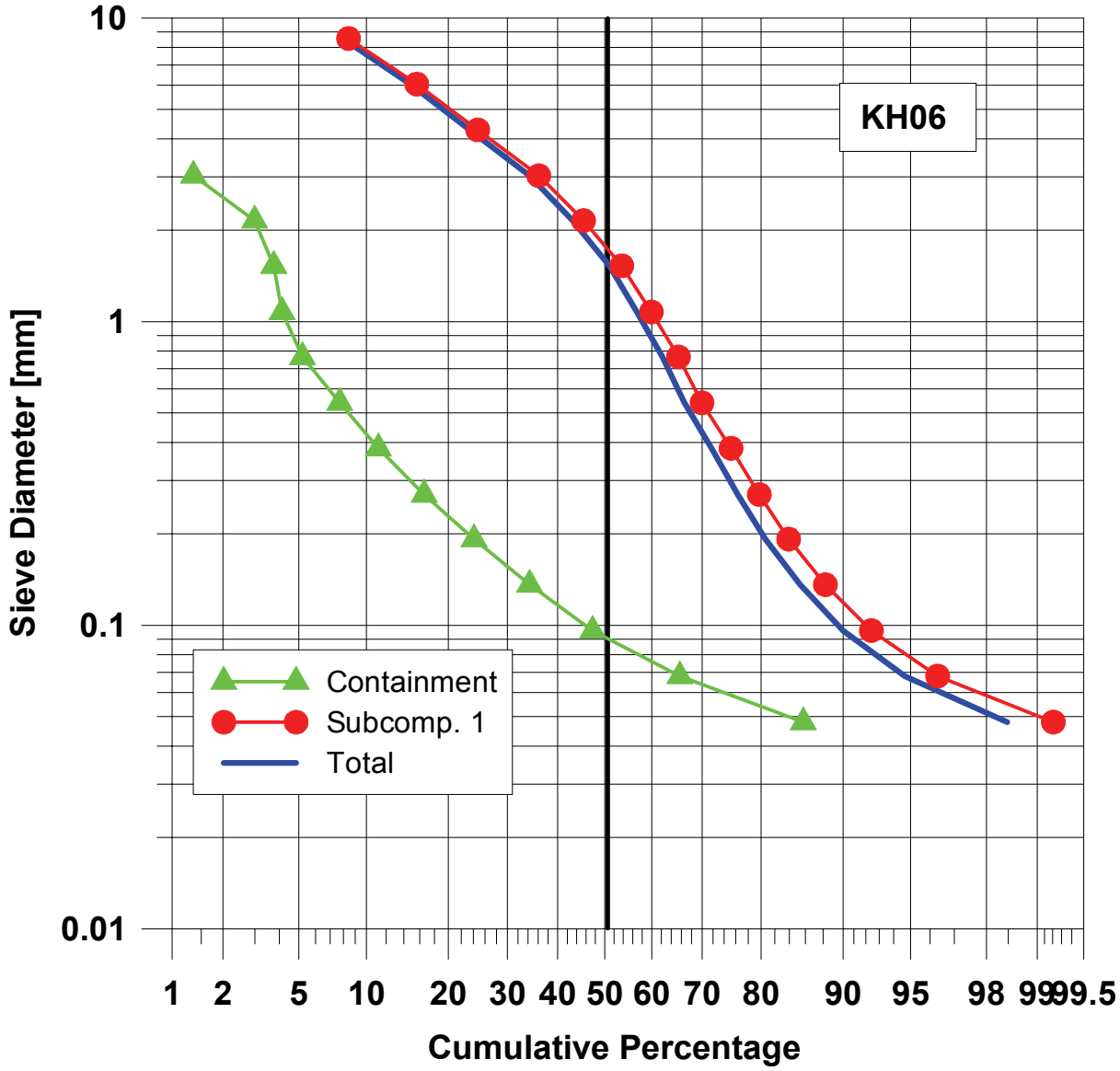

Fig. 4-142. KH06: Cumulative particle size distribution of debris smaller 10 mm

Fig. 4-143. KH06: Post test view of RPV

Fig. 4-144. KH06: Post test view of lower part of RPV

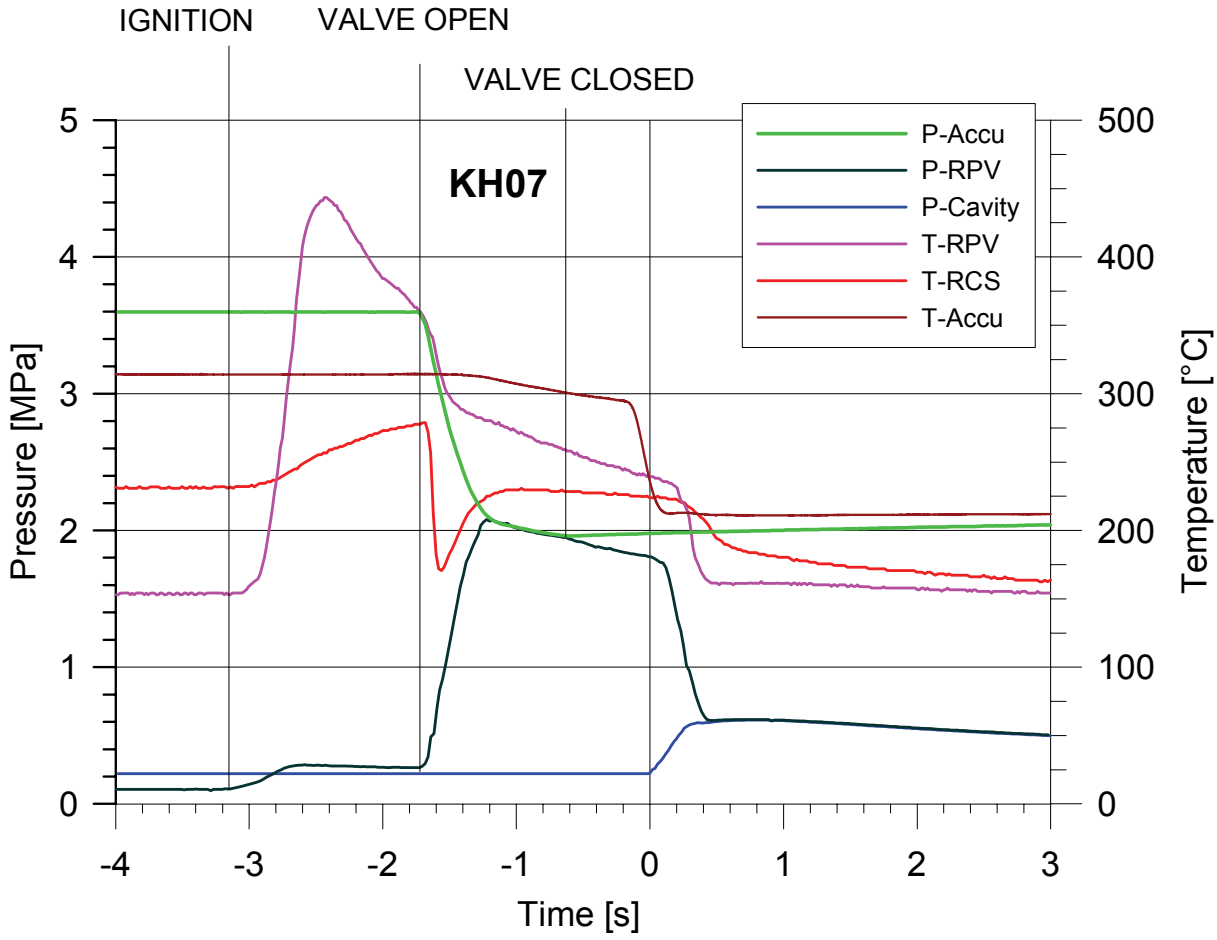

Fig. 4-145. KH 07: Pressure, temperature and timing

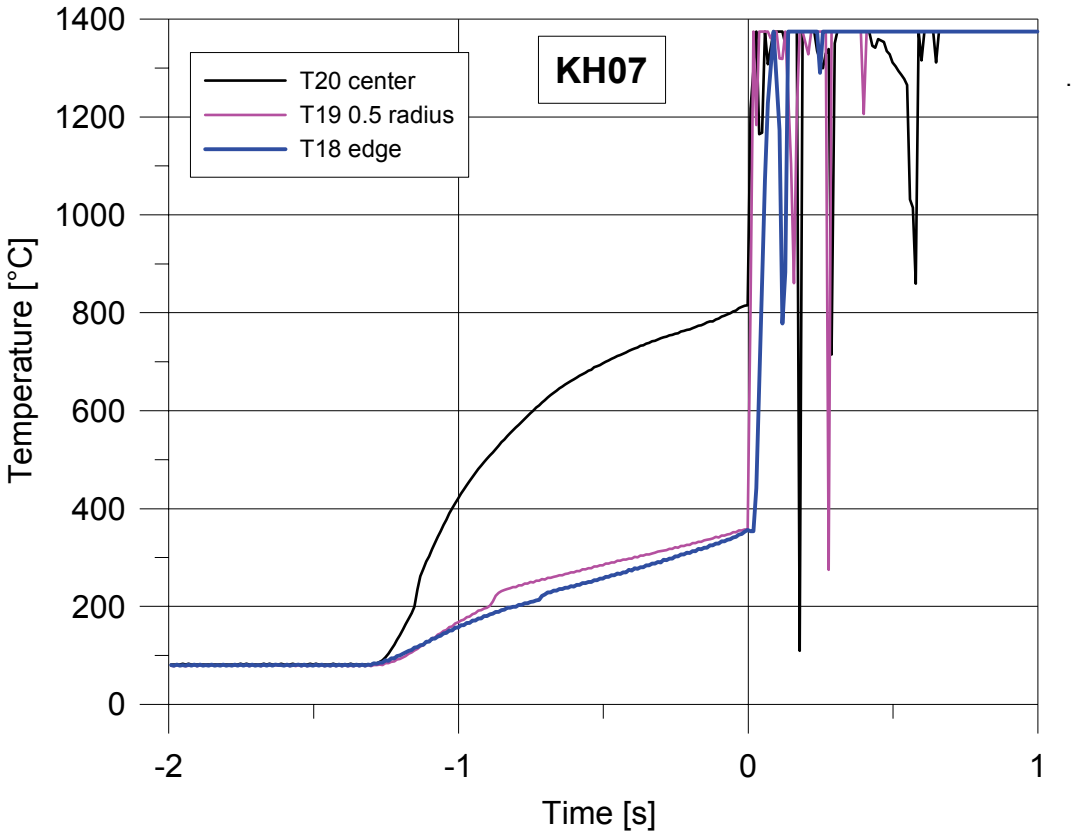

Fig. 4-146. KH07: Thermocouple signals in melt plug

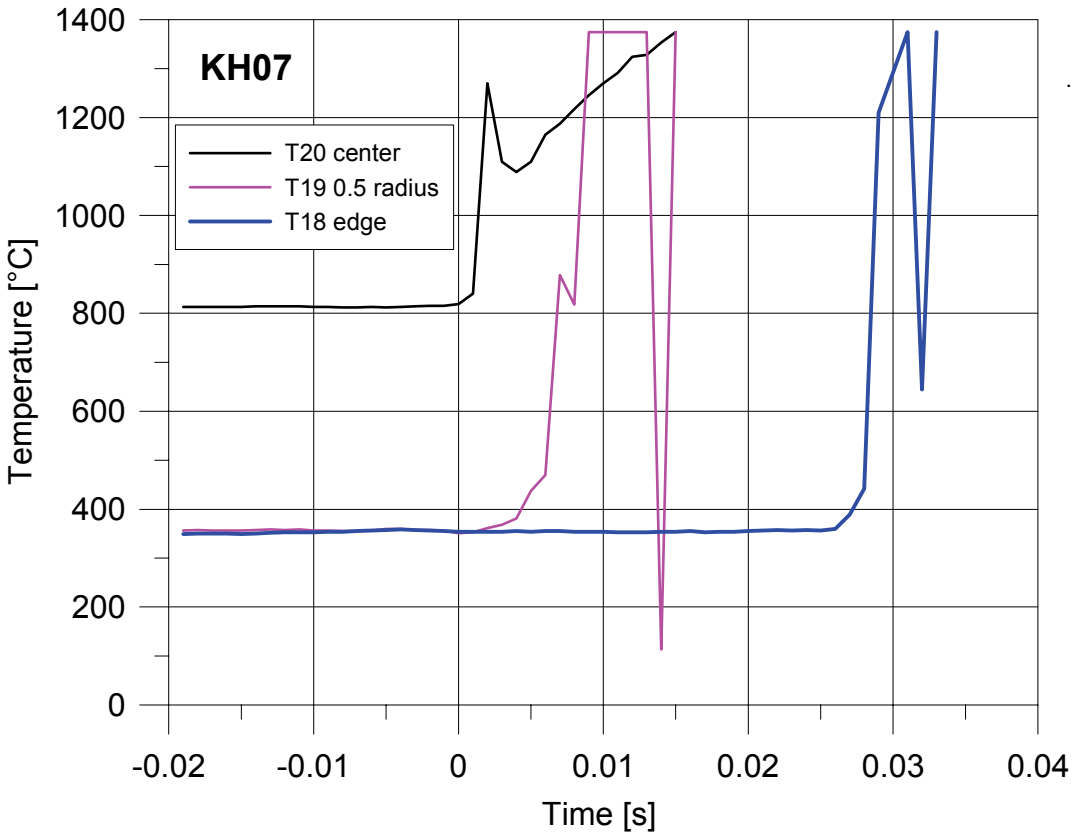

Fig. 4-147. KH07: Thermocouple signals in melt plug, zoom to t = 0 s

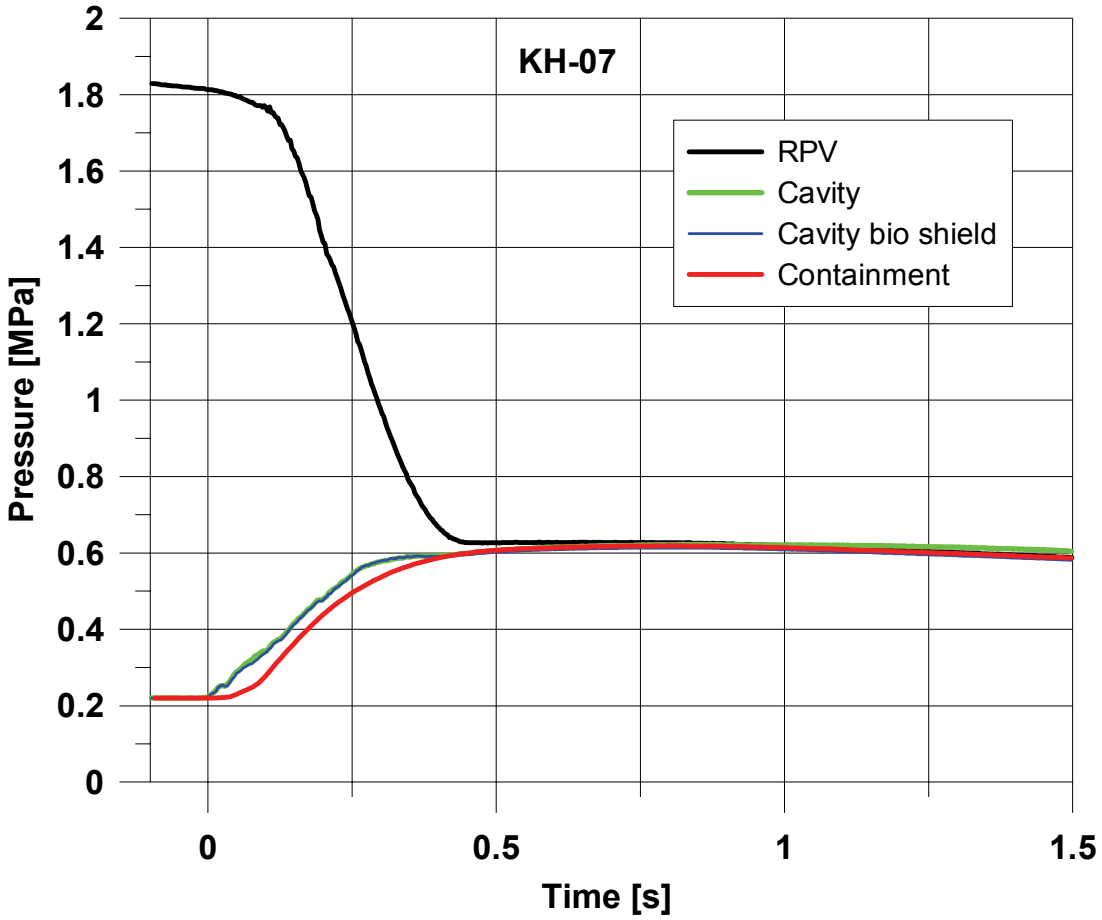

Fig. 4-148. KH07: Pressure in RPV vessel, cavity and containment

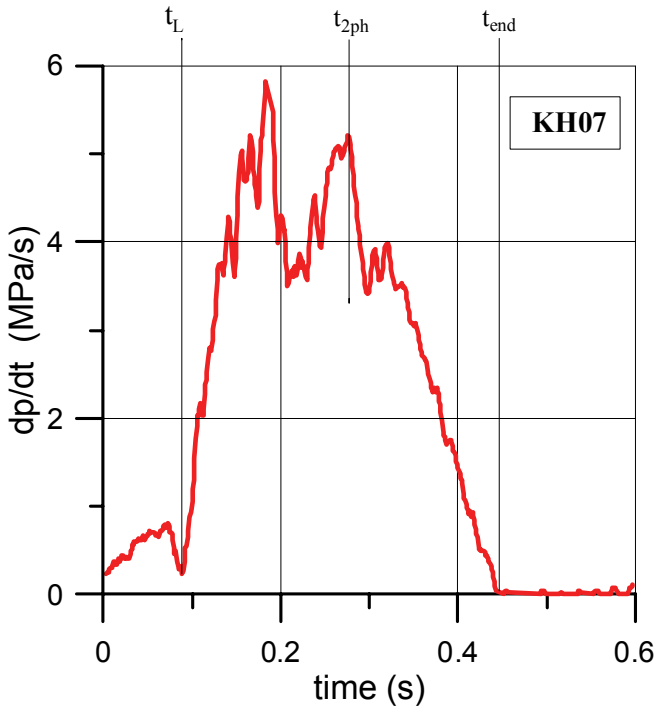

Fig. 4-149. KH07: Pressure gradient in RPV vessel

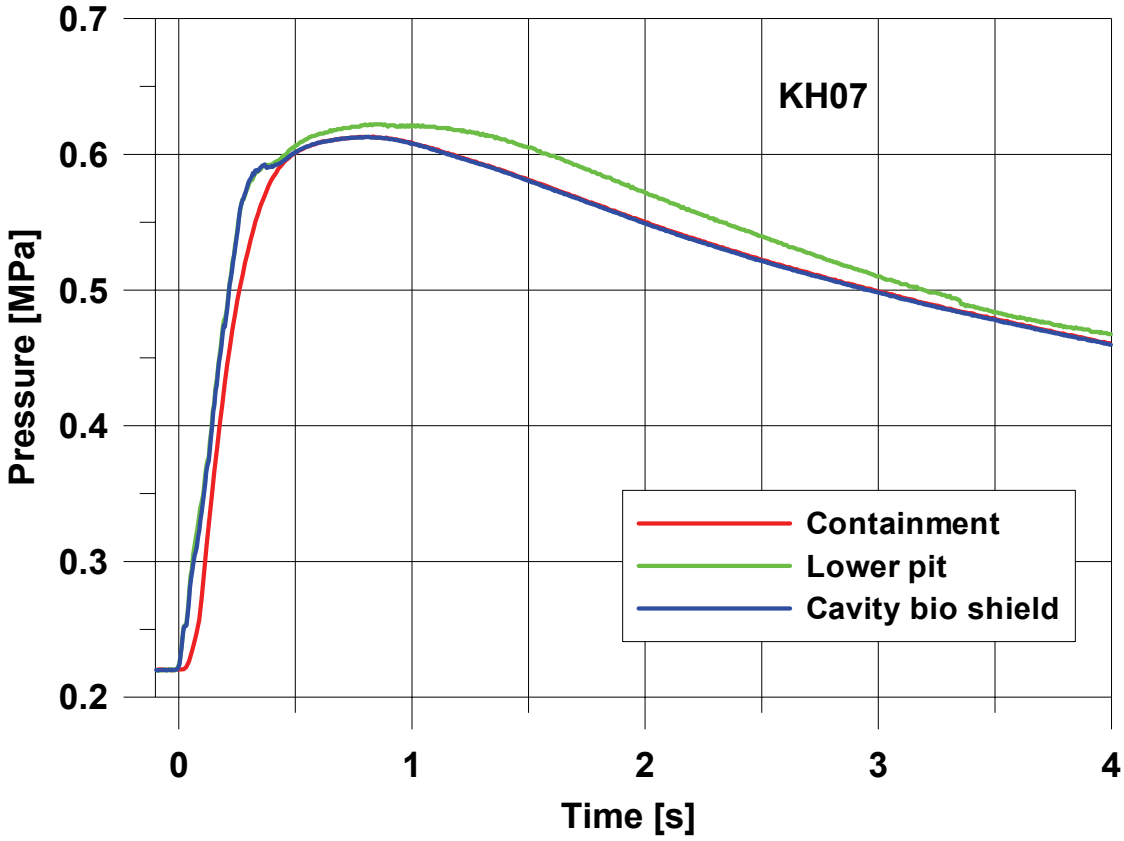

Fig. 4-150. KH07: Pressure in cavity and containment

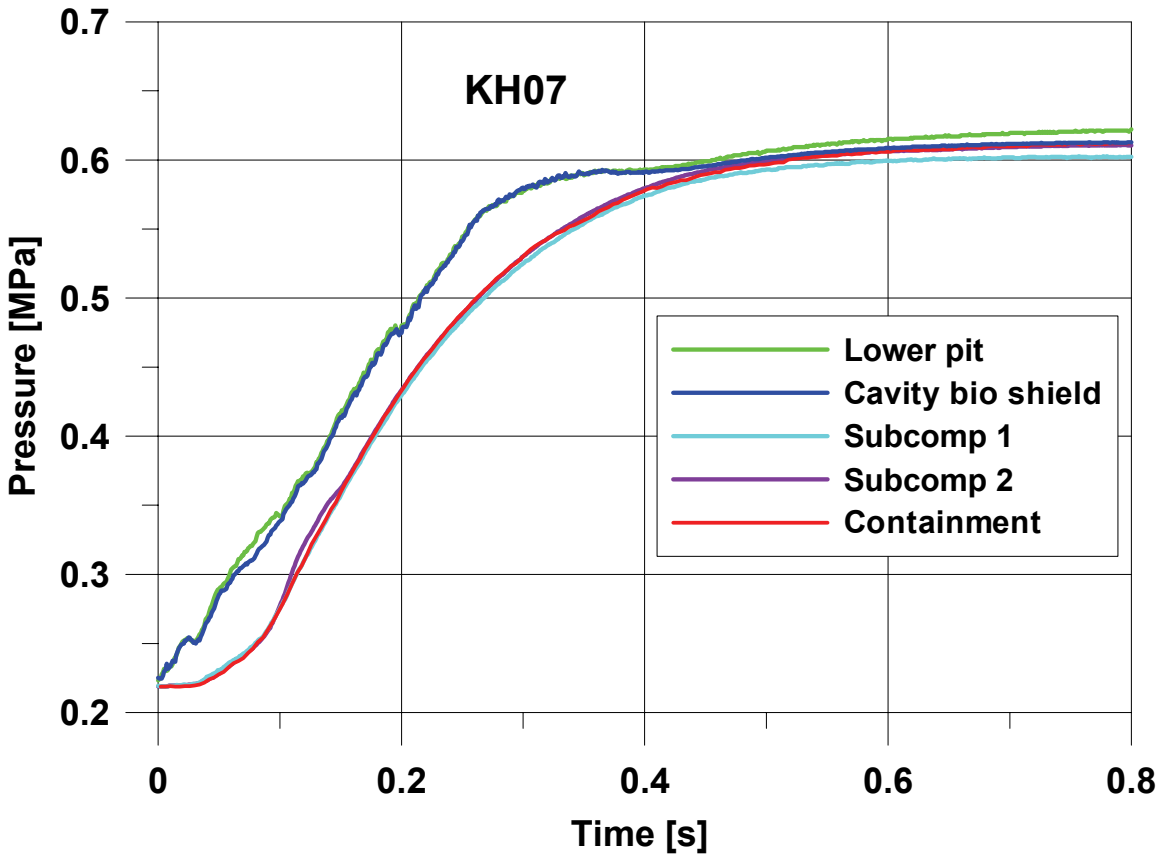

Fig. 4-151. KH07: Pressure in cavity, subcompartment and containment

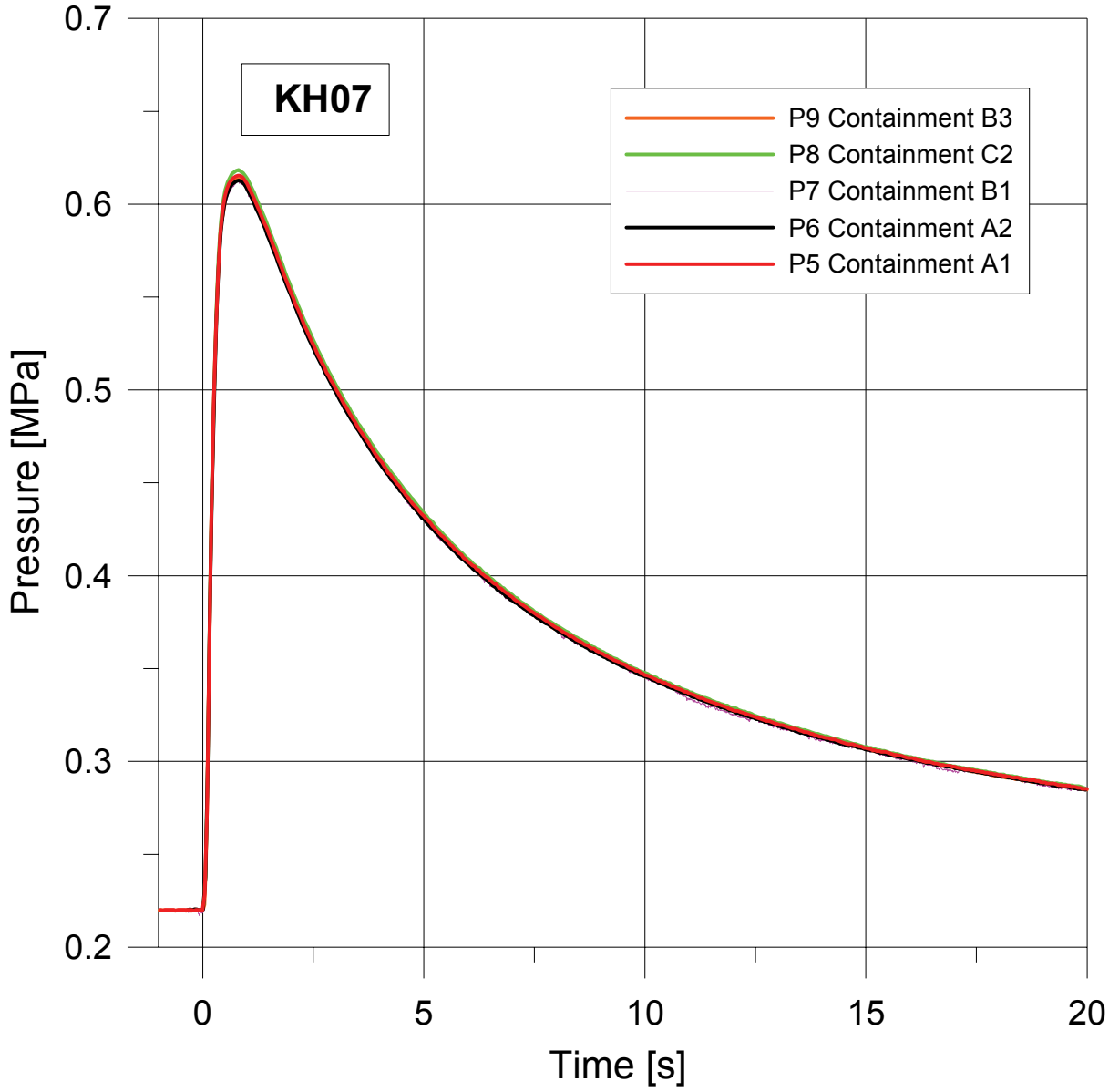

Fig. 4-152. KH07: Pressure in containment

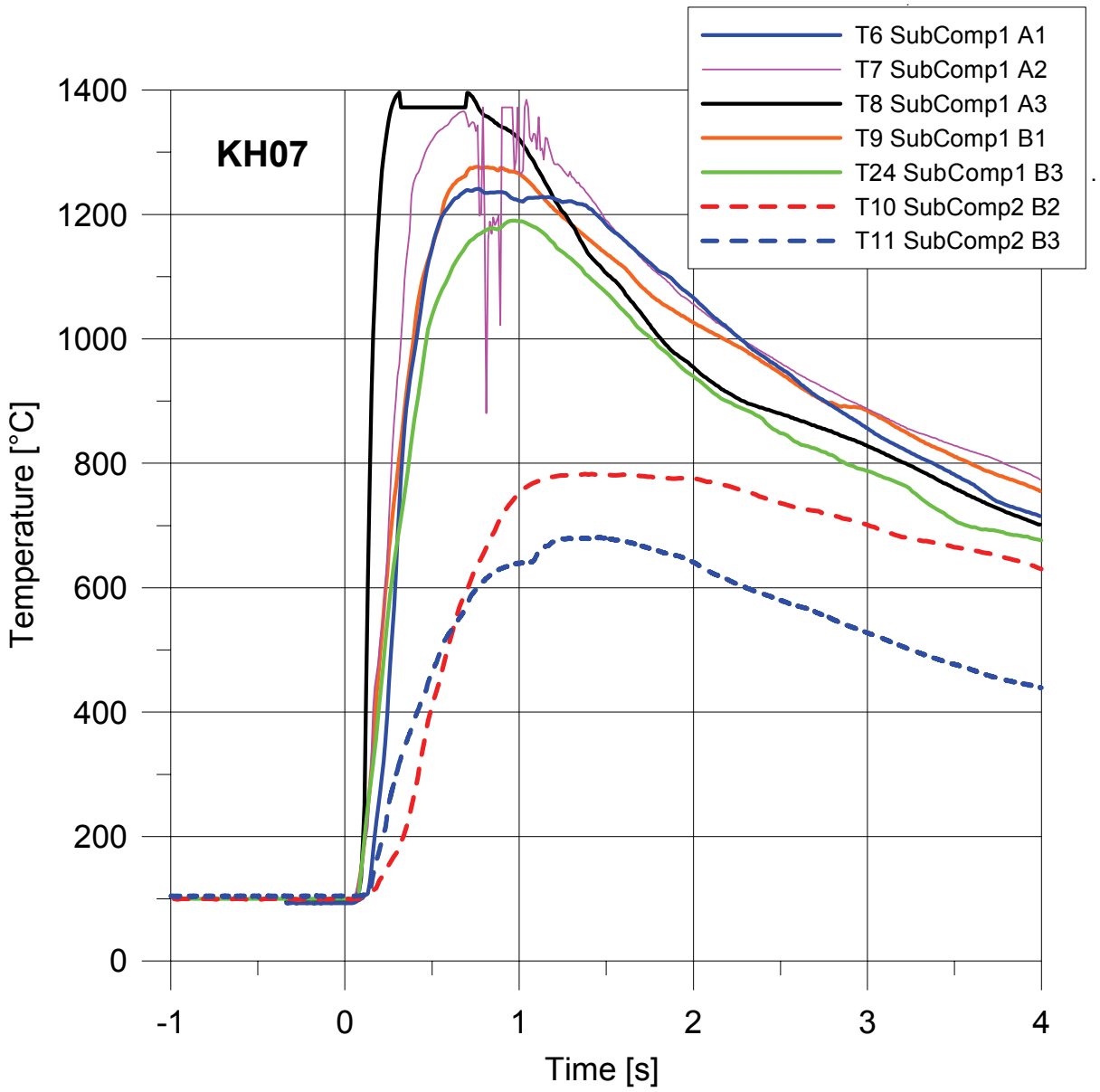

Fig. 4-153. KH07: Temperatures in subcompartments 1 and 2

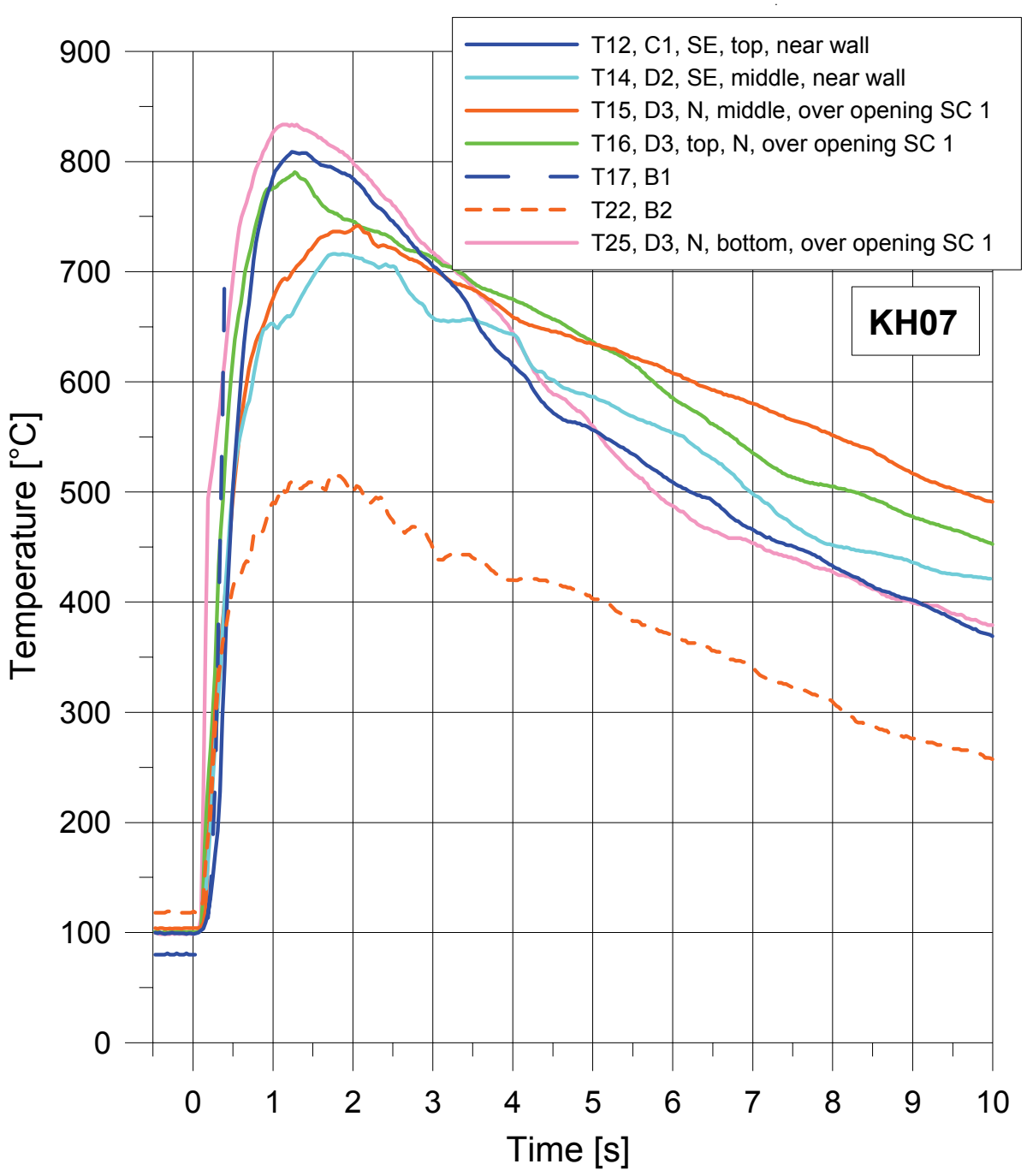

Fig. 4-154. KH07: Temperatures in containment

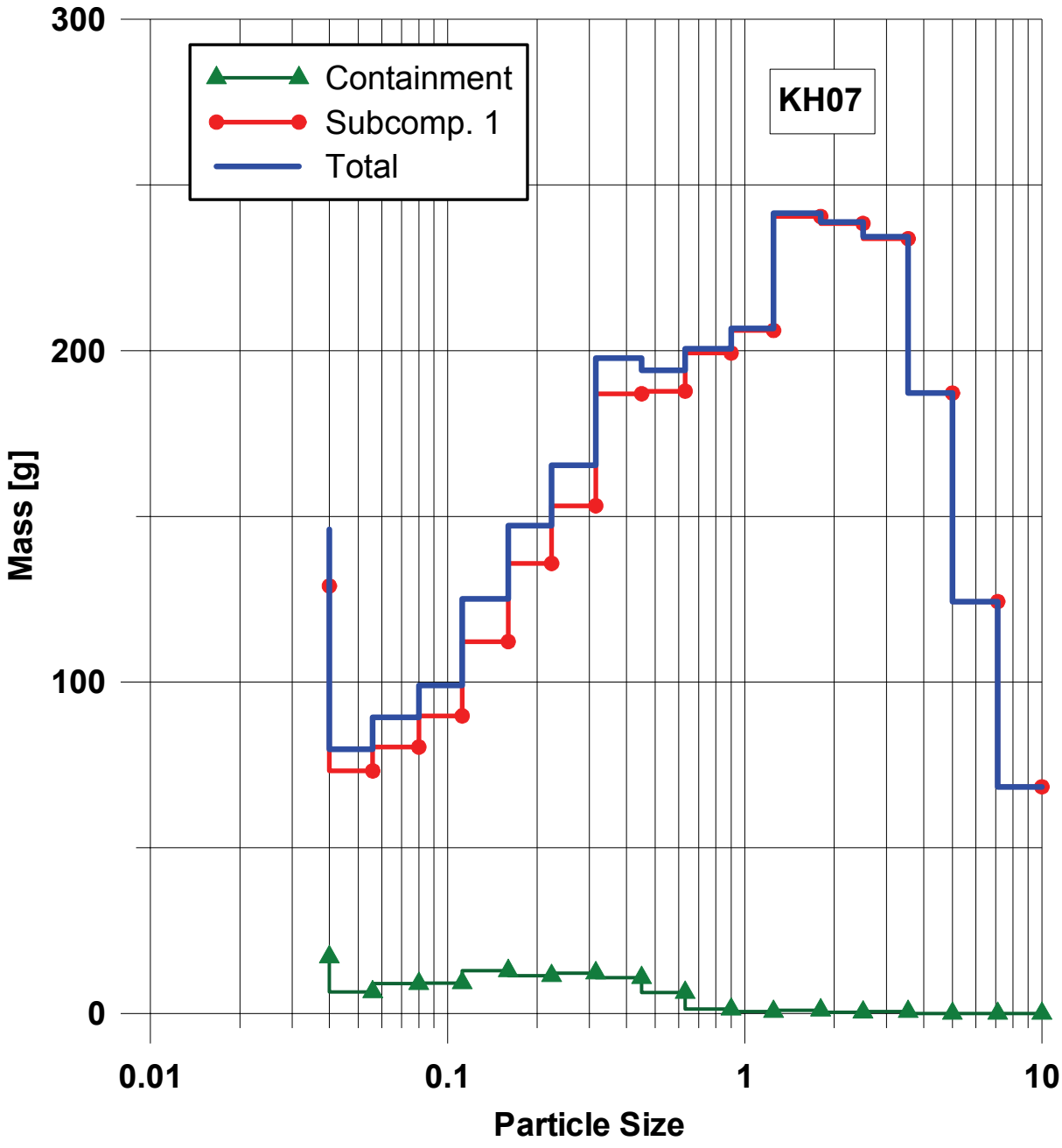

Fig. 4-155. KH07: Size distribution of particles smaller than 10 mm

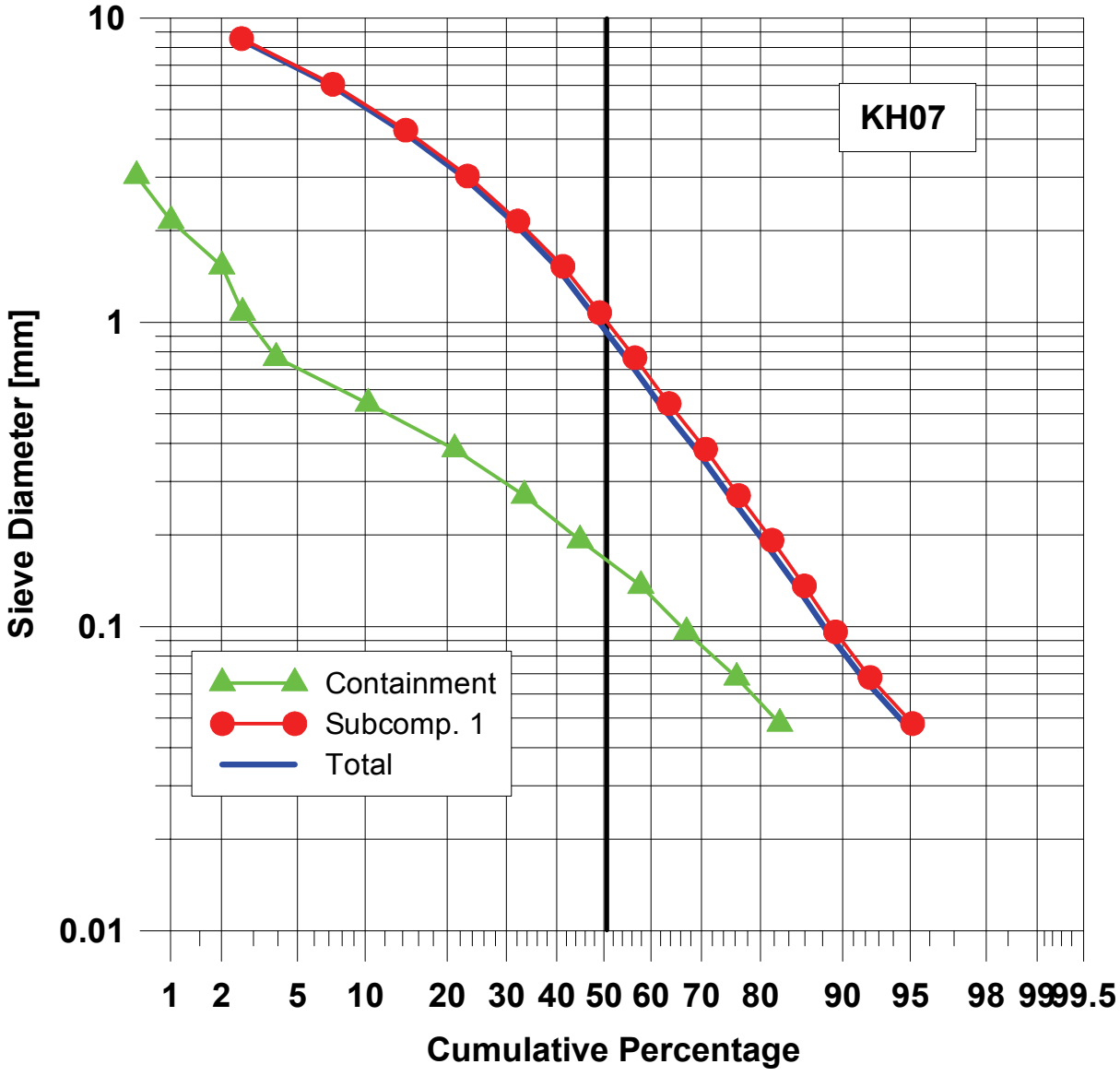

Fig. 4-156. KH07: Cumulative particle size distribution of debris smaller 10 mm

Fig. 4-157. KH07: Posttest view of RPV

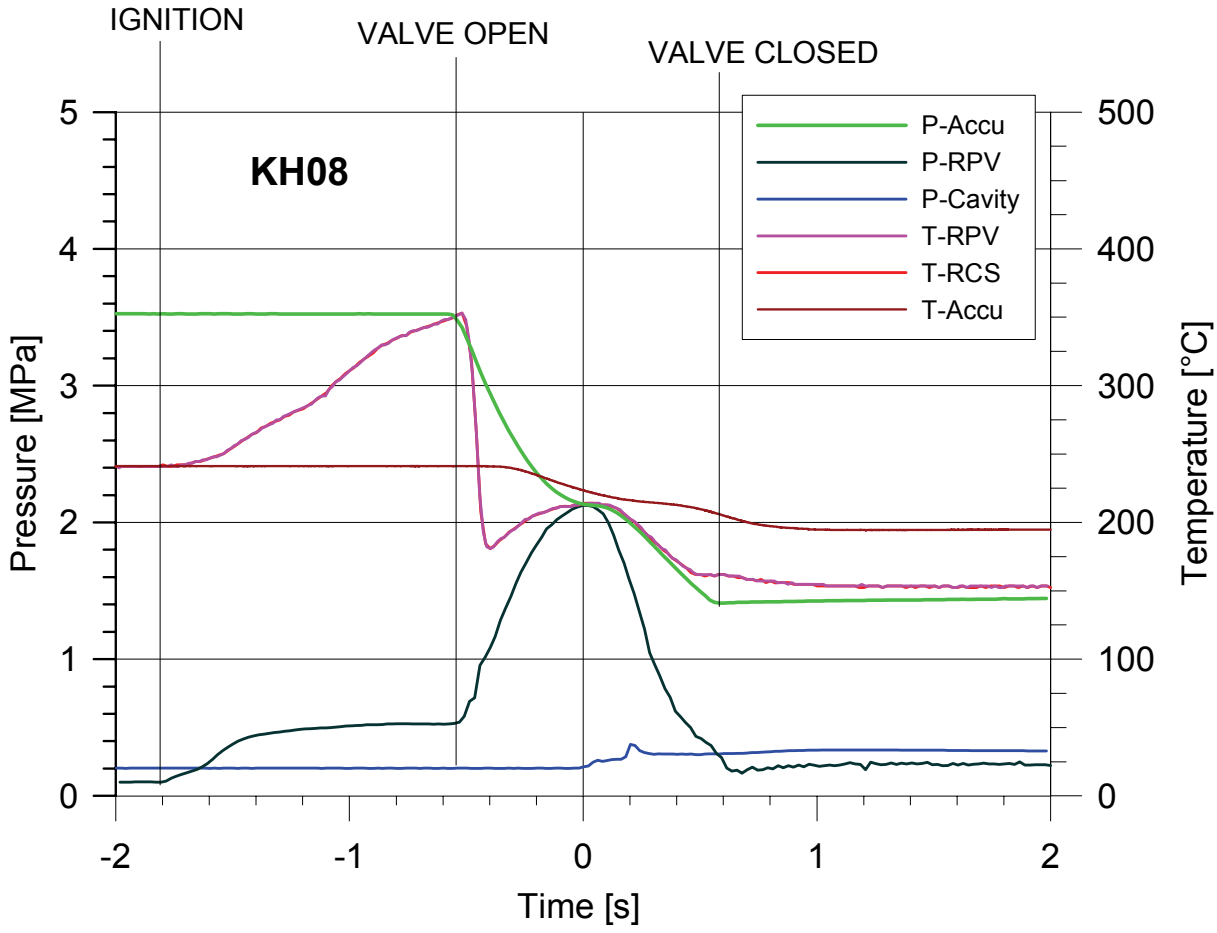

Fig. 4-158. KH08: Pressure, temperature and timing

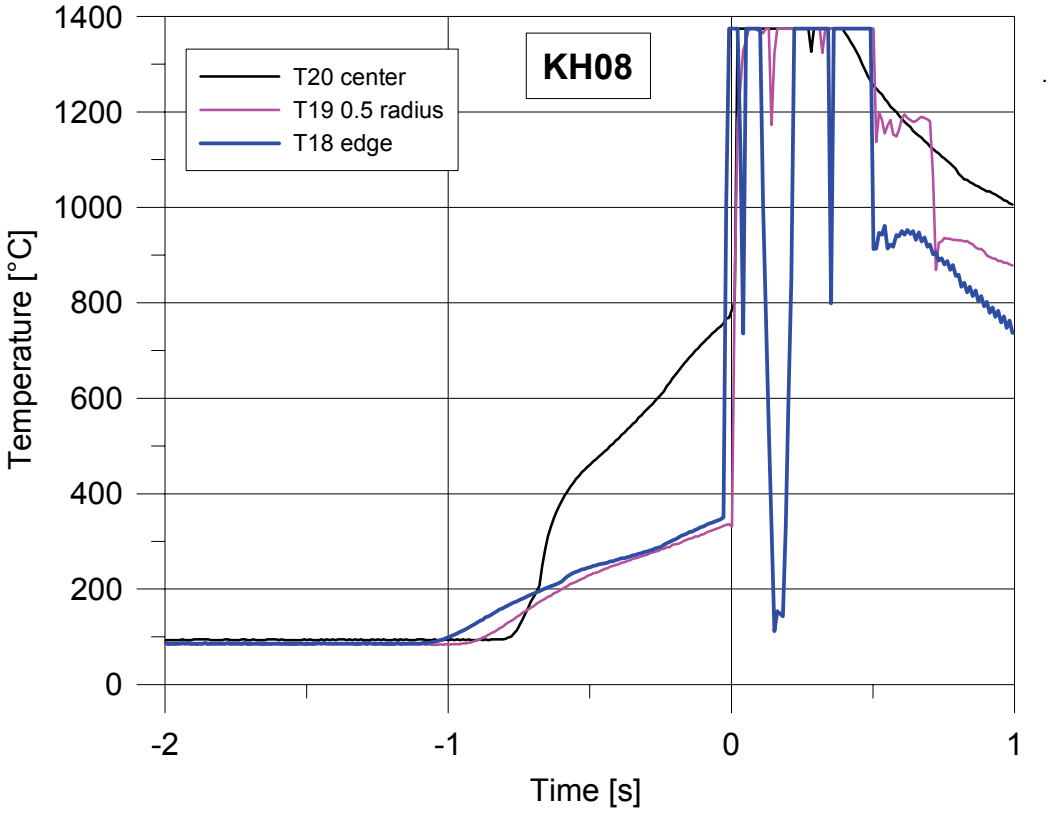

Fig. 4-159. KH08: Thermocouple signals in melt plug

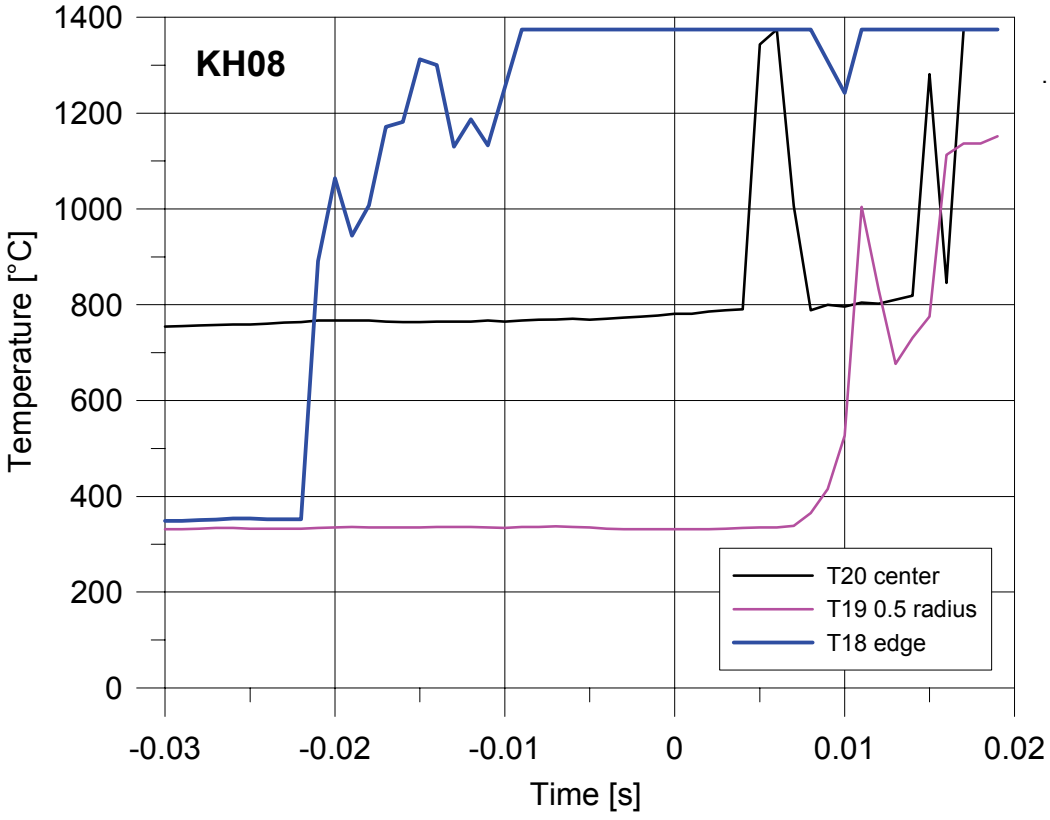

Fig. 4-160. KH08: Thermocouple signals in melt plug, zoom to t = 0 s

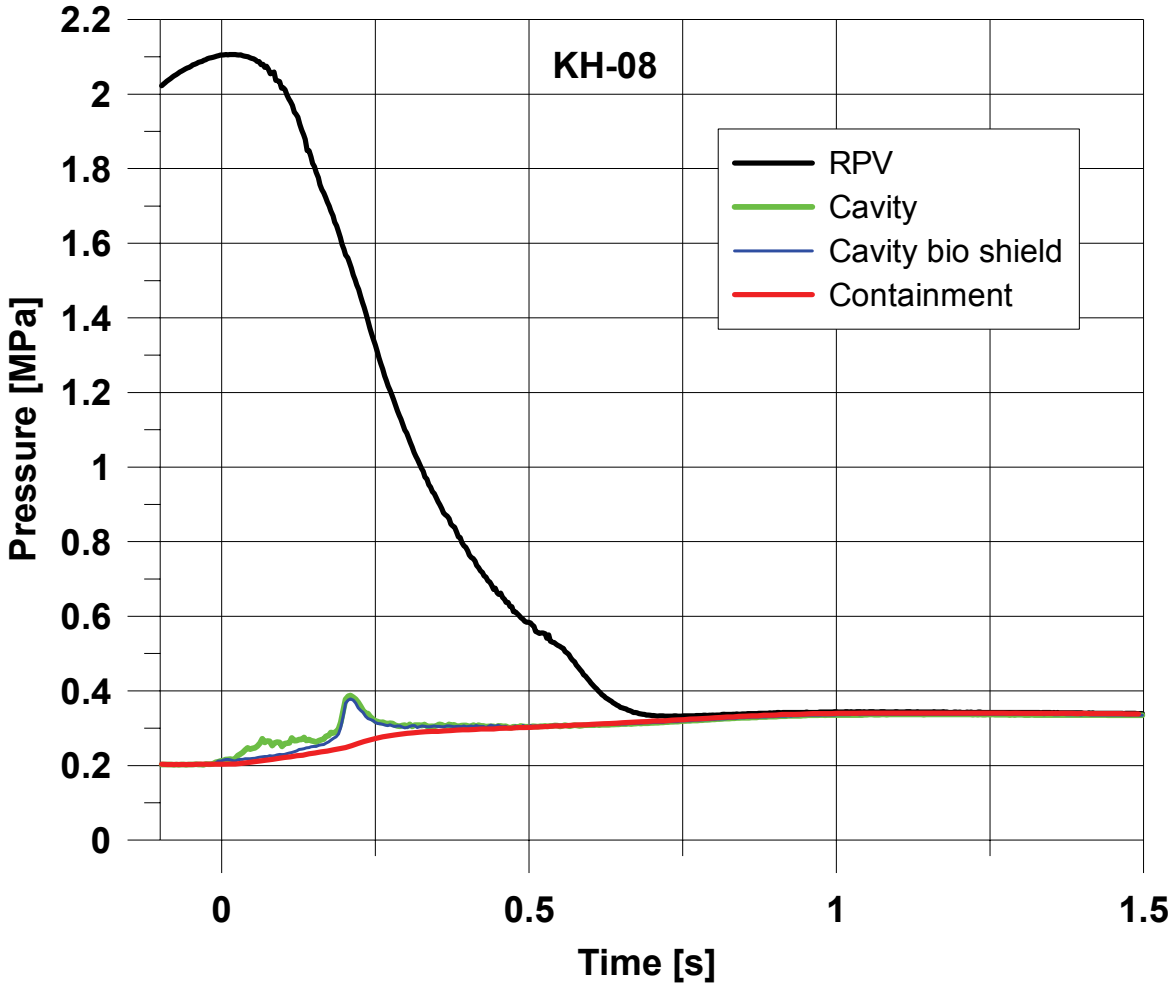

Fig. 4-161. KH08: Pressure in RPV vessel, cavity and containment

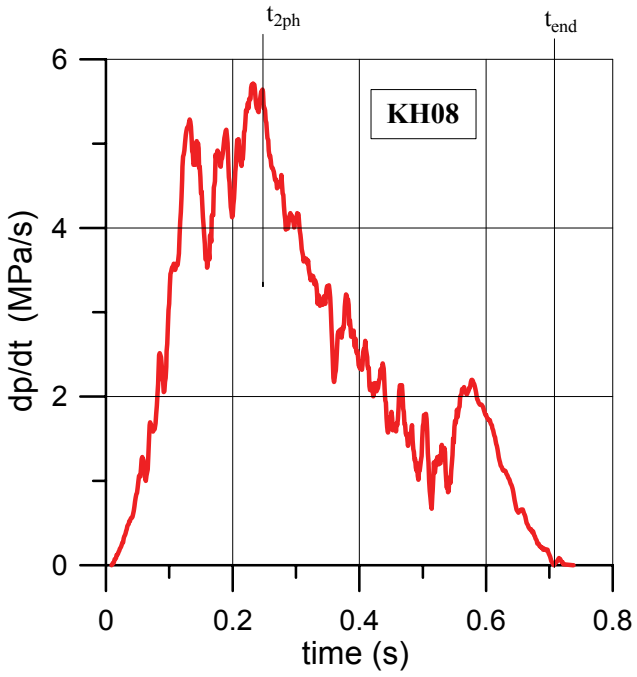

Fig. 4-162. KH08: Pressure gradient in RPV vessel

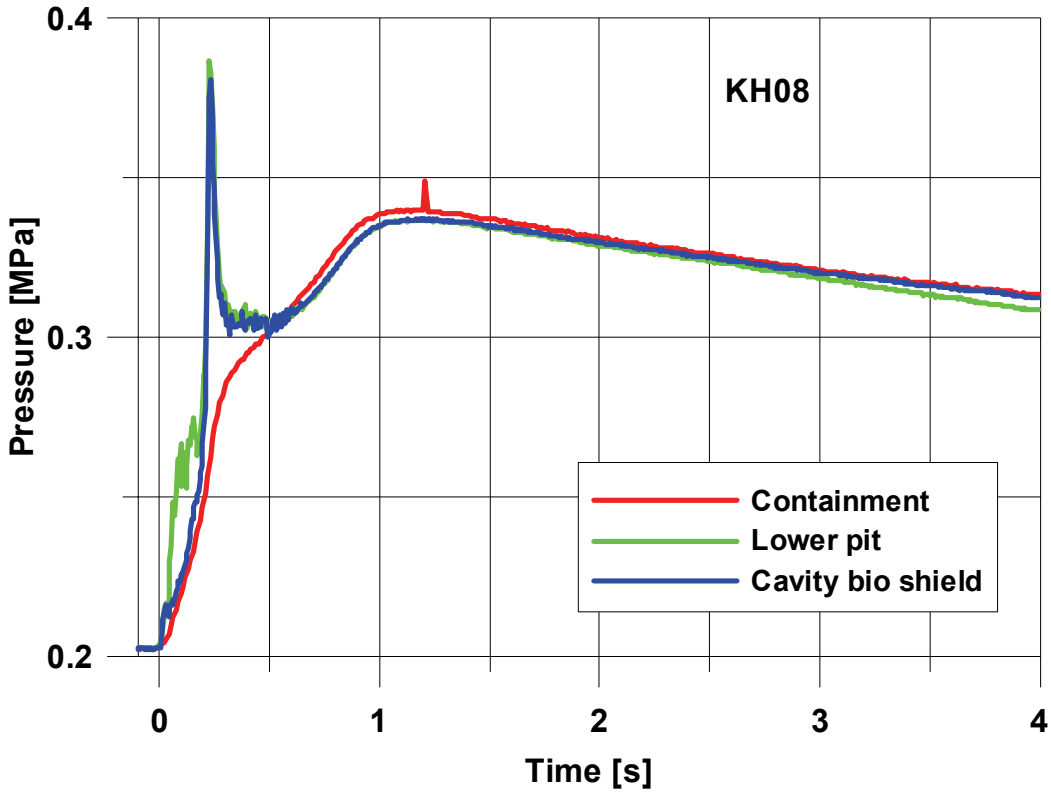

Fig. 4-163. KH08: Pressure in cavity and containment

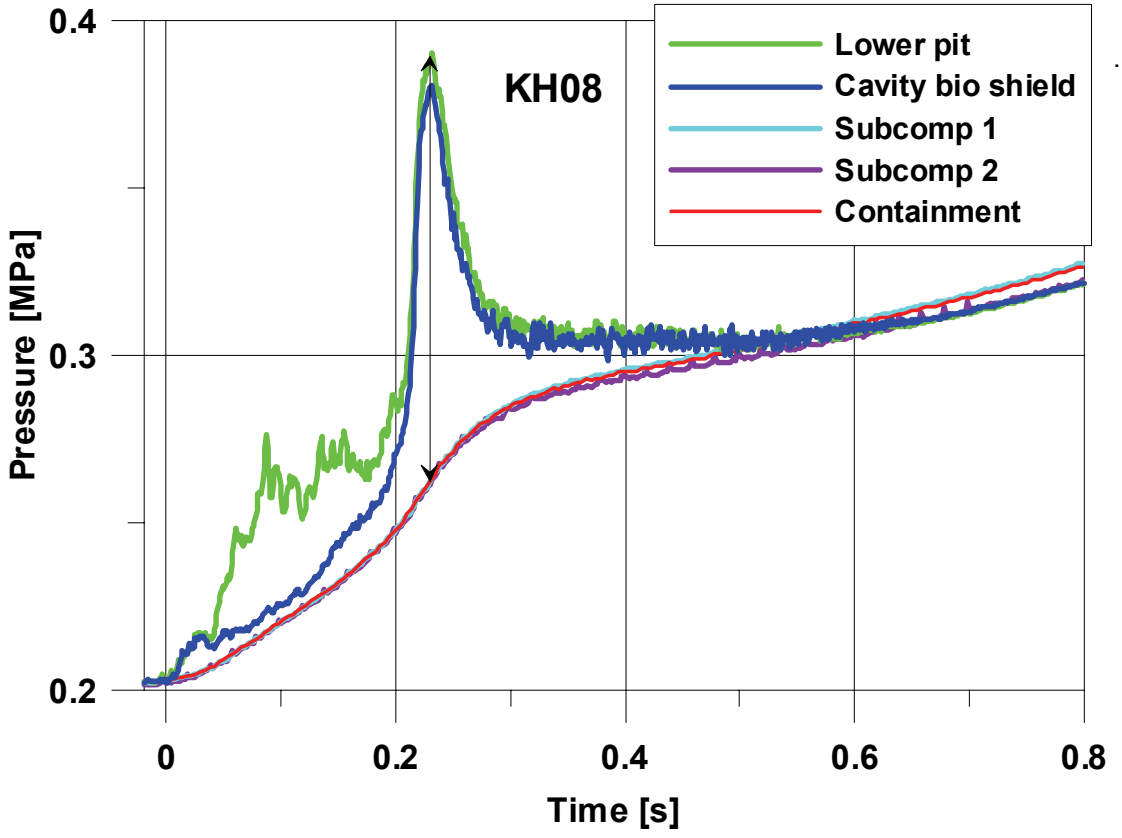

Fig. 4-164. KH08: Pressure in cavity, subcompartment and containment
Δp = 0.126 MPa

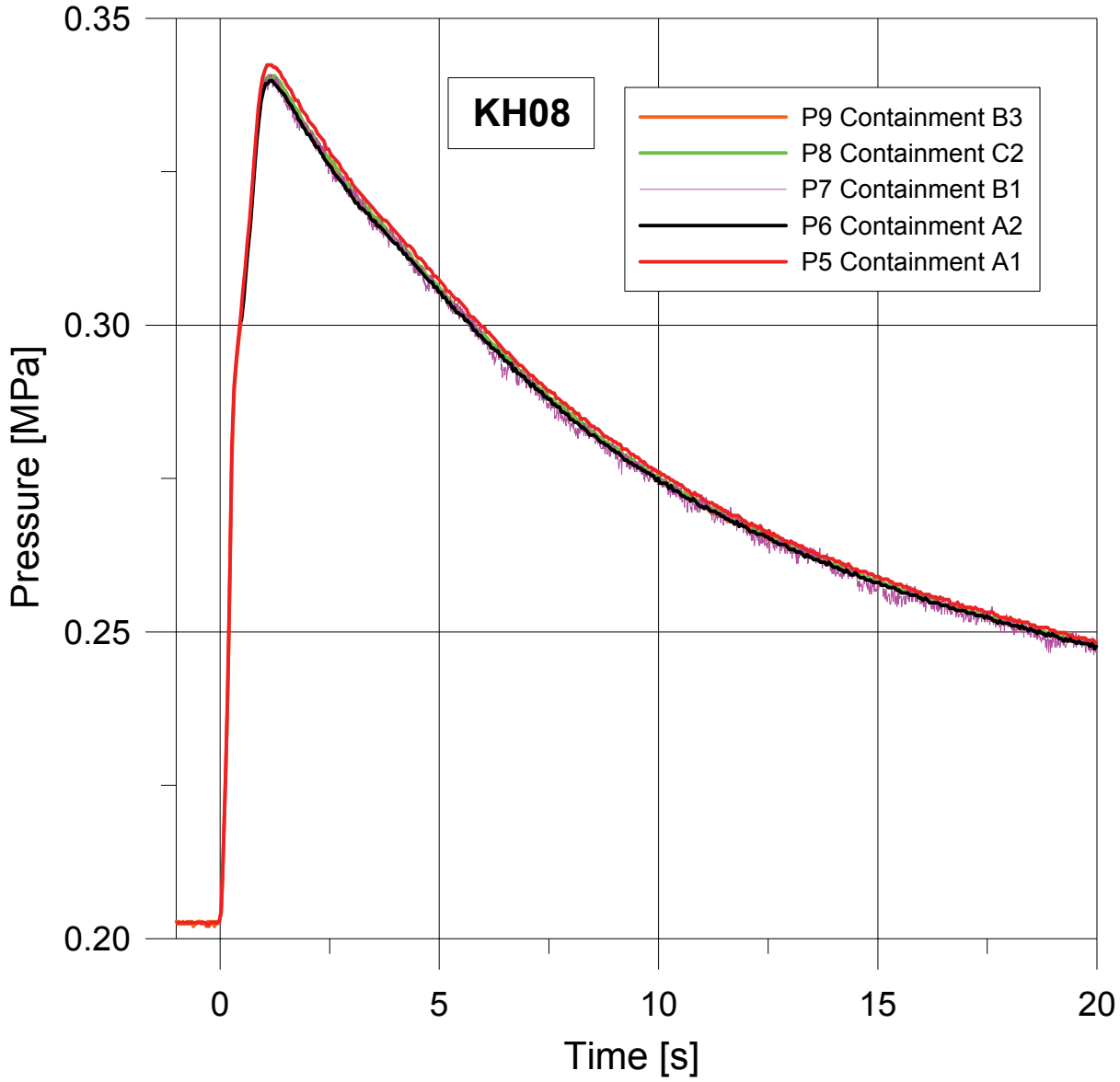

Fig. 4-165. KH08: Pressure in containment

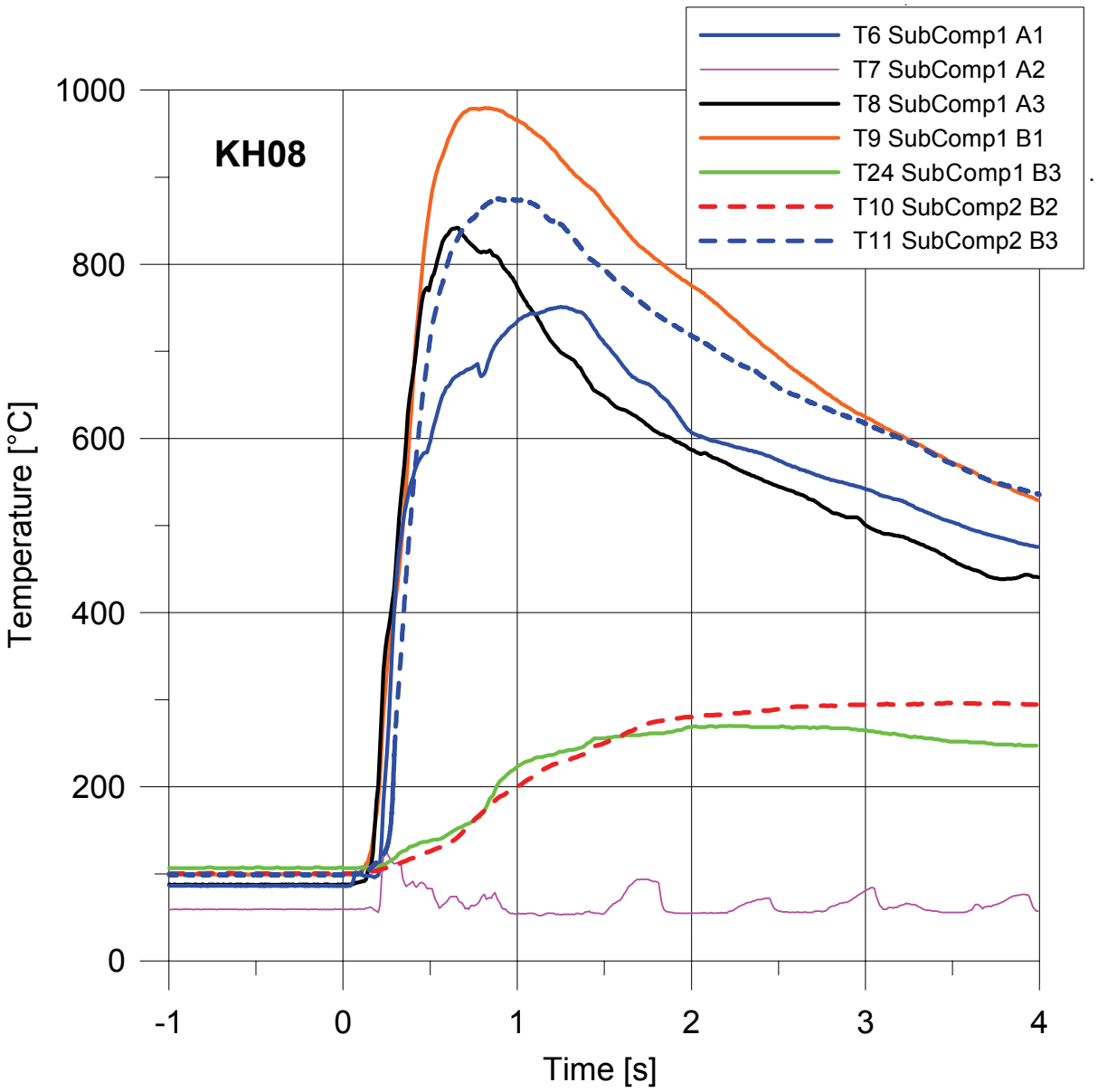

Fig. 4-166. KH08: Temperatures in subcompartments 1 and 2

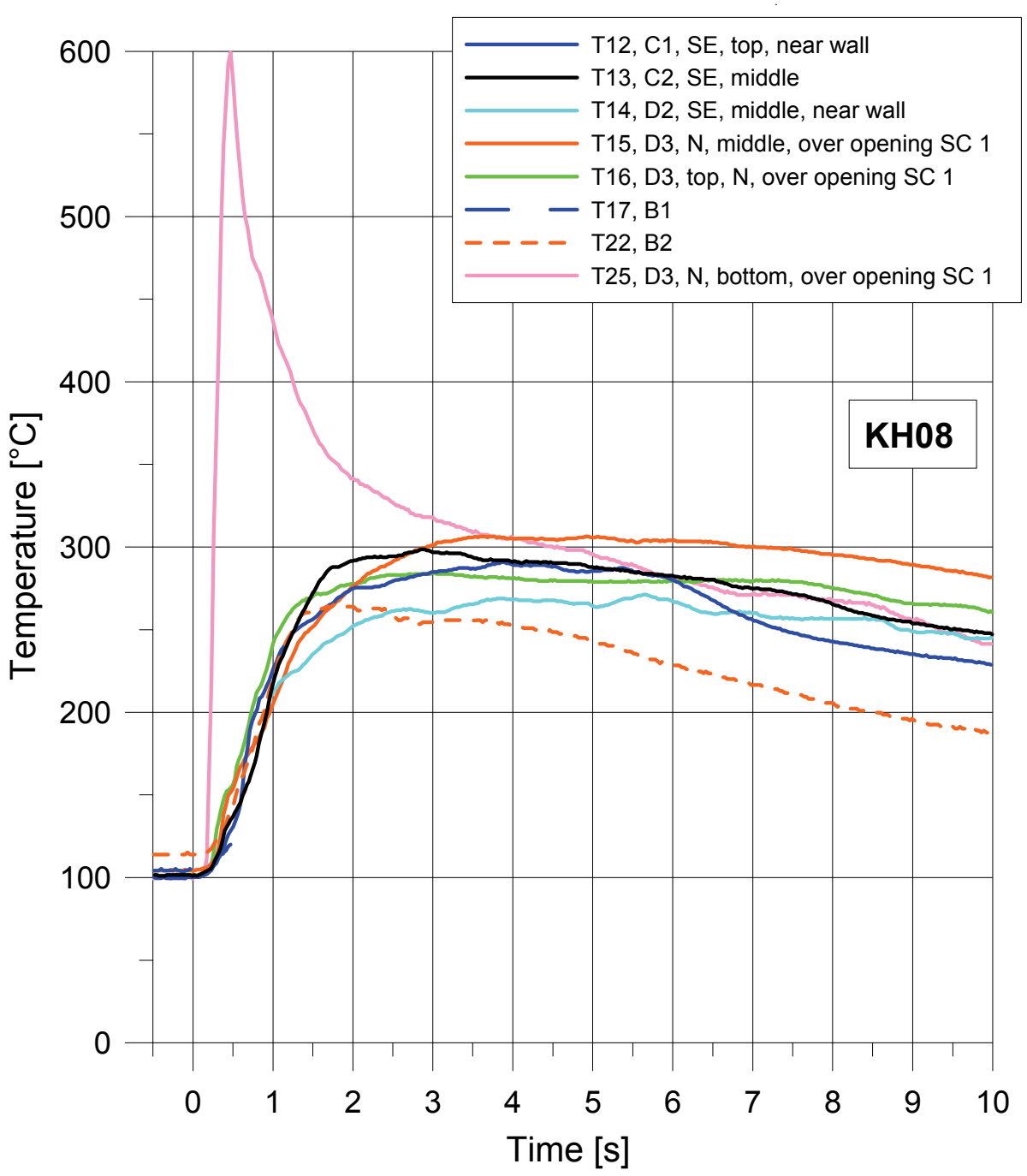

Fig. 4-167. KH08: Temperatures in containment

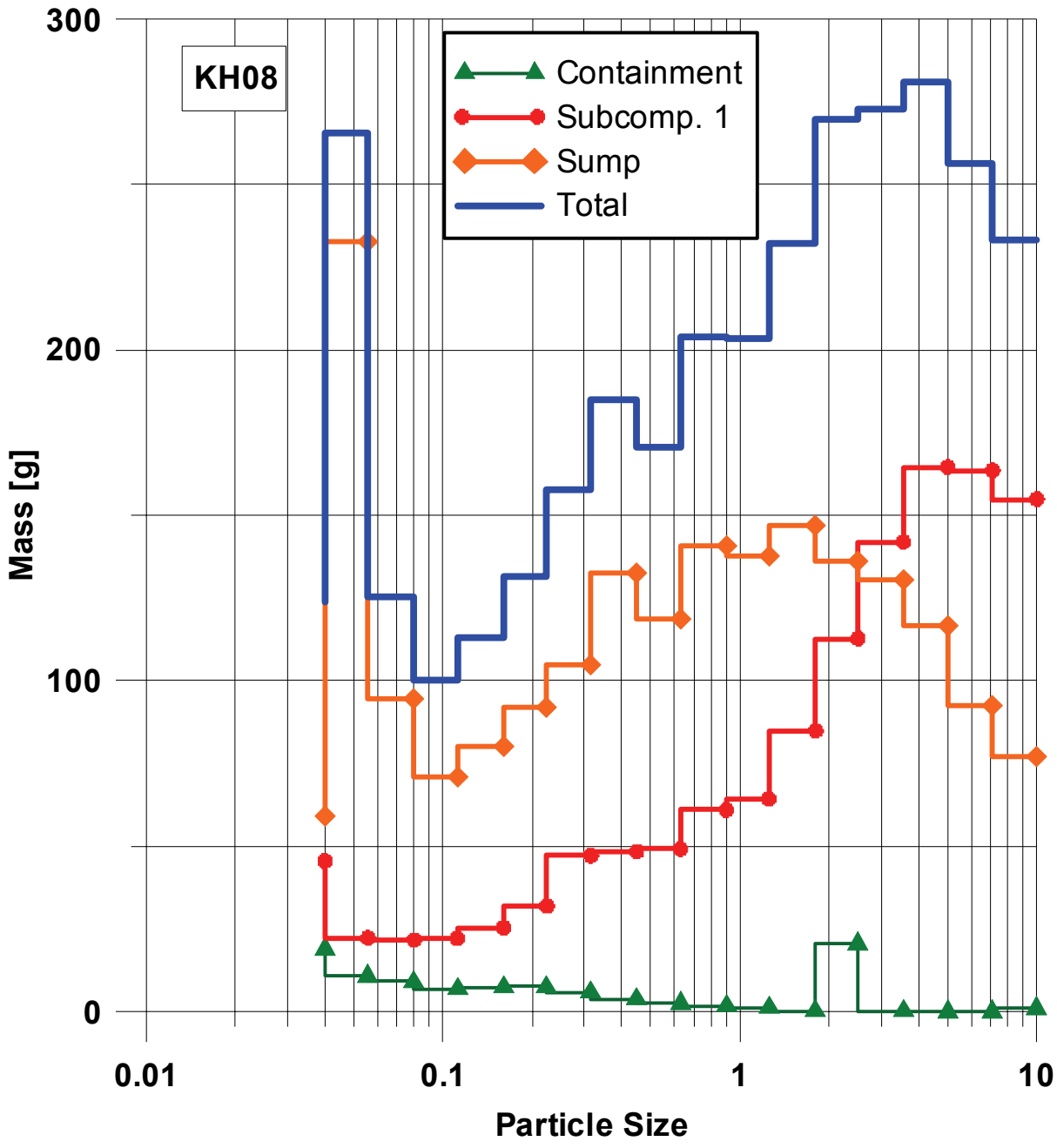

Fig. 4-168. KH08: Size distribution of particles smaller than 10 mm

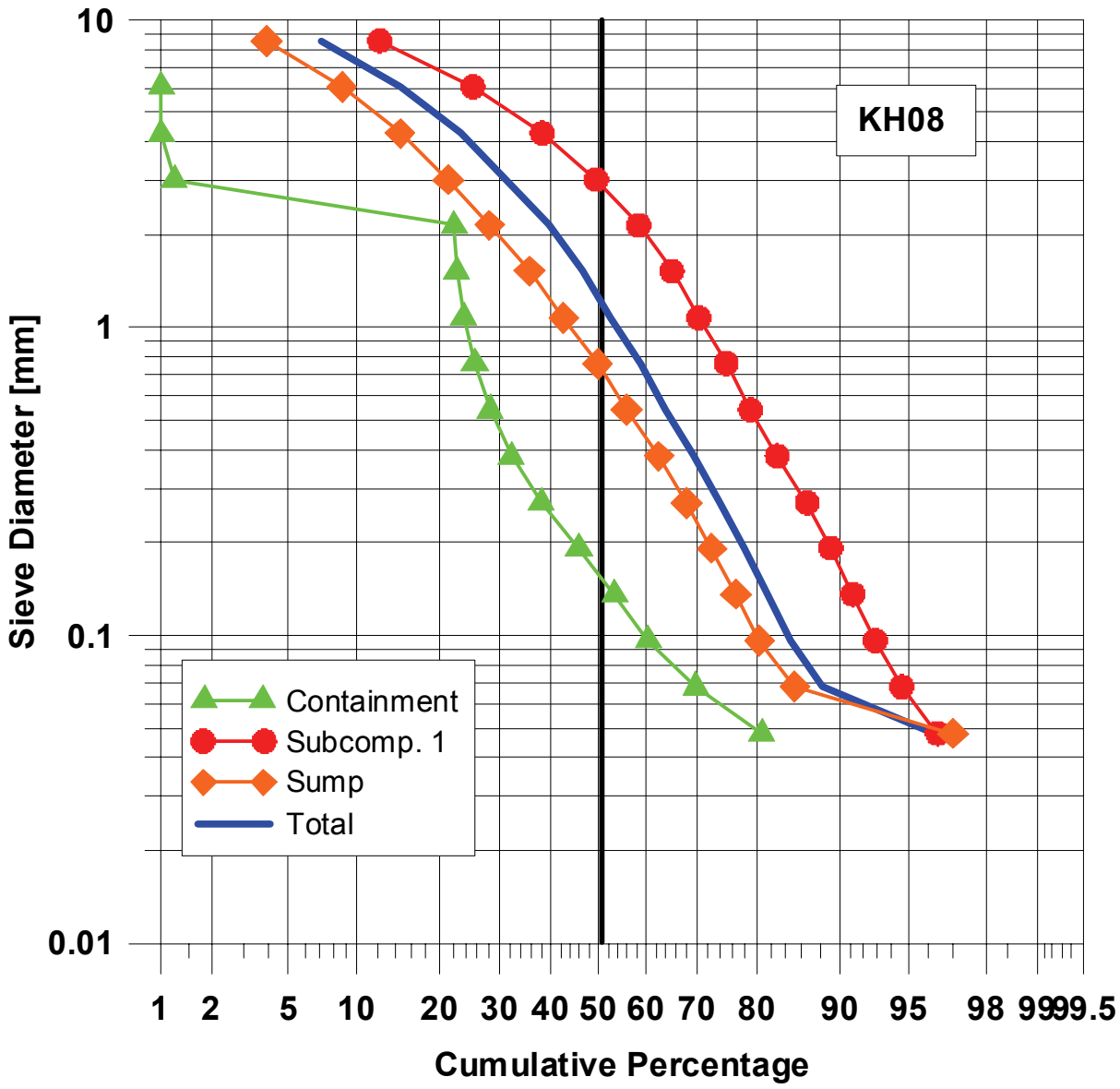

Fig. 4-169. KH08: Cumulative particle size distribution of debris smaller 10 mm

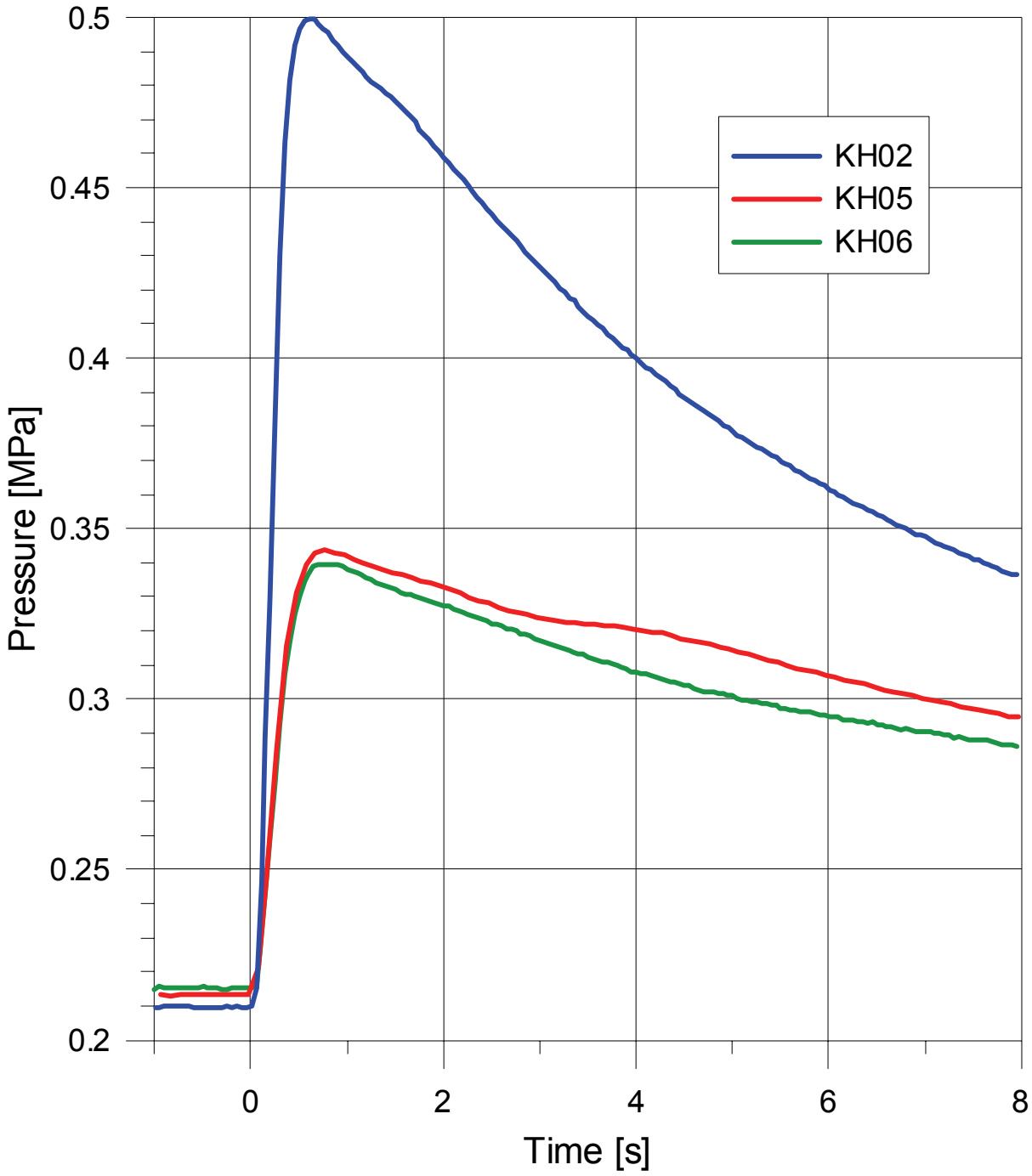

Fig. 4-170. Pressure increase in the containment vessel with different RPV pressures

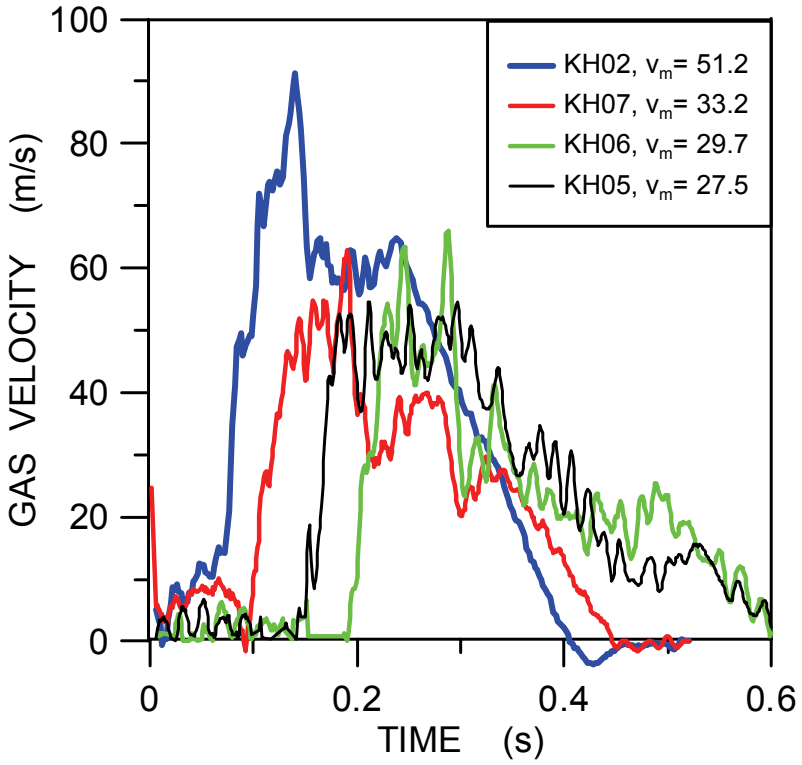

Fig. 4-171. Steam velocity in cavity annular gap around RPV

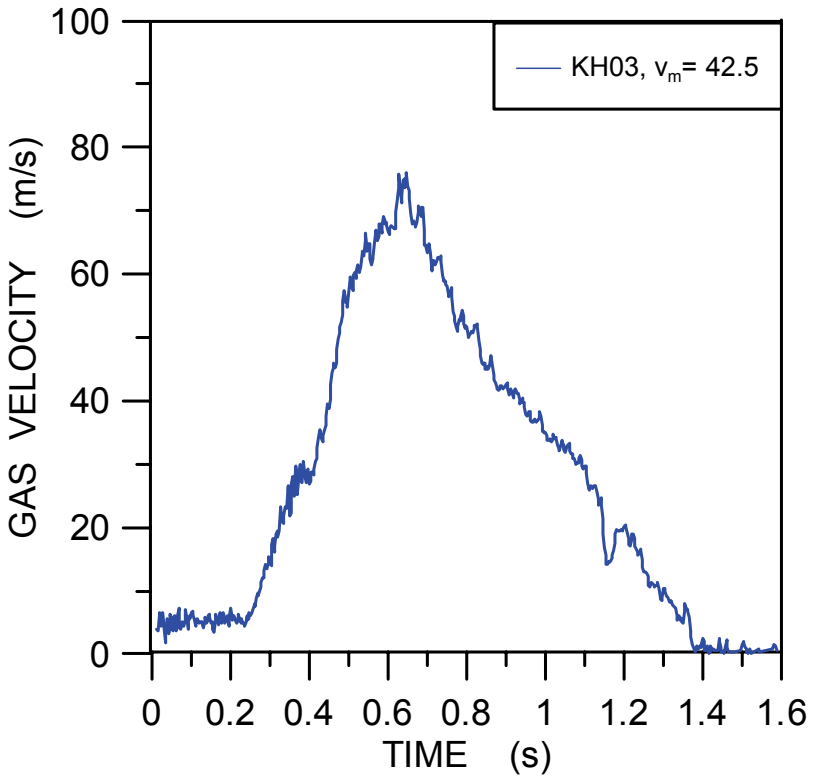

Fig. 4-172. Steam velocity in cavity annular gap around RPV

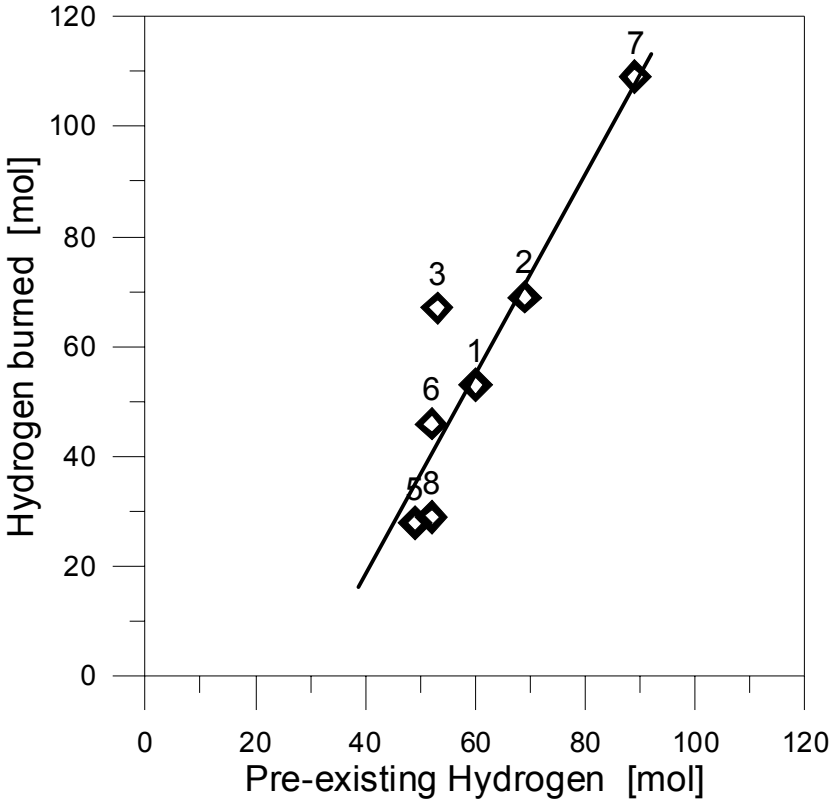

Fig. 4-173. Amount of burned hydrogen over pre-existing hydrogen

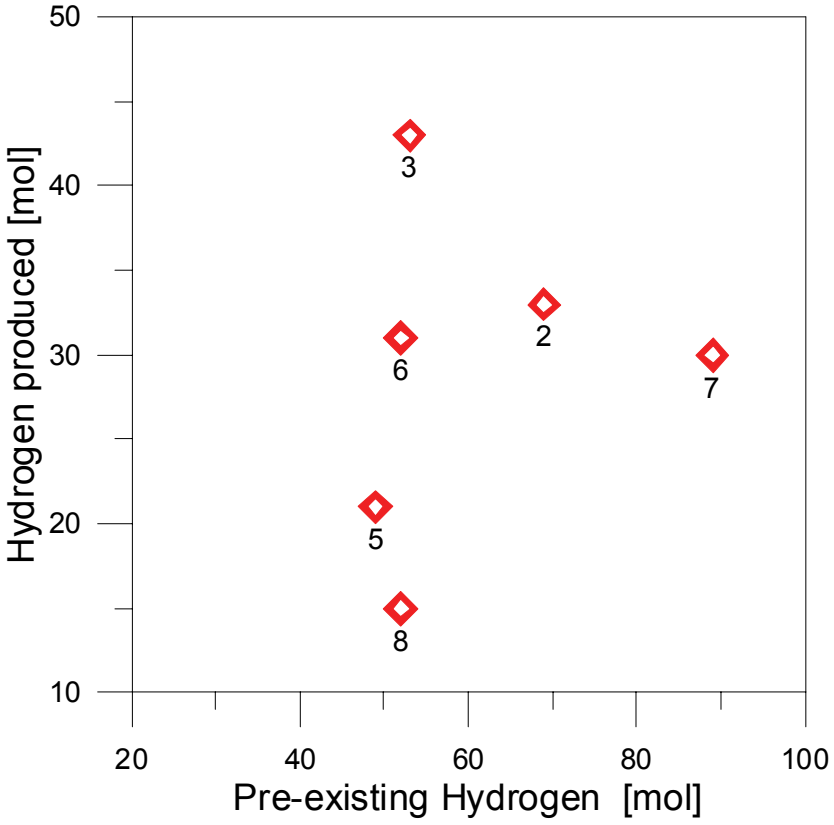

Fig. 4-174. Amount of produced hydrogen over pre-existing hydrogen

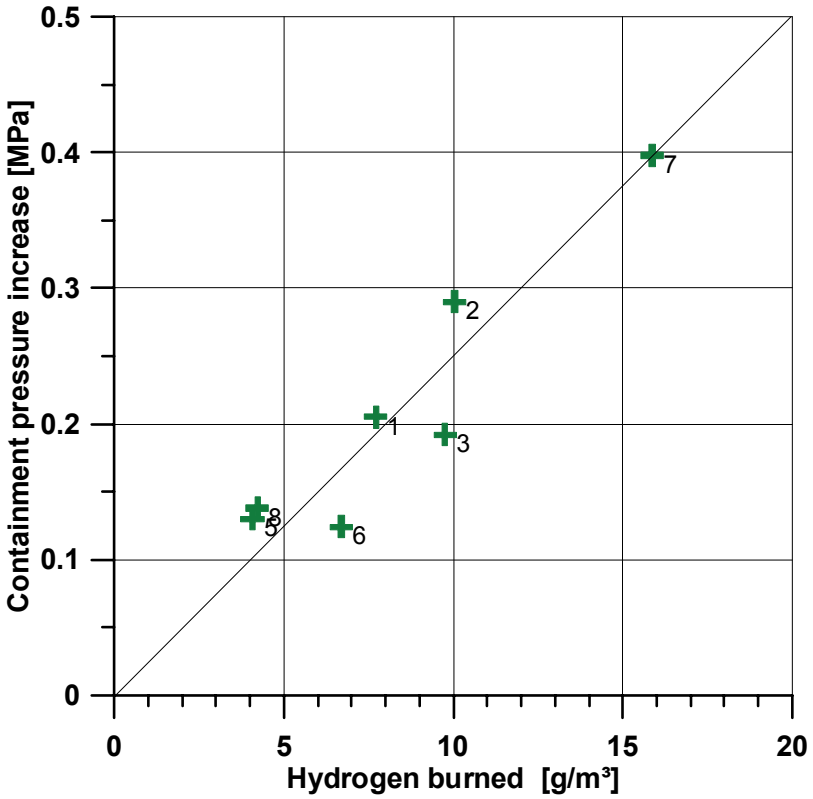

Fig. 4-175. Measured pressure increase in containment over burned hydrogen per volume

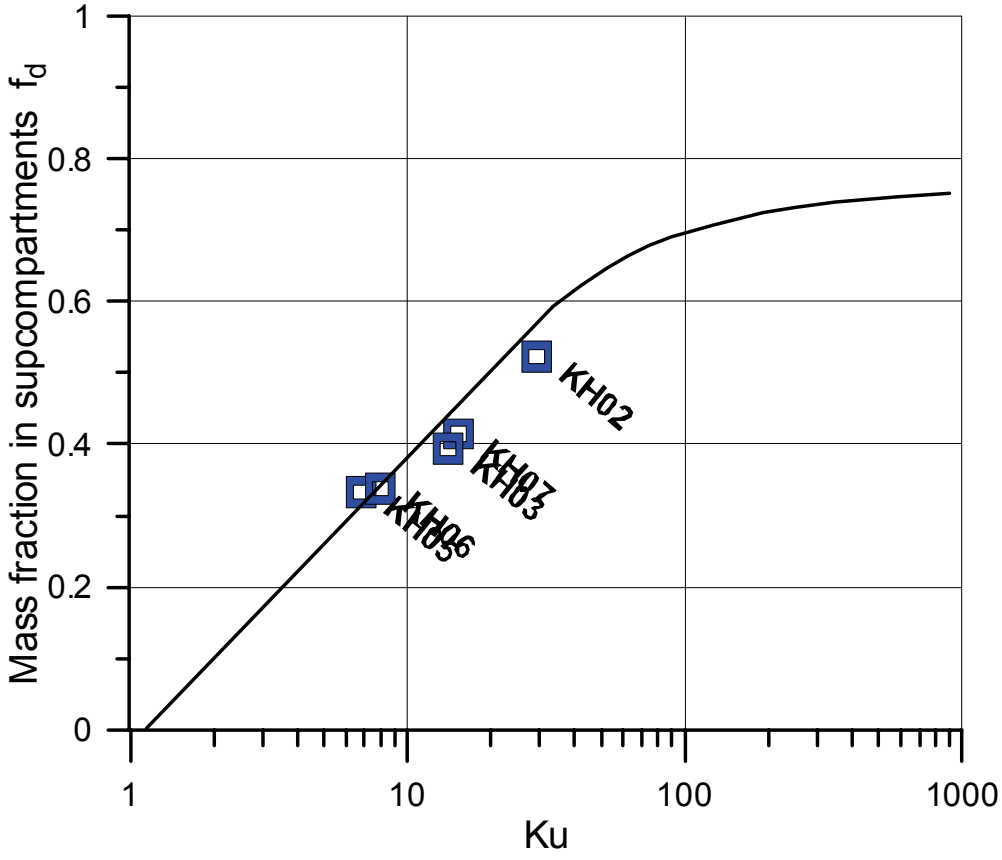

Fig. 4-176. Correlation of dispersed melt fraction with KUTATELADSE Number

5 Conclusions

In the past extensive investigations had been performed for the EPR and a large data base exists for this geometry [Mey03], [Mey04], [Mey06]. The geometries of the reactor pit of the Konvoi plant and the EPR are similar with two distinct differences regarding the flow paths out of the lower pit:

(1) The vessel support structure in the Konvoi plant is above the main cooling lines and sealing-plates block the direct flow path (B) into the refueling room above unless the overpressure in the pit is more than 0.2 MPa. In the EPR the vessel support structure is below the main cooling lines and sealing plates above withstand a higher pressure so the flow path into the refueling room can be considered to be closed for all possible DCH cases.

(2) The Konvoi cavity has a biological shield, which by itself does not have any effect on melt dispersion out of the pit. However, pressure venting flaps behind the shield must be assumed to be open and serve as a large path (C) into the neighboring compartments. The path could be blocked by water if its level is high enough. In any case, melt falling behind the bio-shield would be quenched by water.

Eight tests were performed in Konvoi geometry with holes in the center of the RPV lower head, using an iron-alumina melt driven out of the RPV by steam, and an atmosphere of air, steam and hydrogen of 0.2 MPa in the containment vessel.

The base case of the tests series was chosen with both flow paths (B and C) closed (test KH02). The standard flow path (A) out of the pit was that along the 8 main cooling lines leading into subcompartment 1. To investigate the effect of the breach size test KH03 was conducted with a smaller hole in the lower head. Tests KH05 and KH06 were performed with lower RPV pressures and test KH07 with a higher hydrogen concentration in the containment atmosphere. In test KH04 (and KH01, but leaks prevent a clear conclusion) the flow path (B) into the refueling room was open. Test KH08 was conducted with open pressure venting flaps (C) and a water level behind the bio-shield and in subcompartment 1 which did not block this flow path.

The base case, test KH02, showed a pressure increase in the containment of 0.29 MPa, which is higher than what was seen in the EPR series [Mey04]. The comparable EPR test H03 yielded a pressure increase of 0.114 MPa, however the initial conditions were different: RPV pressure only 1.25 MPa vs. 2.0 MPa in KH02 and hydrogen concentration in containment 2.7% vs. 5.4%. The pressure rise of 0.130 MPa in test KH05, with a RPV pressure of 1.18 MPa was only little higher than the EPR case, but again it had a higher hydrogen concentration. Hence, with identical initial conditions in the EPR and the Konvoi plants similar results for the containment pressure can be expected, provided the flow paths (B) and (C) stay closed and the space behind the bio-shield remains dry.

A pressure of 1.2 MPa at RPV failure reduces the pressure increase in the containment considerably (KH05) compared to a RPV pressure of 2.0 MPa (KH02). However, a further reduction to 1.0 MPa (KH06) does not show a significant effect (Fig. 5-1).

A smaller breach size (KH03) prolongs the blowdown time and leads to less pressure increase in the containment (0.192 MPa). More melt remains in the pit.

A higher initial hydrogen concentration in the containment, as used in KH07 with 8.7%, leads to substantial higher containment pressures (Δp = 0.4 MPa). The more hydrogen exists before the blowdown the higher is the fraction of burnt hydrogen and this correlates with the containment pressure increase (Fig. 4-173, Fig. 4-175).

The differential pressure between pit and refueling room (SC2) was always below the threshold value of 0.2 MPa, which would open the flow path (B) at the vessel support.

For the tests with identical geometry (same flow paths, as in KH02, 03, 05, 06 and 07) the fraction of melt ejected out of the pit increases with the gas velocity in the annular space around the pressure vessel and can be correlated with the same function $f_d = f(Ku)$, (Fig. 4-176), which was established for the experiments with cold model fluids in EPR geometry [Mey06].

If the flow path through the vessel support into the refueling room is open (KH04), a mitigating effect occurs. The containment pressure increase was only 0.179 MPa. A considerable amount of debris and hydrogen is trapped in this small compartment and does not contribute to pressure increase in the containment, provided that the concrete slabs which cover this room stay in place, what they will do up to an overpressure of 0.08 MPa. This pressure difference between the refueling room and the containment vessel was almost reached in this test, with 0.075 MPa. Therefore, this mitigating effect should not be taken for granted. If the overpressure in the pit is high enough to open the path at the vessel support it might well be high enough to lift the concrete plates in the refueling room, and a direct path into the containment would then be available.

Contrary to expectation, the open flow path behind the bio-shield together with the presence of water lead to a large reduction of the pressure increase (test KH08). The amount of debris reaching the subcompartment 1 via the flow path along the main cooling lines was the smallest in the whole test series (24%). Almost the same amount was quenched when the smallest melt droplets were entrained through the venting flaps behind the bio-shield entering the water in SC1 (Fig. 4-1). Very little hydrogen was produced and little burned (Fig. 4-173, Fig. 4-174). Consequently the pressure increase was as low as for the tests with low RPV pressure (Fig. 5-1). This mitigating effect can only arise when water is present behind the bio-shield.

The oxidation of the iron is not complete. Apart from the particle size that inhibits a total oxidation, not enough blow-down steam is available, so the reaction is steam limited, which can also be true for the reactor case.

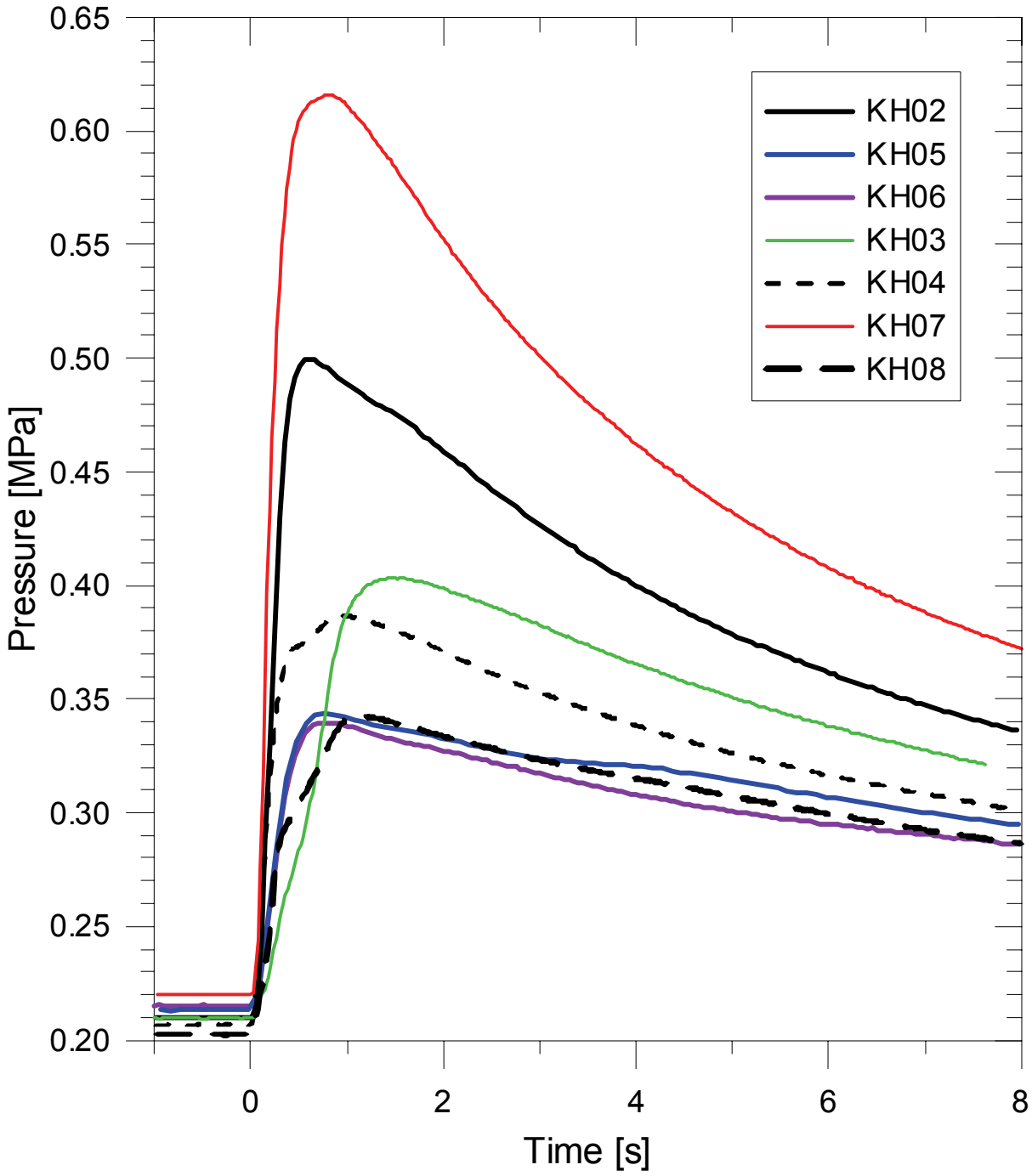

Fig. 5-1. Overview of containment pressure increase

References

[Bla96] T.K. Blanchat, M.D. Allen, “Experiments to Investigate DCH Phenomena with Large-scale Models of Zion and Surry Nuclear Power Plants”, Nuclear Engng. Design, 164, (1996).

[Bla97] T.K. Blanchat, M.M. Pilch, M.D. Allen, “Experiments to Investigate Direct Containment Heating Phenomena with Scaled Models of the Calvert Cliffs Nuclear Power Plant.” NUREG/CR-6469, SAND96-2289, Sandia National Laboratories, Albuquerque, NM., (1997).

[Bla99] T. K. Blanchat, M.M. Pilch, R.Y. Lee, L. Meyer, and M. Petit, “Direct Containment Heating Experiments at Low Reactor Coolant System Pressure in the Surtsey Test Facility,” *NUREG/CR-5746, SAND99-1634*, Sandia National Laboratories, Albuquerque, N,M., (1999).

[Lin01] J. von Linden, H. Löffler, D. Müller-Ecker, et al., „Bewertung des Unfallrisikos fortschrittlicher Druckwasserreaktoren in Deutschland, Methoden und Ergebnisse einer umfassenden Probabilistischen Sicherheitsanalyse (PSA), Entwurf zur Kommentierung“, GRS, GRS-175, (2001).

[Löf02] H. Löffler, S. Meier, A. Scharfe, “Untersuchung auslegungsüberschreitender Anlagenzustände mittels Ereignisbaumtechnik am Beispiel einer Konvoi-Anlage“, BMU, BMU-2002-594, (2002).

[Mei05] R. Meignen, D. Plassart, C. Caroli, L. Meyer, D. Wilhelm, “Direct Containment Heating at Low Primary Pressure: Experimental Investigation and Multidimensional Modeling”, NURETH-11, Avignon, France, (2005).

[Mey03] L. Meyer, M. Gargallo, “Low Pressure Corium Dispersion Experiments with Simulant Fluids in a Scaled Annular Cavity”, Nucl. Technology, 141, 257-274, (2003)

[Mey04] L. Meyer, G. Albrecht, M. Kirstahler, M. Schwall, E. Wachter, G. Wörner, „Melt Dispersion and Direct Containment Heating (DCH) experiments in the DISCO-H test facility“, FZKA 6988, Forschungszentrum Karlsruhe, (2004).

[Mey06] L. Meyer, M. Gargallo, M. Kirstahler, M. Schwall, E. Wachter, G. Wörner, „Low pressure corium dispersion experiments in the DISCO test facility with cold simulant fluids”, Report FZKA-6591, (2006).

[Mey09] L. Meyer, G. Albrecht, C. Cataldo, I. Ivanov, “Direct containment heating integral effects tests in geometries of European nuclear power plants”, Nucl. Eng. Des., 239, 2070-2084, (2009).

[Mia08] A. Miassoedov, et al.,"Results of the Quench-L2, DISCO-L2 and COMET-L2 Experiments Performed within the LACOMERA Project at the Forschungszentrum Karlsruhe", ICONE14, Miami, Florida, (2008).

[Nuc96] Nuclear Engineering and Design, 164, 1996 (Topical Issue on DCH)

[Pil96a] M.M. Pilch, M.D. Allen, "Closure of the direct containment heating issue for Zion", Nucl. Eng. Des. 164, 37-60, (1996).

[Pil96b] M.M. Pilch, "A two-cell equilibrium model for predicting direct containment heating", Nucl. Eng. Des., 164, 61-94, (1996).

[Pil97] M.M. Pilch, M.D. Allen, D.C. Williams, "Heat Transfer During Direct Containment Heating", in Advances in Heat Transfer, G.A. Greene Ed., Academic Press, Vol. 29, (1997).

[Sch07] B. Schwinges, „Überlegungen zur Raumgeometrie in einem Konvoi Sicherheitsbehälter im Hinblick auf ein mögliches DCH", Notiz–scw 2007/1, pers. com., (2007).

[Spe07] C. Spengler, „Auslegung der DISCO-Versuche für KONVOI", pers. com., (2007).

Annex A Gas Analysis

The objective of the gas composition measurements and gas analysis is to obtain data on the chemical reactions taking place during the blow-down, that is, the production of hydrogen by the metal/steam reaction and the hydrogen combustion. We cannot distinguish these processes from direct metal/oxygen reactions, but in terms of total energy release, it makes little difference that direct metal/oxygen reaction initially deposits more energy in the debris and less in the gas, because, for small particles that react efficiently, heat transfer is also efficient.

The composition of the gas in the vessel is measured by taking gas samples. The gas samples are taken from an atmosphere containing a mixture of steam and noncondensible gases. Since the steam condenses the measured mole % of nitrogen, oxygen and hydrogen are given relative to the non-condensible part of the mixture.

The pretest composition of the vessel atmosphere is known and the amount of each gas in moles can be calculated with the volume of the vessel V, the atmosphere pressure p_0 and temperature T_0, and the measured amount of added hydrogen:

Initial number of moles of hydrogen	[kmol]	$N^0_{H2} = m_{H2} / M_{H2}$	(1)
Initial number of moles of air	[kmol]	$N^0_{air} = p_0 V / (\mathbf{R} T_0)$	(2)
Initial mass of air	[kg]	$m_{air} = N^0_{air} \cdot M_{air}$	(3)
Pre-test partial pressure of air	[MPa]	$p_{1\,air} = p_0 T_1 / T_0$	(4)
Pre-test partial pressure of hydrogen	[MPa]	$p_{1\,H2} = m_{H2} R_{H2} T_1 / V$	(5)
Pre-test partial pressure of steam	[MPa]	$p_{1\,steam} = p_1 – p_{1\,air} – p_{1\,H2}$	(6)
Number of steam moles	[kmol]	$N^0_{steam} = p_{1steam} V / (\mathbf{R} T_1)$	(7)
Mass of steam	[kg]	$m_{steam} = N^0_{steam} M_{H2O}$	(8)
Total number of gas moles	[kmol]	$N_{total} = N_{air} + N_{H2} + N_{steam}$	(9)
Number of nitrogen moles	[kmol]	$N_{N2} = 0{,}7803\ N_{air}$	(10)
Number of oxygen moles	[kmol]	$N_{O2} = 0.2099\ N_{air}$	(11)
Number of argon moles	[kmol]	$N_{Ar} = 0.0093\ N_{air}$	(12)

The constants are the molecular weights, M_{H2} = 2.02 kg/kmol, M_{air} = 28.96 kg/kmol, M_{H2O}=18.02 kg/kmol, and the gas constants, R = 8314 J/kmol/K and R_{H2} = 4116 J/kg/K.

The amount of hydrogen, that is produced and burned during the test, can be determined by the nitrogen ratio method [A1]. The data and assumptions required for this method are listed below:

1. The total pretest moles of noncondensible gases must be known.

2. The measured ratios of the pretest and posttest noncondensible gases must be known.

3. It must be assumed that nitrogen is neither produced nor consumed by chemical reactions.

With the measured data of the pretest mole fractions of species i, X^0_i, the initial number of gas moles N^0_i is:

$$N^0_i = X^0_i \, (N^0_{air} + N^0_{H2} + N_{N2\ RCS/RPV}) \tag{13}$$

The calculation is usually performed separately for the subcompartment and the rest of the containment volume. The sum of moles per species determined by gas sampling may deviate from the values determined by the theoretical determination of pretest composition, due to incomplete mixing of the components and the uncertainty in the acquisition and analysis of the gas samples. With the assumption that the number of nitrogen moles has not changed, the post test number of moles of oxygen and hydrogen can be determined from the measured post test mole fractions X^2_i:

$$N^2_{O2} = N^0_{N2} \, X^2_{O2} / X^2_{N2} \tag{14}$$

$$N^2_{H2} = N^0_{N2} \, X^2_{H2} / X^2_{N2} \tag{15}$$

The number of moles of burned hydrogen is linked to the decrease of oxygen moles,

$$N^2_{H2\ burned} = 2 \, (N^0_{O2} - N^2_{O2}) \tag{16}$$

and the balance of hydrogen gives the moles of produced hydrogen:

$$N^2_{H2\ produced} = N^2_{H2} - N^0_{H2} + N^2_{H2\ burned}, \tag{17}$$

The fraction burned is $F_{H2} = N^2_{H2\ burned} / (N^0_{H2} + N^2_{H2\ produced})$. (18)

The ratio of hydrogen moles produced to iron moles oxidized depends on the kind of iron oxide formed. Based on the experience at the Sandia National Laboratories, Blanchat [A2] gives a ratio of 1:1, which implies that in a first step only FeO is formed. For aluminum it is 1.5:1, 3 moles of hydrogen are produced by the oxidation of 2 moles of aluminum with water.

In case that there is a significant nitrogen fraction in the blow down gas, its mass has to be added to N^0_{N2} in equations 14 and 15.

Uncertainty analysis

A comparison of the initial gas concentrations determined by two different methods shows the uncertainty of the gas measurements. The first method is the determination according to relations (1) through (12). Specifically, the amount of hydrogen is determined directly by the difference of the weight of the hydrogen bottle before and after filling it to the containment vessel, while the amount of other gases is determined by applying the law for ideal gas and the natural composition of air.

In the second method the initial composition of the dry gas is determined from the gas samples taken pretest and by application of the relation $N^0_i = X^0_i \, (N^0_{air} + N^0_{H2})$, with X^0_i the fraction of the specific gas listed in Table 4-6 through Table 4-13.

The results are listed in table A1. The percentage difference is defined by:

$$(N_{sample} - N_{weigth(ideal\ gas)}) / N_{weigth(ideal\ gas)} * 100$$

Table A1: Uncertainty in pretest dry gas determination

	KH01	KH02	KH03	KH04	KH05	KH06	KH07	KH08
N^0_{steam} kmol	0.333	0.325	0.293	0.295	0.350	0.329	0.322	0.303
N^0_{N2} - eq.2+10 kmol	0.439	0.442	0.440	0.436	0.426	0.441	0.443	0.446
N^0_{O2} - eq.2+10 kmol	0.118	0.119	0.119	0.117	0.115	0.119	0.119	0.120
N^0_{H2} - weight kmol	0.051	0.051	0.062	0.052	0.049	0.061	0.085	0.050
N^0_{H2} - weight %	***5.42***	***5.37***	***6.74***	***5.69***	***5.15***	***6.45***	***8.67***	***5.39***
N^0_{N2}-sample kmol	0.450	0.444	0.451	0.476	0.431	0.457	0.445	0.456
N^0_{O2}-sample kmol	0.104	0.104	0.121	0.096	0.114	0.117	0.119	0.112
N^0_{H2}-sample kmol	0.060	0.069	0.053	0.039	0.049	0.052	0.089	0.052
N^0_{H2}-sample %	***6.34***	***7.33***	***5.79***	***4.27***	***5.19***	***5.48***	***9.15***	***5.59***
	Percentage difference related to total gas content (including steam):							
N_2	1.12	0.20	1.17	4.36	0.56	1.69	0.15	1.07
O_2	-1.47	-1.58	+0.30	-2.35	-0.05	-0.16	-0.07	-0.82
H_2	***+0.92***	***+1.96***	***-0.95***	***-1.42***	***+0.04***	***-0.97***	***+0.48***	***+0.20***
	Percentage difference related to specific gas fraction:							
N_2	1.16	-0.80	1.20	7.72	0.01	2.37	-0.89	0.97
O_2	-11.76	-12.54	+2.31	-18.13	-0.43	-1.25	-0.61	-6.34
H_2	+16.98	+36.44	-14.12	-25.01	+0.86	-14.99	+5.51	+3.69

Generally, the data determined by the first method are expected to be more precise. The hydrogen concentration determined by the sampling is up to 2% higher, but also up to 1.4% lower than the weighing data. The uncertainty in the evaluation of the gas samples had been improved lately, and was stated by the Engler-Bunte Institute to be 0.1 vol% for H_2, 0.3% for O_2 and 0.4% for N_2. Therefore, the main error must have occurred during the sampling process. In some tests some of the sampling lines were found to have dust inside, which may have impeded the fast filling of the gas bottles. Other possible errors may come from an insufficient mixing of the containment atmosphere while the samples are taken. For reasons of consistency, for the analysis of hydrogen production and combustion the data obtained by sampling are taken throughout.

[A1] T.K. Blanchat, M.D. Allen, M.M. Pilch, R.T. Nichols, "Experiments to Investigate Direct Containment Heating Phenomena with Scaled Models of the Surry Nuclear Power Plant", *NUREG/CR-6152, SAND93-2519*, Sandia Laboratories, Albuquerque, N.M., (1994)

[A2] T.K. Blanchat, M.M. Pilch, R.Y. Lee, L. Meyer, and M. Petit, "Direct Containment Heating Experiments at Low Reactor Coolant System Pressure in the Surtsey Test Facility," *NUREG/CR-5746, SAND99-1634*, Sandia National Laboratories, Albuquerque, N.M., (1999).

ISSN 1869-9669
ISBN 978-3-86644-579-6